

# JUACEP Summer Program 2013 at Nagoya University



Japan-US Advanced Collaborative Education Program

Nagoya University

Copyright © JUACEP 2013 All Rights Reserved.

Published in November, 2013

Leaders of JUACEP

Professor Noritsugu Umehara

Professor Yang Ju

Japan-US Advanced Collaborative Education Program (JUACEP)

Graduate School of Engineering

Nagoya University   
NAGOYA UNIVERSITY

Furo-cho, Chikusa-ku, Nagoya, 464-8603, JAPAN

JUACEP@engg.nagoya-u.ac.jp

<http://www.juacep.engg.nagoya-u.ac.jp>

# Table of Contents

## <1> About the Program

a) Overview	...5
b) Participants	...6
c) Schedule	...8

## <2> Classes & Events

a) Japanese Class	...12
b) Handcraft Exercise	...14
c) Field Trip	...15
d) Research Internship	...16
- Research Reports	...18
e) Workshop	
- The 5 <sup>th</sup> Workshop (for UM students)	...143
- The 6 <sup>th</sup> Workshop (for UCLA students)	...178

## <3> Reports on JUACEP Program

...207

## <4> Appendix

a) Pictures	...226
b) Handout Materials	
-Orientation Agenda	...232
-Campus Information	...234
-Campus Map	...240
-Dining Map	...241
-Hospital Information	...242



<1>

## About the Program



## 1-a. Overview

This program was designed for graduate and doctoral students of University of Michigan and University of California, Los Angeles. The students had research internship at laboratories of Nagoya University (NU) and worked on the specific research projects under their supervisors at NU.

They wrote a research report and gave the final presentation at the workshop about their research findings. The report and presentation were evaluated by each NU supervisor and the students got credits (2 or 3 credits depending on the program period) from Nagoya University. The credits were transferred to ME590 at University of Michigan under the agreement.

Also, the optional Japanese language class, handcraft exercise and factory tours were offered during the program.

### ~Program Contents~

UM students: May 14 – August 8, 2013

UCLA students: June 18 – August 22, 2013

May		
	14	<b>Orientation for UM students</b>
	15	<b>Research Project, Japanese Language Class</b>
Jun.	14	
	18	<b>Orientation for UCLA students</b>
	19	<b>Research Project, Japanese Language Class</b>
	24	<b>Field Trip to Toyota Factory, SCMAGLEV &amp; Railway Park and Ukai on the Nagara River</b>
Jul.	2	<b>Handcraft Exercise</b>
	16	
	18	
Aug.	7	
	8	<b>Workshop and Farewell for UM students</b>
	21	
	22	<b>Workshop and Farewell for UCLA students</b>

## 1-b. Participants

### *Students from University of Michigan*

<b>Weiyu Cao</b>	Aerospace Engineering (M1)
<b>Yu-Shiuan Chu</b>	Electrical Engineering Systems (M1)
<b>Ambarish Krishnanand Desai</b>	Aerospace Engineering (M1)
<b>Michael Bigang Ding</b>	Macromolecular Science and Engineering (D1)
<b>Zhenyu Gan</b>	Mechanical Engineering (M1)
<b>Sriram Ganesan</b>	Aerospace Engineering (D1)
<b>Nishant Mayur Narechania</b>	Aerospace Engineering (M1)
<b>Hao Wang</b>	Mechanical Engineering (M1)
<b>Yi-Kai Wang</b>	Mechanical Engineering (M1)
<b>Yan Zhang</b>	Mechanical Engineering (M1)
<b>Yihao Zheng</b>	Mechanical Engineering (M1)

### *Students from University of California, Los Angeles*

<b>Chung-Wen Chuang</b>	Civil and Environmental Engineering (D4)
<b>Owen Suyuan Liang</b>	Materials Science and Engineering (M1)
<b>Le Nguyen Khuong Ninh</b>	Mechanical Engineering (M1)
<b>Jonathan Timothy Quan</b>	Materials Science and Engineering (D4)
<b>Christopher Charles Roberts</b>	Materials Science and Engineering (D2)
<b>Justin Wang</b>	Materials Science and Engineering (M1)
<b>Yaodong Wang</b>	Materials Science and Engineering (D1)

### *Instructors*

<b>Prof. Yasuhiko Sakai</b>	Director of Creation Plaza
<b>Asst. Prof. Kazue Kaneko</b>	Creation Plaza
<b>Mr. Masafumi Nakakimura</b>	Chief Technical Staff
<b>Mr. Koji Yamamoto</b>	Technical Staff
<b>Mr. Shintaro Goto</b>	Technical Staff
<b>Mr. Kiyonori Saito</b>	Technical Staff
<b>Ms. Sumie Yasui</b>	Japanese Teacher

*Advisors at Nagoya University*

<b>Assoc. Prof. Hosei Nagano</b>	Aerospace Engineering
<b>Prof. Nobuo Kawaguchi</b>	Computational Science and Engineering
<b>Assoc. Prof. Noboru Sakamoto</b>	Aerospace Engineering
<b>Prof. Yang Ju</b>	Mechanical Science and Engineering
<b>Prof. Yoji Yamada</b>	Mechanical Science and Engineering
<b>Assoc. Prof. Dai Okumura</b>	Computational Science and Engineering
<b>Asst. Prof. Keiichi Kitamura</b>	Aerospace Engineering
<b>Prof. Tsuyoshi Inoue</b>	Mechanical Science and Engineering
<b>Prof. Yoshikazu Hayakawa</b>	Mechanical Science and Engineering
<b>Prof. Tatsuya Suzuki</b>	Mechanical Science and Engineering
<b>Prof. Noritsugu Umehara</b>	Mechanical Science and Engineering
<b>Prof. Hikaru Nakamura</b>	Civil Engineering
<b>Prof. Yahachi Saito</b>	Quantum Engineering
<b>Prof. Kenji Fukuzawa</b>	Micro-Nano Systems Engineering
<b>Prof. Naoyuki Kanetake</b>	Materials Science and Engineering
<b>Prof. Hiroshi Amano</b>	Electrical Engineering and Computer Science
<b>Prof. Takashi Ishikawa</b>	Aerospace Engineering
<b>Prof. Toru Ujihara</b>	Materials Science and Engineering

*Coordinators at Partner Universities*

<b>Prof. Katsuo Kurabayashi</b>	Mechanical Engineering, University of Michigan
<b>Prof. Jenn-Ming Yang</b>	Materials Science and Engineering, UCLA

*JUACEP Members*

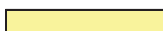
<b>Prof. Yang Ju</b>	Mechanical Science and Engineering
<b>Prof. Noritsugu Umehara</b>	Mechanical Science and Engineering
<b>Assoc. Prof. Hirofumi Aoki</b>	Mechanical Science and Engineering
<b>Assoc. Prof. Yasumasa Ito</b>	Mechanical Science and Engineering
<b>Tomoko Kato</b>	Administrative Officer
<b>Chiharu Yada</b>	Administrative Officer

# 1-c. Schedule

## JUACEP Summer Program 2013 Schedule

Day	Date		8:45-10:15	10:30-12:00		13:00-14:30	14:45-16:15	16:15-	
1	5/13/2013	Mon	Arrival (UM students)						
2	5/14/2013	Tue	Orientation for UM students (10:00@ES Hall)		Lunch @ Chez Jiroud	1.Stipend, tuition, insurance, admission fee, in-bound ticket. 2.Passport, out-bound ticket photocopy 3. Introduction to lab TAs & assignation to each laboratory (13:30- @ ES031)		Research at Lab	
3	5/15/2013	Wed	Japanese Lang (UM)	Research at Each Lab		Research at Each Lab	Introduction to PE 1-1	Research at Each Lab	
4	5/16/2013	Thu	Research at Each Lab	Japanese Lang (UM)		Research at Each Lab			
5	5/17/2013	Fri	Research at Each Lab			Research at Each Lab			
6	5/18/2013	Sat							
7	5/19/2013	Sun							
8	5/20/2013	Mon	Research at Each Lab			Research at Each Lab			
9	5/21/2013	Tue	Research at Each Lab	Japanese Lang (UM)		Research at Each Lab			
10	5/22/2013	Wed	Research at Each Lab			Research at Each Lab	Introduction to PE 1-2	Research at Each Lab	
11	5/23/2013	Thu	Research at Each Lab	Japanese Lang (UM)		Research at Each Lab			
12	5/24/2013	Fri	Research at Each Lab			Research at Each Lab			
13	5/25/2013	Sat							
14	5/26/2013	Sun							
15	5/27/2013	Mon	Research at Each Lab			Research at Each Lab			
16	5/28/2013	Tue	Research at Each Lab	Japanese Lang (UM)		Research at Each Lab			
17	5/29/2013	Wed	Research at Each Lab			Research at Each Lab	Introduction to PE 1-3	Research at Each Lab	
18	5/30/2013	Thu	Research at Each Lab	Japanese Lang (UM)		Research at Each Lab			
19	5/31/2013	Fri	Research at Each Lab			Research at Each Lab			
20	6/1/2013	Sat							
21	6/2/2013	Sun							
22	6/3/2013	Mon	Research at Each Lab			Research at Each Lab			
23	6/4/2013	Tue	Research at Each Lab	Japanese Lang (UM)		Research at Each Lab			
24	6/5/2013	Wed	Research at Each Lab			Research at Each Lab	Introduction to PE 2	Research at Each Lab	
25	6/6/2013	Thu	Research at Each Lab	Japanese Lang (UM)		Research at Each Lab			
26	6/7/2013	Fri	Research at Each Lab			Research at Each Lab			
27	6/8/2013	Sat							
28	6/9/2013	Sun							
29	6/10/2013	Mon	Research at Each Lab			Research at Each Lab			
30	6/11/2013	Tue	Research at Each Lab	Japanese Lang (UM)		Research at Each Lab			
31	6/12/2013	Wed	Research at Each Lab			Research at Each Lab	Introduction to PE 3-1	Research at Each Lab	
32	6/13/2013	Thu	Research at Each Lab	Japanese Lang (UM)		Research at Each Lab			
33	6/14/2013	Fri	Research at Each Lab			Research at Each Lab			
34	6/15/2013	Sat							
35	6/16/2013	Sun							
36	6/17/2013	Mon	Arrival (UCLA students)						
37	6/18/2013	Tue	Orientation for UCLA students (10:00@ES Hall)		Lunch @ Chez Jiroud	Research at Each Lab			
38	6/19/2013	Wed	Japanese Lang (UCLA)	Research at Each Lab		1.Stipend, tuition, insurance, admission fee, in-bound ticket. 2.Passport, out-bound ticket photocopy (13:30- @ ES031)	Introduction to PE 3-2	Research at Lab	
39	6/20/2013	Thu	Research at Each Lab	Japanese Lang (UCLA)		Research at Each Lab			
40	6/21/2013	Fri	Research at Each Lab			Research at Each Lab			
41	6/22/2013	Sat							
42	6/23/2013	Sun							
43	6/24/2013	Mon	Toyota Motor Factory Visit (9:30-10:30), SCMAGLEV & Railway Park (11:30-15:00)						
44	6/25/2013	Tue	Research at Each Lab	Japanese Lang (UCLA)		NUSIP Lecture 1			
45	6/26/2013	Wed	Research at Each Lab			NUSIP Lecture 2			
46	6/27/2013	Thu	Research at Each Lab	Japanese Lang (UCLA)		Research at Each Lab	Introduction to PE 4		
47	6/28/2013	Fri	Research at Each Lab			NUSIP Lecture 3			
48	6/29/2013	Sat							
49	6/30/2013	Sun							

50	7/1/2013	Mon	Research at Each Lab		NUSIP Lecture 4
51	7/2/2013	Tue	Research at Each Lab	Japanese Lang (UCLA)	Handcraft Exercise (Group A)
52	7/3/2013	Wed	Research at Each Lab		NUSIP Lecture 5 Introduction to PE 5-1
53	7/4/2013	Thu	Research at Each Lab	Japanese Lang (UCLA)	Handcraft Exercise (Group B) NUSIP Lecture 6
54	7/5/2013	Fri	Research at Each Lab		NUSIP Lecture 7
55	7/6/2013	Sat			
56	7/7/2013	Sun			
57	7/8/2013	Mon	Research at Each Lab		NUSIP Lecture 8
58	7/9/2013	Tue	Research at Each Lab	Japanese Lang (UCLA)	Handcraft Exercise (Group C)
59	7/10/2013	Wed	Research at Each Lab		NUSIP Lecture 9 Introduction to PE 5-2
60	7/11/2013	Thu	Research at Each Lab	Japanese Lang (UCLA)	NUSIP Lecture 10
61	7/12/2013	Fri	Research at Each Lab		NUSIP Lecture 11
62	7/13/2013	Sat			
63	7/14/2013	Sun			
64	7/15/2013	Mon	Marine Day		
65	7/16/2013	Tue	Research at Each Lab	Japanese Lang (UCLA)	Handcraft Exercise (Group D) NUSIP Lecture 12
66	7/17/2013	Wed	Research at Each Lab		NUSIP Lecture 13
67	7/18/2013	Thu	Research at Each Lab	Japanese Lang (UCLA)	Research at Each Lab
68	7/19/2013	Fri	Research at Each Lab		Research at Each Lab
69	7/20/2013	Sat			
70	7/21/2013	Sun			
71	7/22/2013	Mon			NUSIP Special Lecture
72	7/23/2013	Tue			Research at Each Lab
73	7/24/2013	Wed	Research at Each Lab		NUSIP Lecture 14
74	7/25/2013	Thu			NUSIP Lecture 15
75	7/26/2013	Fri			Research at Each Lab
76	7/27/2013	Sat			
77	7/28/2013	Sun			
78	7/29/2013	Mon			
79	7/30/2013	Tue			
80	7/31/2013	Wed	Research at Each Lab		Research at Each Lab
81	8/1/2013	Thu			
82	8/2/2013	Fri			
83	8/3/2013	Sat			
84	8/4/2013	Sun			
85	8/5/2013	Mon			
86	8/6/2013	Tue	Research at Each Lab		Research at Each Lab
87	8/7/2013	Wed			
88	8/8/2013	Thu	Workshop and Farewell Party for UM students		
89	8/9/2013	Fri	Departure (UM students)		
90	8/10/2013	Sat			
91	8/11/2013	Sun			
92	8/12/2013	Mon			
93	8/13/2013	Tue	Research at Each Lab		Research at Each Lab
94	8/14/2013	Wed			
95	8/15/2013	Thu	The Bon Festival		
96	8/16/2013	Fri	The Bon Festival		
97	8/17/2013	Sat			
98	8/18/2013	Sun			
99	8/19/2013	Mon			
100	8/20/2013	Tue	Research at Each Lab		Research at Each Lab
101	8/21/2013	Wed			
102	8/22/2013	Thu	Workshop and Farewell Party for UCLA students		
103	8/23/2013	Fri	Departure (UCLA students)		

	Japanese Language Class		Field Trip
	NUSIP Lectures		Special Lecture
	Handcraft Exercise		Workshop
			Holidays
	Introduction to Production Engineering (PE)		



<2>

## Classes & Events

## 2-a. Japanese Class

### JUACEP Summer Program 2013      Japanese Course Syllabus

Course name	Japanese Language
Teaching staff	Ms. YASUI Sumie
Course period	① May 15 - June 13, 2013 for University of Michigan students ② June 19- July 18, 2013 for UCLA students
Weekly timetable	Tuesday & Thursday 2nd period (10:30-12:00) * May 15 & June 19 (Wed) 1 <sup>st</sup> period (8:45-10:15)
Classroom	#3 Building, room 441
Textbook	“GENKI An Integrated Course in Elementary Japanese” I (The Japan Times)  This textbook is a comprehensive approach to developing the four basic language skills (listening, speaking, reading and writing) in order to cultivate overall Japanese-language ability.  *Some teaching material will be given in class.
Course Contents	<p><b>Course outline</b></p> <p>The purpose of this course is to introduce the most essential Japanese words and conversations for everyday life. Students will learn the basic grammar and conversational expressions of Japanese.</p> <p><b>Classroom activities</b></p> <p>Basic communication skills required in everyday life will be taught by introducing new vocabulary, new grammar, and practicing listening, conversation and role-playings.</p>
Course schedule	<p>1. ① 5/15(Wed) ② 6/19(Wed)</p> <p>Greeting Expressions, Introducing yourself</p> <p>Noun sentences 1, Occupation, Nationality, Age, Numbers 1-100</p> <p>2. ① 5/16(Thu) ② 6/20(Thu)</p> <p>Shopping, Classroom expressions</p> <p>Noun sentences 2, Price, Numbers 101-1,000,000</p>

---

3. ① 5/21(Tue) ② 6/25(Tue)

Describing where things are, Locations

Placing an order at a restaurant

4. ① 5/23(Thu) ② 6/27(Thu)

Talking about your daily life

Verbal sentences 1, Time reference, Adverbs

5. ① 5/28(Tue) ② 7/2(Tue)

Invitations, Suggestions, Desires

Verbal sentences 2, Days/Weeks/Months/Years, Counting

6. ① 5/30(Thu) ② 7/4(Thu)

Talking about your family

Adjectives, Likes or Dislikes, Degree expressions, Family terms

7. ① 6/4(Tue) ② 7/9(Tue)

Talking about your week-end

Past tense, Time words

8. ① 6/6(Thu) ② 7/11(Thu)

Making a request (Verb-Te-form ), Progressive actions,

Describing your status

9. ① 6/11(Tue) ② 7/16(Tue)

Asking permission, Prohibition, Negative request

Describing two things

10. ① 6/13(Thu) ② 7/18(Thu)

Talking about your interests

Plain form

---

## 2-b. Handcraft Exercise

### *“Demonstration of the Internal Combustion Engine”*

**Date:** Group A – Tue., July 2  
Group B – Thu., July 4  
Group C – Tue., July 9  
Group D – Tue., July 16

**Time:** 13:00-16:00

**Place:** Creation Plaza (5<sup>th</sup> floor, IB Building)

**Staff:** Yasuhiko Sakai, Professor, Director of Creation Plaza  
Kazue Kaneko, Asst. Professor, Creation Plaza  
Masafumi Nakakimura, Chief Technical Staff  
Koji Yamamoto  
Shintaro Goto  
Kiyonori Saito

#### **Schedule:**

- Opening remarks: By Professor Yasuhiko Sakai
- Lecture of the basis of the Internal Combustion Engine  
~History, Characteristic, Operation principle, Practice engine~
- Assembling practice  
~Disassembling, Assembling, Adjustment~
- Performance test



## 2-c. Field Trip

**Date:** Mon., June 24

**Visited Places:**

- \* Toyota Motor Factory (Tsutsumi Plant)
- \* SCMAGLEV and Railway Park
- \* Ukai on the Nagara River



**Schedule:**

Time	Event
08:30	Departure from Nagoya University
09:30	Arrival at Toyota Motor Factory
09:30-10:30	Bus tour of the factory
10:30	Departure from Toyota Motor Factory
11:30	Arrival at SCMAGLEV and Railway Park
11:30-12:30	Lunch
12:30-15:00	Tour of the park
15:00	Departure from SCMAGLEV and Railway Park
16:30	Arrival at Gifu Park
16:30-18:00	Climbing Mt. Kinka and visiting Gifu Catsle
18:00-20:30	Ukai (cormorant fishing) watching on the Nagara River
20:30	Departure from Gifu Park



## 2-d. Research Internship

### Participants from University of Michigan

	Name	Research Theme	Report Title
1	Weiyu Cao	Advanced Two-phase Heat Transfer Device	Study on the Loop Heat Pipe With New Type Evaporator for Mass Production (p.18)
2	Yu-Shiuan Chu	Human Activity Sensing Corpus and Its Application	Design Accuracy Improving Methods in Human Activity Sensing Consortium Project (N/A)
3	Ambarish Krishnanand Desai	Nonlinear Control for Mechanical Systems	Linear and Nonlinear Optimal Control of Furuta Pendulum (p.27)
4	Michael Bigang Ding	Development of Nanostructured Materials and Their Applications	Non-contact AFM Characterization of Au-Si and Au-Glass Substrates (p.40)
5	Zhenyu Gan	Impact Suppression Control of a Cart	Application of Momentum-exchange-impact-damper on Vehicle Collision (p.49)
6	Sriram Ganesan	Monte-Carlo Simulation of Polycrystal Plasticity using a Discrete Dislocation Plasticity Approach	Monte-Carlo Simulation of Polycrystal Plasticity using Discrete Dislocation Plasticity Approach for Lamellar Materials (p.58)
7	Nishant Mayur Narechania	Accurate Hypersonic Heating on Unstructured Grids	A Second Order Accurate Scheme for Ideal Magnetohydrodynamics with Divergence-Free Reconstruction (p.68)
8	Hao Wang	Theoretical and Experimental Verification of Sensorless Magnetic Levitation using Hall Element Signal	Theoretical Analysis and Experimental Verification of Self-sensing Magnetic Levitation using Hall Signal (N/A)
9	Yi-Kai Wang	Visual Feedback Control for Table Tennis Robot	Visual Feedback Control for Table Tennis Robot (p.78)
10	Yan Zhang	Collision Avoidance Control using a Small EV	Automated Steering System for Obstacle Avoidance based on Potential Field Method (p.83)
11	Yihao Zheng	Surface Treatment of Resin for Human Bone Simulation	Bone Analog Material for Orthopedic Surgical Training (p.89)

**Participants from UCLA**

	Name	Research Theme	Report Title
1	Chung-Wen Chuang	Simulation of RC Structures under Earthquake	Simulation of RC Structures under Cyclic Loading (p.95)
2	Owen Suyuan Liang	Electric Transport Properties of Individual Carbon Nanotubes Measured in Electron Microscope	Two Point Probe Resistivity Measurement of Carbon Nanotubes (p.105)
3	Le Nguyen Khuong Ninh	Viscoelastic Properties of Liquid Lubricant Confined in Nanometer-sized Gaps	Evaluation of Slip in Liquid Lubricant Confined in Molecularily Narrow Gap by Fiber Wobbling Method (N/A)
4	Jonathan Timothy Quan	Material Development by Severe Plastic Deformation Process	Low Temperature Development of Metal Matrix Composites through Compression Torsion Process (p.111)
5	Christopher Charles Roberts	Semipolar/Nonpolar LEDs on Patterned Silicon Substrates	III-nitride LEDs on Patterned Silicon Substrates -Fabrication of Backside Contacts via Wet Etching- (p.117)
6	Justin Wang	Mechanics of Polymer Matrix Composite Materials	Hand Layup Fabrication with Vacuum Bagging and Compression Testing of Cross-ply Carbon Fiber Pre-Preg Tubes (p.128)
7	Yaodong Wang	Solution Growth of SiC	Effect of Adding Solvent Element on 4H-SiC by using Top Seed Solution Growth (p.134)

# STUDY ON THE LOOP HEAT PIPE WITH NEW TYPE EVAPORATOR FOR MASS PRODUCTION

**Weiyu Cao**

Department of Aerospace Engineering  
University of Michigan  
Ann Arbor, Michigan 48105  
Email: caoweiyu@umich.edu

**Hosei Nagano**

Department of Aerospace Engineering  
Nagoya University  
Nagoya, Aichi 466-0811  
Email: nagano@naue.nagoya-u.ac.jp

## ABSTRACT

*A mathematical model of LHP with a new type evaporator was built. A test LHP was designed and built to test the performance of the new type evaporator. Results showed that the LHP could work under the heat load range between 20w and 100w. The modeling results could match with the experiment data. However, several limitations were found, such as the weak point of the structure and the high evaporating temperature which might damage the wick. Through the parametric study based on the mathematical model, some influence factors on the operating temperature profile shape were found and discussed.*

## Introduction

Loop Heat pipe (LHP) is a kind of effective and efficient two-phase heat transfer device [1]. It utilizes the evaporation and condensation of a working fluid to transfer heat, and the capillary forces developed in fine porous wicks to circulate the fluid [2]. Because the LHPs do not need extra driving power to maintain the operation and have many other advantages such as flexibility in design and capability of long distance transportation, they have been widely used in the thermal controls in spacecraft [3–6]. Many studies have hence been conducted around LHPs. Ku *et al* [2, 7] introduced the operating characteristic of LHPs and studied the set point control of LHPs via experimental approach. Kaya *et al* [8] established a mathematical model for a LHP under steady state. Hoang *et al* [9] assessed 5 different two-phase pressure drop correlations of pipe flow and improved modeling of the condenser. Chuang *et al* [10] developed a complicated steady-state model and achieved better agreement with the experimental data. Bai *et al* [11] introduced a new two-phase flow model which assumed that the liquid and vapor phases were separated in

the condenser pipe and took the influence of the void fraction in CC in to consideration. Recently, with the increasing demand of energy saving, the application of LHP on terrestrial fields, such as electronic devices, has been considered [12, 13]. However, a main obstacle of extending the LHPs to commercial market was the cost and manufacturing cycle of the evaporator. It would take more than 300 US dollars to make one evaporator. Due to these flaws, mass production of LHPs was difficult. Nagoya University introduced a new design of evaporator, which could be manufactured through impact pressure process. The cost of this kind of evaporator could be less than 1 US dollar and the manufacturing cycle could be reduced significantly. Therefore, present work focused on testing the performance and limitation of a LHP with the evaporator of new design. A mathematical model was first built to get an overview of the operating characteristics and limitations of the LHP and determine the parameters such as the transportation length and the working fluid inventory of the LHP. Then the other parts of the LHP were designed, manufactured and assembled with the evaporator. Finally, experimental measurements were taken to test the performance of the LHP and estimate its potential for commercial use. The mathematical model was also revised according to the experimental data.

## Mathematical Model

Same as a typical LHP, the LHP in this study was also consisted by an evaporator, a condenser, a vapor line, a liquid line and a compensation chamber (CC), where the compensation chamber was made as an integral part of the evaporator, as shown in Fig. 1. The modeling of the different parts of the LHP and the solution algorithm were introduced below.

Fig. 2 showed the inner structure of the newly designed

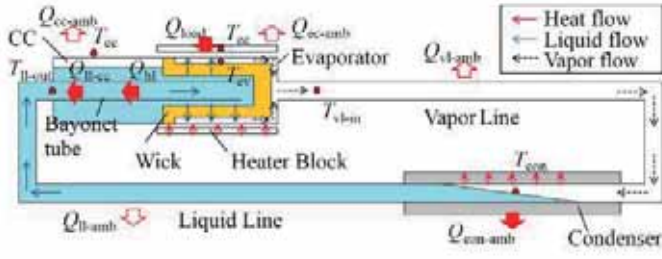


Figure 1. Theoretical configuration of LHP

evaporator-CC integral. The heat transfer in the evaporator and CC could be reduced to the network described in Fig. 3.  $T_{ev}$  was temperature at the liquid-vapor interphase in the wick of evaporator and was usually called evaporating temperature.  $T_{cc}$  was the temperature of the working fluid in CC. Under a steady state, there should be no heat and mass transfer between the evaporator core and CC. Therefore in this reduced model, it was assumed that the pressure and temperature of the fluid in evaporator core and CC were same. This pressure and temperature were also shared by the inner surface of the wick in both evaporator and CC.  $T_{ev,c}$  was the temperature of the evaporator case while  $T_{cc,c}$  was the temperature of CC case.  $T_{bay,in}$  was the temperature at the inlet of the bayonet tube, which was also the outlet temperature of liquid line.  $T_{amb}$  was the ambient temperature.

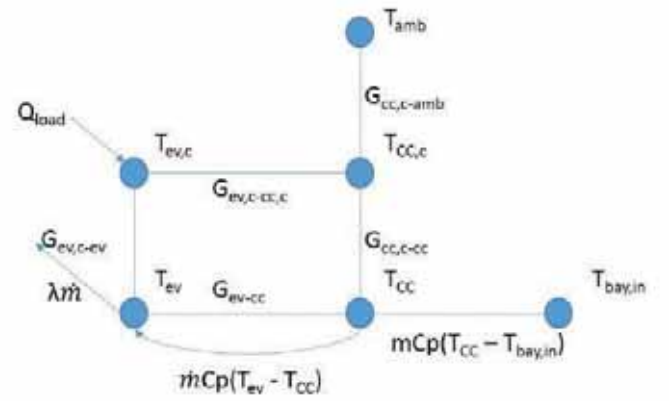


Figure 3. Heat transfer network in evaporator-CC integral

CC case, described as:

$$Q_{ev,c-cc,c} = G_{ev,c-cc,c} \cdot (T_{ev,c} - T_{cc,c}) \quad (1)$$

where  $G_{ev,c-cc,c}$  was the heat conductance between the cases of evaporator and CC and could be gained easily through Fourier's Law; The other path was from the evaporator case to the liquid-vapor interface in the evaporator wick, described as:

$$Q_{ev,c-ev} = G_{ev,c-ev} \cdot (T_{ev,c} - T_{ev}) \quad (2)$$

where  $G_{ev,c-ev}$  was the heat conductance between the evaporator case and the vapor-liquid interphase in the evaporator wick, which would be discussed later.

Part of  $Q_{ev,c-ev}$  would evaporate the liquid at the interface, described as:

$$Q_{ev} = \lambda \cdot \dot{m} \quad (3)$$

The rest was transferred to the evaporator core and CC, in the process of which part of the heat was consumed for raising the temperature of the fluid from  $T_{cc}$  to  $T_{ev}$ , which could be described as the two equations below:

$$Q_{ev-cc,ht} = \dot{m}c_p \cdot (T_{ev} - T_{cc}) \quad (4)$$

$$Q_{ev-cc,ht} = G_{ev-cc} \cdot (T_{ev} - T_{cc}) \quad (5)$$

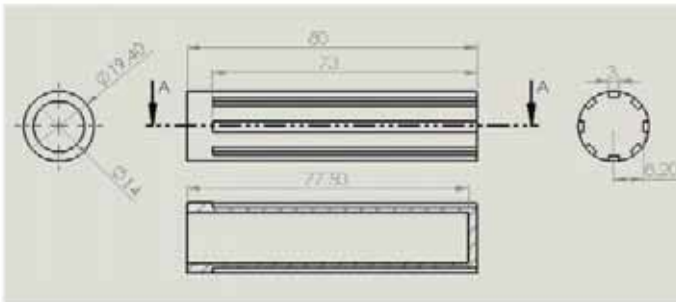
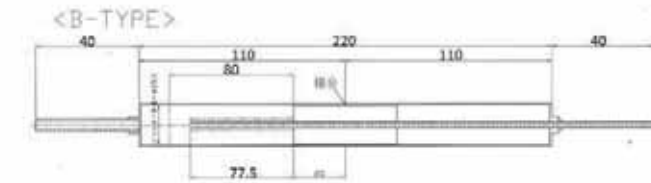


Figure 2. Structure of the new type evaporator

It was assumed all of the heat load was applied on the evaporator case without any leak to the ambient. Hence from the network shown in Fig. 3 it could be found that there were two paths for the heat load: One was from the evaporator case to the

Four thermal conductance:  $G_{ev,c-cc-c}$ ,  $G_{ev,c-ev}$ ,  $G_{ev-cc}$  and  $G_{cc,c-cc}$  could be found in the network shown in Fig. 3. As stated above,  $G_{ev,c-cc-c}$  could be gained easily with Fourier's Law. However, the heat transfer process through the other three paths were much more complicated. Actually,  $G_{ev,c-ev}$  and  $G_{cc,c-cc}$  were usually gained by experimental data or detailed CFD approach while  $G_{ev-cc}$  could be modeled by the following equation [11]:

$$G_{ev-cc} = \frac{\dot{m}C_{pl}}{(r_o/r_i)^\eta - 1} \quad (6)$$

where  $\dot{m}$  was the mass flow rate of the loop,  $C_{pl}$  was the specific thermal capacity of the liquid working fluid,  $R_o/r_i$  were the outer/inner radius of the pipe respectively and  $\eta$  could be expressed as:

$$\eta = \frac{\dot{m}C_{pl}}{(2\pi k_e L_{wi})} \quad (7)$$

where  $L_{wi}$  was the length of the wick and  $k_e$  was the effective thermal conductance of the wick, given by:

$$k_e = (k_{max})^\eta \cdot (k_{min})^{1-\eta} \quad (8)$$

where

$$k_{max} = \Phi \cdot k_f + (1 - \Phi) \cdot k_s \quad (9)$$

$$k_{min} = \frac{k_f k_s}{\Phi k_s + (1 - \Phi) k_f} \quad (10)$$

where  $k_s$  and  $k_f$  were the thermal conductance of the wick material and working fluid each.

### Single Phase Pipe Flow

Under a steady state, flows in the transport lines (vapor and liquid lines), the condenser pipe and the vapor grooves in the evaporator could all be treated as pipe flows due to their common characteristics: the length of the flow path was much longer than the diameter. Therefore, the modeling of the flows in these parts could all be reduced to the two models described in this and the next section: single-phase pipe flow model and two-phase pipe flow model. For single-phase flow, the energy conservation equation of the working fluid could be expressed by:

$$-\dot{m}C_p \frac{dT}{dL} = (UA/L)_{p-a}(T - T_{amb}) \quad (11)$$

where

$$\frac{1}{(UA/L)_{p-a}} = \frac{1}{h_i \pi d_i} + \frac{In d_o/d_i}{2\pi k_s} + \frac{1}{h_o \pi d_o} \quad (12)$$

where  $h_i$ , the heat transfer coefficient at the inner wall was given by:

$$h_i = \frac{Nu \cdot k_f}{d_i} \quad (13)$$

where  $Nu$  was got by:

$$Nu = \begin{cases} 4.36 & Re < 2300 \\ 0.023 Re^{0.8} Pr^n & Re > 2300 \end{cases} \quad (14)$$

The heat transfer between the outer surface of the pipe and ambience varied with the cooling methods and hence it was assumed to be a fixed value and waited to be revised by experiment results. The pressure drop of the single-phase pipe flow could be calculated by:

$$-\frac{dp}{dL} = f \times \frac{1}{2} \rho u^2 \times \frac{4}{d_i} \quad (15)$$

where the friction factor was:

$$f = \begin{cases} 16/Re & Re < 2200 \\ 0.0791 Re^{-0.25} & Re > 2200 \end{cases} \quad (16)$$

### Two Phase Pipe Flow

When both two phases existed, the working fluid could be considered to be under saturation condition, where the local temperature was coupled with local pressure. In this way, the energy conservation equation was independent with temperature:

$$\frac{dX}{dx} = -\frac{1}{\dot{m}\lambda} [(UA/L)_{c-s}(T_{sat} - T_{sink})] \quad (17)$$

where  $\frac{dX}{dx}$  was the changing rate of the mass fraction of vapor phase and

$$\frac{1}{(UA/L)_{c-s}} = \frac{1}{h_i \pi d_i} + \frac{\ln(d_o/d_i)}{2\pi k_s} + \frac{1}{h_{sink} \pi d_o} \quad (18)$$

where  $h_i$  was calculated in the same way as stated in the last section while assumed to be only related with liquid phase,  $h_{sink}$  depended on which kind of cooling method was applied and usually got from experiment data.

The pressure drop of the two-phase flow was modeled by the Lockhart-Martinelli method [14]:

$$\Delta p_{TP} = \Phi_l^2 \times \Delta p_l \quad (19)$$

where  $\Delta p_l$  was the pressure drop when only liquid phase flow existed in the pipe, with its mass flow Rate to be:

$$\dot{m}_l = \dot{m} \times (1 - X) \quad (20)$$

where  $X$  was the mass fraction of gas phase. The  $\Phi_l$  in equation could be calculated with another dimensionless parameter  $\chi$ :

$$\Phi_l = 1 + c/\chi + 1/\chi^2 \quad (21)$$

where the parameter  $\chi$  was expressed as:

$$\chi = \Delta p_l / \Delta p_v \quad (22)$$

where the definition of the  $\Delta p_l$  and the  $\Delta p_v$  were the same as described above

### Compensation Chamber

The compensation chamber (CC) was considered to always be under saturation condition in this mathematical model. Hence the temperature in CC could be calculated from the local pressure in CC following the temperature-pressure coupling relation of saturation condition. From Fig. 3, two energy conservation conditions could be found in CC: For the working fluid in CC:

$$Q_{cc,c-cc} = \dot{m} \times C p_l (T_{cc} - T_{bay}) Q_{ev-cc,hl} \quad (23)$$

where  $T_{bay}$  was the temperature at the outlet of the bayonet tube For the CC casing:

$$Q_{ev,c-cc,c} = Q_{cc,c-amb} + Q_{cc,c-cc} \quad (24)$$

where  $Q_{cc-amb}$  was the heat leak from the CC casing to the ambience.

### Solving Algorithm

The solution flowchart for the model described above was shown in Fig. 4. Once the geometry data and physical properties were determined, the calculation would start with an assumed evaporating temperature. The axial and radial heat leaks were also assumed at first. Then, the mass flow rate could be calculated and the flow properties such as the pressures and temperatures along the loop could be calculated accordingly. When the states in CC was got, the energy conservation described in the last section was checked. The heat leaks were updated and the residual of the conservation equations would be applied to revise the evaporating temperature and started a new loop. The calculation stopped when the conservation equations were converged. Along the loop, the condenser, the vapor line, liquid line and the grooves were discretized into 100, 10, 10 and 10 nodes respectively. The equations described in the former sections would be applied on each node. One point should be noticed was that: as this mathematical model was used for instructing the building of test LHPs, the working fluid inventory and the geometry data were chosen so that the CC would always be under saturation condition. Hence the mass conservation equations and the so caused additional converging steps introduced by Bai *et al* did not need to be considered as the CC would never be flooded with liquid phase.

### Experiment Set Up

The configuration of the test LHP was shown in Fig. 5. The one way transport distance was designed to be 1m. The structure and the parameter of the evaporator-CC integral and the wick inside had been shown in Fig. 2. The evaporator-CC integral was made of aluminum while the wick was made of PTFE porous material, with the pore size to be 1.2  $\mu m$  and the porosity to be 34%. The temperature limitation for the wick was 100 °C. The heat load was applied by 4 cartridge heaters to the evaporator, through a heater block (40 × 50 × 70mm). The cartridge heaters were connected in parallel and supplied by a DC power supply (N6702A). The vapor line and liquid line were pipes with diameter of 1/4 inch and 1/8 inch respectively. The condenser was made of three parts: condenser pipe, condenser plate and cooling plate. The condenser pipe was 1/4 inch diameter pipe, which was the same as the vapor line. The condenser plate was a 380 × 150 × 8mm stainless steel plate, with the channel that the condenser pipe could fit in. The cross section of the channel was 6.50 × 6.50mm. Two cooling plates were attached to the condenser plate. Working fluid of 0°C would flow through the pipes

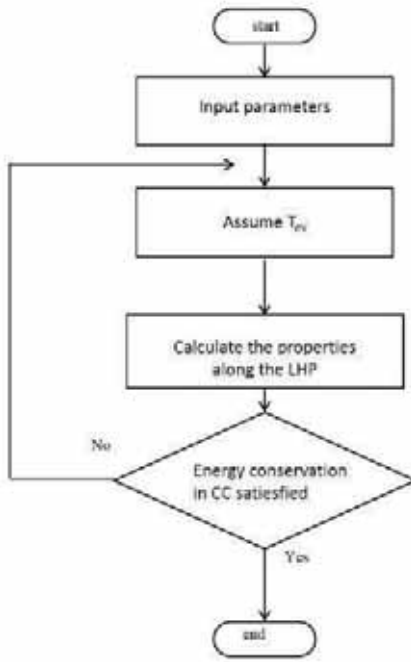


Figure 4. Flowchart for solving algorithm of the mathematical model

Table 1. Table for parameters of test LHP

Heater Block		CC		Evaporator Case	
Length[mm]	70	Length[mm]	135	Length[mm]	75
Height[mm]	40	O. D.[mm]	21	O. D.[mm]	21
Width[mm]	50	I. D.[mm]	19.4	I. D.[mm]	19.4
Vapor Line		Condenser		Liquid Line	
Length[m]	1	Length[m]	1.4	Length[m]	1
O. D.[mm]	6.4	O. D. [mm]	6.4	O. D. [mm]	3.2
I. D. [mm]	4.6	I. D. [mm]	4.6	I. D. [mm]	1.8

on the cooling plate to absorb the heat from the condenser. More details about the test LHP could be found in Table 1.

The working fluid was selected to be Acetone as it had good performance under low temperature circumstance. In this case, as the CC size had been determined already, the transport distance and working fluid inventory were designed accordingly to fit the two equations stated below. Under cold case:

$$M = \rho_{l,c} [V_{loop} + (1 - \beta) V_{cc}] + \rho_{v,c} \beta V_{cc} \quad (25)$$

where the subscribe  $l$  was liquid while  $v$  stand for vapor,

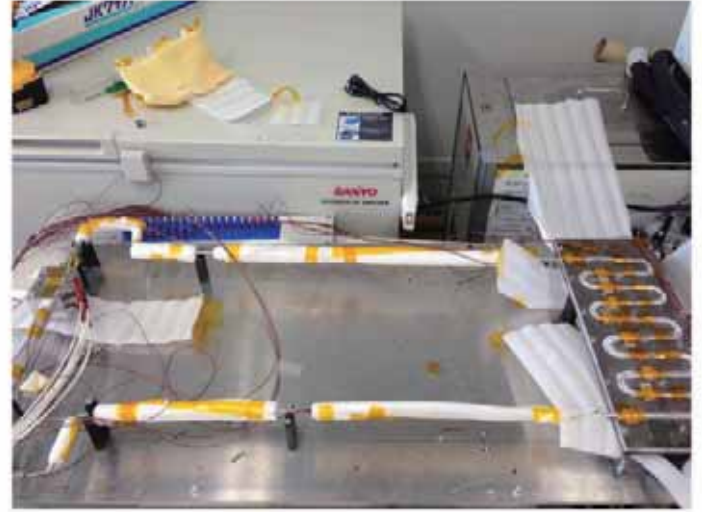


Figure 5. Configuration of the test LHP

$V_{loop}$  was the volume of the whole loop excluding the CC and  $\alpha$  was the volume fraction in CC occupied by vapor under cold case. Under hot case:

$$M = \rho_{l,h} [V_{ll} + V_{wl} + (1 - \alpha V_{cc})] + \rho_{v,h} (V_{gr} + V_{vl} + V_{con} + \alpha V_{cc} \beta) \quad (26)$$

where  $\beta$  was the volume fraction in CC occupied by vapor under hot case. Usually the value of  $\alpha$  should be smaller than 1 so that the CC would not be flooded under hot case and the value of  $\beta$  should be larger than 0.5 to ensure sufficient working fluid supply to the evaporator. When the values of  $\alpha$  and  $\beta$  were determined, the transport distance and the working fluid inventory could be got by solving the two equations above. 29 T-type thermocouples were used to measure the temperatures along the test LHP, where 4 were applied to the evaporator, 4 to the CC, 10 to the condenser, 4 to the vapor line, 4 to the vapor line, 1 to the heat block and the rest to the ambience. Fig. 6 showed the position on the thermocouples. Except the evaporator-CC integral, the whole loop was covered by the thermal isolator. The LHP was suspended about 50mm high from the base to reduce the influence of the base.

## Results and Discussion

### Experiment Result

The experiments were conducted in the environment of 25.5°C. The LHP was vacuumed to the level of  $1 \times 10^{-3} \text{ pa}$  before the test. 50cc Acetone was charged into the loop. The heat load applied to the evaporator varied from 10w to 100w with an interval of 10w. Results showed that the LHP in this experiment could start with a heat load of 20w. However, the LHP could not

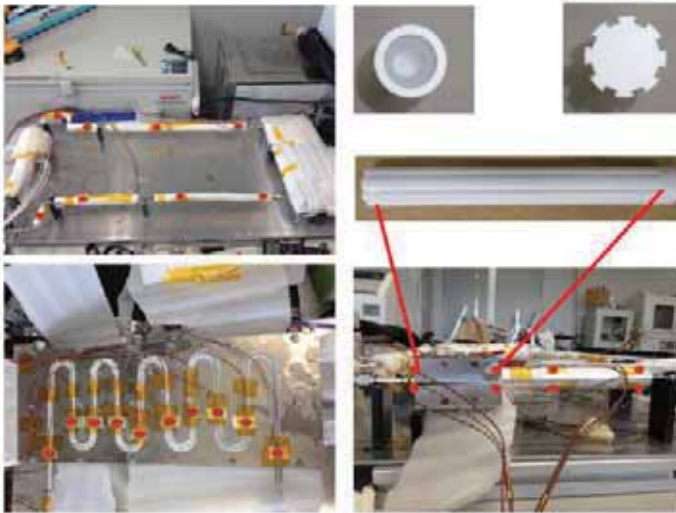


Figure 6. Thermocouple positions on the test LHP.

work with a heat load of 10w, even if a higher heat load was given first to start the LHP and then dropped gradually to 10w. Therefore, the results shown in Fig. 7 only included the temperature profiles with heat loads varied from 20w to 100w. Fig. 7 showed that the temperature of evaporator case kept increasing with the heat load. The classical U-shape operating temperature profile under low heat load did not show up in this tests. The reason for this might lie in many aspects. One possible reason responsible for this phenomenon was over charging of the working fluid inventory. From the equation (25) and (26), the designed inventory for the working fluid was 40cc, so that the volume fraction of the vapor phase in the CC would be 0.2 under cold case and 0.05 under hot case. However, for easy start, the inventory charged into the test LHP was 50cc. Therefore, under hot cases with higher heat load, the CC would be flooded with liquid phase. To satisfy the energy conservation in the evaporator, a higher evaporator temperature was expected under hot cases, as pointed out by Bai *et al* [11]. Actually, the mechanism behind the evaporating temperature profile was much more complicated and influenced by more factors. This would be introduced in the later part. Fig. 8 showed the temperature along the loop in the cases with heat loads of 100w and 40w. From Fig. 8, it could be found that the temperature kept dropping along the condenser in both cases, which meant that the two phase length in the condenser was 0 in both cases. In the other words, the utilization of the condenser was very low. This phenomenon might result from several aspects. First, as the thermocouples were attached on the outer surface of the pipe, the temperature measured might not exactly represented the fluid temperature inside the pipe. From the temperature profile in the vapor line it could be found that in both cases the fluid had reached saturation state before entering the condenser. In real two phase pipe flow, there was a temperature gradient in the liquid layer, which meant that the near wall liquid flow could be sub-cooled and the temperature of it could be

much lower than the saturation temperature. Second, the axial heat leak from the vapor line case to the condenser might be responsible for the phenomenon. As the difference between the saturation temperature in vapor line and the sink temperature of condenser was very large, the axial heat leak might not be neglected. This heat leak would accelerate the condensation in the vapor line, especially in the region close to the condenser, and decrease the two-phase length in the condenser.

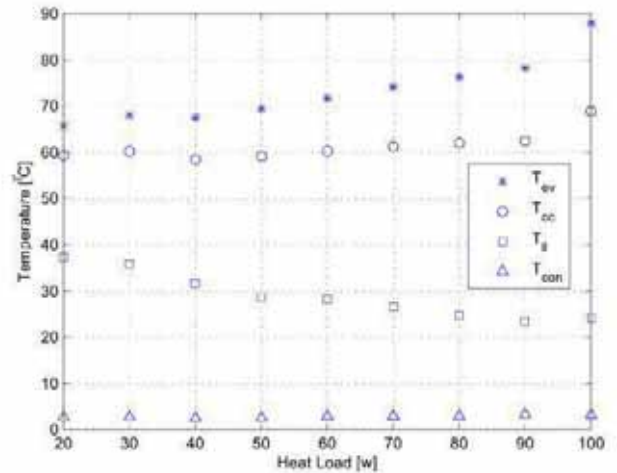


Figure 7. Temperature profile of experiment data varying with heat load

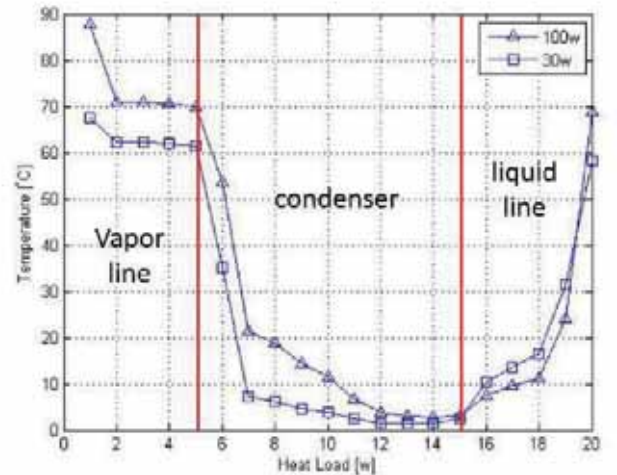


Figure 8. Temperature along the loop

Fig. 9 showed the thermal conductance of the test LHP,

which was defined by the equations

$$G_{LHP} = \frac{Q_{load}}{T_{ev} - T_{con}} \quad (27)$$

The thermal conductance kept increasing with the heat load until 90w. This might indicate that the condenser was fully utilized when the heat load reached 90w. However, this assumption did not match the temperature profile of condenser in Fig. 8. As the heat load in real test could not surpass 100w as the temperature limitation of the evaporator was 100°C, which was the melting point of the PTFE material, it could not be asserted that the decrease of thermal conductance at the heat load of 100w could declare the beginning of fixed conductance region.

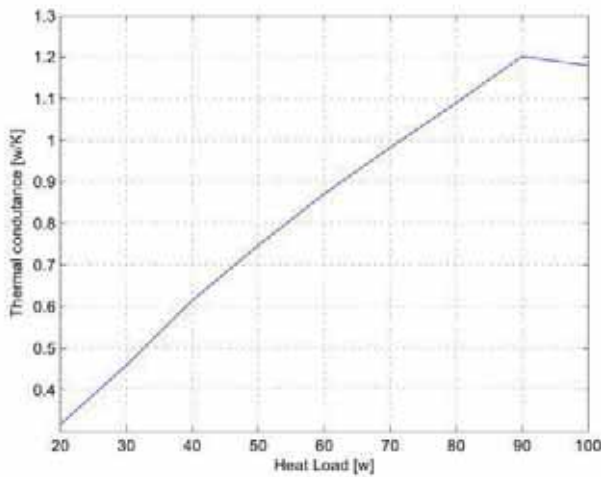


Figure 9. Thermal Conductance of the LHP varying with the heat load

### Comparison between Experiment and Modeling Results

The modeling results were compared with the experimental data in Fig. 10 and Fig. 11. Fig. 10 showed the comparison between the evaporator and CC temperatures in modeling results and experimental data. From Fig. 10 it could be found that the mathematical model matched good with the experimental data for CC temperature. However, the evaporator temperature was estimated higher by the model compared with the experiment results. This might come from the neglecting of the heat leak from the heater block to the ambience. Fig. 11 showed the comparison between the temperature profile along the whole loop from the modeling results and experiment data in the cases with heat load of 40w and 100w. The temperatures in evaporator, CC and along the vapor line of the mathematical model matched good with the

experiment data. However, large difference were found in the temperatures along the former part of the condenser and along the liquid line. The reason for the difference in the former part of the condenser had been introduced in the last section. However, the difference shown in the liquid line could be a problem. As shown in Fig. 11, the temperature at the outlet of liquid line was higher than ambience temperature. This might be caused the heat leak from the CC case to the liquid line pipe wall. Besides, the heat resistance between the liquid line pipe wall and ambience was assumed to be constant along the liquid line. However, due to pipe connectors and the suspension structure, in real test, the heat resistance might be different, which would cause the difference between the experiment data and the modeling results.

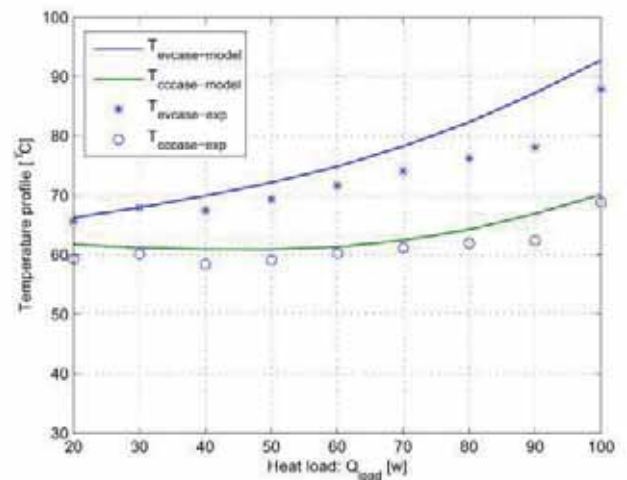


Figure 10. Comparison of temperatures of evaporator case and CC case from experiment data and modeling result varying with the heat load

### Parametric Study by mathematical model

The present diagnostic methods on LHPs were limited. Through the thermal couples, only the outer surface temperature of each parts could be got. However, for two phase heat transfer devices, the pressure drops were also important information. Besides, building the test LHP and the related equipment would take a long time, it was not convenient to test the performance of the LHP with varying parameters through experimental study. Therefore, some of the parametric studies were done based on the mathematical model in present work. Fig. 12 showed the total pressure drops and the pressure drops in each parts of the LHP varying with heat loads. It could be found that the main pressure drop came from the liquid line, which conflicted with many former researchers studies. Actually, this difference was thought to come from two aspects. First, the working fluid in this study was Acetone, the ratio between the vapor and liquid kinematic vis-

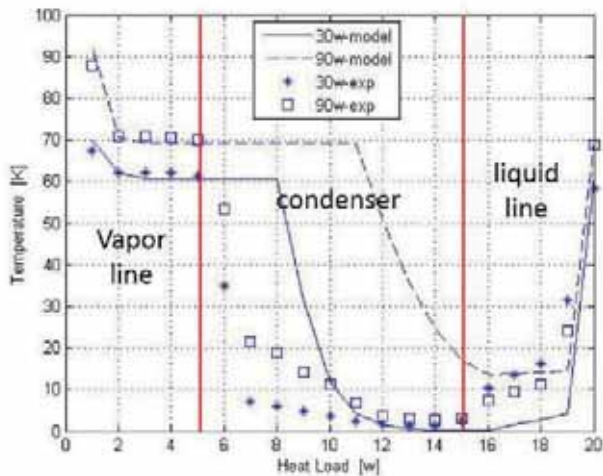


Figure 11. Comparison of temperatures along the loop from experiment data and modeling result

cosity of which was not so large. The inner diameter of the pipe used for liquid line was less than a half of that of vapor line. It was known that the friction was inversely proportional to the diameter of the pipe with exponential of 4. Due to the combination of the two factors described above, the pressure drop in the liquid line might be larger. Second, from the experiment data showed in the former section, the flow in the vapor line reached saturation condition early, which indicated that the flow inside the vapor line was mainly two phase flow, the pressure drop along which would be smaller than the pure vapor. This could also explain the reason for the low pressure drop in the condenser as the flow inside the condenser was mainly in pure liquid phase and the condenser pipe was as same as the vapor line.

Fig. 13 showed the temperature of evaporator case varying with the heat load in the cases where the thermal conductance between the evaporator case and evaporator were different. Results showed that the temperature dropped with the increase of the thermal conductance between the evaporator case and evaporator. The reason for this was obvious. As introduced in the mathematical model section, there were only two path of heat transport for the heat load: one from the evaporator case to the inner side of the evaporator; the others from evaporator case to the CC case. When the thermal conductance of the first path increase, more heat would be transferred into the inner side of the evaporator and utilized to vaporize the working fluid. On the other side, the relatively higher heat resistance of the other path would prevent the axial heat leak, which was used to increase the temperature of the working fluid from the outlet of the liquid line to the temperature in CC. The decrease of such a part of heat would also cause the decrease of the operating temperature. However, as the CC was considered to be under saturation condition and hence highly coupled with the pressure, the mechanism behind Fig. 13 might be more complicated.

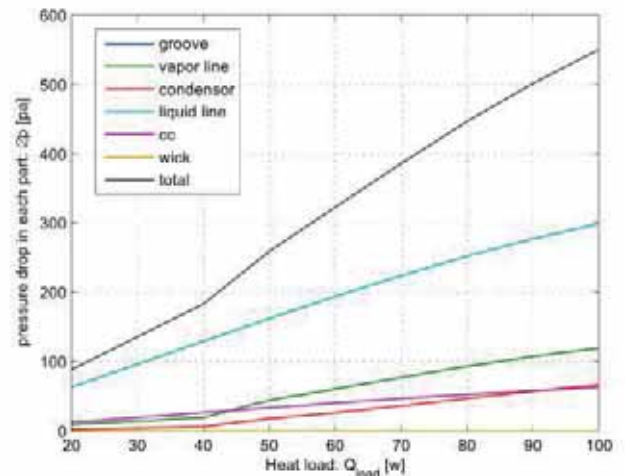


Figure 12. Pressure drop in each part of LHP varying with heat load

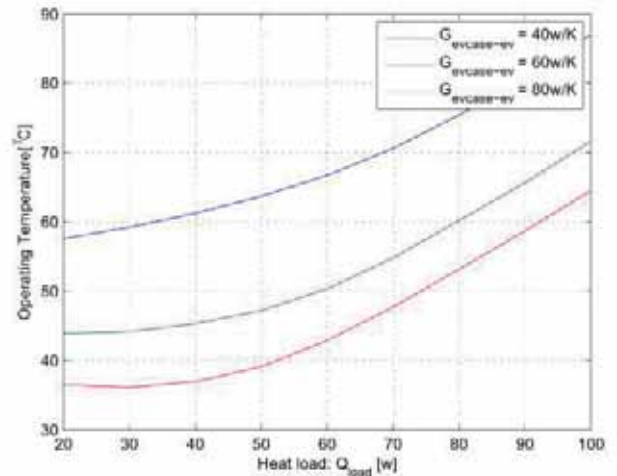


Figure 13. Temperature profile of evaporator case versus heat load of evaporators with varying inner structure

What should also be noticed was that the classical U-shape temperature profile showed up at low heat load when the ratio of the two thermal conductance varied. Former researches such as Bai *et al* [11] only pointed out the influence of the sink and ambient temperature on the shape of operating temperature. The phenomenon in this study indicated that the mechanism behind the shape of the operating temperature profile might be much more complicated and remained further study.

### Limitations of the new type Evaporator

The main purpose of present work was to test the performance and limitation of the new type evaporator. From the test it

could be found that the main weak point of this kind of evaporator was the strength of the liquid line connector. As this kind of evaporator was made of aluminum and the liquid line connector was only 1/8 inch in diameter, this part was very easy to break. Actually during the experiment, two evaporators were broken. As it could not sustain large moment, the evaporator might not be able to be utilized in hard working environment before this problem was solved. Second, the seal between the evaporator and the CC might not be enough. There was supposed to be vapor leak from the evaporator to CC due to the high CC temperature. Because the CC was made as an integral of the evaporator, the heat leak and vapor leak from the evaporator to CC would be much easier. Besides, the malleable of aluminum was high, which might cause the vapor leak from evaporator to CC through the gap between evaporator case and wick at high temperature. Whats more, as suggested in the parametric study by mathematical model, the axial heat leak in this type of condenser was large and caused the high operating temperature. The high evaporating temperature would influence the performance of the LHP in real thermal protection application and limit the heat load that the LHP could sustain. The axial heat leak was believed to relate to the ratio of the thermal conductance between evaporator case and evaporator and that between evaporator case and CC case. Adjust the inner structure of the evaporator-CC integral might help solve this problem.

## Conclusion

In this work, a new type of evaporator was studied through both modeling and experimental methods. Results showed that the evaporator could be started with a minimum heat load of 20w and could work under a maximum heat load of 100w. The mathematical modeling results were compared with the experiment data and the model was verified and adjusted accordingly. Some parametric studies were done based on the verified mathematical model. It was found from the modeling study that the ratio between the thermal conductance from the evaporator case to the evaporator and the evaporator case to the CC case was important as it could control the evaporating temperature. It was also found that the shape of the operating temperature profile varying with heat load was influenced by a lot of factors and the mechanism behind it was complicated. The limitation of the kind of evaporator focused by this study was concluded, it was suggested to strengthen the connecting part of the liquid line connector and evaporator body for application in harder environment. It was also suggested to improve the inner structure of the evaporator to extend the application of this kind of evaporator.

## REFERENCES

[1] Y.F. Maidanik, S.V. Vershinin, V. K. e. a., *Heat Transfer Apparatus*, United States, 1985.  
 [2] Ku, J., "Operation characteristics of loop heat pipes," v,

Denver, Colorado, July 12-15 1999, SAE Paper 1999-01-2007.  
 [3] G.H. Wang, D. Mishkinis, N., "Capillary heat loop technology: space applications and recent Canadian activities," *Applied Thermal Engineering*, Vol. 28, 2008, pp. 284–303.  
 [4] Maydanik, Y., "Loop heat pipes," *Applied Thermal Engineering*, Vol. 25, 2005, pp. 635–657.  
 [5] Goncharov, K. A., e. a., "Loop Heat Pipes in Thermal Control Systems for OBZOR Spacecraft," *SAE Paper*, , No. 95, 1995.  
 [6] Birur, G., R. J. and Nikitkin, M., "Loop Heat Pipe Applications for Thermal Control of Martian Landers/Rovers," *10th Annual Spacecraft Thermal Control Technology Workshop*, The Aerospace Corporation, El Segundo, California, February 24-26 1999.  
 [7] Jentung Ku, K. P., "Loop Heat Pipe Transient Behavior Using Heat Source Temperature for Set Point Control with Thermoelectric Converter on Reservoir," *9TH ANNUAL INTERNATIONAL ENERGY CONVERSION ENGINEERING CONFERENCE*, San Diego, California, 31 July - 03 August 2011, AIAA Paper 2011-5644.  
 [8] T. Kaya, T.T. Hoang, J. K., "Mathematical Modeling of Loop Heat Pipes," *AIAA*, , No. 99, 1999.  
 [9] T.T. Hoang, T. K., "Mathematical Modeling of Loop Heat Pipes with Twophase Pressure Drop," *AIAA*, , No. 99, 1999.  
 [10] P.A. Chuang, J.M. Cimbala, C. C. e. a., "Comparison of experiments and 1D steady-state model of a loop heat pipe," *IMECE*, New Orleans, LA USA, 17-22 November, 2002-33542.  
 [11] L. Bai, G. Lin, H. Z. D. W., "Mathematical modeling of steady-state operation of a loop heat pipe," *ATE*, , No. 2643, 2009.  
 [12] V.G. Pastukhov, Y. M., "Low-noise cooling system for PC on the base of loop heat pipes," *Applied Thermal Engineering* 27, 2007.  
 [13] Y.F. Maydanik, S.V. Vershinin, M. K. e. a., "Miniature loop heat pipes a promising means for cooling electronics," *IEEE Transaction on Components and Packaging Technology*, 2005.  
 [14] R. W. Lockhart, R. C. m., "Proposed correlation of data for isothermal two-phase, two-component flow in pipes," *Chemical Engineering Progress*, 1949.

# LINEAR AND NONLINEAR OPTIMAL CONTROL OF FURUTA PENDULUM

Ambarish Desai

Department of Aerospace Engineering,  
H. H. Rackham Graduate School, University of Michigan Ann Arbor  
ambar@umich.edu

Supervisor : Dr. Noboru Sakamoto

Department of Aerospace Engineering  
Graduate School of Engineering, Nagoya University  
sakamoto@nuae.nagoya-u.ac.jp

## Abstract

This document presents the work done in modeling and control of a rotary single inverted pendulum. Subsequently it moves on to modeling and control of a rotary double inverted pendulum. Both the systems are linearized and LQ theory is used to determine optimal gains for stabilizing the pendulum in unstable equilibrium. Further, nonlinear control based on stable manifold theory is used for swing up and stabilization of a rotary single inverted pendulum. Simulations and experiment results are presented.

## 1. INTRODUCTION

Inverted pendulum is a significant system used in control theory as a first hand example to test and verify various control laws. Its mechanical simplicity yet strong nonlinear characteristics makes it an excellent tool to test both linear and nonlinear control systems.

It is most commonly used as an underactuated system. An underactuated system has fewer actuators than degrees of freedom. Rotary inverted pendulum were first studied by Dr. Furuta [8] [2], from which the system also derives its name.

Inverted pendulums are used in two basic configurations. One in which the inverted pendulum is mounted on a cart which can slide along an axis. This system has a physical limit on the length of the sliding rail which has to be accounted for, in the control techniques. The other system is the one in which the inverted pendulum is attached to a rotating body and hence does not have the aforementioned limitation.

Extensive work has been done in implementation of LQ control for stabilizing inverted pendulum near the region of unstable equilibrium. [10] deals with implementation LQ

control of inverted pendulum on cart. [2], [11] deals with implementing swing up and LQ control for stabilizing of rotary single inverted pendulum. However they use different control laws each for swing up and stabilizing. In addition, most of the nonlinear theories are applicable only to a few or a particular type of systems.

In this work we start with implementing LQ control and then move on to derive a single nonlinear optimal control feedback law for swing up and stabilization of the inverted pendulum. The feedback law is obtained by approximating the solution to Hamilton-Jacobi equation based on stable manifold theory. Even though the inverted pendulum has been used here, the theory in itself is general and can be applied to any system.

## 2. SYSTEM MODELING

### 2.1. ROTARY SINGLE INVERTED PENDULUM

Rotary single inverted pendulum (RSIP) consists of a body  $\mathcal{B}_1$  rotating in a horizontal plane parallel to the ground and another pendulum body  $\mathcal{B}_2$  attached to it which can oscillate in the vertical plane as can be seen in figure 1. Equations of motion for this system can be derived using

Euler-Lagrangian methods. Both the bodies are considered to be rigid and thin homogenous rods with frictionless joints. It should be noted that in this derivation the inertia tensors of the body along the longitudinal axis is neglected. Also rotational symmetry is assumed such that the moments of inertia in two of the remaining principal axes are equal. For a more accurate but complex model one can refer to [6] and [1].

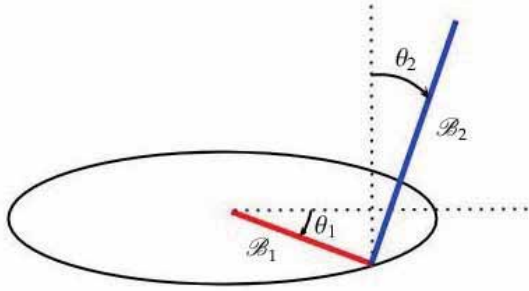


Fig. 1: Rotary single inverted pendulum

The equations of motion are derived using Lagrange's equation (1) as per the methods illustrated in [4].

$$\frac{d}{dt} \frac{\partial L}{\partial \dot{\theta}} - \frac{\partial L}{\partial \theta} = Q \quad (1)$$

where  $L = T - P$  is the Lagrangian,  $Q$  is denotes generalized forces and moments arising from non-conservative contact,  $T$  is the kinetic energy and  $P$  is the potential energy of the system. Both the kinetic and potential energies of the system are given by the sum of the energies of its individual components.

The rotating body is powered by a DC motor which is modeled using the equation (2)

$$\tau = n(KDCu + \mu\dot{\theta}_1) \quad (2)$$

where  $\tau$  is the torque provided by the motor to  $\mathcal{B}_1$ ,  $n$  is gear ratio,  $KDC$  is torque constant,  $\mu$  is a factor to account for friction and counter electromotive force and  $u$  is the voltage supplied to the motor. A reference to this model can be found in [5].

After rearranging and simplification the equations of motion can be written in a compact

matrix form as:

$$D(\theta)\ddot{\theta} + C(\theta, \dot{\theta}) + Gu = 0 \quad (3)$$

where

$$D(\theta) = \begin{bmatrix} I_1 + I_2 (\sin \theta_2)^2 + m_2 L_1^2 & m_2 L_1 l_2 \cos \theta_2 \\ m_2 L_1 l_2 \cos \theta_2 & I_2 \end{bmatrix} \quad (4)$$

$$C(\theta, \dot{\theta}) = \begin{bmatrix} -2I_2 \dot{\theta}_1 \dot{\theta}_2 \cos \theta_2 \sin \theta_2 + m_2 \dot{\theta}_2^2 L_1 l_2 \sin \theta_2 + n\mu\dot{\theta}_1 \\ \sin \theta_2 (I_2 \dot{\theta}_1^2 \cos \theta_2 + m_2 g l_2) \end{bmatrix} \quad (5)$$

$$G = \begin{bmatrix} nKDC \\ 0 \end{bmatrix} \quad (6)$$

where  $m$  is mass of the body,  $L$  is the length,  $l$  is the distance of center of mass from the pivot point and  $I$  is the mass moment of inertia with respect to the pivot point. The subscript used for these symbols are for the corresponding bodies.

Equation (3) can be rearranged as

$$\ddot{\theta} = -D(\theta)^{-1}C(\theta, \dot{\theta}) - D(\theta)^{-1}Gu \quad (7)$$

Equation (7) can be then used to formulate ordinary differential equation for developing models suitable for use with Matlab programs.

### 2.1.1 2D-RSIP System Model

To reduce computational load the RSIP is simplified to a 2 dimensional (2D) system for use in algorithm to compute the nonlinear feedback law . A 2D-RSIP has the same configuration as RSIP described in previous section and is simplified using the following assumptions - the mass and hence the inertia of  $\mathcal{B}_1$  is assumed to be zero; all the terms with  $\dot{\theta}_1$  are neglected; and  $\mu$  in equation (2) is zero. Thus the equations of motion  $\mathcal{B}_2$  depend only on  $\theta_2$  and  $\dot{\theta}_2$  thereby reducing the state vector to 2 dimensions. The state vector is given in equation (8) and equations of motion for

2D-RSIP can be found in appendix B

$$x = [\theta_2 \dot{\theta}_2]^T \quad (8)$$

## 2.2. ROTARY DOUBLE INVERTED PENDULUM

An extension to the rotary single inverted pendulum is the rotary double inverted pendulum (RDIP). This system has an one more body  $\mathcal{B}_3$  attached to the  $\mathcal{B}_2$  through a planar revolute joint as shown in figure 2. Although the system dynamics are an extension of the system discussed earlier it is much more complex and sensitive to nonlinearities. Hence it is very difficult to control this system in practical.

$$x = [\theta_1 \dot{\theta}_1 \theta_2 \dot{\theta}_2 \theta_3 \dot{\theta}_3]^T \quad (9)$$

Solving for the equations of motion, the kinetic and potential energy of the body  $\mathcal{B}_3$  is taken into consideration. Reformulating as in the previous case the set of equations can be written as in Equation (3) where now  $\theta \in R^3$  and the state defined as (9). The matrix equations for RDIP can be found in A.

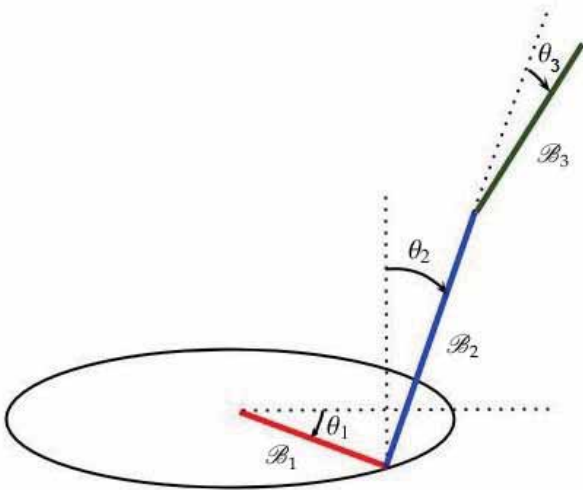


Fig. 2: Rotary double inverted pendulum

## 2.3. STATE SPACE REPRESENTATION

To proceed with designing a controller, Lagrange equations of motion are modified into first-order ordinary differential equations. With the state vector defined in the previous sections the

dynamics of RSIP (and similarly for RDIP) can be written as

$$\begin{aligned} \dot{x} &= \begin{bmatrix} x(2) \\ -D^{-1}C(1) \\ x(4) \\ -D^{-1}C(2) \end{bmatrix} + \begin{bmatrix} 0 \\ -D^{-1}G(1) \\ 0 \\ -D^{-1}G(2) \end{bmatrix} u \quad (10) \\ &= f(x) + g(x)u \end{aligned}$$

The above set of equations is linearized about  $x = 0$ . It is interesting to note that while deriving the system dynamics care should be taken to select the reference which will lead to the desired equilibrium state when  $x = 0$ . In this case the desired unstable equilibrium is when the  $\mathcal{B}_2$  (and  $\mathcal{B}_3$ ) is vertically upright. This system is nonlinear and the linearized model holds valid only for a small range of the state vector. Linearizing, the system can be written in the state-space representation as

$$\dot{x} = Ax + Bu \quad (11)$$

The linearized state space representain is used for determining the optimal gains required to maintain the system in the unstable equilibrium.

## 3. LINEAR OPTIMAL CONTROL

The general approach of designing an optimal control mostly involves minimizing a cost function [3]. The linear quadratic regulator (LQR) provides an effective solution which strikes a desired balance between the state trajectory and control input required. Here we consider LQ control over infinite time ( $t \rightarrow \infty$ ).

### 3.1. LINEAR QUADRATIC REGULATOR

Consider a time invariant system

$$\dot{x} = Ax + Bu \quad (12)$$

with a state feedback

$$u = Kx \quad (13)$$

such that the cost function

$$J = \int_0^{\infty} (x^T Qx + u^T Ru) dt \quad (14)$$

is minimized. Using the state feedback and equation (12) we obtain a closed loop system as

$$\dot{x} = (A + BK)x \quad (15)$$

with solution

$$x = e^{(A+BK)t}x_0 \quad (16)$$

where  $x(0) = x_0$ .

Using equations (13) and (16) the cost function (14) can be written as

$$\begin{aligned} J &= \int_0^\infty (x^T Q x + x^T K^T R K x) dt \\ &= x_0^T \int_0^\infty [e^{(A+BK)^T t} (Q + K^T R K) e^{(A+BK)t} dt] x_0^T \\ &= x_0^T P x_0 \end{aligned} \quad (17)$$

System (15) is asymptotically stable if and only if the matrix  $P$  defined in (17) is the unique positive-definite solution of Lyapunov equation

$$(A + BK)^T P + P(A + BK) + Q K^T R K = 0 \quad (18)$$

Assuming

$$K = -R^{-1} B^T P \quad (19)$$

the equation (18) reduces down to

$$A^T P + P A + Q - P B R^{-1} B^T P = 0 \quad (20)$$

which is the algebraic Riccati equation. Hence the optimal solution of infinite-time LQ problem is given by a solution to the algebraic Riccati equation (20) and the stabilizing input by

$$u = -(R^{-1} B^T P)x \quad (21)$$

One of the many advantages of this controller is that the optimal input signal  $u$  can be obtained from a full state feedback. In addition it provides very good stability margins and hence is very robust. Also the solution  $P$  is constant for a given set of  $Q$  and  $R$  due to which the gains can be computed off-board and not in real time. However, obtaining a solution to the Riccati equation (20) is quite difficult even for simple systems. Further, unlike pole placement techniques, the process to find a controller to exactly match required response

is iterative. Various combinations of  $Q$  and  $R$  need to be tried to provide the desired system response.

#### 4. NONLINEAR OPTIMAL CONTROL

The equations of motion of any system can be written in the form

$$\dot{x} = f(x) + g(x)u, \quad f(0) = 0 \quad (22)$$

and the cost function as

$$J = \int_0^\infty (x^T Q x + u^T R u) dt \quad (23)$$

then the optimal feedback control law is given by

$$u = -g(x)^T p(x) \quad (24)$$

where  $p$  is the solution of the corresponding Hamilton-Jacobi equation

$$p^T f(x) - \frac{1}{2} p^T g(x) g(x)^T p + q(x) = 0 \quad (25)$$

##### 4.1. STABLE MANIFOLD THEORY

Consider a system

$$\dot{x} = Ax, \quad x \in R^n \quad (26)$$

This system has stable, center and unstable subspace associated with eigenvalues of  $A$  lying on the open left half plane, the imaginary axis and the open right half plane, respectively. Each of these subspaces are invariant under the flow of  $\dot{x} = Ax$ . The same theory can be extended to nonlinear system in the form of invariant manifolds.

Consider a dynamical system

$$\dot{x} = f(x), \quad x \in R^n \quad (27)$$

with a solution  $\phi(x_0, t)$  where  $\phi(x, 0) = x_0$ . Then a manifold  $M \subset R^n$  is an invariant manifold if for every  $x_0 \in M$  the solution  $\phi(x_0, t) \in M$ .

Now consider the system (27) written as

$$\dot{x} = Ax + F(x), \quad x \in R^n \quad (28)$$

where  $f(0) = 0$ ,  $A = \left. \frac{\partial f}{\partial x} \right|_{x_0}$ , with nonlinear terms given by  $F(x) = f(x) - Ax$ , has  $k \leq n$  eigenvalues with  $Re(\lambda) < 0$ . Then there exist a  $k$ -dimensional stable manifold  $S$  tangent to the stable subspace of

$A$  at 0 such that  $\forall t \geq 0 \phi(S, t) \subset S$  and  $\forall x_0 \in S$

$$\lim_{t \rightarrow \infty} \phi(x_0, t) = 0$$

This theory is used to compute an approximate solution to HJ equation (25). Starting with a general HJ equation

$$H(x, p) = p^T f(x) - \frac{1}{4} p^T R(x) p + q(x) \quad (29)$$

$$= 0$$

where  $p_1 = \frac{\partial V}{\partial x_1}, \dots, p_n = \frac{\partial V}{\partial x_n}$  with  $V(x)$  an unknown function,  $R(x)$  is a symmetric matrix for all  $x$ ,  $f(x) = Ax + h.o.t$  (higher order terms) and  $q(x) = x^T Q x$ , with  $Q \in R^{n \times n}$  a positive semidefinite matrix. We also assume that  $f$  satisfies  $f(0) = 0$ . If  $V(x)$  is a solution of (29) then the set

$$\Lambda = \left\{ (x, p) \mid p = \frac{\partial V}{\partial x}(x) \right\}$$

is invariant [12] under the space of associated with Hamiltonian system given by (30). A solution  $V(x)$  of (29) is called a stabilizing solution if  $f(x) - \frac{1}{2} R(x) p$  is an asymptotically stable vector field.

$$\dot{x} = f(x) - \frac{1}{2} R(x) p \quad (30)$$

$$\dot{p} = -\frac{\partial f}{\partial x}(x)^T p + \frac{1}{4} \frac{\partial (p^T R(x) p)^T}{\partial x} - \frac{\partial q^T}{\partial x}(x)$$

The Riccati equation (31) is the linearization of HJ equation (29). A solution  $P$  that we obtain for equation (31) is called a stabilizing solution when  $A - R(0)P$  is stable. If such  $P$  exists then a stabilizing solution to (29) locally exists around the origin [12]. We already know from LQ control that a solution to equation (31) exists.

$$PA + A^T P - PR(0)P + Q = 0 \quad (31)$$

Assuming that a stabilizing solution to equation (31) denoted by  $\Gamma$  exists then a linear transformation

$$T = \begin{bmatrix} I & S \\ \Gamma & \Gamma S + I \end{bmatrix} \quad (32)$$

where  $S$  is the solution of Lyapunov equation  $(A - R(0)\Gamma)S + S(A - R(0)\Gamma)^T = R(0)$  can be used to write

$$\begin{pmatrix} x' \\ p' \end{pmatrix} = T^{-1} \begin{pmatrix} x \\ p \end{pmatrix}$$

to define the Hamiltonian system

$$\begin{pmatrix} \dot{x}' \\ \dot{p}' \end{pmatrix} = \begin{pmatrix} A - R(0)\Gamma & 0 \\ 0 & -(A - R(0)\Gamma)^T \end{pmatrix} \begin{pmatrix} x' \\ p' \end{pmatrix} + H.O.T \quad (33)$$

#### 4.1.1 Stable Manifold Algorithm

Consider the following system

$$\begin{aligned} \dot{x} &= Fx + n_s(t, x, y) \\ \dot{y} &= -F^T y + n_u(t, x, y) \end{aligned} \quad (34)$$

where  $F$  is an asymptotically stable  $n \times n$  matrix and  $n_s, n_u$  are higher order terms.

Define the sequences  $\{x_k(t, \xi)\}$  and  $\{y_k(t, \xi)\}$  as

$$\begin{aligned} x_{k+1} &= e^{Ft} \xi + \int_0^t e^{F(t-s)} n_s(s, x_k(s), y_k(s)) ds \\ y_{k+1} &= -\int_t^\infty e^{-F^T(t-s)} n_u(s, x_k(s), y_k(s)) ds \end{aligned} \quad (35)$$

for  $k = 0, 1, 2, \dots$  and

$$\begin{aligned} x_0 &= e^{Ft} \xi \\ y_0 &= 0 \end{aligned}$$

with  $\xi \in R^n$

The sequences  $\{x_k(t, \xi)\}$  and  $\{y_k(t, \xi)\}$  are convergent to zero [7] for sufficiently small  $|\xi|$ , that is  $\{x_k(t, \xi)\}$  and  $\{y_k(t, \xi)\} \rightarrow 0$  as  $t \rightarrow \infty$  for all  $k = 0, 1, 2, \dots$ . As  $k \rightarrow \infty$  the sequences (35) approach limit functions  $\{x(t, \xi)\}, \{y(t, \xi)\}$  which is the solution of (34) with

$$\lim_{t \rightarrow \infty} \{x(t, \xi)\}, \{y(t, \xi)\} = 0$$

implying that it is on the stable manifold of (34).

For each  $k$ , the algorithm calculates sequences (35) for the system (33) to obtain  $(x', p')$  and thus  $(x, p)$  using the transformation  $T$ . Refer to [12] for proof and examples using this algorithm.

## 5. EXPERIMENT

Experiment was done to demonstrate LQ control for RSIP. The apparatus used for all the

experiments in this study is shown in figure 3. It consists of a rotating arm, encoders and a DC motor. The pendulum is attached at right angles to the rotating arm and can rotate freely around the axis  $\theta_2$ . The rotating arm ( $\theta_1$ ) is connected to a DC motor through a gear drive with reduction  $n$ . Rotating arm angle is observed by an encoder inside the DC motor whereas the pendulum swing angle is observed by an encoder connected to it by a belt and pulley drive.

All the sensors feed the signals to a computer on which Labview programs were used for real time visualization and also for the controller which provided the input to the DC motor.



Fig. 3: Hardware setup for experiment.

Figure 4 and 5 show typical response of RSIP from experiment data. The weighing matrices  $Q$  and  $R$  need to be selected in such a way that the stabilizing input should be large enough for robust stability of the system. Some values used for testing were

$$\begin{aligned}
 R &= 0.5 \\
 Q &= \text{diag}(1 \ 1 \ 10 \ 1) \\
 Q &= \text{diag}(1 \ 3 \ 10 \ 1) \\
 Q &= \text{diag}(1 \ 10 \ 10 \ 1)
 \end{aligned} \tag{36}$$

The set of above values were found to be in

increasing order of value of stabilizing input and robustness as observed in the experiment. In the experiment the RSIP oscillates about the unstable equilibrium position in the steady state. However for the last value of matrix  $Q$  the RSIP achieved the unstable upright equilibrium and stopped oscillating.

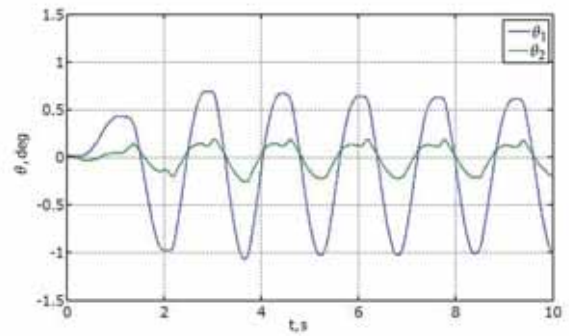


Fig. 4: Experiment results showing the state response of the RSIP

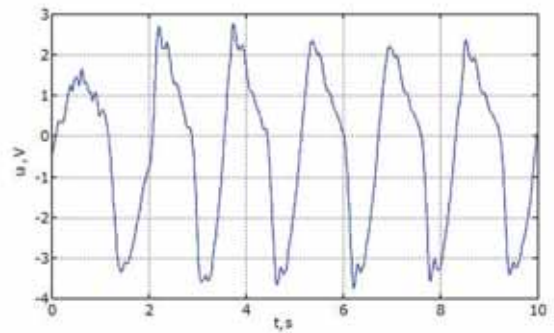


Fig. 5: Experiment results showing the input response of the RSIP

With the same setup as shown in figure 3 the RDIP was also tested. The calculated gains were able to stabilize RDIP in up-up position however the system was not robust enough to maintain this position for a long time. To remedy this, some tweaking was required in the filters used in the Labview control programs. However due to time constraint and lack of extensive knowledge of Labview this was not pursued.

## 6. SIMULATION

Simulations are necessary to prove whether the derived system dynamics are correct and to test the response of the system to various control methods. Matlab and SimMechanics were used for simulations in this work.

SimMechanics is a toolbox in Matlab Simulink which can be used to simulate mechanical systems with 3D visualizations. The *mechimport* feature of the toolbox lets you import CAD models and automatically generates a SimMechanics model file. The CAD file has to be an assembly with appropriate mating conditions defined between various parts. The toolbox substitutes corresponding joints in between the bodies depending upon the mating condition specified between them. Refer to [9] for more details.

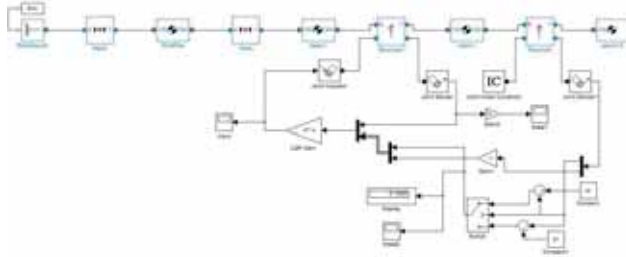


Fig. 6: Simulink block of RSIP

The CAD model of pendulum assembly was done in SolidWorks. All the joints in a rotary pendulum are revolute hence the concentric mating condition is specified between the bodies of the assembly. In addition a distance mating condition is specified between the mating circles. This is to prevent Matlab from identifying the joint as cylindrical. It is also important to build the assembly in one of its equilibrium states. Depending on the state you choose, Matlab selects a reference from which all the required measurements are made. It is necessary to keep this reference in mind when developing the model for further analysis.

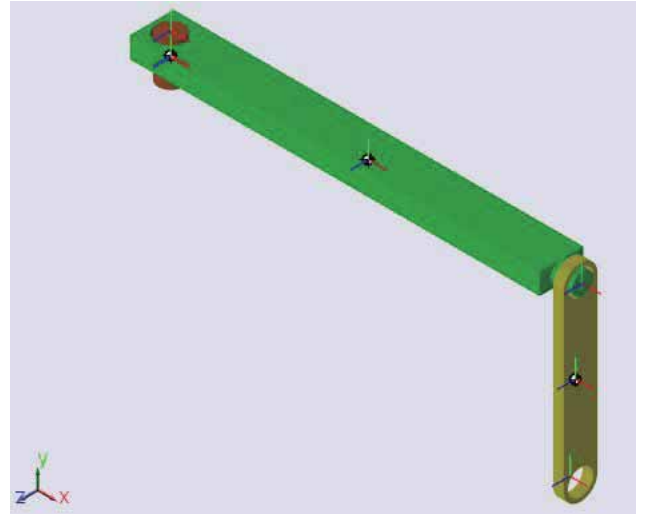


Fig. 7: Machine model of RSIP

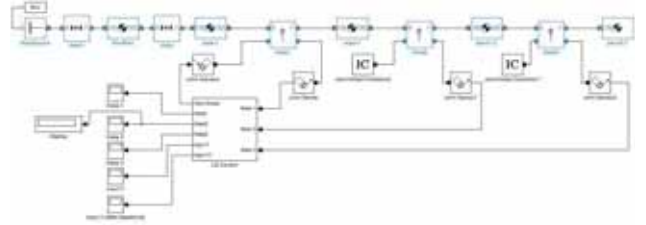


Fig. 8: Simulink block of RDIP with state feedback and deadzone

In this case both, the single and double pendulum assemblies are completed in stable equilibrium i.e. the pending (down) state. Hence the reference for measuring of the state variables is the axis pointed downwards along the body  $B_2$ . On the contrary the system dynamics are derived with the reference pointing up towards the unstable equilibrium. Hence it is important that measurements are modified before a comparison with the derived system dynamics is made.

In addition to reference, the direction of measurement can also be different for Matlab and simulink. For the simulations in this study the sign of individual controller gains for RSIP had to be changed to  $++--$  to suit the simulink model. Whereas for RDIP it had to be  $+++++$ .

Free response of the system can be simulated by providing the desired initial condition. In Matlab the free response was generated using ODE solver for solving the nonlinear set of equations (7).



Fig. 9: Machine model of RDIP

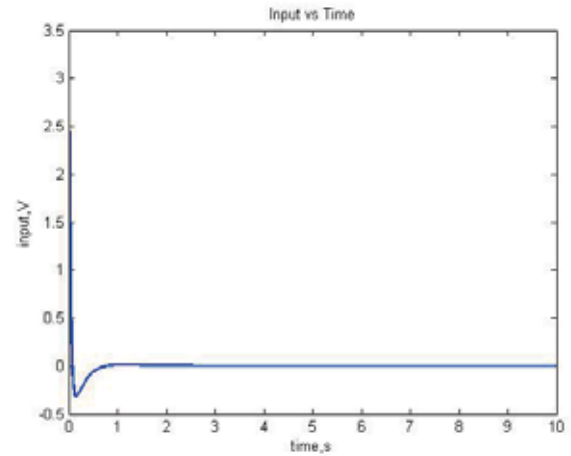


Fig. 11: Input response for the same conditions as in figure 10

### 6.1. LQR SIMULATIONS

In this work, Maple was used for the mathematical derivations and Matlab for solving for the optimal controller. Matlab commands *lqr* and *care* were used to determine gain values for different values of Q and R. The gain was determined using the linear state space model but the response of the system was simulated using the nonlinear model. It was noted that for different values of Q and R the maximum range of the state vector for which the system moves towards the stable state varies.

#### 6.1.1 LQ Control with Deadzone

The system dynamics do not account for friction, backlash in gears, DC motor inertia and other factors affecting real systems. It can be assumed due to all these factors the system will not respond until the input crosses a certain threshold. The region or zone encapsulated by this threshold for which the system does not respond or essentially remains dead can be described as deadzone. It is easy to incorporate deadzone in simulations which provide results that are very close to the behavior of the actual system.

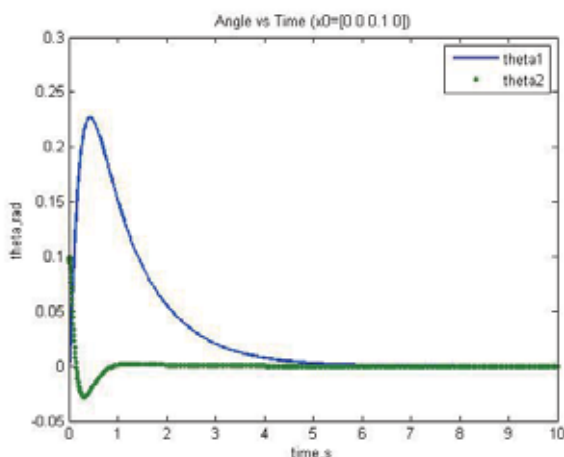


Fig. 10: Response of non-linear model of RSIP in state feedback.  $x_0$  is the initial condition of the system

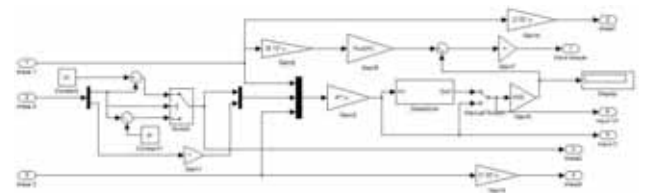


Fig. 12: LQ controller block with deadzone

Figure 10 and 11 respectively show typical state and input response of RSIP with LQ control.

In this work a deadzone of  $\pm 1.5V$  has been used. A deadzone has been incorporated in Matlab .m files and also in the Simulink block model. A simulated response was found to be much similar to the response seen in the experiments.

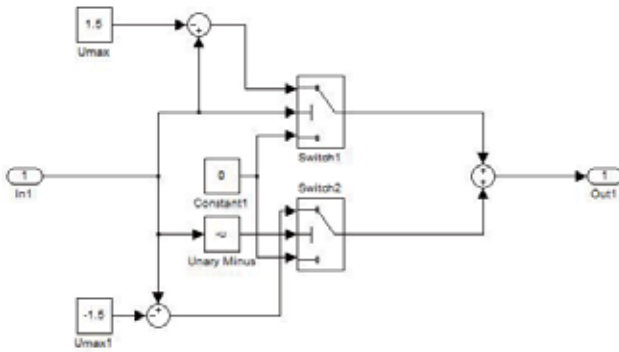


Fig. 13: Deadzone block model

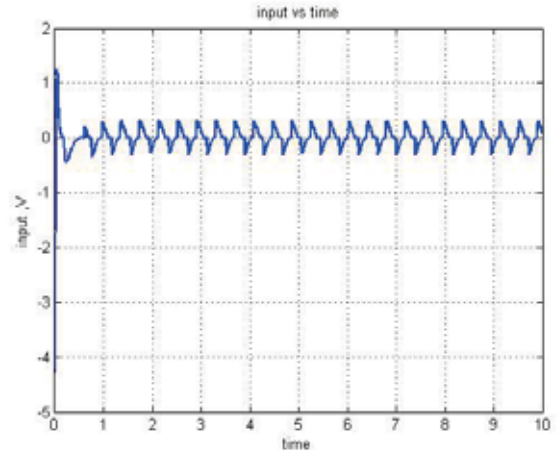


Fig. 15: Plot from .m files showing the response of the stabilizing input for RDIP accounted for deadzone

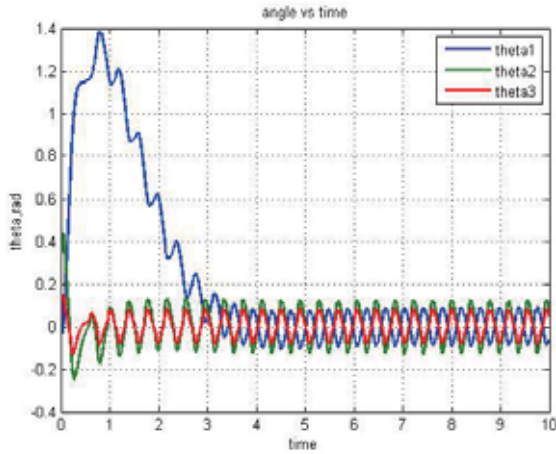


Fig. 14: Plot from .m files showing the response of the three angles of RDIP accounted for deadzone

The figures 14 and 15 show the output from the .m files of the RDIP. As expected in steady state the response of the state and hence the input oscillates about zero.

The figures 16 and 17 show the output from the Simulink for the RDIP. As seen they match the output from the .m files implying the modeling of the system is correct.

The plots shown in figures 14 to 17 were obtained using the weight matrices  $R = 0.2$  and  $Q = \text{diag}([0.1 \ 0.1 \ 0.3 \ 0.1 \ 0.1])$ . In the presence of deadzone it seems evident that the state and input will keep oscillating about zero in the steady state.

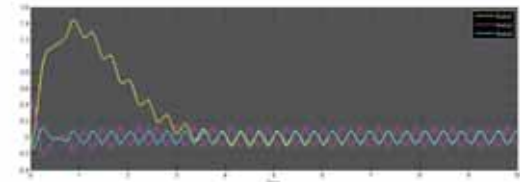


Fig. 16: Simulink output plot showing the response of the three angles of RDIP accounted for deadzone

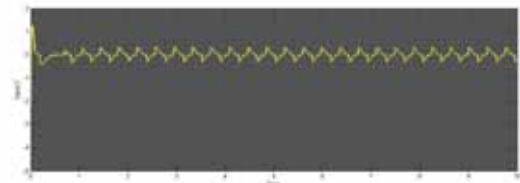


Fig. 17: Simulink output plot showing the response of the stabilizing input for RDIP accounted for deadzone

## 6.2. OPTIMAL SWING UP AND STABILIZATION

Using the stable manifold approach a nonlinear control feedback law is calculated to swing up the 2D-RSIP from initial pending state  $x = [\pi \ 0]^T$  and stabilize it in the inverted position. The Hamiltonian matrix for the system is calculated as shown in equation (37)

$$H = \begin{pmatrix} A & -\frac{1}{2}BR^{-1}B^T \\ -2Q & -A^T \end{pmatrix} \quad (37)$$

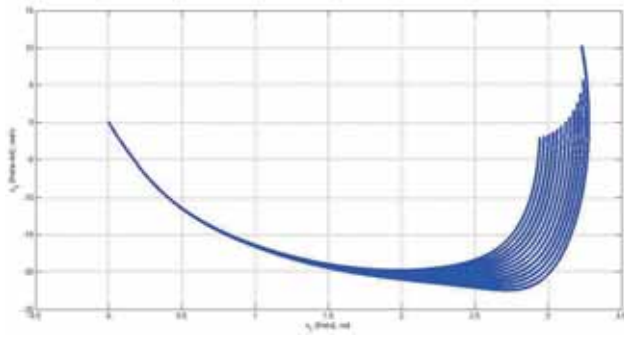


Fig. 18: Plot showing the closed loop state trajectories

A number of iterations were done with different values of radius of convergence  $\zeta$  to compute sequences (35) and get the state trajectories to pass through the initial condition. However for the trajectories to reach the initial condition the accuracy to which the Hamiltonian is calculated had to be reduced to  $10^{-2}$ . A number of individual  $\zeta$  were chosen in the region of interest to get the state trajectory to pass through the initial state as shown in figure 18.

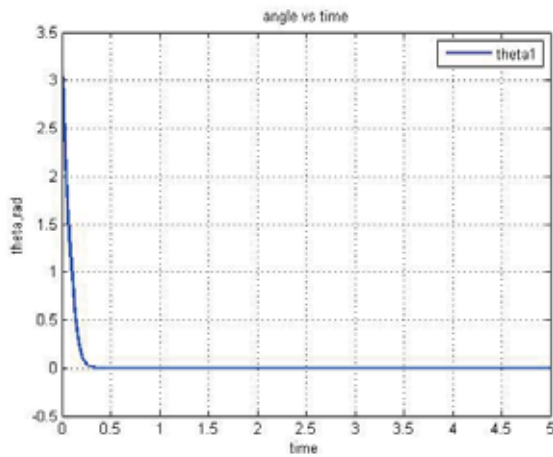


Fig. 19: Plot showing the  $\theta_2$  response with nonlinear control

Once this is achieved a polynomial function in  $x$  is used to fit this data and thereby calculate the approximate solution  $p(x)$  which then is used to compute the closed loop feedback law as stated in equation (24). The figure 19 shows that RSIP swings up in one swing and the figure 20 shows the input response for the swing up.

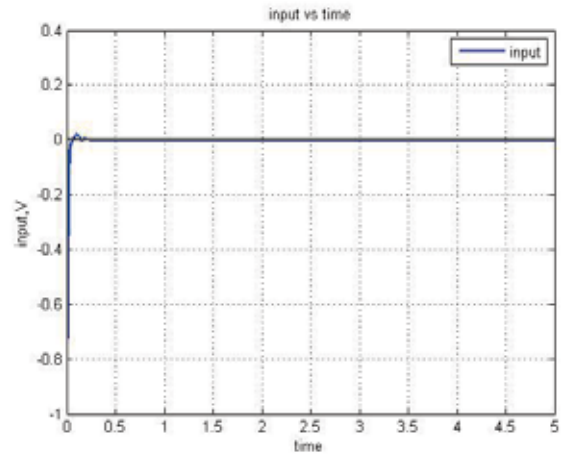


Fig. 20: Plot showing the input response with nonlinear control

The controller designed drives the RSIP from the initial pending position to the upright position in one swing. The figure 19 shows first state response with a nonlinear optimal feedback controller, whereas the figure 20 shows the input response.

The closed loop system dynamics were also simulated using SimMechanics. The block diagram with the nonlinear feedback control law is shown in figure 21.

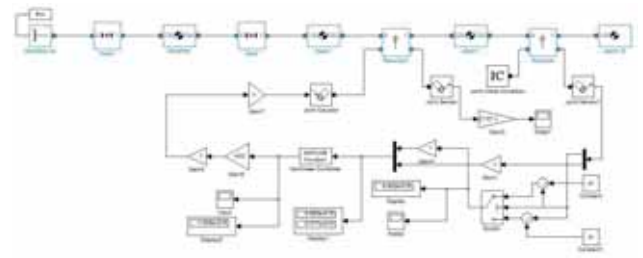


Fig. 21: Block diagram of 2D-RSIP with closed loop nonlinear controller

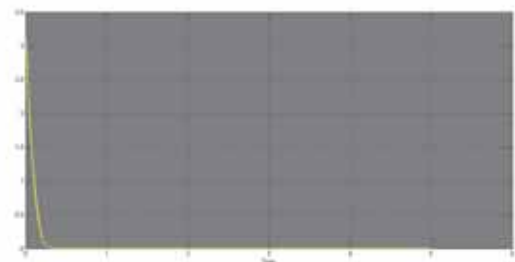


Fig. 22: Simulink output showing response of  $\theta_2$

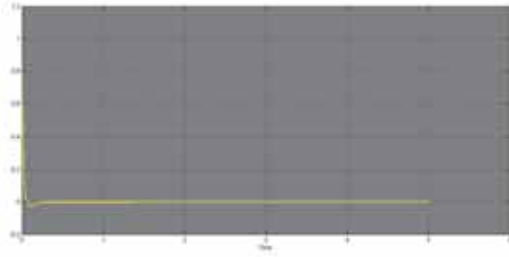


Fig. 23: Simulink output showing input response

Figures 22 and 23 show the angle response and the input response respectively. It can be seen that the results match closely with Matlab simulation of the system dynamics seen in figures 19 and 20. The figure 24 shows a sequence of images of the swing up as simulated by SimMechanics. It should be noted that the angle  $\theta_1$  is not included in the system dynamics and is not controlled.

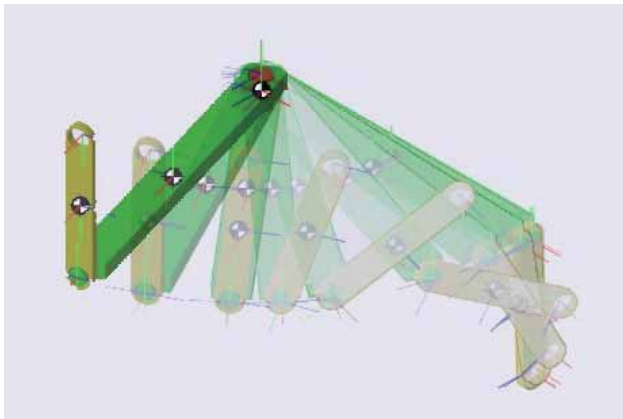


Fig. 24: Image sequence of swing up

## 7. CONCLUSION AND FUTURE WORK

In this work the RSIP and RDIP system models were derived and LQ control used to stabilize them in the inverted position. The models were shown to work well both in simulations and experiments. SimMechanics provided another platform to test and verify system dynamics and control laws. Further, stable manifold theory was used to find solution to HJ equation albeit for a simpler system. The solution was then used to derive a single nonlinear optimal feedback law to drive the state from initial pending position and stabilize in

inverted position. Simulations demonstrated the closed loop nonlinear control for a 2D-RSIP system.

A subsequent task will be to use the stable manifold theory to derive a nonlinear controller for a full state (4-dimension) RSIP. Although the work towards this was started it could not be completed in the stipulated time. Once a simple nonlinear feedback law is derived and verified using simulations it should be further improved upon to reduce the maximum magnitude of input to practical levels, which will have swing up in two or more swings. Practical limitations like input saturation can also be handled by the algorithm as shown by [7]. However to conclude this needs to be implemented for the RSIP to experiment the swing up and stabilization on a real system.

## REFERENCES

- [1] J. A. Acosta. Furuta's pendulum: A conservative nonlinear model for theory and practise. *Mathematical Problems in Engineering*, 2010, 2010.
- [2] K.J. Astrom and K. Furuta. Swinging up a pendulum by energy control. *Automatica*, 36:287–295, 2009.
- [3] John S Bay. *Fundamentals of Linear State Space Systems*. Boston: WCB/McGraw-Hill, 1999.
- [4] Dennis S. Bernstein. *GEOMETRY, KINEMATICS, STATICS AND DYNAMICS*. Princeton University Press, 2012.
- [5] V. Casanova, R. Piza J. Salt, and A. Cuenca. Controlling the double rotary inverted pendulum with multiple feedback delays. *International Journal of Computers, Communications and Control*, VII:20–38, 2012.
- [6] Benjamin Seth Cazzolato and Zebb Prime. On the dynamics of the furuta pendulum. *Journal of Control Science and Engineering*, page 8, 2011.
- [7] Ryu Fujimoto and Noboru Sakamoto. The stable manifold approach for optimal swing up and stabilization of an inverted pendulum with input saturation. *IFAC World Congress, Milano, Italy*, 2011.

- [8] K. Furuta, M. Yamakita, and S. Kobayashi. Swing-up control of inverted pendulum using pseudo-state feedback. *Journal of Systems and Control Engineering*, 206, 1992.
- [9] MathWorks. Mechanical import. <http://www.mathworks.com/help/physmod/sm/mech/vis/introducing-mechanical-import.html>.
- [10] Stepan Ozana, Martin Pies, Zdenek Slanina, and Radovan Hajovsky. Design and implementation of LQR controller for inverted pendulum by use of REX control system. *International Conference on Control, Automation and Systems*, 2012.
- [11] Minho Park, Yeoun-Jae Kim, and Ju-Jang Lee. Swing-up and lqr stabilization of a rotary inverted pendulum. *Artif Life Robotics*, pages 94–97, 2011.
- [12] Noboru Sakamoto and Arjan J. van der Schaft. Analytical approximation methods for the stabilizing solution of the hamilton-jacobi equation. *IEEE Transactions on Automatic Control*, 53, 2008.

## APPENDIX

### A. RDIP EQUATIONS

The matrices in equation (3) for RDIP are as follows

$$D = \begin{bmatrix} p1 & p2 & -m_3 l_3 L_1 \cos(\theta_2 - \theta_3) \\ p3 & m_3 L_2^2 + I_2 + I_3 + 2 m_3 L_2 l_3 \cos(\theta_3) & m_3 L_2 l_3 \cos(\theta_3) + I_3 \\ -m_3 l_3 L_1 \cos(\theta_2 - \theta_3) & m_3 L_2 l_3 \cos(\theta_3) + I_3 & I_3 \end{bmatrix}$$

where

$$p1 = -2 m_3 L_2 l_3 \sin(\theta_2) \sin(-\theta_2 + \theta_3) - m_3 L_2^2 (\cos(\theta_2))^2 + m_3 L_1^2 + m_3 L_2^2 - I_3 (\cos(\theta_2 - \theta_3))^2 - I_2 (\cos(\theta_2))^2 + m_2 L_1^2 + I_2 + I_3 + I_1$$

$$p2 = m_3 L_1 \sin(\theta_2 - \theta_3) L_2 \sin(\theta_3) - m_3 L_2 \cos(\theta_3) L_1 \cos(\theta_2 - \theta_3) - m_2 L_1 l_2 \cos(\theta_2) - m_3 l_3 L_1 \cos(\theta_2 - \theta_3)$$

$$p3 = m_3 L_1 \sin(\theta_2 - \theta_3) L_2 \sin(\theta_3) - m_3 L_2 \cos(\theta_3) L_1 \cos(\theta_2 - \theta_3) - m_2 L_1 l_2 \cos(\theta_2) - m_3 l_3 L_1 \cos(\theta_2 - \theta_3)$$

$$C = \begin{bmatrix} F1 \\ F2 \\ F3 \end{bmatrix}$$

where

$$\begin{aligned} F1 = & -m_2 (\dot{\theta}_2)^2 L_1 l_2 \sin(\theta_2) + 2 m_3 L_2 l_3 (\dot{\theta}_1) \sin(\theta_2) \cos(\theta_2 - \theta_3) \dot{\theta}_3 \\ & - 2 m_3 L_2 l_3 (\dot{\theta}_1) \sin(\theta_2) \cos(\theta_2 - \theta_3) \dot{\theta}_2 - 2 m_3 L_2 l_3 (\dot{\theta}_1) \cos(\theta_2) (\dot{\theta}_2) \sin(\theta_2 - \theta_3) - 2 m_3 L_2^2 (\dot{\theta}_1) \cos(\theta_2) \sin(\theta_2) \dot{\theta}_2 - \\ & m_3 L_1 \cos(\theta_2 - \theta_3) L_2 (\dot{\theta}_2)^2 \sin(\theta_3) - \\ & m_3 L_2 (\dot{\theta}_2)^2 \cos(\theta_3) L_1 \sin(\theta_2 - \theta_3) - 2 I_2 (\dot{\theta}_1) \cos(\theta_2) \sin(\theta_2) \dot{\theta}_2(t) - m_3 l_3 (\dot{\theta}_2)^2 L_1 \sin(\theta_2 - \theta_3) + m_3 l_3 (\dot{\theta}_3)^2 L_1 \sin(\theta_2 - \theta_3) \\ & 2 I_3 (\dot{\theta}_1) \cos(\theta_2 - \theta_3) \sin(\theta_2 - \theta_3) \dot{\theta}_2 + \\ & 2 I_3 (\dot{\theta}_1) \cos(\theta_2 - \theta_3) \sin(\theta_2 - \theta_3) \dot{\theta}_3 + n \mu_\phi \dot{\theta}_1 \end{aligned}$$

$$F2 = 2 m_3 l_3 (\dot{\theta}_3) L_2 (\dot{\theta}_2) \sin(\theta_3) + m_3 L_2 l_3 (\dot{\theta}_1)^2 \cos(\theta_2) \sin(\theta_2 - \theta_3) +$$

$$m_3 L_2 l_3 (\dot{\theta}_1)^2 \sin(\theta_2) \cos(\theta_2 - \theta_3) + 2 m_3 l_3 (\dot{\theta}_3) L_1 (\dot{\theta}_1) \sin(\theta_2 - \theta_3) + m_3 l_3 (\dot{\theta}_3)^2 L_2 \sin(\theta_3) + m_3 L_2^2 (\dot{\theta}_1)^2 \cos(\theta_2) \sin(\theta_2) + I_2 (\dot{\theta}_1)^2 \cos(\theta_2) \sin(\theta_2) + m_2 g l_2 \sin(\theta_2) + m_3 g L_2 \sin(\theta_2) + I_3 (\dot{\theta}_1(t))^2 \cos(\theta_2 - \theta_3) \sin(\theta_2 - \theta_3) + m_3 g l_3 \sin(\theta_2 - \theta_3)$$

$$F_3 = -2 m_3 l_3 (\dot{\theta}_2) L_1 (\dot{\theta}_1) \sin(\theta_2 - \theta_3) - m_3 L_2 l_3 (\dot{\theta}_1)^2 \sin(\theta_2) \cos(\theta_2 - \theta_3) - I_3 (\dot{\theta}_1)^2 \cos(\theta_2 - \theta_3) \sin(\theta_2 - \theta_3) - m_3 g l_3 \sin(\theta_2 - \theta_3) - m_3 L_2 l_3 (\dot{\theta}_2)^2 \sin(\theta_3)$$

$$G = \begin{bmatrix} nKDC \\ 0 \\ 0 \end{bmatrix}$$

## B. 2D-RSIP EQUATIONS

In the format of equation (22)

$$\ddot{\theta}_2 = \frac{m_2 l_2 \sin \theta_2 (m_2 L_1^2 l_2 \dot{\theta}_2^2 \cos \theta_2 - I_2 g + I_2 (\cos \theta_2)^2 g - m_2 L_1^2 g)}{-I_2^2 + I_2^2 (\cos \theta_2)^2 - I_2 m_2 L_1^2 + m_2^2 L_1^2 l_2^2 (\cos \theta_2)^2} + \frac{m_2 L_1 l_2 \cos \theta_2 nKDC}{-I_2^2 + I_2^2 (\cos \theta_2)^2 - I_2 m_2 L_1^2 + m_2^2 L_1^2 l_2^2 (\cos \theta_2)^2} \cdot u$$

## C. PHYSICAL PARAMETERS

	Experiment	Simulation*	
$m_1$	0.7125	0.0393584	kg
$m_2$	0.02	0.00643434	kg
$m_3$	0.037	0.0137624	kg
$L_1$	0.19	0.19	m
$L_2$	0.082	0.082	m
$L_3$	0.18	0.18	m
$I_1$	5.058E-3;	-	kgm <sup>2</sup>
$g$	9.8	9.8	m/s <sup>2</sup>
$n$	5	5	
KDC	0.0169	0.0169	
$\mu$	2.486E-4	2.486E-4	

\*The mass and inertia values for simulations were as obtained by SimMechanics from CAD data. The length  $l = 0.5L$ .

## Non-contact AFM Characterization of Au-Si and Au-Glass Substrates

Michael Ding

Macromolecular Science and Engineering, University of Michigan at Ann Arbor  
dingm@umich.edu

Professor Yang Ju

Department of Mechanical Science and Engineering, Nagoya University  
ju@mech.nagoya-u.ac.jp

### ABSTRACT

I present the theory and experimental data of classical non-contact atomic force microscopy [abbrev. NC-AFM] and microwave-based AFM. My substrates of interest are Au-glass and Au-silicon, all of which were self-fabricated. Microfabrication techniques such as *wet etching* and *E-beam vapor* were used to fabricate patterns of Au-Si and Au-glass. Initially, topographic and force curve data were collected with classical frequency-modulation AFM techniques. In addition, different types of classical AFM tips were used to collect topographic images of substrates. These results are compared and analyzed. Microwave-based AFM is a relatively new research topic and requires a very different tip that allows for the propagation of microwaves. The microwave AFM tips used are made from GaAs and covered with a thin layer of Au. Au-Si and Au-glass microwave data are then given and discussed. The final results demonstrate the versatility of classical non-contact AFM and microwave-based AFM instrumentation for characterization of different materials on the nanoscale.

### I. Introduction

Atomic force microscopy [AFM] is an essential tool used for the characterization of materials at very small length scales. There are two main types of AFM instrumentation: non-contact and contact AFM. Here, we shall focus on non-contact atomic force microscopy. Non-contact AFM is also referred to FM-AFM, which stands for *Frequency Modulation Atomic Force Microscopy*. During the scanning of the material substrate, the instrument only allows for the cantilever to modulate its mechanical vibrational frequency while keeping the amplitude constant. The frequency modulation can then be directly related to the electromagnetic interaction between the tip and surface. This experimental data will then allow us to analyze the substrate and obtain important physical properties of that

substrate material such as its surface topography. Like the name suggests, non-contact AFM requires no physical contact with the substrate surface.

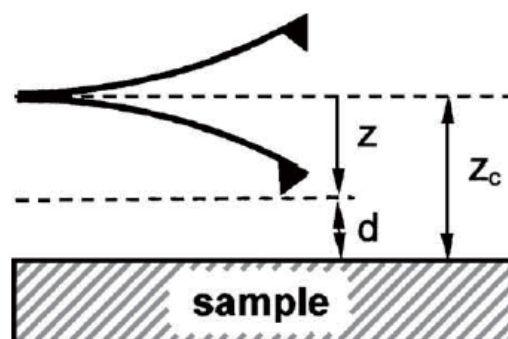


Figure 1. Non-Contact Mode AFM Cantilever<sup>1</sup>

There are several advantages to this design scheme when compared to contact-AFM. (Refer to *Figure 1*.) First of all, we will not need to concern ourselves with tip deformation. This allows us to preserve the mechanical integrity of our cantilever during experimentation. We also need not take into consideration the frictional forces between the AFM tip and the surface of the substrate. Hence, there will be one less experimental parameter to incorporate into our final result. Furthermore, mechanical contact between the tip and surface may cause the tip to stick onto the surface. All vibrations will then cease along with all of the experimental data. Because non-contact AFM [NC-AFM] operates at fixed amplitude, we do not need to worry about the tip running into our material substrate.

In recent years, a special type of NC-AFM, called microwave-based AFM has been introduced. Much of the operating principles remain unchanged when compared to “classical” NC-AFM. However, the classical AFM’s cantilever-tip structure needs to be replaced by a new cantilever that allows for the propagation of microwaves. By using microwave-based probes,

one can simultaneously obtain topographic data and electrical properties of the material substrate in question. Such probes can be fabricated from GaAs substrates and coated with Au to allow for propagation of electromagnetic waves.

## II. Substrate Fabrication

In order to carry out measurements with NC-AFM, the material substrate must first be properly prepared. In my experiments, I specifically focused on the Au-glass and Au-Si substrates. However, the versatility of NC-AFM has been well proven. The materials of interest need not be limited to just conductors, semiconductors, or insulators. Non-contact AFM has already been used for the characterization of biological materials (e.g. DNA, proteins) and polymeric systems as well. Liquid substrates with high viscosities are also suitable for NC-AFM analysis because the tip cantilever never comes into contact with the substrate. Any contact between the tip and a viscous fluid may easily cause the tip to “stick” onto the fluid. Again, we see that non-contact mode AFM has definite advantages for such material substrates.

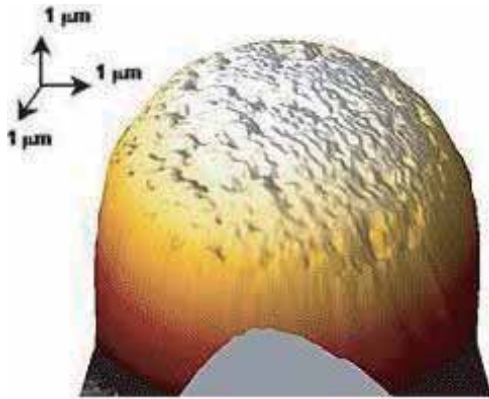
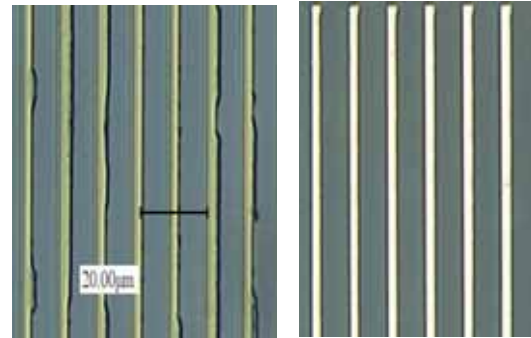


Figure 2. NC-AFM Scan of Polymer Sphere<sup>2</sup>

My substrates, namely Au-glass and Au-Si, were fabricated by using standard photolithographic techniques and with the help of an *E-Beam* vapor instrument. Gold (Au) was deposited on both the glass and silicon substrates with the E-Beam vapor instrument. Each substrate contains vertical line patterns that had the following Au thicknesses: 2, 4, and 6  $\mu\text{m}$ . The vertical height of each Au line is approximately around 100-150 nm. A 2 $\mu\text{m}$ -fabricated sample has lines of Au that are too thin to be accurately measured and analyzed by our non-contact AFM instrument. From my own experience, I found that the 4 $\mu\text{m}$  pattern worked best with the NC-AFM instrument.

Our AFM is capable of scanning a substrate area of 10 $\mu\text{m}$  x 10 $\mu\text{m}$  at a rate of 5  $\mu\text{m}/\text{sec}$ . An entire scan at these settings should typically take 20 minutes to complete. Higher resolution images require a slower scanning rate and thus, more time for each individual scan. *Figures 3 and 4* show photographs of my fabricated substrates, which were used in the experimentation. Please note that the actual distance between two lines of Au remains constant regardless of how thick the Au lines are.



*Figures 3 & 4. Au-Si substrate with 4 $\mu\text{m}$  thick Au lines on left. Au-Glass substrate with 4 $\mu\text{m}$  thick Au lines on right. The distance between two Au lines is approximately 8  $\mu\text{m}$ .*

## III. Surface-Tip Interaction

Non-contact atomic force microscopy requires us to maintain the cantilever’s mechanical vibrational amplitude while allowing for the cantilever frequency to modulate. Each AFM cantilever has its own spring constant  $k$  with units of [N/m] along with a natural resonant frequency denoted by  $f_0$ . The mechanics of an AFM cantilever-tip structure can be described by two important parameters: amplitude and frequency shift. The frequency shift<sup>a</sup>, denoted by  $\Delta f$ , is defined as the difference between the experimental frequency and the cantilever’s natural resonance frequency:  $\Delta f = f - f_0$ .

Van der Waal forces are responsible for most surface-tip interactions in non-contact mode AFM. These fundamentally electromagnetic interaction forces can be either attractive or repulsive. The vibrational frequency of the cantilever explicitly depends on such surface-tip interactions. Ultimately, the spatial dependence (in our case, the  $z$ -axis) of the tip and the frequency shift ( $\Delta f$ ) provides the necessary contrast that allows for the AFM characterization of the material substrate. Modern NC-AFM

<sup>a</sup> Frequency shift is also known as *phase shift*.

instruments are very sensitive and can detect very subtle changes in  $\Delta f$ . In fact, it has been already demonstrated that NC-AFM is capable of producing atomic-scale resolution images of the surface topography. Albrecht et al.<sup>3</sup> have shown that the lowest detectable frequency shift was given by

$$\delta(\Delta f) = \sqrt{(f_0 k_B T B / 2\pi k Q \langle z^2_{osc} \rangle)} \quad (1)$$

where  $k_B T$  is the thermal energy,  $B$  is the bandwidth,  $k$  is the cantilever stiffness factor, and  $Q$  is the quality factor. The quantity  $\langle z^2_{osc} \rangle$  is the “mean-square amplitude of the driven oscillator<sup>1</sup>.” Actual values for  $Q$  and  $\langle z^2_{osc} \rangle$  can be measured by any AFM instrument and given by its operating software. The cantilever stiffness factor is related to the natural resonant frequency by the expression  $f_0 = (1/2\pi) \sqrt{k/m}$ .

#### IV. Sample-Tip Interaction and $\Delta f$

In order to obtain the topography of the substrate and its associated force curve measurements, the frequency shift  $\Delta f$  must be experimentally found.  $\Delta f$  is the single most important parameter when using NC-AFM to probe topographic properties of materials. While finding the topography of a sample substrate, the NC-AFM instrument keeps the cantilever frequency fixed while the tip-sample distance modulates. The separation distance between the tip and substrate must change in order to compensate for the effect of the sample-tip interaction forces. In turn, this produces the topography of the substrate sample that we are looking for. The same arguments also apply for microwave-based AFM.

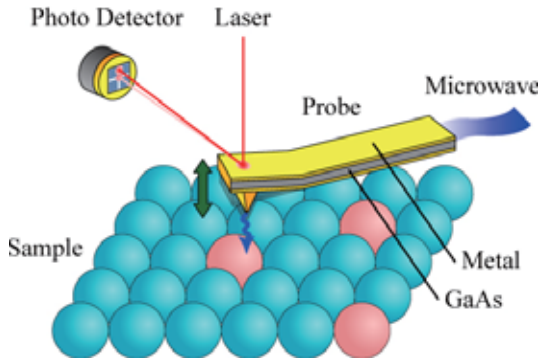


Figure 5. A microwave-based AFM in use<sup>4</sup>  
The laser and photo detector work together to control and measure the movement of the cantilever<sup>4</sup>. Applies for all NC-AFM systems not just microwave-based AFM.

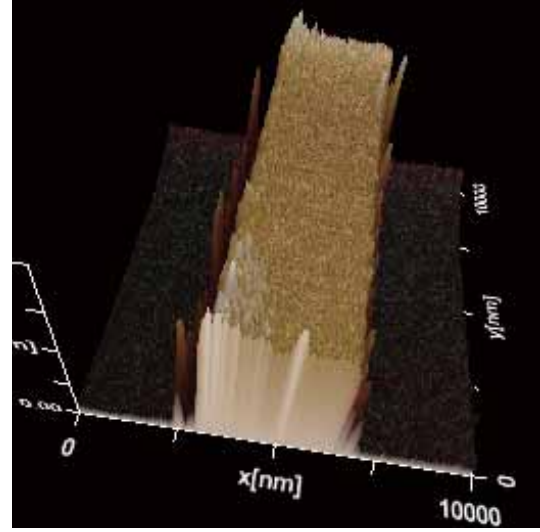


Figure 6. Topography of Au-Si Substrate  
One of the topographic images obtained with my NC-AFM instrument. The center-raised structure is that of Au. Image resolution: 256x256 pixels.

The specific atomic force microscope that I used for these experiments is the *JSPM-5200 Scanning Probe Microscope*, which is manufactured by *JEOL*. Once a topographic image is obtained, we can then proceed to get the atomic force curve at different positions on the surface of the substrate. In order to find the relationship between the frequency shift  $\Delta f$  and surface-tip interaction, the AFM instrument first has to measure  $V_{ts}$ , also known as the *tip-sample interaction potential*. As the standoff distance between the tip and substrate changes, so does the  $V_{ts}$  parameter. To calculate  $\Delta f$  from  $V_{ts}$ , we use the relation

$$\Delta f = (V_{ts} - V_0) \times 200 \text{ [Hz/V]} \quad (2)$$

where the parameter  $V_0$  is defined as the reference voltage of the instrument. The AFM software automatically provides the reference potential  $V_0$  during every experimental run. A conversion factor of 200 Hz/Volt is required to make the formula consistent unit-wise. Equation (2) provides the crucial link between the interaction potential and frequency shift. Once  $\Delta f$  has been calculated, we can find the force curve with the help of the following expression<sup>1</sup>

$$dF/dz = -2k(\Delta f/f_0) \quad (3)$$

where the spring constant  $k$  represents the cantilever's stiffness. From equation (3), we see that the frequency shift and natural resonant frequency are the only two parameters that

control the value of  $dF/dz$ . The frequency shift  $\Delta f$  comes from the van der Waals interaction between the tip and the material substrate. And the natural frequency  $f_0$  is completely determined by the mechanical structure of the cantilever. By using formulas (2) and (3), one can calculate the force derivative curve of any material substrate. Furthermore, formulas (2) and (3) remain valid for microwave-based atomic force microscopy. In fact, the only requirement for us is to conduct the experiment in non-contact mode.

## V. Results and Analysis

Classic non-contact atomic force microscopy experiments can be conducted by using prefabricated tips such the *Olympus Series* tips, which are composed of Si. In my experiments, I selected the *Olympus AC160TS Series* tip with a spring constant value of  $k = 42$  N/m. After obtaining the interaction potential  $V_{ts}$  at different standoff distances, formulas (2) and (3) are then used to calculate the cantilever frequency shift ( $\Delta f$ ) and its corresponding the force curve ( $dF/dz$ ). In *Figure 7*, we can see the topographic features of the Au-glass substrate. Different locations were selected on this specific pattern for atomic force derivative measurements.

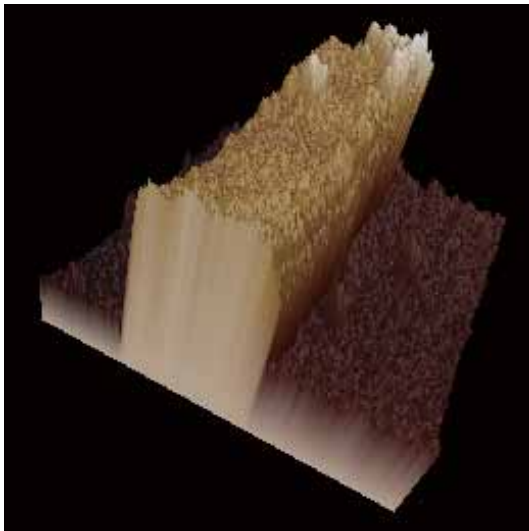


*Figure 7. Au-glass Substrate Topography Image was obtained with Olympus 3C tip. The center column is Au with a thickness of  $4 \mu\text{m}$ .*

Sets of atomic force curve data were collected for both the Au and glass regions of the substrate. From the experimental data, it seems that after a surpassing certain *threshold distance*, the interaction potential  $V_{ts}$  remains more or less constant. Tip-surface interaction forces are electromagnetic in nature and regarded as van

der Waal forces. At long distances away from the surface of the material, these intermolecular interactions start diminishing very quickly<sup>5</sup>. Therefore, the experimental data confirm what we knew all along about van der Waal forces. Mathematically speaking, van der Waal forces are proportional to  $1/z^6$  for large values of  $z$ . *Figures 8 and 9* demonstrate this physical effect.

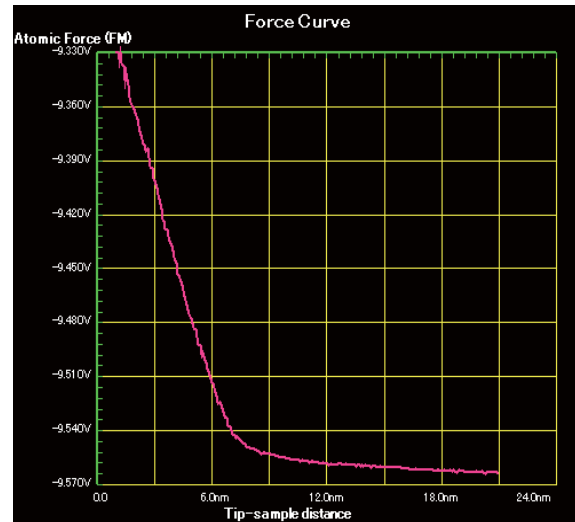


*Figure 8. Potential Curve of Au (conductor) After going beyond 8 nm, the atomic force curve starts to level down i.e. become flat. This implies that the van der Waals forces start to die down and has very little appreciable effect on the cantilever.*

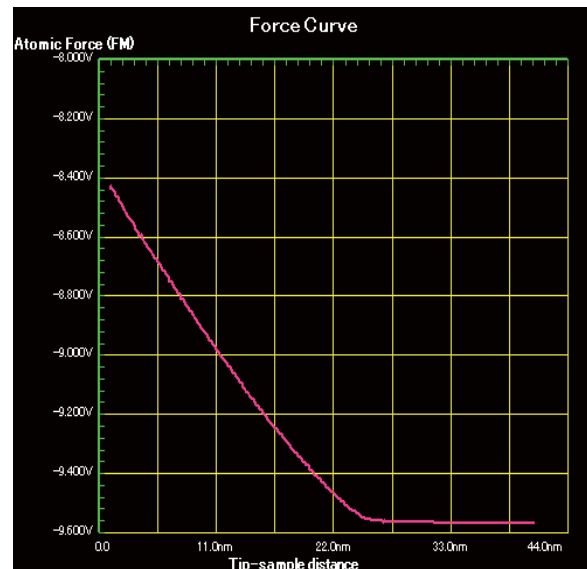


*Figure 9. Potential Curve of Si (semiconductor) Here, the threshold distance was measured at approximately 23 nm. Apparently, a longer-range interaction force may exist between the cantilever and a semiconductor material like Si.*

In order to conduct an AFM force curve measurement, one must first select a specific point of interest on the substrate. Not all positions on the material substrate turn out to be useable. For instance, some positions contain too much *noise*. Refer to *Figure 10*. It is usually best not to select measurement points that are located near the boundary of two materials e.g. Au and Si. Three sets of force curve data were taken for each section of the substrate. Afterwards, these results were analyzed and compared by graphing them on the same plot.

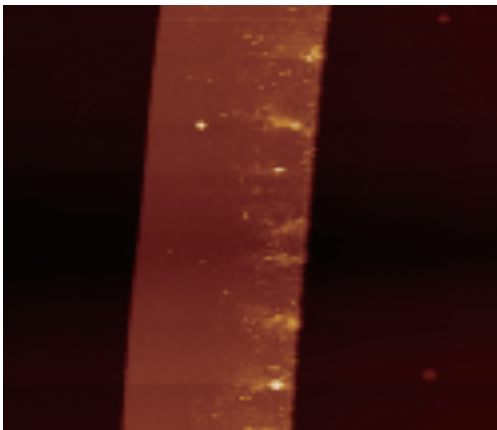


*Figure 10. Au-Si Topographic Image – Top View*  
The bright, center stripe is that of Au, which has a thickness of  $4\ \mu\text{m}$ . The two darker parts of this image are Si. The blemishes found on the right hand part of the Au stripe bordering Si come from experimental noise.

When using expression (3) to calculate  $dF/dz$ , it is important to realize where the value of natural frequency  $f_0$  originates. For manufactured AFM tips like the *Olympus 3B*, the manufacturer usually provides its natural resonant frequency. However, the AFM instrument can also detect the cantilever's resonant frequency through a process known as cantilever *tuning* and in many cases it differs from the manufacturer's specifications. For instance, the original factory specifications for my *Olympus* tip gave a value of  $f_0 = 300\ \text{kHz}$  while the actual measured value came in at approximately  $244.529\ \text{kHz}$ . This discrepancy may have been caused by the fact that my experiments had not been conducted in UHV conditions. One should use the actual measured value of natural frequency  $f_0$  instead of the manufacturer's specifications. Thus, the experimentally determined value of  $f_0 = 244.529\ \text{kHz}$  was inserted into the governing equations. Because the same AFM tip was used for both Au-Si and Au-glass measurements, the value of

$f_0$  remained constant. Hence, there was no need to *retune* and obtain another  $f_0$  value. Refer to *Figure 11 & 12* for the atomic force curves of Au-glass substrate. These data points were collected with the *Olympus 3B* tip at a reference potential of  $V_0 = -8.028\ \text{V}$ . Note:  $V_0$  was also experimentally obtained by using the *tuning* feature of the AFM instrument.

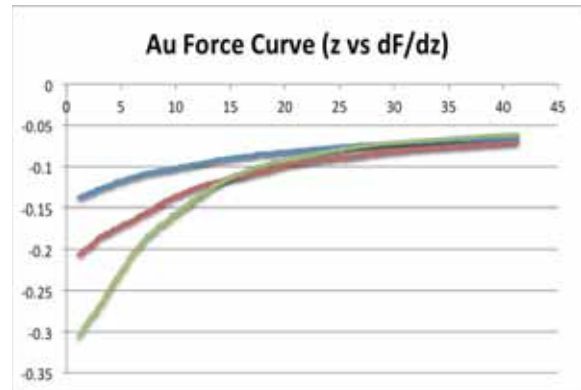


*Figure 11. Au Force Curve obtained by 3B tip*  
The horizontal axis corresponds to the distance between the tip and surface. It is labeled as  $z$  and measured in  $[\text{nm}]$  units. The vertical axis, labeled  $dF/dz$ , has units of  $[\text{N/m}]$ . This data was that of the Au-Glass substrate.

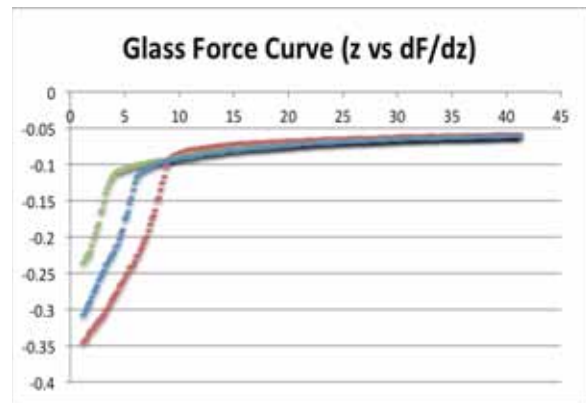


*Figure 12. Glass Force Curve obtained by 3B tip*  
The horizontal and vertical axes have the same units as *Figure 11*. This data was that of the Au-Glass substrate.

For the Au-Si substrate, the same *Olympus 3B* AFM tip had been used at the original reference voltage of  $V_0 = -8.028\ \text{volts}$ . Even though the top surface layer was deposited with Au, the entire substrate was made out of silicon as opposed to glass in the Au-glass substrate. In other words, both of the substrates were coated with a layer of Au but their bulk substrate materials were fundamentally different. From my experimental

results, I found that the bulk substrate material played an important role in influencing the AFM characterization of the surface layer (e.g. Au). When examining *Figure 11*, one can see that  $dF/dz < 0$  for all values of  $z$  ranging from 0 to 40 nm. However, the same is not true for the Au surface of the Au-Si substrate.

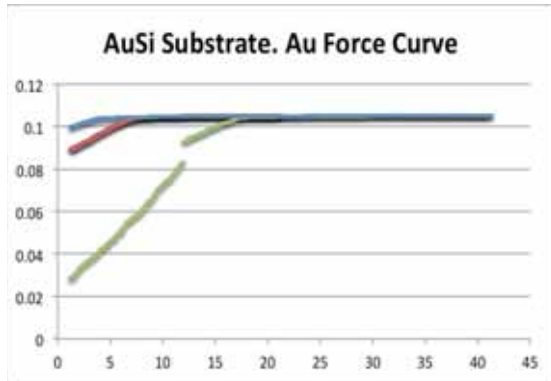


*Figure 13. Au portion of Au-Si Substrate*  
The vertical axis represents the quantity  $dF/dz$  in units of  $N/nm$ . Data was taken with 3B tip.

For the Au-Si substrate, the atomic force curve associated with the Au surface is positive [ $dF/dz > 0$ ] for all values of  $z$  ranging from 0 to 40 nm. Despite both having Au surfaces, their bulk substrates played the determining role in their atomic force curves. In order to find out whether the interaction force is attractive or repulsive, one must calculate the actual force  $F(z)$  experienced by the cantilever.  $F(z)$  can be determined by numerically integrating over the atomic force derivative curve ( $dF/dz$ ). A positive value implies that the interaction is repulsive; this is apparently the case for Au surface on the bulk silicon substrate. As for the Au surface deposited on the glass substrate, the surface-tip interaction is inherently attractive. I end the discussion of classical NC-AFM by giving the force curve for Si in Au-Si substrate.

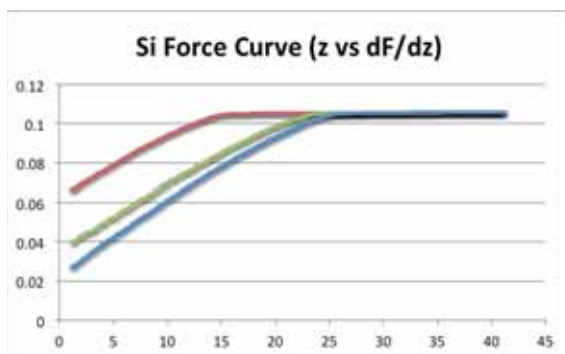
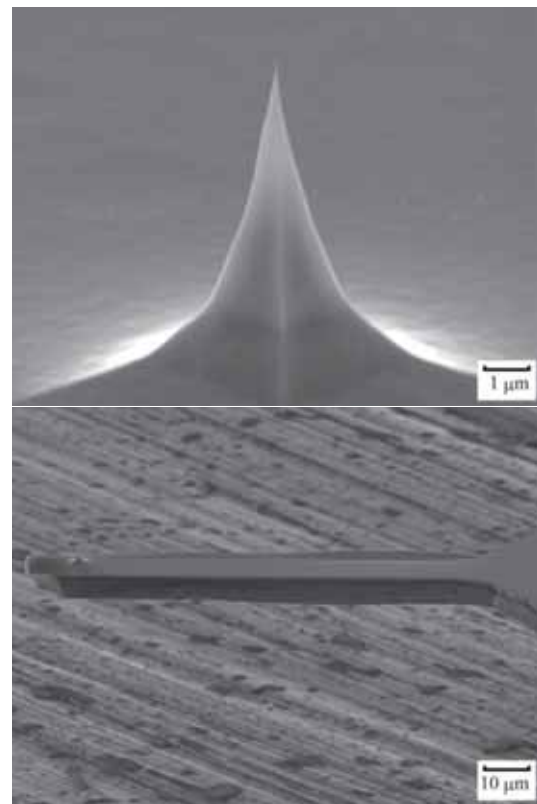


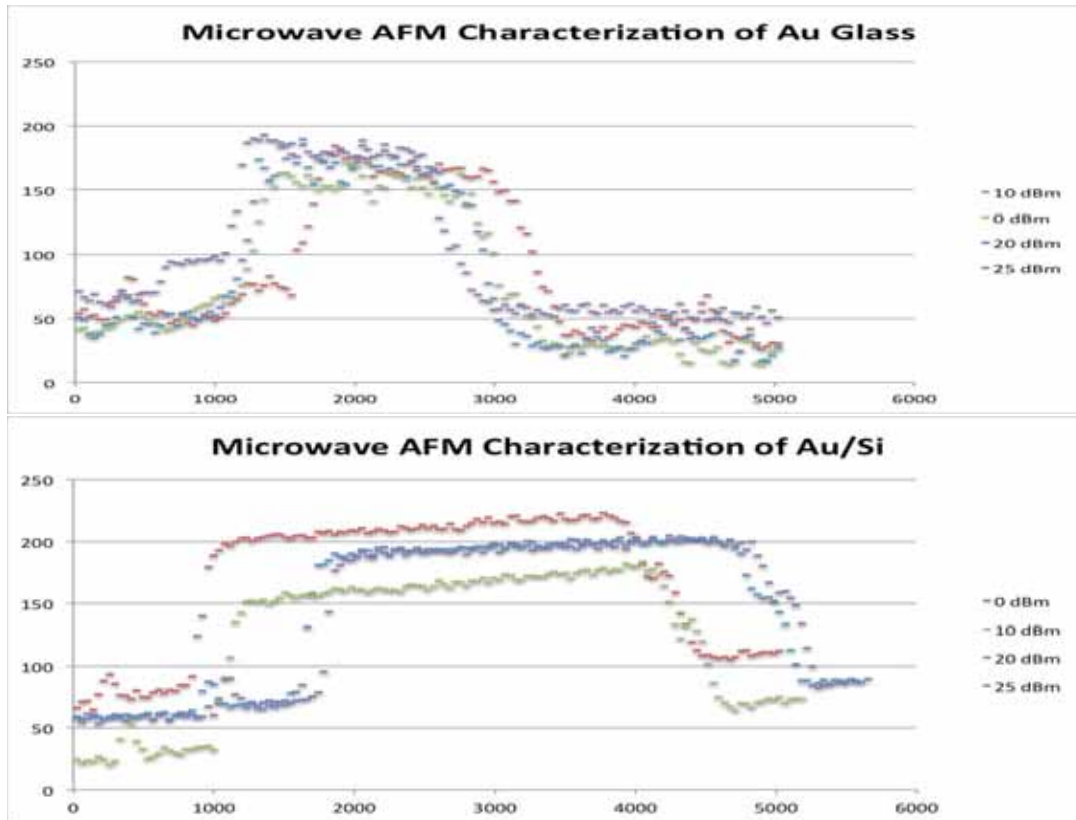
*Figure 14. Si portion of Au-Si Substrate*

The last section of this chapter is devoted towards microwave-based NC-AFM. Please refer back to *Figure 5* for a general pictorial description of a microwave-based AFM system<sup>b</sup>. The microwave cantilever allows for the transmission of electromagnetic through the tip of the cantilever. The most ideal microwave frequency for this experimental setup was determined to be at 94.00 GHz. With the help of a signal wave generator, different microwave amplitudes can be generated with ease. I focused on the following amplitudes: 0, 10, 20, and 25 dBm. Of course, a 0 dBm microwave experiment should be completely equivalent to that of a classical NC-AFM experiment.



*Figures 15(T) & 16(B). SEM Images*  
The top image is that of a tip that allows for microwave propagation. A nanoslit fabricated by FIB process<sup>6</sup> can be seen down the middle. Microwaves will propagate through the slit and eventually impact the substrate's surface. The bottom shows a SEM image of the microwave-based cantilever. The cantilever is fabricated from a GaAs substrate. Its resonant frequency  $f_0$  and spring constant  $k$  can be experimentally determined by completing the tuning process.

<sup>b</sup> A full schematic is given in the appendix.



Figures 17(T) & 18(B). Topographic data of substrates obtained by using microwave-based AFM

Once the generated microwave propagates through the tip, it will eventually impact the surface of the substrate. The transmission and reflection coefficients of the substrate's surface can theoretically be determined. When the incoming microwave hits the surface of the substrate, part of the wave will be reflected back towards the cantilever. That reflected microwave will be partially absorbed by the tip-cantilever structure. The absorption of electromagnetic radiation by the material surface may then induce a mechanical dampening effect on the cantilever. As a result, the tip-surface interaction forces will be reduced. A decrease in the atomic force derivative ( $dF/dz$ ) will naturally occur.

Au-Si and Au-glass were both characterized by our microwave AFM. Instrument. During the tuning procedure for the microwave cantilever, the frequency  $f_0$  was measured to be 140.64 kHz. Please refer to Figures 17 & 18 for the topographies of both the Au-Si and Au-Glass substrates. The x-axis, measured in [nm], gives us the horizontal profile of the substrate. The y-axis, also measured in [nm], provides us with the vertical height of the substrate. The raised structures, with approximate heights of 150 nm

in both images, are that of Au. This value coincides with our original microfabrication specifications of around 100 to 150 nm. Unfortunately, this microwave-based AFM cantilever did not produce meaningful atomic force derivative curve results.

## VI. Future Work

If the opportunity to continue this research ever presents itself, I would like to reattempt measuring the force derivative curve data gathered by the microwave-based AFM at different wave amplitudes. There may exist a fundamental relation that will allow us to calculate the frequency shift from the amplitude and frequency of the generated microwave.

In addition, I would like to use microwave AFM to explore the electrical conductivities of different materials (e.g. semiconductors) with application and value to industry. Kundhikanjana et al.<sup>7</sup> studied the effects of grapheme impurities on its electrical properties. Developing AFM methodologies to detect impurities and defects in crystalline material can potentially be another future area of research.

## VII. Acknowledgements

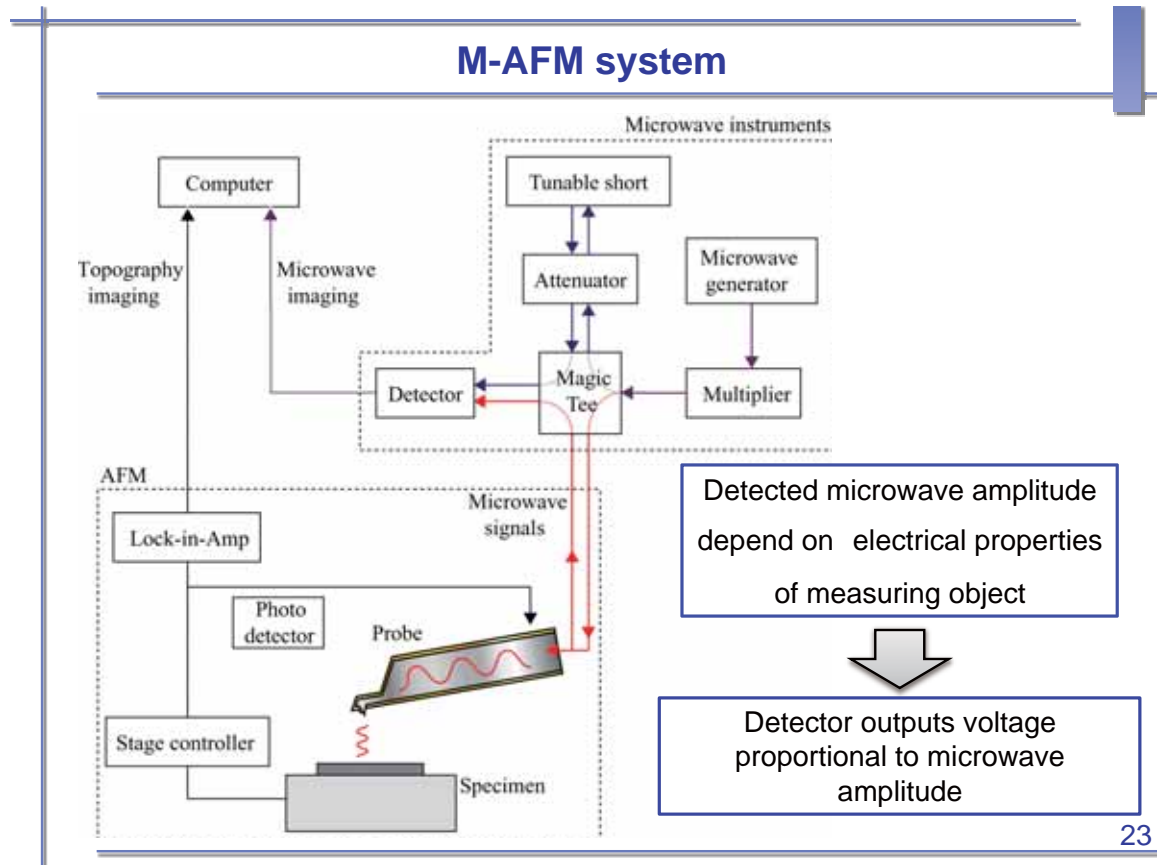
I would like to thank Prof. Yang Ju, Prof. Atsushi Hosoi and everyone else in the research group for giving me the opportunity to conduct AFM research this summer. A special thanks goes out to Takahiro Nakashima, a master's student in Prof. Ju's lab, for his valuable assistance. Also, this research opportunity would not have been possible without the kind and generous financial support from the *JASSO* organization.

## VIII. References

1. R. Garcia, R. Perez, *Surface Science Reports* 47, 197 (2002)
2. Parker Systems Corp, *Non-contact mode AFM*, [www.parkerafm.com/AFM-guide](http://www.parkerafm.com/AFM-guide)
3. T. Albrecht, P. Grütter, D. Horne, D. Rugar, *J. Appl. Physics* 69, 668 (2004)
4. L. Zhang, Y. Ju, A. Hosoi, A. Fujimoto, *Review of Scientific Instruments* 81, 123708 (2010)
5. S. Ke, T. Uda, R. Perez, I. Stich, K. Terakura, *Phys. Rev B* 59, 13267 (1999)
6. L. Zhang, Y. Ju, A. Hosoi, A. Fujimoto, *Applied Physics Express* 5, 016602 (2012)
7. W. Kundhikanjana, K. Lai, H. Wang, H. Dai, M. Kelly, Z. Shen, *Nano Letters* 9, 3762 (2009)

## Appendix

Detailed M-AFM Schematic (courtesy of Takahiro Nakashima)



# APPLICATION OF MOMENTUM-EXCHANGE-IMPACT-DAMPER ON VEHICLE COLLISION

Zhenyu GAN

Department of Mechanical Engineering, Graduate School of Engineering, University of Michigan  
ganzheny@umich.edu

Supervisor: Susumu HARA

Department of Mechanical Science and Engineering, Graduate School of Engineering, Nagoya University  
haras@mech.nagoya-u.ac.jp

## ABSTRACT

A conventional structure safety design for collision is plastic damping, by controlled plastic deformation, the energy of collision is released. However this method works at expends of destroy of the structure and fail to effect when the speed of the system larger than certain level. In this paper, a novel collision safety method based on Momentum-Exchange-Impact-Damper (MEID) system is investigated. With MEID, the impact of the controlled object is reduced by transferring part of its momentum to the damper mass thus reducing the maximum acceleration and the rebound distance. The performance of a simplistic vehicle model with MEID system and the effectiveness of the proposed system by simulations and experiments will be shown. Followed by the parameters study on this system.

## 1. INTRODUCTION

Collision safety has become a common problem in industrial and engineering fields. The large shock load and trip over of spacecraft landing are examples of collision safety problems found in aerospace engineering [1]. Another example of collision safety problems are the large acceleration and shock energy during impact of vehicle accidents. It was estimated in 2004 that 1.2 million people were killed and 50 million more were injured in motor vehicle collisions, which makes motor vehicle collisions the leading cause of injury death all over the world [2].

Traditionally, there are various collision safety systems have been proposed and they can be categorized into three types: 1) elastic damping; 2) plastic damping; and 3) fluid damping (these three types mechanisms are discussed in [3]). Conventionally, collision safety equipments by means of plastic deformation are used most frequently. The spacecraft in the surveyor series and the later Luna series used an aluminium honeycomb material in the swing-arm design [4]. The landers in the later Venera series and Vega series employed a crushable impact bumper [5]. As for vehicle structure, crumple zones [6] are always located in the front part of the vehicle, in order to absorb the impact of a head-on

collision. This method uses crushable materials such as honeycomb material, foam or controlled weakening of sacrificial outer parts to dissipate shock energy and reduces the maximum acceleration during impact. However, the drawbacks of this method are that they cannot be reused after the mechanism crushed and making the functional test of the same equipment before using impossible. So a reusable collision safety gear is highly desired from the viewpoint of reliability.

The momentum exchange impact damper (MEID) has been proposed to suppress impact responses induced by the external excitation force. This approach is different to the previous mentioned methods in that, with MEID, the impact of the controlled object is reduced by transferring part of its momentum to the damper mass. The application of MEID to floor shock vibrations problems has been proposed by Son *et al.* [7] which could effectively reduce both the acceleration response and the transmitted force to the slab. The other application of MEID is landing gear system for spacecraft proposed by Hara *et al* [8] which also reduce the maximum acceleration at the time of landing and prevent rebound or trip up of the spacecraft.

In this paper, the author applies MEID to horizontal vehicle collision case. First, the effectiveness of MEID in horizontal situation to reduce rebound distances and accelerations are verified. Additionally, a practical mechanism with MEID will be proposed and analyzed. Experiments are conducted to verify the simulation results. Following by the optimal parameters study of this model and further analysis.

## 2. MOMENTUM EXCHANGE IMPACT DAMPER THEORETICAL ANALYSES

The theoretical analyses of the vertical MEID have been conducted by Kushida, *et al.* [9], however to apply MEID on a horizontal vehicle, the single-legged mass-spring (MS) models need to be built to verify the effectiveness of MEID. Then the parameter optimization problem of the MEID is

discussed. With the optimization results, the effectiveness of MEID system is verified by simulations.

## 2.1 Theoretical Models of MEID

The paradigm of this system could be illustrated by two single-legged mass-spring models connected in parallel as shown in Fig. 1.

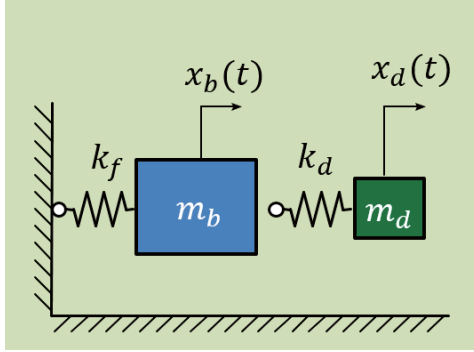


Figure 1 Basic model of horizontal MEID system

If neglect the friction on the ground, there are only four parameters in this model namely, front spring stiffness  $k_f$ , damper spring stiffness  $k_d$ , base mass  $m_b$  and damper mass  $m_d$ . Normally, the damper mass  $m_d$  is much less than base mass  $m_b$ ; and the damper spring stiffness  $k_d$  is smaller than the base spring stiffness  $k_f$ . The nominal values of the parameters in this paper are summarized in Table 1.

Table 1 Nominal parameters of MEID

Parameter	Value	Unit
$k_f$	$1.0 \times 10^4$	N/m
$k_d$	$1.0 \times 10^3$	N/m
$m_c$	7.4	kg
$m_d$	0.8	kg

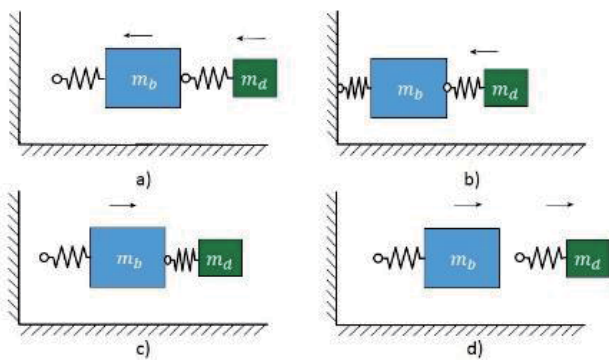


Figure 2 Phase transitions of MEID

According to the force analysis, from Fig. 2 that the dynamics of this system could be categorized into the following four phases: a) phase 0: before collision, no spring forces generate in the system, base mass and damper mass rush to the obstacle with same velocity; b) phase 1: after collision, before base mass separate from the obstacle, both

springs generate forces; c) phase 2: after base mass separation, before damper mass separate from the base, only damper spring generates force; d) phase 3: after damper mass separation, no spring forces generate.

The transitions of the phases could be defined by three instantaneous events: a) event 1: base collision, at this event as  $t = t_0$  the base displacement for the first time transit from positive to negative value; b) event 2: base separation, at this event as  $t = t_1$  the base displacement for the first time transit from negative to positive value; c) event 3: damper separation, at this event as  $t = t_2$  the difference between base displacement and damper displacement for the first time transit from negative to positive value.

For simplicity, this paper does not deal with cases in which the damper separates before base mass separation. From phases 1 to 3, the state equation of MEID [9] is described as follows:

$$\dot{\mathbf{x}}_m(t) = \mathbf{A}_{m_i} \mathbf{x}_m(t) + \mathbf{e}_m, (i=1,2,3) \quad (1)$$

$$\text{Where } \mathbf{x}_m(t) = \begin{bmatrix} x_d(t) \\ x_b(t) \\ \dot{x}_d(t) \\ \dot{x}_b(t) \end{bmatrix}, \mathbf{e}_m(t) = \begin{bmatrix} 0 \\ 0 \\ -\frac{f_2}{m_d} \\ \frac{f_1 + f_2}{m_d} \end{bmatrix},$$

$$\mathbf{A}_{m1} = \begin{bmatrix} 0 & 0 & 1 & 0 \\ 0 & 0 & 0 & 1 \\ \omega_d^2 & -\omega_d^2 & 0 & 0 \\ -\rho_d \omega_d^2 & \rho_d \omega_d^2 + \omega_b^2 & 0 & 0 \end{bmatrix},$$

$$\mathbf{A}_{m2} = \begin{bmatrix} 0 & 0 & 1 & 0 \\ 0 & 0 & 0 & 1 \\ \omega_d^2 & -\omega_d^2 & 0 & 0 \\ -\rho_d \omega_d^2 & \rho_d \omega_d^2 & 0 & 0 \end{bmatrix},$$

$$\mathbf{A}_{m3} = \begin{bmatrix} 0 & 0 & 1 & 0 \\ 0 & 0 & 0 & 1 \\ 0 & 0 & 0 & 0 \\ 0 & 0 & 0 & 0 \end{bmatrix},$$

$$\omega_d = \sqrt{\frac{k_d}{m_d}}, \omega_b = \sqrt{\frac{k_f}{m_b}}, \rho_d = \frac{m_d}{m_b}.$$

where dot “ $\cdot$ ” means the time derivative and generates corresponding velocities.

To simplify the problem we first assume that there is no friction in this model, to find out the optimal parameters for MEID system, the final velocity of base mass is evaluated. Based on the previous descriptions of MEID system, this value could demonstrate the energy level of base mass and the performance of the MEID system. At each event, the terminal state of previous phase corresponds to the initial state of the following phase. MEID model states  $x_{m0}$ ,  $x_{m1}$  and  $x_{m2}$  represents the system states at  $t = t_0$ ,  $t_1$  and  $t_2$  respectively.

$$\mathbf{x}_m(t_0) = \mathbf{x}_{m0} = [0 \quad 0 \quad v_0 \quad v_0]^T \quad (2)$$

where  $v_0$  is the collision velocity.

$$\mathbf{x}_m(t_i) = \mathbf{x}_{mi} = e^{A_{mi}(t_i - t_{i-1})} \mathbf{x}_{m(i-1)}, (i = 1, 2, 3) \quad (3)$$

$$v_{b2} = \frac{1}{1 + \rho_d} \left\{ -\rho_d \sqrt{(v_{d1} - v_{b1})^2 + \hat{\omega}_d^2 (x_{d1} - x_{b1})^2} + (\rho_d v_{d1} + v_{b1}) \right\} \quad (4)$$

$$\hat{\omega}_d = \sqrt{1 + \rho_d \omega_d}.$$

So from Eq. (4) the rebound base velocity equals to  $v_{b2}$  and this value depends on the initial velocity  $v_0$  and system parameters  $k_f$ ,  $k_d$ ,  $\rho_d$ .

## 2.2 MEID Optimization

From previous research [8] MEID could effectively reduce both the acceleration response and the rebound distance, but there is one important problem: the parameters of MEID should be selected appropriately to obtain optimal damper performance. So in this section, the optimization results of two important parameters namely  $k_d$  and  $m_d$  are shown.

### 2.2.1 Optimization of Damper Spring Stiffness $k_d$

When varies damper spring stiffness  $k_d$ , the corresponding acceleration of the base mass decreases dramatically at first then increases and has minimum acceleration at around  $k_d = 5200$  N/m as could be observed from Fig. 3.

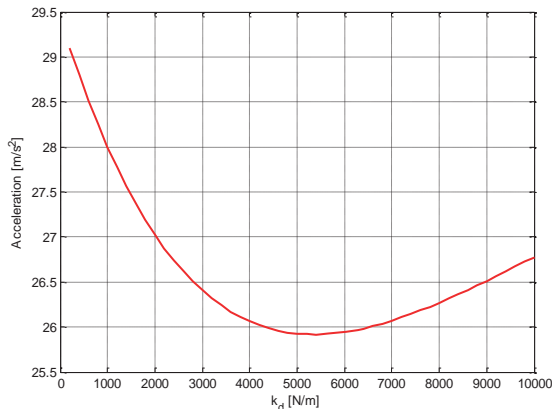


Figure 3 Optimal  $k_d$  for acceleration reduction

From Fig. 4 the accelerations of the systems with optimal PMEID, nominal PMEID and the system without MEID are

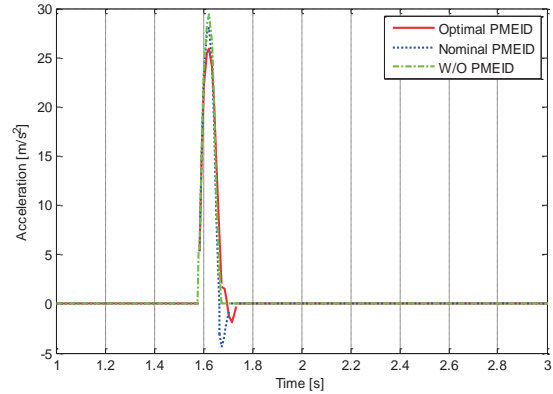


Figure 4 Acceleration reduction of MEID systems

compared. As indicated in Fig. 3 the maximum acceleration of base mass reduced from about 29 m/s<sup>2</sup> to 26 m/s<sup>2</sup>. However, from Fig. 5 that the minimum value of base rebound velocity cannot be found because the rebound velocity of base mass monotonically increases when increases  $k_d$  and generally

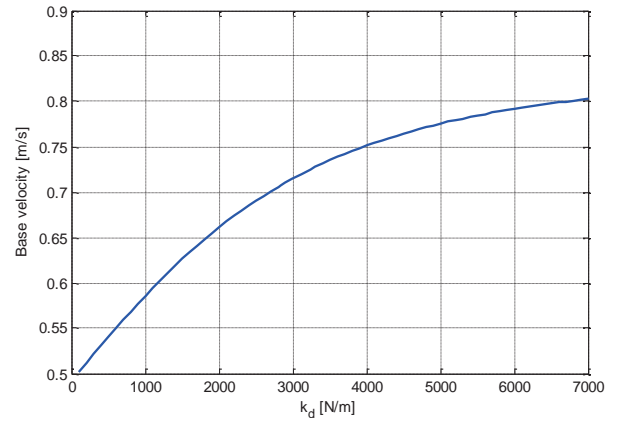


Figure 5 Optimal  $k_d$  for base velocity reduction

the smaller value of  $k_d$  the larger effects of MEID velocity reduction. The time response of base velocity of the system with optimal MEID, nominal MEID and the system without MEID are compared in Fig. 6.

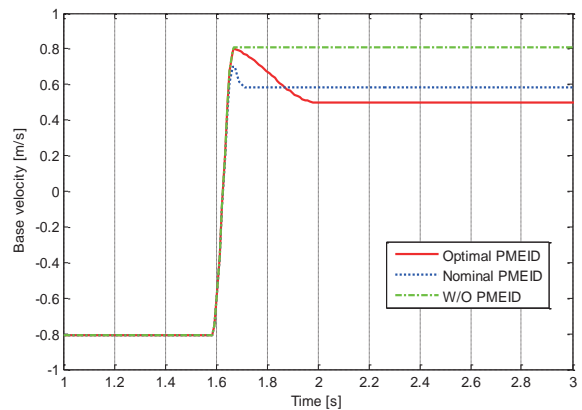


Figure 6 Base velocity reduction of MEID systems

### 2.2.2 Optimization of Damper Mass $m_d$

The other important MEID parameter, damper mass  $m_d$ , also has great influence on the reductions of acceleration and base velocity.

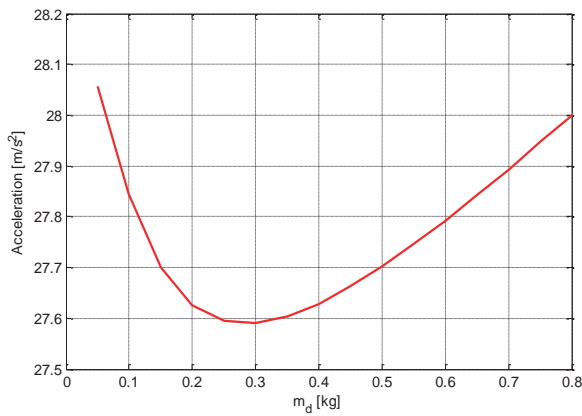


Figure 7 Optimal  $m_d$  for acceleration reduction

As increasing  $m_d$ , the maximum acceleration of base mass demonstrates a convex tendency as from Fig. 7 that the optimal value of  $m_d$  equals to 0.3 kg with minimum acceleration about  $27.6 \text{ m/s}^2$ . However, from the comparisons of the systems with optimal MEID, nominal MEID and the system without MIED in Fig.8, the variance of  $m_d$  have limited effects on the acceleration reduction.

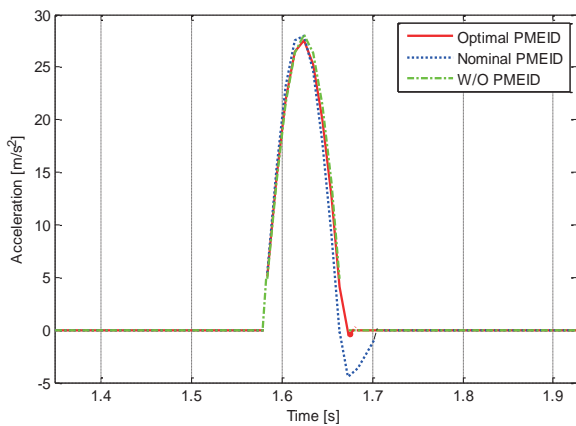


Figure 8 Acceleration reduction of MEID systems

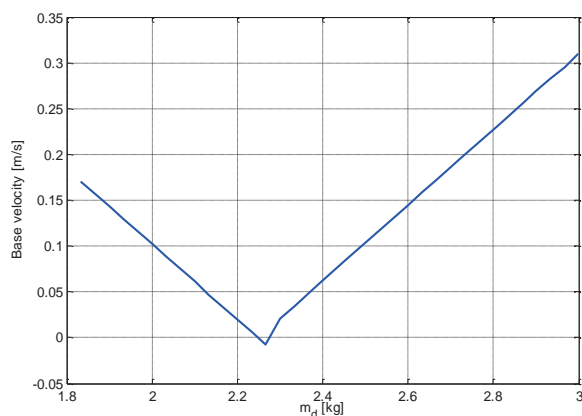


Figure 9 Optimal  $m_d$  for base velocity reduction

On the other hand, when  $m_d$  varies, the velocity of base mass changes dramatically as could be observed from Fig. 9 that the velocity almost decreases to zero when  $m_d$  equals to 2.25 kg. These effects are also shown in the time response of the base velocity in Fig. 10.

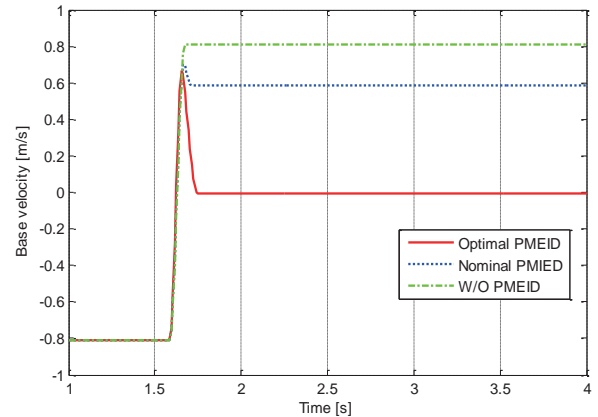


Figure 10 Base velocity reduction of MEID systems

So far we have analysed the basic model of MEID system and two parameters optimization in reductions of base acceleration and base velocity. In the following part we will present a practical model to apply MEID system with the previous knowledge of MEID performance.

## 3. APPLICATION OF MOMENTUM EXCHANGE IMPACT DAMPER TO CART SYSTEM

In this section, a practical model with PMEID system will be presented and discussed, following with the brief introduction of the simulation method and system dynamics, then the simulation results will be analyzed to see to what degree the PMEID system works on decreasing the rebound distance and maximum velocity.

### 3.1 Modeling System

To build the model of this system, there are two major problems to be solved before applying of the MEID system to vehicles. The first problem is to determine the number of parameters in this model, a simplistic model with smallest set of parameters is needed. Different from previous theoretical analysis, in practice, friction cannot be neglect because it is the major way to dissipate energy in the system. There are two major surfaces generate frictions in this model, ground

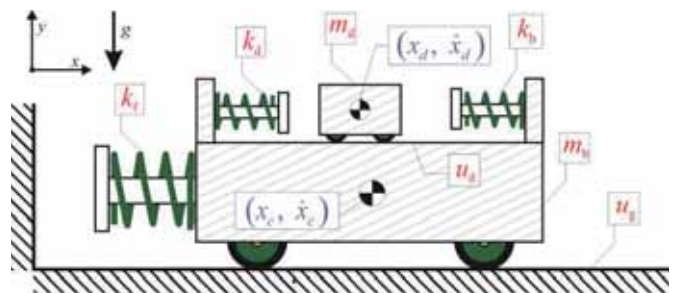


Figure 11 Simplistic model for a cart system

and the upper surface of the cart. So in this model two parameters  $U_g$  and  $U_d$  are assigned to match the real cases.

Table 2 Parameters of horizontal MEID system

Parameter	Symbol
Front cart spring stiffness	$k_f$
Damper spring stiffness	$k_d$
Damper mass	$m_d$
Cart mass	$m_c$
Back cart spring stiffness	$k_b$
Ground friction ratio	$U_g$
Cart friction ratio	$U_d$

The second problem caused by the limitation of the MEID system. After the momentum of the vehicles absorbed by the damper mass, the damper mass will be released by the vehicles and hard to be recycled. Additionally, the damper mass with large momentum also could be dangerous for the objects behind the system. To solve this problem, an additional spring is fixed at the back of the cart. This spring could prevent the damper mass rush out of the cart system and reuse the MEID system again, however when the damper mass pushes this spring, it increases the rebound distance thus weakening the effects of MEID. So there is a trade off in this mechanism and an extended model will be discussed later in this paper.

### 3.2 Simulation Method

The main method used in this model is Hybrid Dynamic Modelling [10]. Most of the case, the dynamics of the system always changes during different phases. To simulate the dynamics we use three files build the framework [11].

Flow map (Dynamics): The flow map  $\dot{y} = f(y, z, p)$  describes the continuous dynamics of the system (left side of Fig. 12) by means of a set of ordinary differential equations. Since a mechanical system is of second order, we need to include all velocities in the state vector. According to different phases, the system dynamics is different. For example, in phase 1 the whole system only subject to friction forces and no spring forces; on the other hand, in phase 2 both cart and damper mass subject to spring forces.

Jump map (Phase): The jump map describes the discrete dynamics that occur during so called 'Events'. They map the state before an event to the state after and event:

$$\begin{bmatrix} y^+ \\ z^+ \end{bmatrix} = g(y^-, z^-, p) \quad (5)$$

For instance, after the event 1 (front spring touch the wall) happens, the discrete state  $z$  changes from  $z^- = 1$  to  $z^+ = 2$ , then the system continuous with the dynamics of Phase 2. The system continues in the following sequence: 1-

2-3-4-5-4-3-4-5-4-3 ... until the total system energy (sum of kinematic energy and spring potential energy of cart and damper mass) less than a small threshold.

Jump set (Events): Events are normally encoded by the zero crossing of event functions:  $e(y, z, p) = 0$ , with  $\dot{e} > 0$ . These functions (one for each event) encode the jump set of the hybrid dynamic model. For example, the function for event 1 is:

$$E_1 = -(x - l_{spring} - \frac{1}{2}l_{cart}) \quad (6)$$

The jump set file detects the change of  $E_1$  from positive to negative when the cart front spring touch the wall.

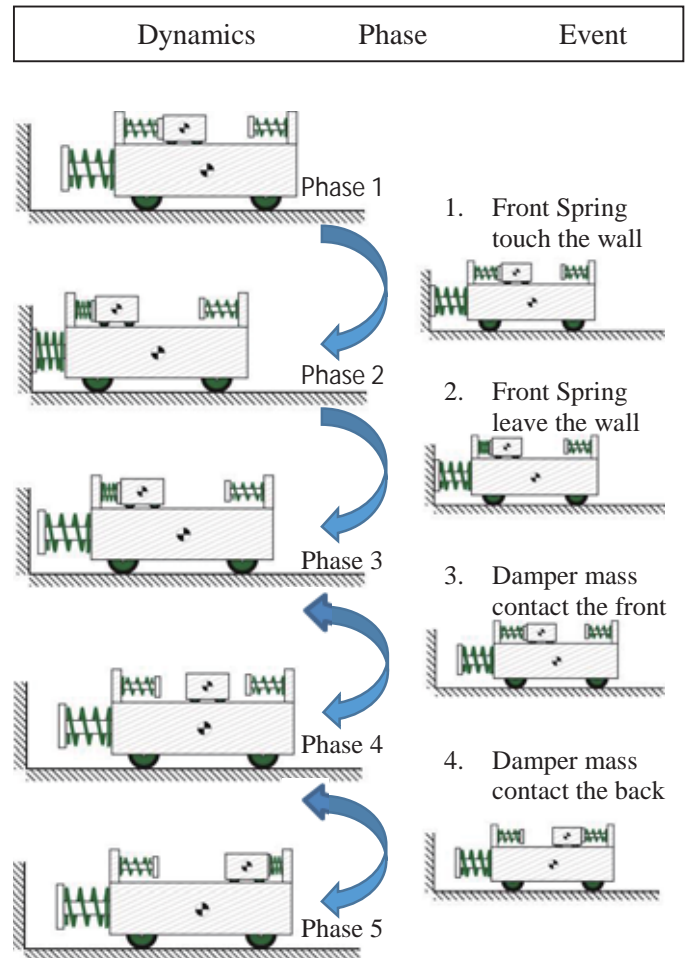


Figure 12 Hybrid dynamics for the cart system

### 3.3 Simulation Results

For simplicity, the simulation starts with given initial condition and these values are not fixed. To get better matching of the experiment system, the initial condition of the simulation are optimized. The optimal results can be found by some optimal method such as Nelder-Mead simplex method [12]. The optimal simulation corresponding to the nominal experimental results can be seen from Fig. 14. The coordinates in Fig. 14 are changed to match the experimental system.

## 4. EXPERIMENTS

In this section, experimental investigation is shown and following by the comparison with the simulation results. Figure 13 shows the experimental cart system designed to conduct experiments. In this system an encoder is installed to measure the position of the base cart and an accelerometer is installed to measure the acceleration. The velocity of the system is calculated by taking the derivative of the position data. The total length of the experiment platform is 1.8 m as could be observed in first figure of Fig. 14; the cart starts from a ramp and by verifying the height of the slope of the ramp, the cart system could starts with different initial velocities.



Figure 13 Experimental cart system

### 4.1 Parameter Identification

The parameter values of the experimental system match with previous simulation and are shown in Table 3.

Table 3 Parameters of experimental system

Parameter	Symbol	Value
Front cart spring stiffness	$k_f$	$1 \times 10^4$ N/m
Damper spring stiffness	$k_d$	$1 \times 10^3$ N/m
Damper mass	$m_d$	0.8 kg
Cart mass	$m_c$	7.4 kg
Back cart spring stiffness	$k_b$	$1 \times 10^3$ N/m
Ground friction ratio	$U_g$	0.015
Cart friction ration	$U_d$	0.010

### 4.2 Experimental Results

Because we only care of the system after collision, the experiment data here shows from the 3rd second. From the comparison of the simulation results with experimental data in Fig. 14, we can see that the positions match very well. On the other hand from the figures of velocities and accelerations there are two discrepancies: First, according to the simulation results, there are at least two more oscillations after 6th second. It is obvious that the oscillation stops only when energy of the damper mass decreases to zero. In the simulation, the only way to consume energy is the friction between the damper mass and surface of the cart. However, in reality except this friction there are other ways such like the collision of damper mass and spring and oscillation of the spring also contribute to energy losses.

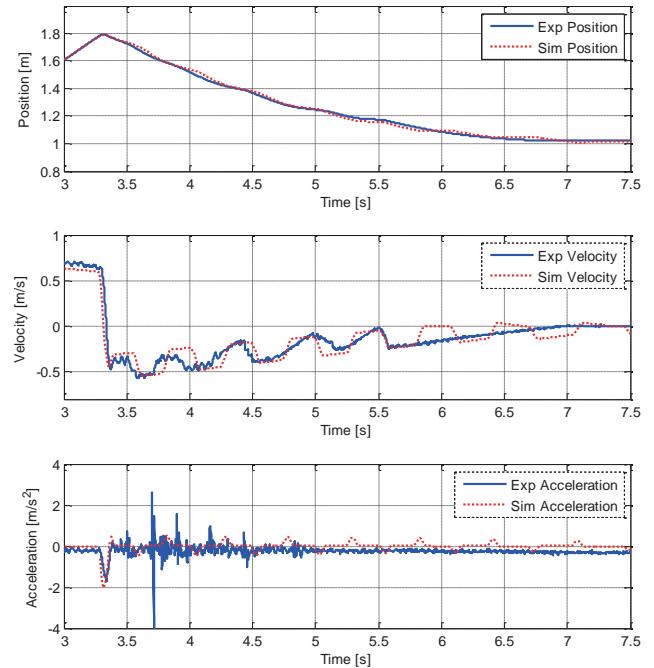


Figure 14 Comparison between simulation and experiment

Second, there is a delay about 0.1 s in the simulation results especially from 3.5 s to 5.5 s. First of all some optimization methods are applied to improve this problem: two friction ratios, damper spring stiffness, initial conditions (positions, velocities), and length between the two springs are optimized, but when decrease the differences of accelerations and velocities the differences of position data increases. And there are other problems such like the delay effects of the filter and inaccuracy of the accelerometer can also result in these differences.

### 4.3 Effects of MEID System

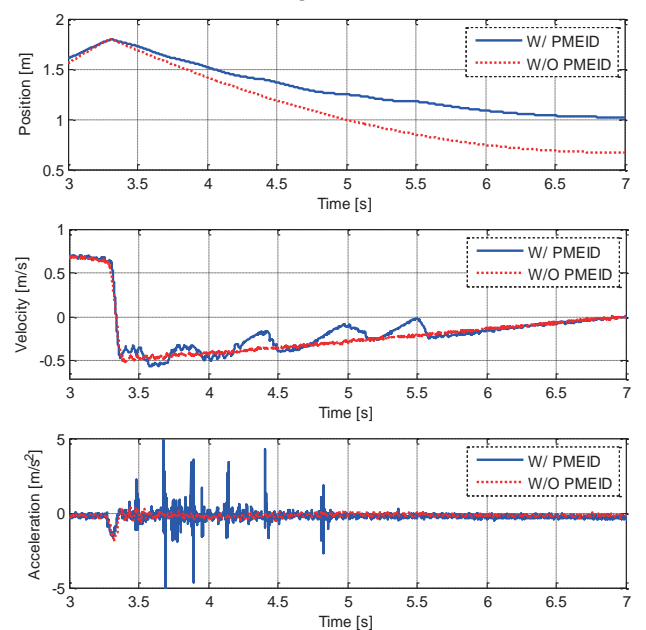


Figure 15 Effects of PMEID system

The effects of PMEID system also verified by a series of experiments. From Fig. 15, the comparison between the system with PMEID (blue solid line) and the system without PMEID (red dotted line), the position, velocity and acceleration are shown. The rebound distance of the base mass reduces about 30 % (from 1.15 m to 0.82 m); and the first large acceleration about 17 % (from 1.94 m/s<sup>2</sup> to 1.61 m/s<sup>2</sup>). So from this experiment result, we could confirm that the PMEID could reduce the rebound distance and the maximum accelerations.

## 5. PARAMETER ANALYSIS

In this section, we discuss effects of different parameters in the simplistic model. For single parameter study, the model with both front and back spring will be used. Because of this model including friction forces thus making the system nonlinear. For the multidimensional parameter study, to simplify the problem, a model with only front spring will be used.

### 5.1 Mass Ratio

First, for MEID system, the mass of damper is critical in the effects on rebound distance. So for a specific case we tend to find the optimal damper mass to get the smallest rebound distance. In this case, as can be seen from Fig. 16 that fixed the other parameters, increasing mass ratio from 0.09 to 0.32 (increase  $m_d$  from 0.8 to 2.6 kg) we could find the minimum rebound distance at  $m_d = 2.05$  kg.

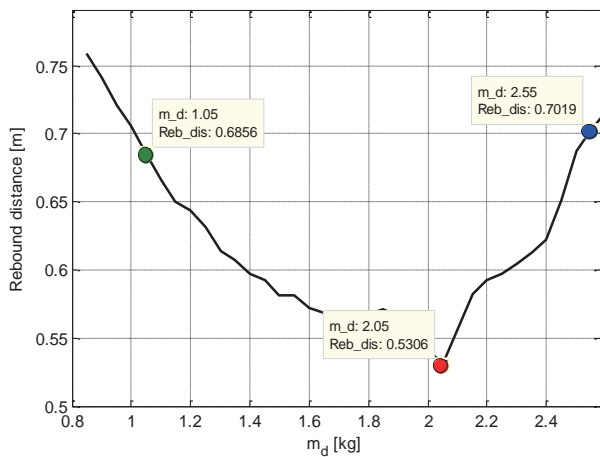


Figure 16 Parameter study on mass ratio

Figure 17 shows the displacement of three cases in Fig. 16. It is obvious that the rebound distance first decreases, when mass ratio is large than 0.25, the rebound distance increases again. By affecting the frequency of the oscillation of the MEID system, mass ratio has a critical effect on the rebound distance, as increasing the damper mass, the frequency of the oscillation decreases. However, as frequency of oscillation decreases, the frequency of MEID system used in this dynamics also decreases thus weakening the effects of MEID system. So there is a trade-off in frequency of oscillations.

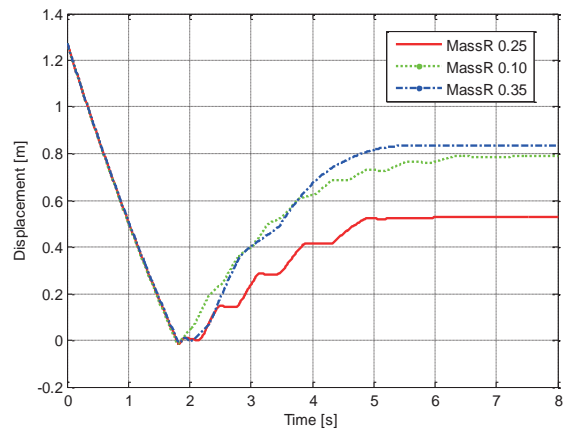


Figure 17 Comparison to optimal results

### 5.2 Damper Spring Stiffness $k_d$

In this case, we argue that the damper spring stiffness  $k_d$  also has major effects on the rebound distance. If fixed other parameters, increase damper spring stiffness from 200 N/m to 2000 N/m, we can see from Fig. 18 that the minimum rebound distance at  $k_d = 490$  N/m. Comparing with the simulation results with  $k_d = 1800$  N/m, we can see from Fig. 19 that the damper spring stiffness affects the contact time of the damper and the spring thus having major influence on the number of collisions.

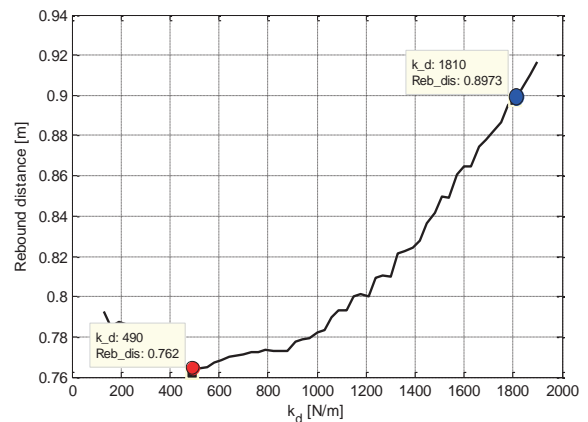


Figure 18 Parameter study on damper spring stiffness

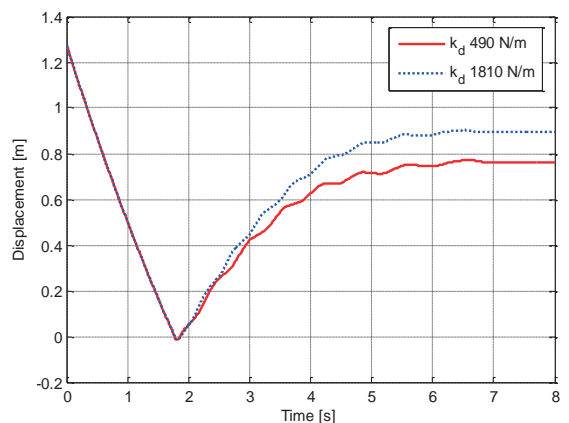


Figure 19 Comparison to optimal results

## 6. FUTURE WORKS

From the parameter study, we can see the trade-off between the times of MEID system used in the system and the push forces of the damper mass applied on the front spring. Hereto, the fundamental method to solve this problem is changing the mechanism of the simplistic model. One way possible is that by using a bending spring to transform the horizontal momentum to vertical pressure, as the normal pressure of the cart system increases, so does the friction forces, thus decrease the velocity and rebound distance of the system. The mechanism of this type of model could be illustrated as in Fig. 20.

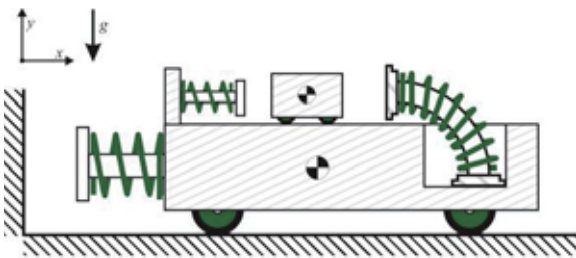


Figure 20 Modification of system model

Above discussion are based on the passive momentum exchange impact damper (PMEID). By adding linear motors to realize the active control of momentum exchange impact damper to get optimal results and improve the efficiency of momentum exchange. Combined with PMEID system, the hybrid type momentum exchange impact damper (HMEID) [13] could increase the robustness of the system.

## 7. CONCLUSION

This paper proposes a novel collision safety mechanism based on passive MEID. The effectiveness of the system is evaluated by simulations and experiments. The results are summarized as follows:

- 1) The theoretical basis for the time responses of the velocities of momentum exchange impact dampers (MEIDs) is explained. The influence of the two parameter  $k_d$  and  $m_d$  on the performance of MEID are analyzed.
- 2) The proposed horizontal collision safety system is modelled and the optimization of  $k_d$  and  $m_d$  are finished.
- 3) The effectiveness of above system is verified by both simulations and experimental results.

## ACKNOWLEDGEMENTS

Thanks to the JUACEP Program for providing me this opportunity to join this research and thanks to Mr. T. Watanabe for his invaluable advice in modeling this system. The friendly atmosphere in Yamada Laboratory made many things easier and I wish to thank all my other colleagues for making my job so much fun.

## REFERENCES

- [1] Laurini, K.C., Hufenbach, B., Kawaguchi, J., Piedboeuf, J.C., Schade, B., Curtis, J., and Kim, H., An International Strategy for Human Exploration of the Moon: The International Space Exploration Coordination Group (ISECG) Reference Architecture For Human Lunar Exploration, *Proceedings of the 61st International Astronautical Congress*, IAC-10.A5.2.9 (2010).
- [2] Peden, M., Scurfield, R., Sleet, D., Mohan, D., Hyder, A. A., and Mathers, C., World Report on Road Traffic Injury Prevention. Geneva, World Health Organization, 2002 ([http://www.who.int/violence\\_injury\\_prevention/publications/road\\_traffic/world\\_report/en](http://www.who.int/violence_injury_prevention/publications/road_traffic/world_report/en), accessed 30 July, 2013).
- [3] Ueno, S., and Yamaguchi, Y., 3-Dimensional Near-Minimum Fuel Guidance Law of a Lunar Landing Module, *AIAA Guidance, Navigation, and Control Conference and Exhibit*, pp. 1999- 3983 (1999).
- [4] Chistensen, E.M., Batterson, S.A., Benson, H.E., Chandler, C.E., Jones, R. H., Scott, R.F., Shipley, E.N., Sperling, F.B., and Sutton, G.H., Lunar Surface Mechanical Properties: Surveyor 1, *Journal of Geophysical Research, Solid Earth and Planets*, Vol. 72, No. 2, pp. 801-813 (1967).  
doi:10.1029/JZ072i002p00801
- [5] Johnson, N.L., Handbook of Soviet Lunar and Planetary Exploration, Science and Technology Series, Univelt, Inc., San Diego, CA, Vol. 47, pp. 160–161 (1979).
- [6] Brian O'Neill, Preventing Passenger Vehicle Occupant Injuries by Vehicle Design: A Historical Perspective from IIHS, *Traffic Injury Prevention*, Vol. 10, No. 2, pp. 113-126 (2009).  
doi: 10.1080/15389580802486225
- [7] Son, L., Kawachi, M., Matsuhisa, H., and Utsuno, H., Reducing Floor Impact Vibration and Sound Using a Momentum Exchange Impact Damper, *Journal of System Design and Dynamics*, Vol. 1, No. 1, pp. 14-26 (2007).  
doi:10.1299/jsdd.1.14
- [8] Hara, S., Ito, R., Otsuki, M., Yamada, Y., Kubota, T., Hashimoto, T., Matsuhisa, H., and Yamada, K., Momentum-Exchange-Impact-Damper-Based Shock Response Control for Planetary Exploration Spacecraft, *Journal of Guidance, Control, and Dynamics*, Vol. 34, No. 6, pp. 1828-1838 (2011).  
doi:10.2514/1.53769
- [9] Kushida, Y., Hara, S., Yamada, Y., and Otsuki, M., Shock Response Control Using MEIDs -Consideration of a Single-Axis Falling Type Problem-, *Proceedings of the 28th International Symposium on Space Technology and Science*,(2011).
- [10] Goebel, R., Sanfelice, R.G., and Teel, A.R., *Hybrid Dynamical Systems, Control Systems*, Vol. 29, No. 2, pp. 28-93 (2009).  
doi: 10.1109/MCS.2008.931718
- [11] Remy, C.D., Buffinton, K.W., and Siegwart, R.Y., A MATLAB Framework for Efficient Gait Creation, *Proceedings of the 2011 IEEE*, pp. 190-196 (2011).
- [12] Everitt, B., Nelder-Mead Simplex Algorithm, *The Cambridge Dictionary of Statistics*, Cambridge University Press, pp. 261 (2002).

- [13]Kushida, Y., Hara, S., Otsuki, M., Yamada, Y., Hashimoto, T., and Kubota, T., Robust Landing Gear System Based on Hybrid Momentum Exchange Impact Damper, *Journal of Guidance, Control and Dynamics*, Vol. 36, No. 3, pp. 776-789 (2013).  
doi: 10.2514/1.58373

# MONTE-CARLO SIMULATION OF POLYCRYSTAL PLASTICITY USING DISCRETE DISLOCATION PLASTICITY APPROACH FOR LAMELLAR MATERIALS

Sriram Ganesan

Graduate Student, Department of Aerospace Engineering, University of Michigan, Ann Arbor  
[sriramg@umich.edu](mailto:sriramg@umich.edu)

Supervisor : Dr. Dai Okumura

Associate Professor, Graduate School of Engineering, Nagoya University  
[okumura@mech.nagoya-u.ac.jp](mailto:okumura@mech.nagoya-u.ac.jp)

## ABSTRACT

In the present work Monte-Carlo simulation of polycrystal plasticity is performed using discrete dislocation plasticity approach for lamellar materials to find the effect of grain size on the mean distance of dislocation activation across the grain boundary  $\lambda$ . The approach is based on applying periodic homogenization to the superposition method of Van der Giessen and Needleman [1], and on decomposing displacements into macro and perturbed components [2]. The simulations are performed for layer thickness of 1-10 $\mu\text{m}$  and the range of  $\lambda$  is estimated. The results are compared with other grain structure arrangements and experimental results on pure Aluminum specimens.

## 1. INTRODUCTION

Within the materials science and mechanics communities it is widely recognized that the key ingredient needed for the development of a predictive model for the mechanical behavior of polycrystalline materials has to come from a deeper understanding of the dynamical interplay between dislocation and grain microstructures. The underlying microstructural length and time scales are critical because in functional materials the spatial arrangement of the dislocations and grain boundaries in the microstructure may be controlled and optimized via sophisticated materials synthesis and processing techniques. The resulting microstructurally designed materials are important not only as light-weight components with superior mechanical performance but also in high-temperature applications. Light-weight aluminum alloys are a key component of creating commercially viable, highly fuel-efficient and pollution-free automobiles.

How polycrystalline materials deform under stress is important not only scientifically, for the understanding of plastic flow, but also technologically. The mean grain size in polycrystalline materials,  $d$ , plays a critical role in mechanical properties as it limits the free path of moving dislocations. The piling up of moving dislocations against the grain boundaries gives rise to a strengthening of the material with decreasing grain size; this is known as the Hall-Petch (HP) effect.

The superposition method [1] was based on superposing the analytical solutions for the displacement, strain, and stress fields induced by individual dislocations in an infinitely isotropic elastic medium, and on correcting for the actual boundary conditions and the presence of inclusions. The superposition method has been widely applied to metal matrix composites, thin films, polycrystals, micropillars, void growth and nano-indentation.

The discrete continuum model [3] and the extended finite element method [4] introduced the contributions of discrete dislocations as plastic strains and as discontinuous

displacements, respectively. Henceforth, in specific cases that require introducing elastic anisotropy, these alternative methods will continue to be used. In this study, lamellar materials are assumed to be isotropic; consequently we focus on the superposition method to carry out the discrete dislocation plasticity analysis of the representative volume elements (RVEs) of lamellar materials.

## 2. DISCRETE DISLOCATION PLASTICITY APPROACH

### 2.1 SUPERPOSITION METHOD

The superposition method of Van der Giessen and Needleman [1] is discussed here. The problem to be solved is decomposed into the dislocation problem which gives the solution of self-equilibrated fields for dislocations in the infinite medium of the homogeneous matrix and the complementary problem which gives the solution of fields to correct for the presence of inclusions as well as the macroscopic uniform deformation. The summation of these two contributions leads to the solution of the original problem. Thus the microscopic fields of displacement  $u_i$ , elastic strain  $\epsilon_{ij}$ , and stress  $\sigma_{ij}$  are respectively written as

$$u_i = \tilde{u}_i + \hat{u}_i, \epsilon_{ij} = \tilde{\epsilon}_{ij} + \hat{\epsilon}_{ij}, \sigma_{ij} = \tilde{\sigma}_{ij} + \hat{\sigma}_{ij} \quad (1)$$

where the fields of ( $\tilde{\sim}$ ) and ( $\hat{\sim}$ ) represent the fields of the dislocation problem and the complementary problem, respectively.

The ( $\tilde{\sim}$ ) field of the dislocation problem is obtained by superposing analytical solutions for individual dislocations under self-equilibrium in the infinitely large medium [5]. When the elastic stiffness of the material is  $c_{ijkl}$ , the governing equations of the dislocation problem are written as

$$\tilde{\sigma}_{ij,j} = 0, \tilde{\sigma}_{ij} = c_{ijkl} \tilde{\epsilon}_{kl}, \tilde{\epsilon}_{kl} = (u_{k,l}^{\tilde{\sim}} + u_{l,k}^{\tilde{\sim}}) / 2 \quad (2)$$

where  $u_k^{\tilde{\sim}}$  includes discontinuous components due to the gliding of dislocations,  $\tilde{\epsilon}_{ij}$  is the elastic strain and does not include the contribution of the gliding. The fields of  $\tilde{\sigma}_{ij}$ ,  $\tilde{\epsilon}_{ij}$  and  $u_k^{\tilde{\sim}}$  are independently calculated by the superposition manner so that Eq. (2)<sub>2</sub> and (2)<sub>3</sub> do not have to be used in fact.

The ( $\hat{\sim}$ ) field of the complementary problem is governed by

$$\hat{\sigma}_{ij,j} = 0, \hat{\sigma}_{ij} = c_{ijkl} \hat{\epsilon}_{kl}, \hat{\epsilon}_{kl} = (u_{k,l}^{\hat{\sim}} + u_{l,k}^{\hat{\sim}}) / 2 \quad (3)$$

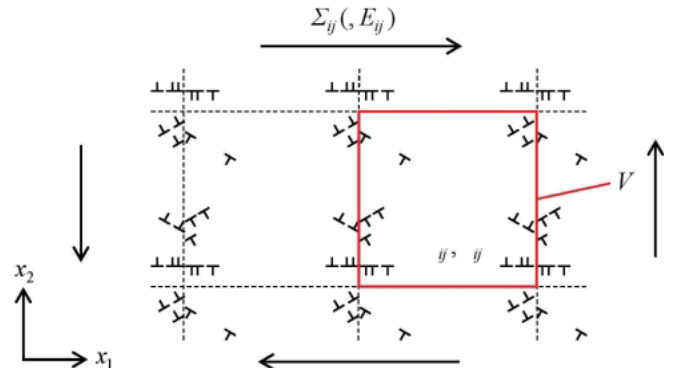


Fig. 1 Periodic unit subjected to macroscopic uniform deformation

In general, the complementary problem is analyzed computationally using Eqn. (3) under adequate boundary conditions. The boundary conditions require the displacement field of the dislocation problem, in order to correct for actual boundary conditions [1]. Thus, superposition of analytical solutions of displacements caused by individual dislocations should be performed before solving the complementary problem. By contrast, in this study periodic boundary value problems for the complementary problem are derived based on decomposing displacements into macroscopic and perturbed components, as will be shown in Section 2.4. Furthermore, the decomposition circumvents the calculation of the displacement field of the dislocation problem. The derivation of the periodic boundary value problems will be achieved using the fundamental equations given in Sections 2.2 and 2.3.

### 2.2. MACROSCOPIC RELATIONS AND PERTURBED DISPLACEMENT

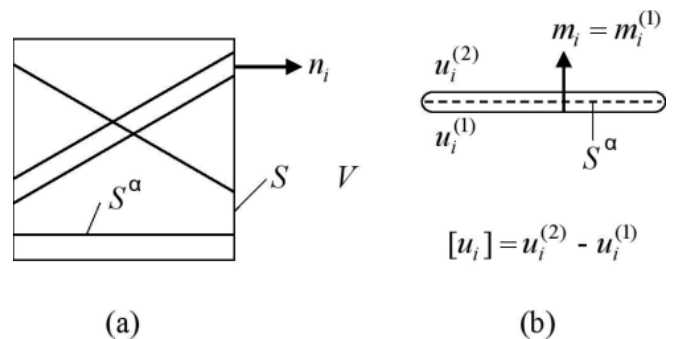


Fig. 2 Definitions of surfaces and its normal vectors (a) for periodic unit  $V$ , and (b) for each slip plane  $S^\alpha$  with jump of displacement  $u_i$

The macroscopic variables are described by averaging each field over the periodic unit  $V$ . The macroscopic stress  $\Sigma_{ij}$  is hence connected with the stress field  $\sigma_{ij}$  by the relation

$$\Sigma_{ij} = \frac{1}{V} \int_V \sigma_{ij} dV \quad (4)$$

It should be noted that the macroscopic strain  $E_{ij}$  is not obtained in the same manner when the displacement  $u_i$  is not continuous. The displacement field with discontinuous components gives the following relation as a general expression for the macroscopic strain  $E_{ij}$  [6]

$$E_{ij} = \frac{1}{2V} \int_S (u_i n_j + n_i u_j) dS \quad (5)$$

As shown in Fig. 2a,  $S$  is the surface of the periodic unit, and  $n_i$  is the outward unit vector normal to  $S$ . Application of the divergence theorem to the volume average of the strain  $\epsilon_{ij}$  gives another expression equivalent to Eq. (5)

$$E_{ij} = \frac{1}{V} \int_V \epsilon_{ij} dV + \frac{1}{2V} \int_{S_D} ([u_i] m_j + m_i [u_j]) dS \quad (6)$$

Here  $S_D$  is a set of inter surfaces  $S^\alpha$  ( $\alpha = 1, 2, 3, \dots$ ) on which the gliding of each dislocation sweeps and the displacement is not continuous. Furthermore,  $[u_i]$  in Eq. (6) denotes the jump of the displacement across  $S^\alpha$ , and  $m_j$  represents the unit vector normal to  $S^\alpha$  as shown in Fig. 2b. The second term on the right hand side of Eq. (6) indicates the contribution of the gliding of dislocations in this study, and is generally known as the effect due to microcracks [6].

The macroscopic strain  $E_{ij}$  enables the displacement  $u_i$  to be decomposed into two components;

$$u_i = E_{ij} x_j + u_i^* \quad (7)$$

Here  $E_{ij} x_j$  is the macroscopic uniform component and therefore  $u_i^*$  is the perturbed component. Substitution of Eq. (7) for Eq. (5) and use of divergence theorem give

$$\int_S (u_i^* n_j + n_i u_j^*) dS = 0 \quad (8)$$

This relation is always correct if the perturbed displacement  $u_i^*$  on the surface  $S$  is periodic since the normal vector  $n_j$  is anti-periodic. Therefore, when periodic materials subjected to macroscopically uniform deformation are considered, the periodic boundary condition expressed as  $u_i^{*(+)} = u_i^{*(-)} (\neq 0)$  on  $S$  is correct. Here  $u_i^{*(+)}$  and  $u_i^{*(-)}$  are perturbed displacements at opposite points on  $S$ , respectively. The next subsection will be devoted to

discussing the contributions of the dislocation problem to macroscopic relations and perturbed displacements.

### 2.3. MICRO/MACRO FEATURES OF DISLOCATION PROBLEM

In order to investigate the contributions of the dislocation problem to macroscopic relations, we focus on one dislocation in the periodic unit and consider the periodic arrangements of this dislocation in an infinite matrix medium. This dislocation structure in the infinite medium creates a self-equilibrated stress field in the periodic unit, which might contribute to the macroscopic stress. However, the integration of the stress field over the periodic unit is identical to that of one dislocation over the infinite medium because of the superposition principle. Thus the self-equilibrated stress field makes no contribution to the macroscopic stress. The average value of the stress  $\sigma_{ij}$  satisfies

$$\frac{1}{V} \int_V \tilde{\sigma}_{ij} dV = 0 \quad (9)$$

In the infinite matrix medium, the elastic stiffness is  $c_{ijkl}^M$  and is not a variable, that is

$$\frac{1}{V} \int_V \tilde{\epsilon}_{ij} dV = 0 \quad (10)$$

Eqs. (9) and (10) indicate that the elastic fields of the dislocation problem do not contribute to macroscopic properties at all.

Eq. (10) means that in the dislocation problem, the first term on the right hand side of Eq. (6) vanishes leaving only the second term which, induced by the discontinuous displacement due to the dislocation gliding, only contributes to the macroscopic strain  $E_{ij}$ . The macroscopic strain of the dislocation problem is a plastic component, and thus can be considered as the macroscopic plastic strain  $E_{ij}^P$ .

Consider that the periodic unit at time  $t$  has inter surfaces  $S^\alpha$  swept by each dislocation  $a$  ( $\alpha = 1, 2, \dots$ ). The individual dislocations belong to a slip system described by  $b_i^{(\alpha)}$  and  $m_j^{(\alpha)}$ . Here  $b_i^{(\alpha)}$  is Burgers' vector and  $m_j^{(\alpha)}$  is the unit vector normal to the glide plane. These relations result in replacing  $[u_i]$  and  $m_j$  of Eq. (6) with  $b_i^{(\alpha)}$  and  $m_j^{(\alpha)}$ , respectively, and  $b_i^{(\alpha)}$  is uniform on the surface  $S$ . Hence, Eq. (8) together with Eq. (10) gives the macroscopic plastic strain by the relation

$$E_{ij}^P = \frac{1}{2V} \sum_\alpha S^\alpha (b_i^{(\alpha)} m_j^{(\alpha)} + m_i^{(\alpha)} b_j^{(\alpha)}) \quad (11)$$

The rate form of the above equation is obtained as

$$\dot{E}_{ij}^p = \frac{1}{2V} \sum_{\alpha=1}^N \left( \int_{l^{(\alpha)}} v^\alpha dl^\alpha \right) (b_i^{(\alpha)} m_j^{(\alpha)} + m_i^{(\alpha)} b_j^{(\alpha)}) \quad (12)$$

Here  $l^{(\alpha)}$  is the line of dislocation  $\alpha$ , and  $v^{(\alpha)}$  is the velocity defined by  $v^{(\alpha)} = dx^{(\alpha)}/dt$ . In Eqs. (11) and (12),  $\Sigma$  represents the summation over one periodic unit. Discrete dislocation plasticity simulations [1] use constitutive rules to estimate the velocity of individual dislocations and to move them. Thus, it is convenient to calculate the rate form of the macroscopic plastic strain. The macroscopic plastic strain is incrementally analyzed using the rate form in this study.

Consequently, in the dislocation problem, Eq. (9) shows that the contribution to the macroscopic stress is zero, and Eqs. (10) and (11) show that the contribution to the macroscopic strain is only the macroscopic plastic strain due to dislocation gliding. The fields of  $\epsilon_{kl}^-$  and  $\sigma_{ij}^-$  as well as  $u_i^*$  are periodic.

## 2.4. DERIVATION OF PERIODIC BOUNDARY VALUE PROBLEMS

The displacement field,  $u_i^\wedge$ , for the complementary problem is continuous because the discontinuous component in the total displacement field  $u_i$  is included only in the field  $u_i^-$ . Using Eqs. (1), (6), (10), and (11), the contribution of  $u_i^\wedge$  to the macroscopic strain is  $E_{ij} - E_{ij}^p$

$$\frac{1}{V} \int_V \tilde{\epsilon}_{ij} dV = E_{ij} - E_{ij}^p \quad (13)$$

and thus the displacement field  $u_i^\wedge$  is written as

$$\hat{u}_i = (E_{ij} - E_{ij}^p) x_j \quad (14)$$

The expression for stress  $\sigma_{ij}^\wedge$  indicates that the total stress  $\sigma_{ij}$  has the following form

$$\sigma_{ij} = c_{ijkl} (E_{kl} - E_{kl}^p) + c_{ijkl} \tilde{\epsilon}_{kl} \quad (15)$$

Substituting Eq. (15) into (4) we get

$$\Sigma_{ij} = c_{ijkl} (E_{ij} - E_{ij}^p) \quad (16)$$

## 2.5. ANALYSIS PROCEDURES

Fig. 3 outlines the employment of equations and the procedures used to perform the incremental analysis. Incremental analysis is considered [2] under the condition that all variables and distributions are known at time  $t$ . Following this, the macroscopic deformation at time  $t+dt$  is given as a set of components of the macroscopic stress  $\Sigma_{ij}$

and the macroscopic strain  $E_{ij}$ . Next, the dislocation velocity, and the generations and annihilations of dislocations are considered using the constitutive rules explaining their mechanisms, resulting in the update of the locations of all dislocations and the macroscopic plastic strain  $E_{ij}^p$ . Consequently, the strain field  $\epsilon_{kl}^-$  for the dislocation problem is calculated. Thus, the unknown components of the macroscopic stress  $\Sigma_{ij}$  and the macroscopic strain  $E_{ij}$  are analyzed using the macroscopic stress expression Eq. (16). Finally, the microscopic stress that takes the form of Eq. (15) is calculated. This analysis is advanced incrementally by repeating the above-mentioned procedures.

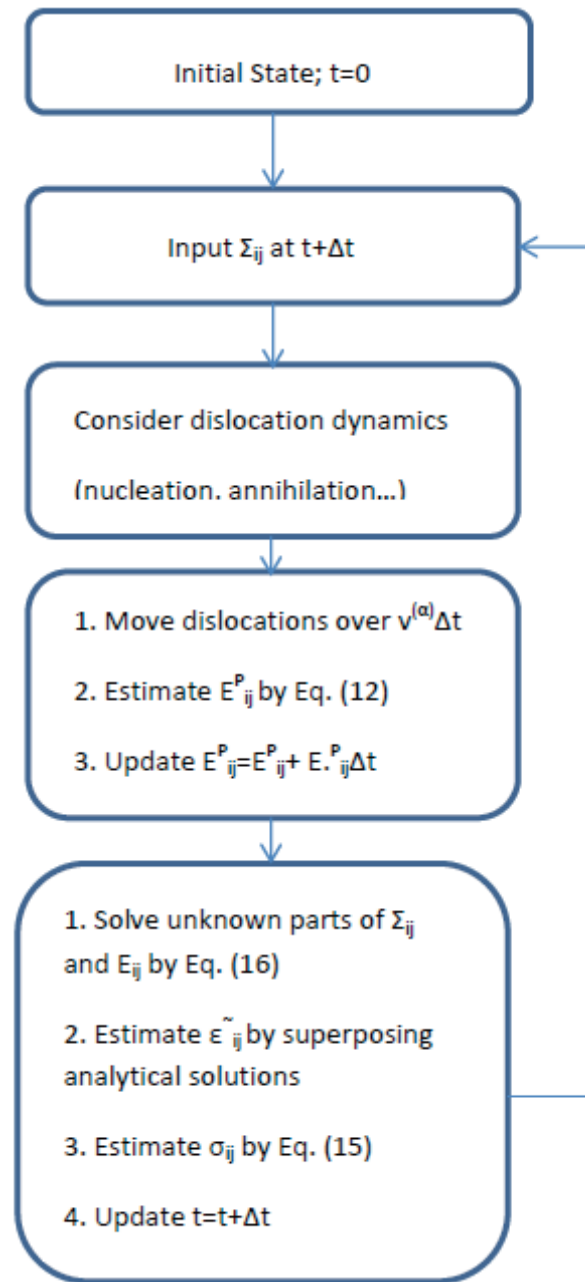


Fig. 3 Employment of equations and analytical procedures

### 3. GRAIN BOUNDARY STRENGTHENING

The interception of dislocation motion by some obstacles, leading to grain boundary strengthening is called Hall-Petch relationship (H-P effect). The magnitude of the observed strengthening depends upon the structure of the grain boundaries and the degree of misorientation between grains and the degree of misorientation between grains. Several models describe grain boundary strengthening. Nearly all of them reduce to the form of the original Hall-Petch relationship. When dislocations generated by sources approach obstacles on slip planes, they often pile up.

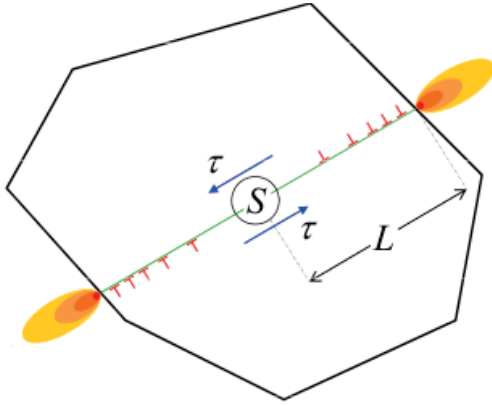


Fig. 4 Grain with a single dislocation source

Consider a grain that contains a single dislocation source (S) in its center as shown in the Fig. 4 above. Dislocations emitted from point sources within individual grains (e.g., Frank-Read sources) encounter a lattice friction stress, i.e. a Peierls stress  $\tau_0$ , as they move on a slip plane towards a grain boundary. The lattice friction stress opposes the applied shear stress  $\tau_{\text{applied}}$ . The effective shear stress that contributes to plastic deformation is given by

$$\tau_{\text{eff}} = \tau_{\text{applied}} - \tau_0 \quad (17)$$

The shear stress at the GB is given by

$$\tau_{\text{gb}} = \tau_{\text{eff}} \sqrt{\frac{D}{4r}} = (\tau_{\text{applied}} - \tau_0) \sqrt{\frac{D}{4r}} \quad (18)$$

where D is the grain size and r is the distance from the source. If we assume that Bulk Yielding occurs at a critical value of  $\tau_{\text{gb}}$ , we can rearrange the preceding equation in terms of applied shear stress.

$$\tau_{\text{applied}} = \tau_0 + \tau_{\text{gb}} \sqrt{\frac{4r}{D}} \quad (19)$$

A.H. Cottrell [7] modified the original Hall-Petch model. He assumed that stress concentration that produced a pile-up in one grain activated a dislocation source in adjacent grain. The maximum shear stress at a distance  $\lambda$

ahead of the boundary is given by

$$\tau_B = (\tau - \tau_0) \sqrt{\frac{d}{4\lambda}} \quad (20)$$

where  $\tau_B$  is the stress required to activate the source in the adjacent grain. Assuming stress concentration is large enough to activate dislocation in the adjacent grain

$$\tau_{\text{ys}} = \tau_0 + \sqrt{4\lambda} \tau_B d^{-1/2} \quad (21)$$

Shibutani et. al. [8] have investigated the dependence of Hall-Petch effect on plastic strain and Temperature. Experiments on pure Aluminum specimens were performed and a power law relationship between the H-P coefficient and plastic strain was obtained. This model suggests that the internal stress due to piled-up dislocations in front of GB activates the dislocation sources in the adjoining grain. The present study involves measuring the mean distance of dislocation activation across grain boundary  $\lambda$ .

### 4. LAMELLAR MATERIAL ANALYSIS

In this section, two models of polycrystalline grain arrangement, the checker-board arrangement and the lamellar arrangement are discussed. The former problem has already been addressed in previous studies and the latter problem is analyzed in this study.

The analyzed problems fall into the plane strain problem. The elastic-plastic layers contain edge dislocations with Burgers vector  $b=0.25\text{nm}$  in the horizontal direction, with the horizontal gliding plane, and with the dislocation lines perpendicular to the plane. The Young's Modulus of the elastic-plastic layer is taken as  $E=70\text{GPa}$  and the poisson ratio of the layers are taken as  $\nu=0.33$  to match with the material properties of Aluminum. The Material parameters and calculation conditions are given in Table 1

Table 1 Material parameters and calculation conditions

Parameters	Values
$\rho_{\text{nuc}}$	$20\mu\text{m}^{-2}$
$\tau_{\text{nuc}}(\text{mean})$	50MPa
$\tau_{\text{nuc}}(\text{sd})$	5MPa
$\rho_{\text{obs}}$	$40\mu\text{m}^{-2}$
$\tau_{\text{obs}}$	150MPa
b	0.25nm
E	70GPa
$\nu$	0.33
B	0.1MPa ns
$E'_{12}$	$1000\text{s}^{-1}$
$\Delta t$	0.5ns

#### 4.1 CHECKER-BOARD MODEL

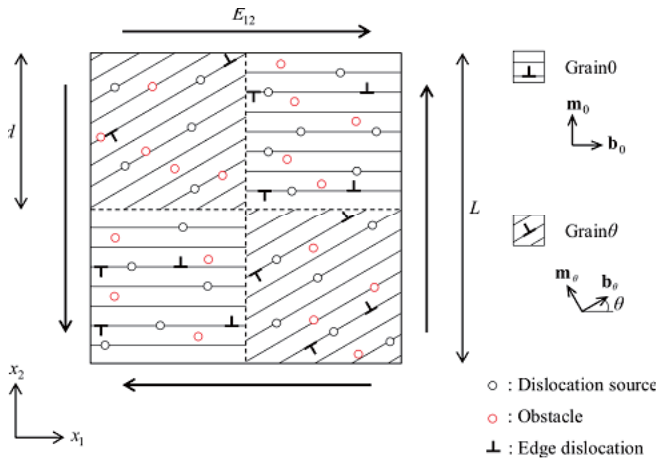


Fig. 5 Schematic illustration of polycrystalline model with checker-board arrangement and boundary conditions

The checker-board arrangement of the polycrystalline model is shown in the Fig. 5. The polycrystal is composed of two types of single-slip grains. Grain0 has slip direction parallel to  $x_1$ -axis, and Grain30 has slip direction with 30 degrees from  $x_1$ -axis.

It consists of square grains of side length 'd' and the dislocation sources and obstacles are randomly distributed with their densities  $\rho_{nuc}$  and  $\rho_{obs}$  respectively.

#### 4.2 LAMELLAR MODEL

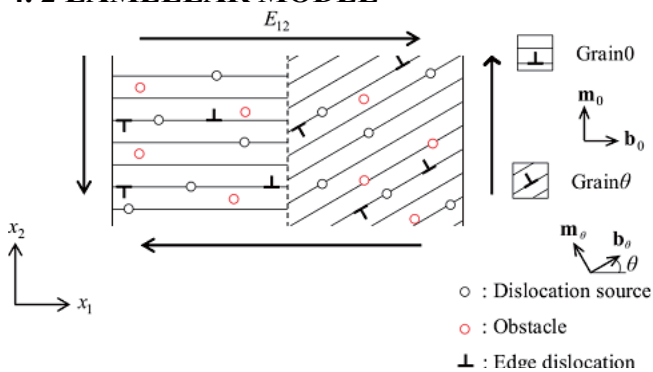


Fig. 6 Schematic illustration of polycrystalline model with lamellar arrangement and boundary conditions

The lamellar arrangement of the polycrystalline model is shown in the Fig. 6. In this case also, the polycrystal is composed of two types of single-slip grains, Grain0 and Grain30 respectively.

The differences between the checkerboard board arrangement and lamellar arrangement are

1. In the checkerboard arrangement, all four edges constitute the grain boundary, whereas in the lamellar arrangement the grain boundary is along two edges of the representative periodic unit.

2. Dilocation pile ups can occur along all 4 edges of an angular grain in the checker-board arrangement whereas it occurs along 2 edges of an angular grain.

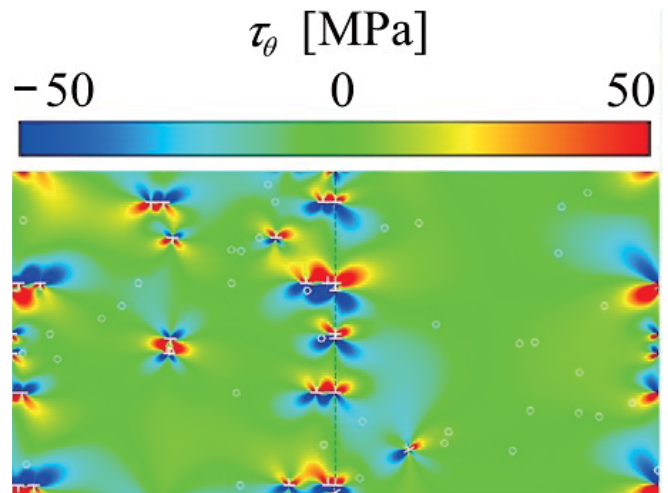


Fig. 7 Stress field  $\tau_{30}$  for lamellar model layer width  $1\mu\text{m}$

Fig. 7 depicts the stress field for a lamellar model grain size of  $1\mu\text{m}$ . The stress field  $\tau_{30}$  implies that the stress is computed along the slip plane 30 degrees from the  $x_1$  axis

### 5. RESULTS AND DISCUSSION

The Monte-Carlo simulations are performed for grain sizes of  $1\mu\text{m}$ ,  $5\mu\text{m}$  and  $10\mu\text{m}$  and Grain angle of the adjacent grain as 30 degrees. The results are presented in order of grain size. In all the cases the lamellar arrangement consists of two layers of thickness 'w' between  $1-10\mu\text{m}$  and height 'h'  $1-10\mu\text{m}$

#### 5.1 NUMBER OF ACTIVATIONS

The plots in the Figs. 8-10 give the no. of dislocations sources in each region with distance from grain boundary  $\lambda$ , for various layer thickness. The activations are counted by excluding the dislocations which annihilate. The plots show that most dislocations are emitted near the grain boundary.

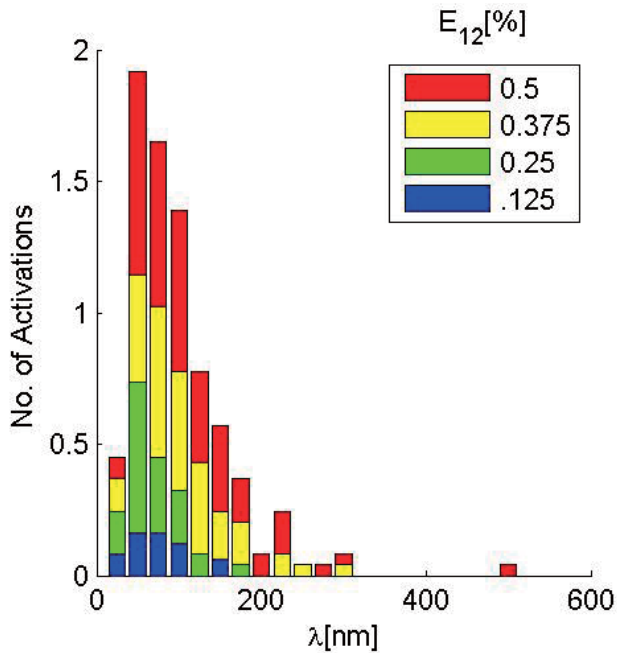


Fig. 8 Number of activations of dislocation sources in each region with distance from grain boundary  $\lambda$ ,  $w=1.0 \mu\text{m}$ ,  $h=1.0 \mu\text{m}$

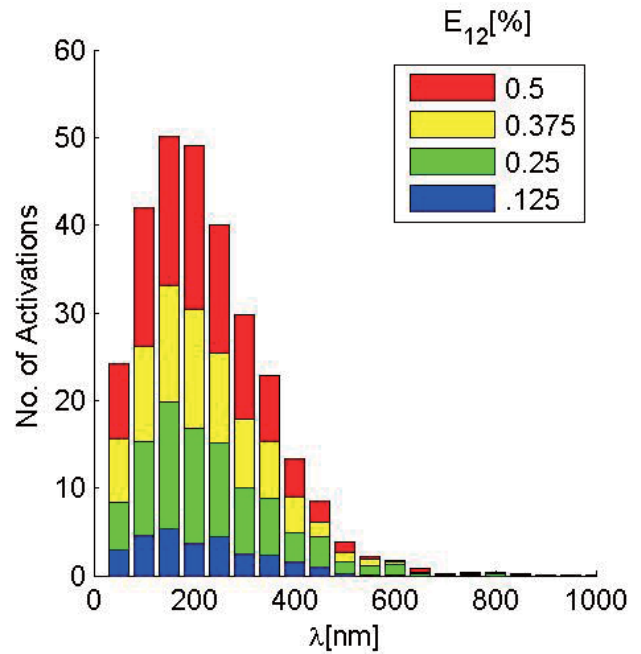


Fig. 10 Number of activations of dislocation sources in each region with distance from grain boundary  $\lambda$ ,  $w=10.0 \mu\text{m}$ ,  $h=10.0 \mu\text{m}$

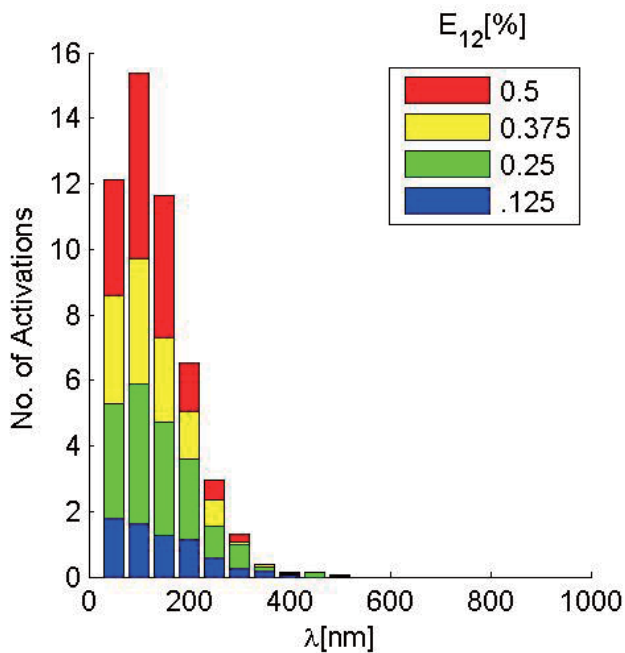


Fig. 9 Number of activations of dislocation sources in each region with distance from grain boundary  $\lambda$ ,  $w=5.0 \mu\text{m}$ ,  $h=5.0 \mu\text{m}$

It is visible from the plots that the maximum dislocations are emitted at a small finite distance  $\lambda$  from the grain boundary. This is due to interaction between the competing long range stress due to dislocation pile-ups vs the back stress induced by the dislocation pile-ups in the corresponding layer. Therefore the conducive region for dislocation emission in Grain30 occurs at some distance from the grain boundary.

Table 2 Comparison of estimated activated source position from the grain boundary  $\lambda$ , for the lamellar and checker-board arrangement

S. No	Grain Size, width ( $\mu\text{m}$ )	$\lambda(\text{nm})$ -Lamellar Arrangement	$\lambda(\text{nm})$ -Checker-board arrangement
1	1	25-50	NA
2	5	50-100	200-300
3	10	100-150	300-400

It is seen that the estimates of activated source position vary a lot between the Lamellar and checker-board arrangement and also the experimental results of [8]. This shows that  $\lambda$  is very sensitive to the grain structure arrangement.

## 5.2 ACTIVATION RATE

The plots in the Figs. 11-13 give the activation rate of dislocations sources in each region with distance from grain boundary  $\lambda$ , for various layer thickness. The activation rate is defined as the ratio of no. of active dislocation sources to the total no. of sources in a region.

The activations are counted by also including the dislocations which annihilate. The plots again show that most dislocations are emitted near the grain boundary, and the back-stress doesn't hinder the emission of dislocation near the grain boundary.

Comparing with the plots in Figs. 8-10, the mechanism of activation of dislocation across the grain boundary can be appreciated. While many dislocations sources are activated nearest to the grain boundary, due to back stress many of them annihilate. The stable dislocations are emitted at a short distance from the grain boundary.

It is also seen from the plots that activation rate decreases with increase in the layer thickness and that the increase in strain rate leads to an uniform increase in the activation rate for all cases.

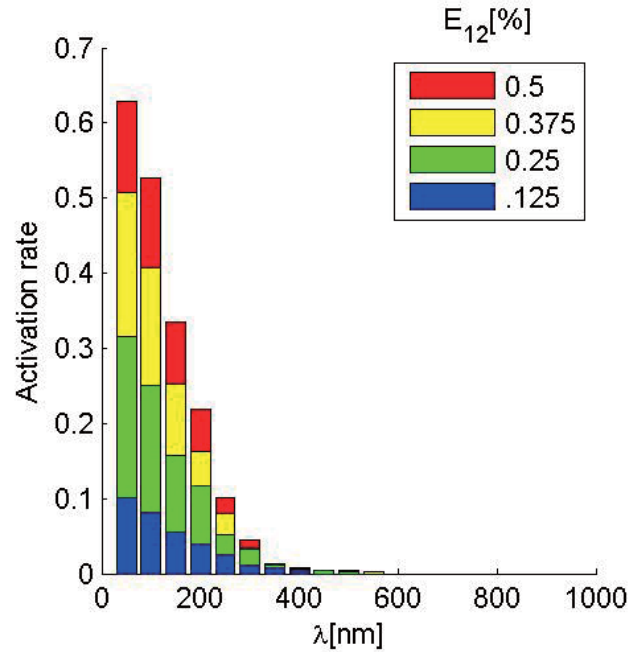


Fig. 12 Activations rate of dislocation sources in the region Grain30 with distance from grain boundary  $\lambda$ ,  $w=5.0\ \mu\text{m}$ ,  $h=5.0\ \mu\text{m}$

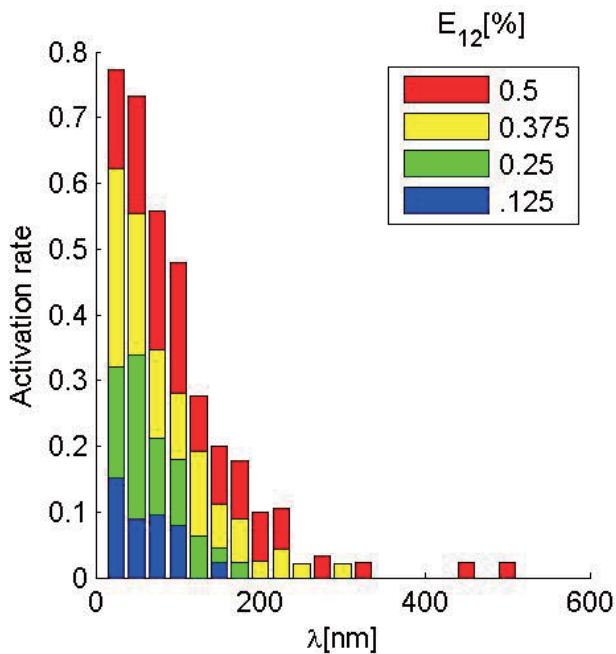


Fig. 11 Activations rate of dislocation sources in the region Grain30 with distance from grain boundary  $\lambda$ ,  $w=1.0\ \mu\text{m}$ ,  $h=1.0\ \mu\text{m}$

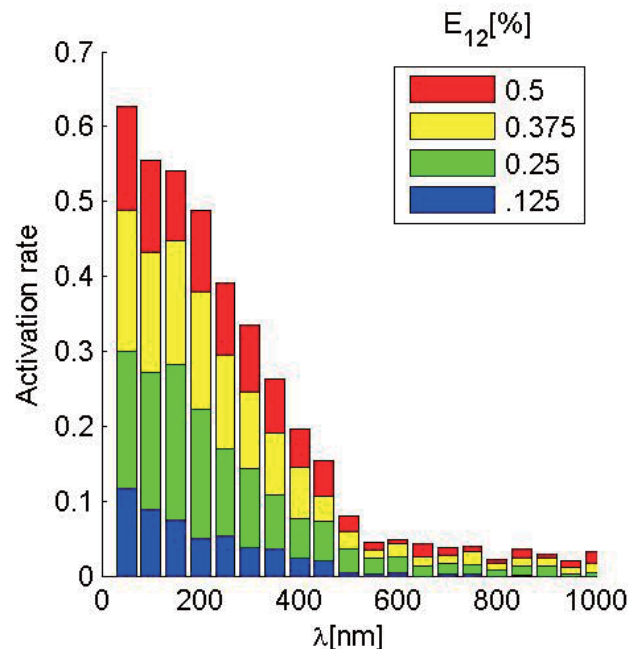


Fig. 13 Activations rate of dislocation sources in the region Grain30 with distance from grain boundary  $\lambda$ ,  $w=10.0\ \mu\text{m}$ ,  $h=10.0\ \mu\text{m}$

### 5.3 STRESS FIELD

The plot in the Fig. 14 shows the variation of Macro shear stress  $\Sigma_{12}$  versus macro shear strain  $E_{12}$ . The plot is w.r.t to the global  $x_1$ - $x_2$  axis. The effect of Grain Boundary strengthening is seen as the layer with thickness  $1.0\mu\text{m}$  undergoes strain hardening whereas the other two layers undergo softening upon yield. This softening behaviour explains the low value of activated source position from the grain boundary in the present study compared to the checker-board arrangement. It is also seen that yielding begins to occur after the emission of first dislocation, which happens at about the same Stress for all the cases.

The plots in Figs. 15-17 show the micro shear stress fields for various layer thickness at macro shear strain  $E_{12}=0.125\%$ . The shear stress is shown along the Grain30 slip plane which is at 30 degrees to the  $x_1$  axis.

$$\tau_0 = \sigma_{12} \quad (22)$$

$$\tau_{30} = (\tilde{\sigma}_{22} - \tilde{\sigma}_{11}) \sin 60^\circ + \tilde{\sigma}_{12} \cos 60^\circ \quad (23)$$

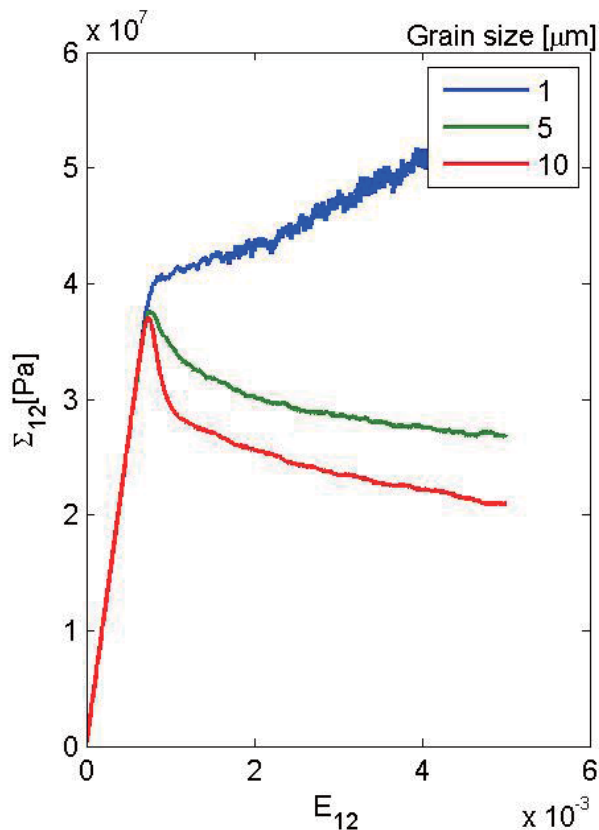


Fig. 14 Macro shear stress  $\Sigma_{12}$  versus macro shear strain  $E_{12}$

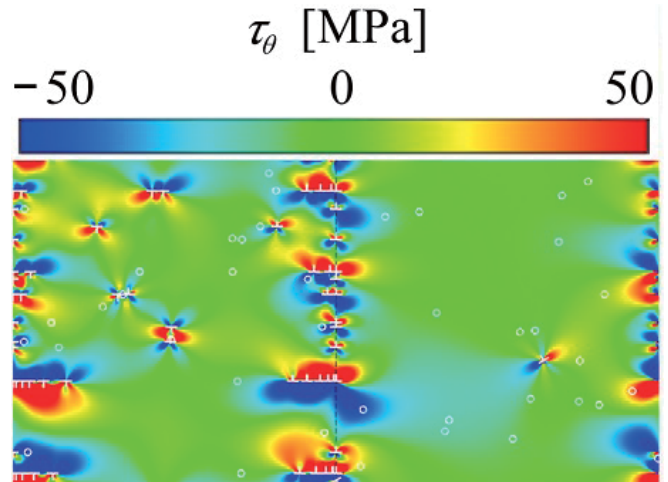


Fig. 15 Micro shear stress field,  $E_{12}=0.125\%$ ,  $w=1.0\mu\text{m}$

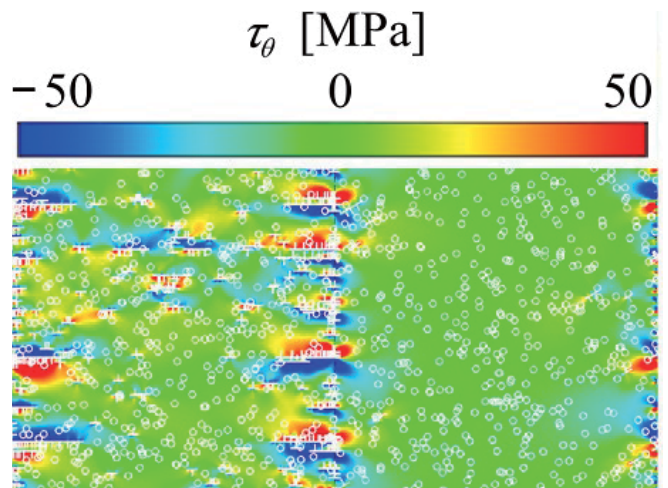


Fig. 16 Micro shear stress field,  $E_{12}=0.125\%$ ,  $w=5.0\mu\text{m}$

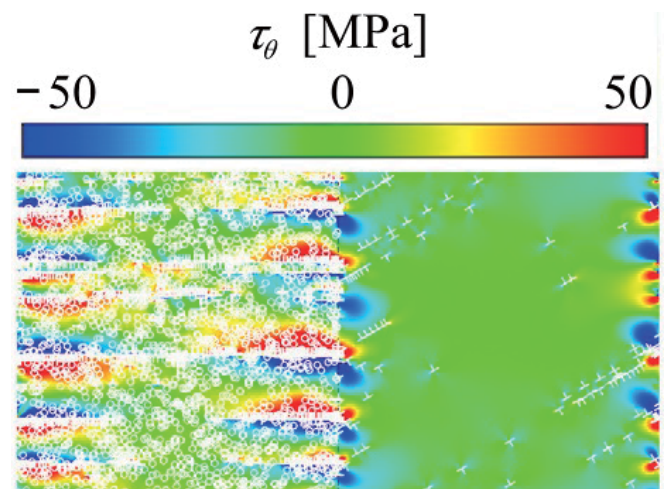


Fig. 17 Micro shear stress field,  $E_{12}=0.125\%$ ,  $w=10.0\mu\text{m}$

- [8] Shibutani, Y., Matsunaka, D., Tarumi, R., 2012. Plastic strain and temperature dependencies of Hall-Petch effect, *Journal of the society of Materials Science (in Japanese)*, Vol.61, No. 8, 724-729

## 6. CONCLUSIONS

In this study, Monte-Carlo simulation of polycrystal plasticity is performed using discrete dislocation plasticity approach for lamellar materials, which was based on applying periodic homogenization to the superposition method for discrete dislocation plasticity.

The Monte-Carlo simulations were performed for layer thickness of 1 $\mu$ m, 5 $\mu$ m and 10 $\mu$ m and grain angle of the adjacent grain as 30 degrees. The values of activated source position from grain boundary  $\lambda$  were obtained and showed the predicted trend of being at a distance from the grain boundary. Hall-Petch Grain Boundary Strengthening was observed for small grain sizes. The range of  $\lambda$  varies from the values obtained from the checker-board arrangement and the experimental evidence in [8]. This shows that  $\lambda$  is very sensitive to grain structure arrangement. It must be noted that the present study was performed on lamellar materials that do not contain multiple slip systems. More realistic models should be employed for accurate prediction of  $\lambda$  and for comparing experiments and simulations.

## ACKNOWLEDGEMENTS

This study was supported by the Japan-US Advanced Collaborative Education Program. The author would like to acknowledge Dr. Nobutada Ohno, Dr. Dai Okumura and Mr. Akira Sasaki for their contributions towards this research.

## REFERENCES

- [1] Van der Giessen, E., Needleman, A., 1995. Discrete dislocation plasticity: a simple planar model. *Modelling and Simulation in Materials Science and Engineering* 3, 689–735.
- [2] Okumura, D., Ohno, N., Yamaguchi, K., 2011. Plastic size effect analysis of lamellar composites using a discrete dislocation plasticity approach, *International Journal of Plasticity* 27, 2040-2055
- [3] Lemarchand, C., Devincere, B., Kubin, L.P., 2001. Homogenization method for a discrete-continuum simulation of dislocation dynamics. *Journal of the Mechanics and Physics of Solids* 49, 1969–1982.
- [4] Belytschko, T., Gracie, R., 2007. On XFEM applications to dislocations and interfaces. *International Journal of Plasticity* 23, 1721–1738.
- [5] Hirth, J.P., Lothe, J., 1982. *Theory of Dislocations*, second ed. John Wiley & Sons.
- [6] Nemat-Nasser, S., Hori, M., 1993. *Micromechanics: Overall Properties of Heterogeneous Materials*. North-Holland.
- [7] Cottrell, A.H., 1958. Theory of brittle fracture in steel and similar metals, *Trans. AIME*, 212

# A Second Order Accurate Scheme for Ideal Magnetohydrodynamics with Divergence-Free Reconstruction

Nishant Narechania

Department of Aerospace Engineering, University of Michigan, USA  
nishantn@umich.edu

Supervisor : Keiichi Kitamura

Department of Aerospace Engineering, Nagoya University, Japan  
kitamura@fluid.nuae.nagoya-u.ac.jp

## ABSTRACT

Many of the phenomena in space plasma physics can be accurately modeled by the equations of ideal Magnetohydrodynamics(MHD). One of the most critical aspects of numerical MHD is the divergence-free requirement of magnetic fields. Without a zero discrete divergence, we may obtain unphysical and spurious solutions due to magnetic monopoles arising out of the finite volume formulation of the conservation laws. We present a staggered grid approach by Balsara[1] to attain a divergence-free evolution of magnetic fields. Such a technique can be used for any other system requiring divergence-free evolution of vector fields. Second order accuracy in time is achieved through a two-step Runge-Kutta time update strategy. Second order accuracy in space is obtained by a linear reconstruction technique. The magnetic fields are updated using electric fields found at the cell corners and a solenoidal reconstruction is employed for second order accuracy. We also extend two AUSM-family schemes, namely AUSM<sup>+</sup> and SLAU2 to be used in MHD.

The structure of this report is as follows : The governing equations of ideal MHD are expressed in conservative form in section 1. The staggered mesh formulation for updating magnetic fields is described in section 2. The Runge-Kutta 2<sup>nd</sup> order time update is described in section 3. The 2<sup>nd</sup> order reconstruction for zone-centered variables and the solenoidal reconstruction for face-centered variables is described in section 4. The AUSM-type fluxes and its higher order extension used here are described in sections 5 and 6, respectively. Finally, in section 7, the solver is validated on a some 2-D test cases and in section 8, the higher order accuracy is confirmed, the discrete divergence is calculated and comparison is made with other schemes.

## 1. THE EQUATIONS OF IDEAL MHD

The equations governing the laws of ideal magnetohydrodynamics in conservative form suitable for a Finite Volume numerical formulation are :

$$\frac{\mathbf{U}}{t} + \frac{\mathbf{F}}{x} + \frac{\mathbf{G}}{y} = 0 \quad (1)$$

where  $\mathbf{U}$  is the vector of conserved variables and  $\mathbf{F}$  and  $\mathbf{G}$  are the fluxes in the x and y directions, respectively. The conservative form is converted to a Finite Volume discretization for the construction of numerical solution techniques. It is the Finite Volume form of the equation that is finally implemented into the final solver. The vectors  $\mathbf{U}, \mathbf{F}, \mathbf{G}$  are given by :

$$\mathbf{U} = \begin{Bmatrix} \rho \\ \rho v_x \\ \rho v_y \\ \rho v_z \\ \varepsilon \\ B_x \\ B_y \\ B_z \end{Bmatrix} \quad (2)$$

$$\mathbf{F} = \begin{Bmatrix} \rho v_x \\ \rho v_x v_x + p_g + \frac{1}{2} \mathbf{B}^2 - B_x B_x \\ \rho v_x v_y - B_x B_y \\ \rho v_x v_z - B_x B_z \\ (\varepsilon + p_g + \frac{1}{2} \mathbf{B}^2) v_x - B_x (\mathbf{v} \cdot \mathbf{B}) \\ 0 \\ v_x B_y - v_y B_x \\ v_x B_z - v_z B_x \end{Bmatrix} \quad (3)$$

$$\mathbf{G} = \left\{ \begin{array}{c} \rho v_y \\ \rho v_y v_x - B_y B_x \\ \rho v_y v_y + p_g + \frac{1}{2} \mathbf{B}^2 - B_y B_y \\ \rho v_y v_z - B_y B_z \\ (\varepsilon + p_g + \frac{1}{2} \mathbf{B}^2) v_y - B_y (\mathbf{v} \cdot \mathbf{B}) \\ v_y B_x - v_x B_y \\ 0 \\ v_y B_z - v_z B_y \end{array} \right\} \quad (4)$$

Where  $\varepsilon = \frac{1}{2} \rho v_x^2 + p_g / (\gamma - 1) + \frac{1}{2} \mathbf{B}^2$  is the total energy (kinetic + internal + magnetic). Also,  $p_g$  is the thermodynamic gas pressure.

## 2. The $\nabla \cdot \mathbf{B}$ CONSTRAINT AND THE STAGGERED MESH FORMULATION

The Gauss's Law for Magnetism states the existence of a divergence-free magnetic fields devoid of any magnetic monopoles. A conservative formulation described above does not ensure a zero numerical divergence leading to unphysical and erroneous results which can sometimes also cause the solution to grow unstable. Hence, here we use a staggered mesh update strategy for a divergence-free update of magnetic fields.

The magnetic fields are evaluated at the face centers of the control volume and the electric fields are evaluated at the corners of the control volume. The other primitive variables ( $\rho_g, \rho, \mathbf{v}$ ) from the pure Euler Equations are evaluated at the control volume centers as usual. See Fig. 1 for a clearer idea.

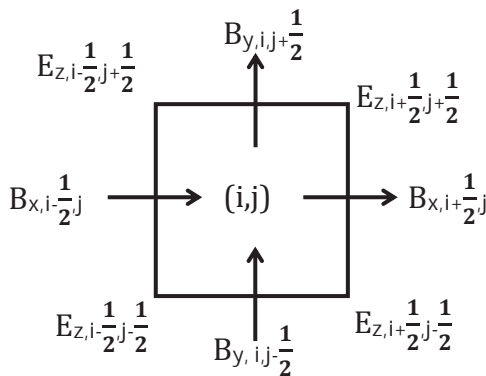


Fig. 1: Staggered mesh for magnetic fields

The electric field is given by :

$$\mathbf{E} = -\mathbf{v} \times \mathbf{B} \quad (5)$$

Thus,  $E_z = v_y B_x - v_x B_y$

We can see that  $E_z$  is directly related to the fluxes as :  $E_z = G_6 = -F_7$

We thus evaluate  $E_z$  from the fluxes calculated at the zone corners. For a 2-D variation, we would only require the z-component of the electric field.

According to Faraday's Law of Induction :

$$\frac{\mathbf{B}}{t} = -\nabla \times \mathbf{E} \quad (6)$$

Discretizing this equation (Forward Euler) and assuming no variation in z direction for 2-D flow gives :

$$\frac{B_{x,i+\frac{1}{2},j}^{n+1} - B_{x,i+\frac{1}{2},j}^n}{\Delta t} = \frac{E_{z,i+\frac{1}{2},j-\frac{1}{2}} - E_{z,i+\frac{1}{2},j+\frac{1}{2}}}{\Delta y} \quad (7)$$

$$\frac{B_{y,i,j+\frac{1}{2}}^{n+1} - B_{y,i,j+\frac{1}{2}}^n}{\Delta t} = \frac{E_{z,i+\frac{1}{2},j+\frac{1}{2}} - E_{z,i-\frac{1}{2},j+\frac{1}{2}}}{\Delta x} \quad (8)$$

We update the face centered magnetic fields using equations 7 and 8.

The discrete divergence in any cell (i,j) is given by :

$$\nabla \cdot \mathbf{B}_{i,j} = \frac{B_{y,i,j+\frac{1}{2}} - B_{y,i,j-\frac{1}{2}}}{\Delta y} + \frac{B_{x,i+\frac{1}{2},j} - B_{x,i-\frac{1}{2},j}}{\Delta x} \quad (9)$$

Note that the above update ensures a divergence-free evolution of the magnetic field i.e. the discrete divergence in any cell remains zero if it is zero to begin with. This is the main purpose of using a staggered mesh.

The calculation of the fluxes at the zone corners and the subsequent calculation of the electric field is described in section 6.

## 3. SECOND ORDER RUNGE-KUTTA TIME UPDATE STRATEGY

The conservative equations are written in the form:

$$\frac{U}{t} = L(U) \quad (10)$$

The time discretization of the above equation is done in two steps to make the scheme second order as follows :

$$U^{(1)} = U^n + \frac{1}{2} \Delta t L(U^n) \quad (11)$$

$$U^{n+1} = U^n + \Delta t L(U^{(1)}) \quad (12)$$

## 4. SECOND ORDER RECONSTRUCTION OF PRIMITIVE VARIABLES

We use the reconstruction techniques described by Balsara[1] in our solver. The zone-centered, cell-averaged variables are calculated using a linear reconstructed profile in both directions. The reconstruction is done using the Minmod limiter. Thus, the linear slopes are calculated using the

minimum undivided differences obtained from the neighboring cells.

The face centered magnetic fields are reconstructed in such a way that the following criteria are satisfied :

- 1) Divergence remains zero throughout the control volume.
- 2) The reconstructed profile along the face is same when calculated using both adjacent cells sharing the face. This is necessary because the magnetic field component perpendicular to the face should be constant across the face for a 1-D MHD Riemann Problem.

Let the profiles of the magnetic field components in the control volume (i,j) be given by :

$$B_x(x,y) = a_0x + a_x x + a_y y + a_{xx}x^2 + a_{xy}xy + a_{yy}y^2 \quad (13)$$

$$B_y(x,y) = b_0x + b_x x + b_y y + b_{xx}x^2 + b_{xy}xy + b_{yy}y^2 \quad (14)$$

For a divergence-free reconstruction we must satisfy :

$$\frac{B_x(x,y)}{x} + \frac{B_y(x,y)}{y} = 0 \quad (15)$$

From Figure 1, we know that the two values for  $B_x$  (denoted as  $B_x^-$  and  $B_x^+$ ) are available on the left and right faces and two values for  $B_y$  ( $B_y^-$  and  $B_y^+$ ) are available on the bottom and top faces.

The linear slope for the  $B_x$  profile on the right face is found using the minimum undivided difference obtained using from the top and bottom neighboring faces. Thus, the profile on the right face is :

$$B_x\left(\frac{\Delta x}{2}, y\right) = B_x^+ + \frac{\Delta_y B_x^+}{\Delta y} y \quad (16)$$

where  $\Delta_y B_x^+$  is the minimum undivided difference on the right face showing the variation of  $B_x$  in the y-direction.

Similarly, the profiles on the other three faces are :

$$B_x\left(\frac{-\Delta x}{2}, y\right) = B_x^- + \frac{\Delta_y B_x^-}{\Delta y} y \quad (17)$$

$$B_y\left(x, \frac{\Delta y}{2}\right) = B_y^+ + \frac{\Delta_x B_y^+}{\Delta x} x \quad (18)$$

$$B_y\left(x, \frac{-\Delta y}{2}\right) = B_y^- + \frac{\Delta_x B_y^-}{\Delta x} x \quad (19)$$

The profiles (eqns. 13 and 14) are found using the divergence-free condition (eqn. 15). Note that since the  $B_x$  profile is linear in the y-direction on the right and left faces,  $a_{yy} = 0$ . The other five coefficients for  $B_x(x,y)$  are :

$$a_x = \frac{B_x^+ - B_x^-}{\Delta x} \quad (20)$$

$$a_y = \frac{\Delta_y B_x^+ + \Delta_y B_x^-}{2\Delta x} \quad (21)$$

$$a_{xy} = \frac{\Delta_y B_x^+ - \Delta_y B_x^-}{\Delta x \Delta y} \quad (22)$$

$$a_0 = \frac{B_x^+ + B_x^-}{2} - a_{xx} \frac{\Delta x^2}{4} \quad (23)$$

$$a_{xx} = -\frac{\Delta_x B_y^+ - \Delta_x B_y^-}{2\Delta y \Delta x} \quad (24)$$

The coefficients for  $B_y(x,y)$  are found in an analogous manner.

This 2<sup>nd</sup> linear reconstruction is used to calculate the fluxes as later described in section 6.

## 5. THE AUSM-FAMILY FLUXES

Various numerical fluxes originally meant for the Euler Equations of gas dynamics have been extended to MHD by different researchers. For example, the HLLC[2], HLLC[2,3] and HLLD[2] solvers with increasing levels of refinement, the AUSM Solver[4] and the Roe Linearized Solver[5]. Here, we propose extensions of AUSM<sup>+</sup> and SLAU2 schemes for MHD. We extend the AUSM<sup>+</sup> scheme proposed in [6] and SLAU2 proposed in [7] to the system of MHD equations.

The 1-D MHD equations are first written in the following form as described in [4]:

$$\frac{\mathbf{U}}{t} + \frac{\mathbf{E}_1}{x} + \frac{\mathbf{E}_2}{x} + \frac{\mathbf{G}}{y} = 0 \quad (25)$$

where  $\mathbf{F} = \mathbf{E}_1 + \mathbf{E}_2$ .

Thus, the x-direction flux  $\mathbf{F}$  is split into two components  $\mathbf{E}_1$  and  $\mathbf{E}_2$ , out of which  $\mathbf{E}_1$  is the advective component which is upwinded and  $\mathbf{E}_2$  is the pressure component which is found using a splitting method.

$$\mathbf{E}_1 = \left\{ \begin{array}{c} \rho v_x \\ \rho v_x v_x \\ \rho v_x v_y \\ \rho v_x v_z \\ (\varepsilon + p_g + \frac{1}{2} \mathbf{B}^2 - B_x^2) v_x \\ 0 \\ v_x B_y \\ v_x B_z \end{array} \right\} \quad (26)$$

$$\mathbf{E}_2 = \left\{ \begin{array}{c} 0 \\ \rho_g + \frac{1}{2} \mathbf{B}^2 - B_x B_x \\ - B_x B_y \\ - B_x B_z \\ - B_x (v_y B_y + v_z B_z) \\ 0 \\ - v_y B_x \\ - v_z B_x \end{array} \right\} \quad (27)$$

Now,  $E_1$  is split into  $E_1^+$  and  $E_1^-$  and  $E_2$  is split into  $E_2^+$  and  $E_2^-$  as follows :

$$\mathbf{E}_1^\pm = M^\pm(M) c_w \left\{ \begin{array}{c} \rho \\ \rho v_x \\ \rho v_y \\ \rho v_z \\ (\epsilon + p_g + \frac{1}{2} \mathbf{B}^2 - B_x^2) \\ 0 \\ B_y \\ B_z \end{array} \right\} \quad (28)$$

$$\mathbf{E}_2^\pm = P^\pm(M) \left\{ \begin{array}{c} 0 \\ \rho_g + \frac{1}{2} \mathbf{B}^2 - B_x B_x \\ - B_x B_y \\ - B_x B_z \\ - B_x (v_y B_y + v_z B_z) \\ 0 \\ - v_y B_x \\ - v_z B_x \end{array} \right\} \quad (29)$$

Here, the Mach No. splitting is given by :

$$M^\pm(M) = \begin{cases} \frac{1}{2}(M + |M|), & |M| \geq 1 \\ M_\beta^\pm(M), & \text{else} \end{cases} \quad (30)$$

with

$$M_\beta^\pm(M) = \pm \frac{1}{4}(M \pm 1)^2 \pm \beta(M^2 - 1)^2, \quad -\frac{1}{16} \leq \beta \leq \frac{1}{2}$$

The pressure flux splitting is given by :

$$P^\pm(M) = \begin{cases} \frac{1}{2}(1 + \text{sgn}(M)), & |M| \geq 1 \\ P_\alpha^\pm(M), & \text{else} \end{cases} \quad (31)$$

with

$$P_\alpha^\pm(M) = \frac{1}{4}(M \pm 1)^2(2 \mp M) \pm \alpha M(M^2 - 1)^2, \quad -\frac{3}{4} \leq \alpha \leq \frac{3}{16}$$

We have used in our code the optimum values of  $\alpha$  and  $\beta$ , i.e.  $\frac{3}{16}$  and  $\frac{1}{8}$  respectively. Details on how to obtain these values are given in [6].

Here Mach No.  $M$  is defined as  $\frac{v_x}{c_w}$

$$\text{where } c_w = \left\{ \frac{\gamma p + |\mathbf{B}|^2}{\rho} \right\}^{1/2}$$

In the AUSM<sup>+</sup> numerical flux, unlike the AUSM flux, we find a common intermediate wavespeed  $c_{w,i+\frac{1}{2}}$  at the cell interface and it is hence shown outside the bracket in equation 28.

The intermediate wavespeed  $c_{w,i+\frac{1}{2}}$  can be found using an arithmetic or geometric mean as the most obvious options. We use the arithmetic average in our code for the purpose. The code was run using both kinds of averages for calculating the intermediate wavespeed and we found that the type of averaging used hardly makes any difference in the results. The intermediate Mach No. is found using the two Mach Nos. as follows :

$$M_{i+\frac{1}{2}} = M^*(M_i) + M^*(M_{i+1}) \quad (32)$$

where  $M^*$  are found using the above splitting. The intermediate Mach No. is then used to calculate the split fluxes  $E_1^\pm$  and  $E_2^\pm$  as an argument to the functions  $M^\pm(M)$  and  $P^\pm(M)$ .

This AUSM<sup>+</sup> formulation can analogously be extended to the y-direction. We do not go into details of the SLAU2 scheme.

## 6. HIGHER ORDER EXTENSION FOR FLUX

Here, the flux at a face is not calculated directly using cell-averaged values from adjacent cells sharing the face, as in a first order approach. The primitive variables are

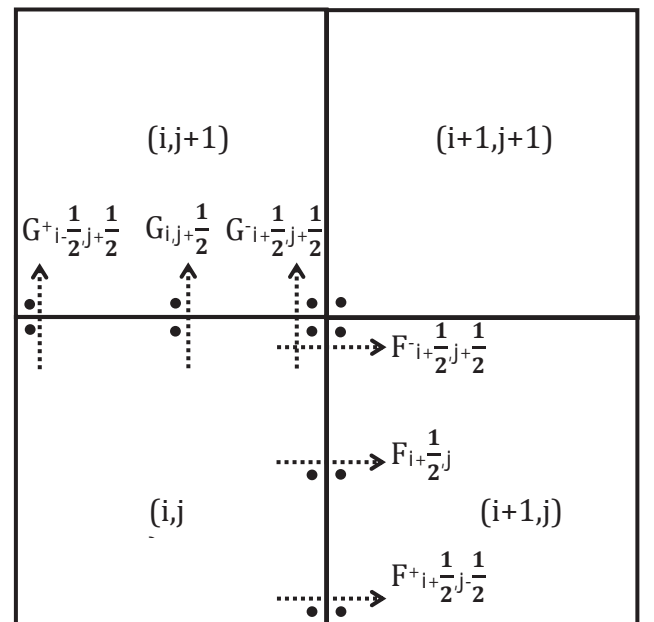


Fig. 2: Higher order extension for flux

calculated at the corners of each cell and at the face centers using the reconstruction described in section 4. At these points, the fluxes are calculated using the two states found using reconstruction from each of the adjacent cells sharing that face. Thus, the values are calculated at the same point but using reconstruction from different cells. These two states are used in the numerical flux for the calculation of the flux component at that point. See Fig. 2 for a clearer idea. The solid dots indicate the points where the reconstructed variables are found.

Thus, the net flux across face  $(i+\frac{1}{2},j)$  is calculated using Simpson's Rule as :

$$F_{i+\frac{1}{2},j} = \frac{F_{i-\frac{1}{2},j+\frac{1}{2}}^+ + 4G_{i,j+\frac{1}{2}} + G_{i+\frac{1}{2},j+\frac{1}{2}}^-}{6} \quad (33)$$

Similarly, the flux across face  $(i,j+\frac{1}{2})$  is calculated as :

$$F_{i,j+\frac{1}{2}} = \frac{G_{i+\frac{1}{2},j-\frac{1}{2}}^+ + 4F_{i+\frac{1}{2},j} + F_{i+\frac{1}{2},j+\frac{1}{2}}^-}{6} \quad (34)$$

The superscripts (+) and (-) indicate the upper/right and lower/left limit of the flux components calculated at the corner point. Thus,  $G_{i+\frac{1}{2},j+\frac{1}{2}}^-$  indicates the flux calculated at the corner  $(i+\frac{1}{2},j+\frac{1}{2})$  using reconstructed variables from the cells  $(i,j)$  and  $(i,j+1)$  whereas  $G_{i+\frac{1}{2},j+\frac{1}{2}}^+$  indicates the flux calculated at the same point using reconstructed variables from the cells  $(i+1,j)$  and  $(i+1,j+1)$ .

Coming back to the electric field  $E_z$  calculated at the corner  $(i+\frac{1}{2},j+\frac{1}{2})$ , let us recall that  $E_z = G_6 = -F_7$ .

Thus, the electric field is calculated using the four flux components found at the corner itself :

$$E_{z,i+\frac{1}{2},j+\frac{1}{2}} = \frac{G_{i+\frac{1}{2},j+\frac{1}{2}}^+ + G_{i+\frac{1}{2},j+\frac{1}{2}}^- - F_{i+\frac{1}{2},j+\frac{1}{2}}^+ - F_{i+\frac{1}{2},j+\frac{1}{2}}^-}{4} \quad (35)$$

This higher order extension is described in [1].

## 7. 2D TEST CASE RESULTS

We now run a few 2-D benchmark test cases with our solver. The CFL number is 0.6 for all cases.

### 7.1. Cloud-Shock Interaction

We look at the interaction between a high-density cloud and a strong magnetized shock. The initial discontinuity is a combination of a fast shockwave and a rotational discontinuity. The initial data for this problem[8] consists of a shock located at  $x = 0.05$  with Rankine-Hugoniot conditions as :

$(\rho, v_x, v_y, v_z, B_x, B_y, B_z, p)$   
 $= (3.86859, 11.2536, 0, 0, 0, 2.1826182, -2.1826182, 167.345)$   
for  $x < 0.05$

$(\rho, v_x, v_y, v_z, B_x, B_y, B_z, p)$   
 $= (1.0, 0, 0, 0, 0, 0.56418958, 0.56418958, 1.0)$   
for  $x > 0.05$

The total computational domain is  $[0,1] \times [0,1]$  and also contains a circular cloud of density  $\rho = 10.0$  and a radius of 0.15, centered at  $(x,y) = (0.25,0.5)$ . Inlet boundary conditions are used at the boundary  $x = 0$  and zero-gradient boundary

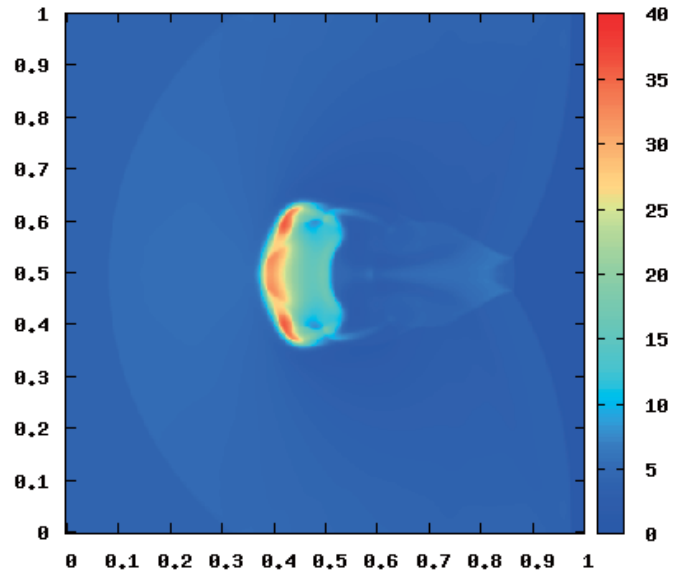


Fig. 3: Density distribution for cloud-shock interaction

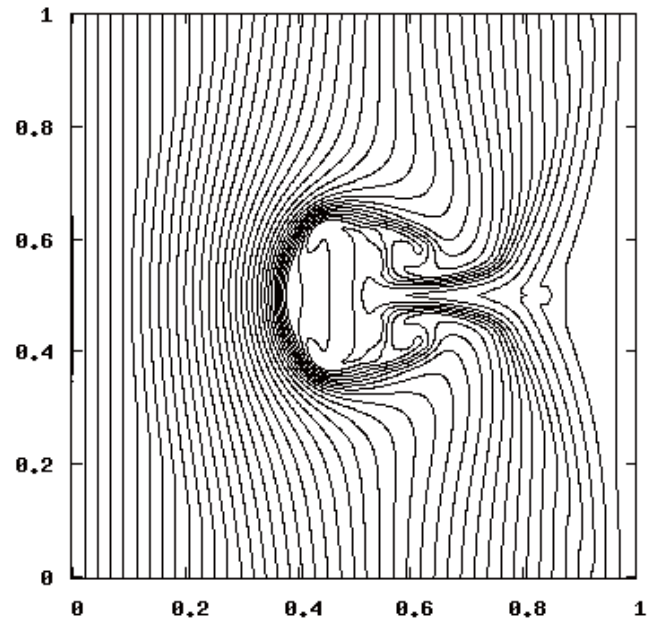


Fig. 4: Magnetic field lines for cloud-shock interaction

conditions everywhere else. The density contours at  $t = 0.06$  are shown in Fig. 3. The magnetic field lines are shown in

Fig. 4. We have used a mesh of 400 x 400 grid cells. The specific heat ratio  $\gamma$  is 1.66.

These results match well with those shown in the paper by Gabor Toth[9]. The solution consists of a bow shock in the front, trailing shocks at the back and a turbulent structure in the middle.

## 7.2. Magnetized Blast Problem

This test case is described in the paper by Gardiner and Stone[10]. Initially,  $\rho = 1$  and  $\mathbf{v} = 0$  everywhere. Also,  $B_x = B_y = \sqrt{50}$  and  $B_z = 0$ . The gas pressure is 100 inside a circle of radius 0.125 centered at (0.5,0.5) and 1 everywhere else. The computational domain is  $[0,1] \times [0,1]$  and zero-gradient boundary conditions are imposed on all boundaries. The density, pressure and magnetic pressure distributions found using HLLC in the form of gray-scale images consistent with Gardiner and Stone[10] are plotted at time  $t = 0.02$  in Figs. 5, 6, 7 respectively. We have used a mesh of 400 x 400 grid cells. The specific heat ratio  $\gamma$  is 1.66.

In this problem, a very fast and almost spherical magnetosonic shockwave propagates through the ambient plasma. Note that the AUSM<sup>+</sup> and SLAU2 schemes could not maintain pressure positivity in this benchmarked case.

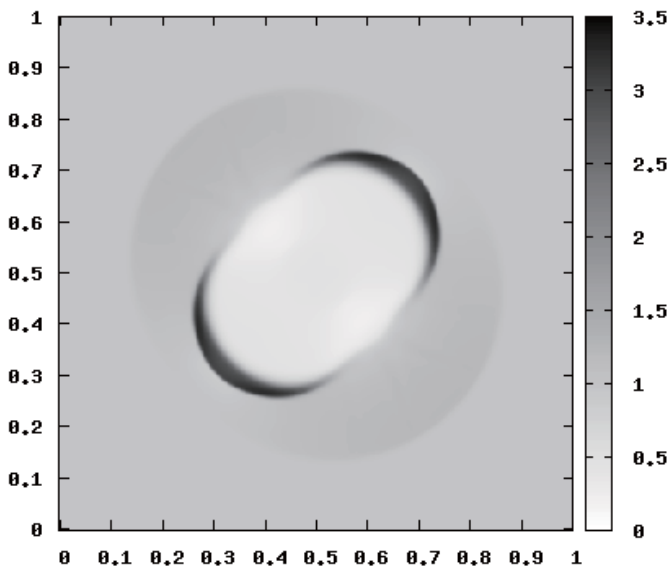


Fig. 5: Gray-scale density distribution for blast problem

## 7.3. The Rotor Problem

This problem, first given in the paper by Balsara and Spicer[11], demonstrates loss of angular momentum through torsional Alfvén waves in star formation. We use the data from the first rotor problem as described in the paper by Toth[9]. Initially, there is a fast spinning rotor at the center of an ambient stationary fluid. The rotor has a radius of 0.1 units and spins with a uniform angular velocity such that it has a toroidal velocity of 2 units at radius 0.1.

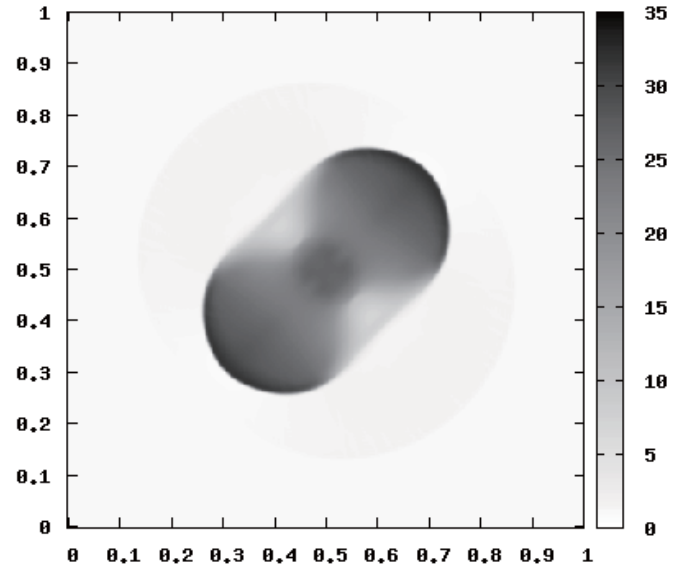


Fig. 6: Gray-scale pressure distribution for blast problem

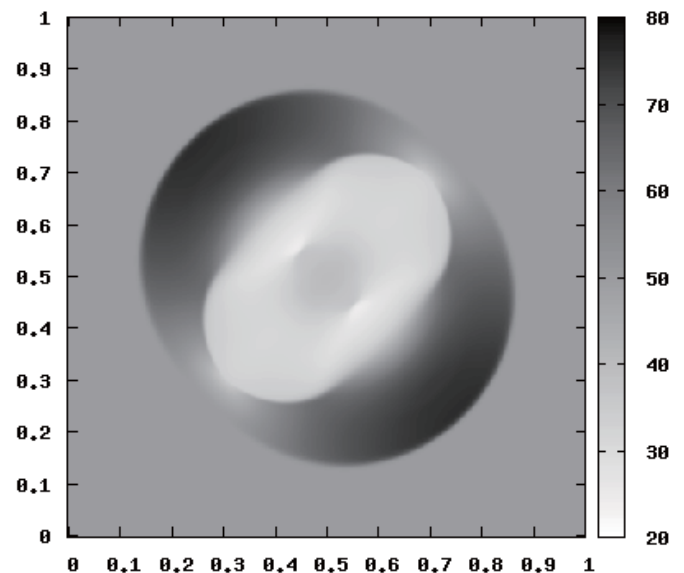


Fig. 7: Gray-scale magnetic pressure distribution for blast problem

The density of fluid in the rotor is set to 10 whereas the ambient fluid has unit density. A linear taper is applied to the density so that it varies linearly in the radial direction from value 10 at radius 0.1 to the ambient density at a radius of 0.115. Similarly, the toroidal velocity drops linearly from a value of 2 units at radius 0.1 to zero at a radius of 0.115. This taper is applied to ensure that no strong gradients are formed in the beginning. There is a uniform initial magnetic field of magnitude  $5/\sqrt{4\pi}$  in the x-direction and unit pressure throughout the computational domain.

The computational domain is  $[0,1] \times [0,1]$  and zero-gradient boundary conditions are imposed on all boundaries. The density, Mach No., pressure and magnetic pressure contour lines are plotted at time  $t = 0.15$  in Figs. 8, 9, 10, 11

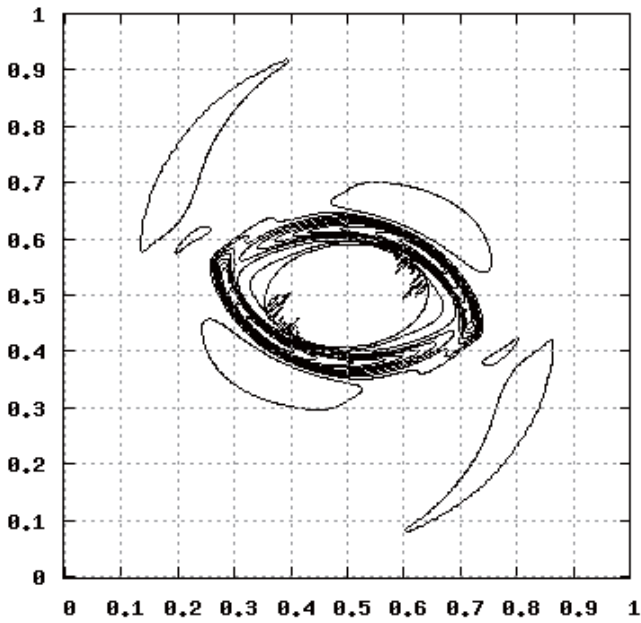


Fig. 8: Density contours for first rotor problem

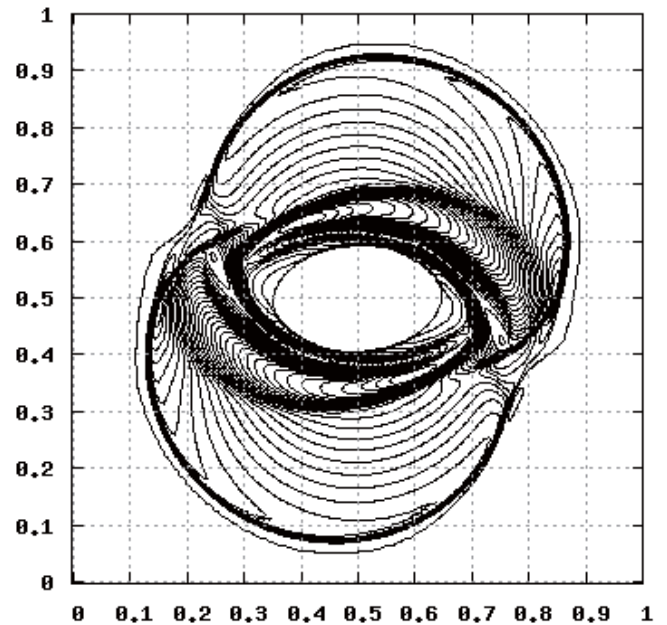


Fig. 10: Pressure contours for first rotor problem

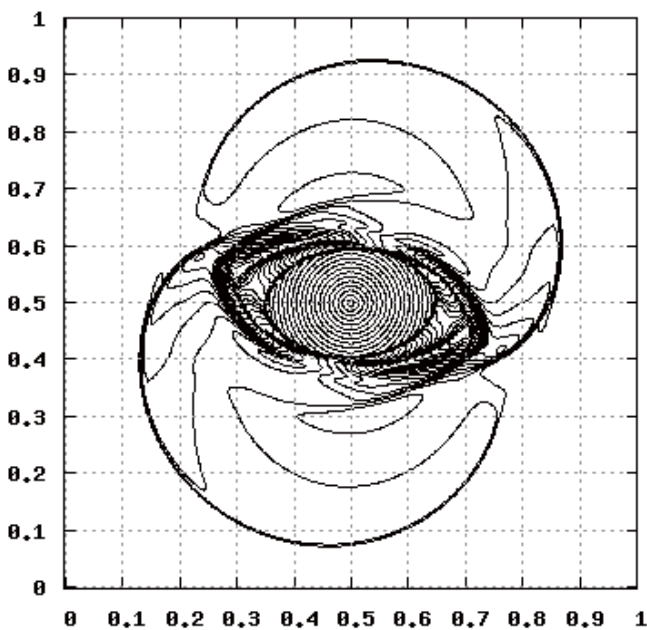


Fig. 9: Mach No. contours for first rotor problem

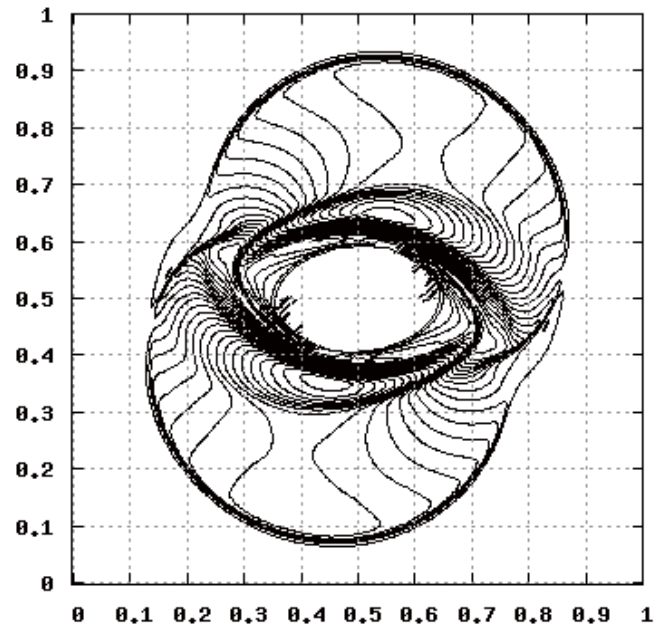


Fig. 11: Magnetic pressure contours for first rotor problem

respectively. We have used a mesh of  $400 \times 400$  grid cells. The specific heat ratio  $\gamma$  is 1.4. The results show striking resemblance to those in [9].

The second rotor problem[9] also looks similar except a few differences in values. The ambient pressure is 0.5 here and the magnetic field has an initial value of  $2.5/\sqrt{4\pi}$ . The angular velocity of the cylinder is such that the toroidal velocity at a radius 0.1 is 1. Also, the simulation time is 0.295 and the specific heat ratio  $\gamma$  is 1.66.

The density, Mach No., pressure and magnetic pressure color plots are plotted at time  $t = 0.295$  in Figs. 12, 13, 14, 15. These plots can be compared to those in [1].

The rotor is initially in non-equilibrium because there is not enough centrifugal force to sustain the rotating motion. As time progresses, magnetic pressure builds up around the rotor and confines it into an oblong shape. The rotor generates torsional Alfvén waves which propagate almost till the domain boundary at the end of the simulation. One can refer to the paper by Mouschovias and Paleologou[12] for a theoretical description of this problem and the motivation behind studying it.

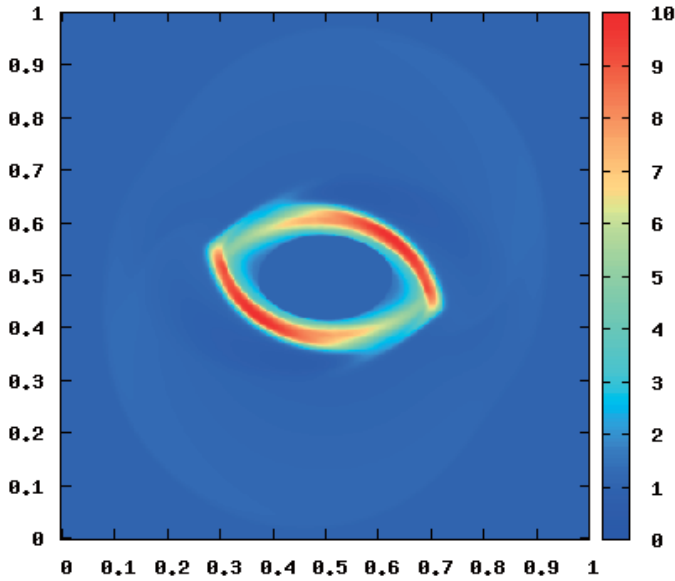


Fig. 12: Density distribution for second rotor problem

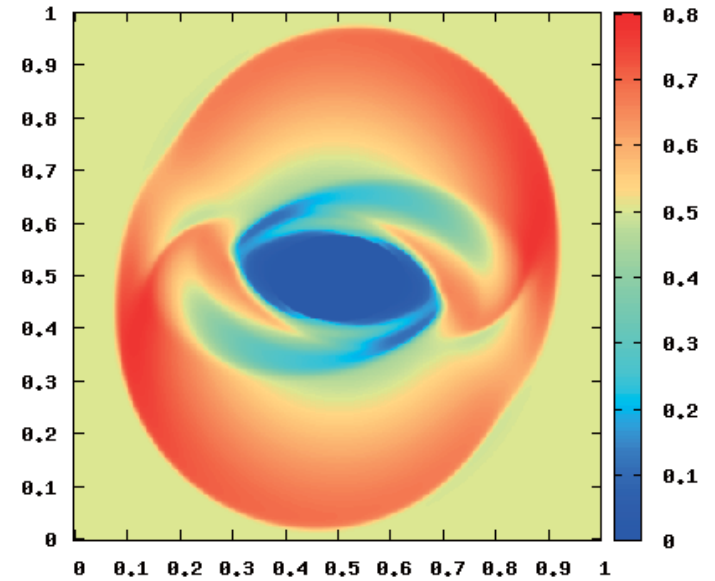


Fig. 14: Pressure distribution for second rotor problem

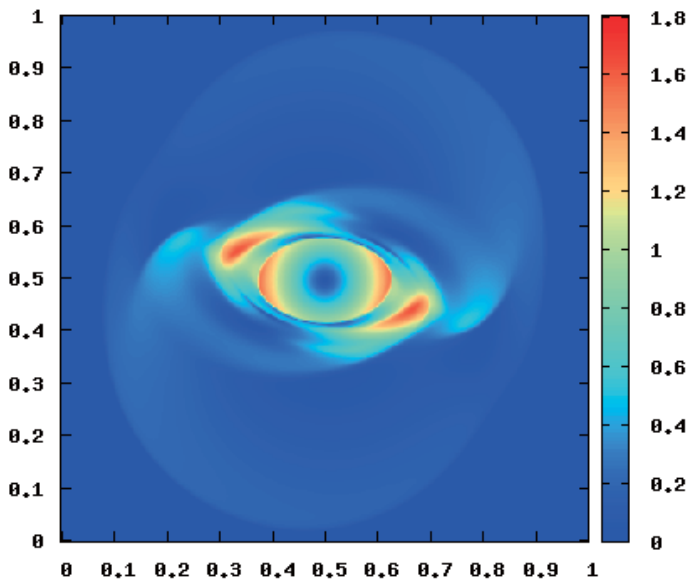


Fig. 13: Mach No. distribution for second rotor problem

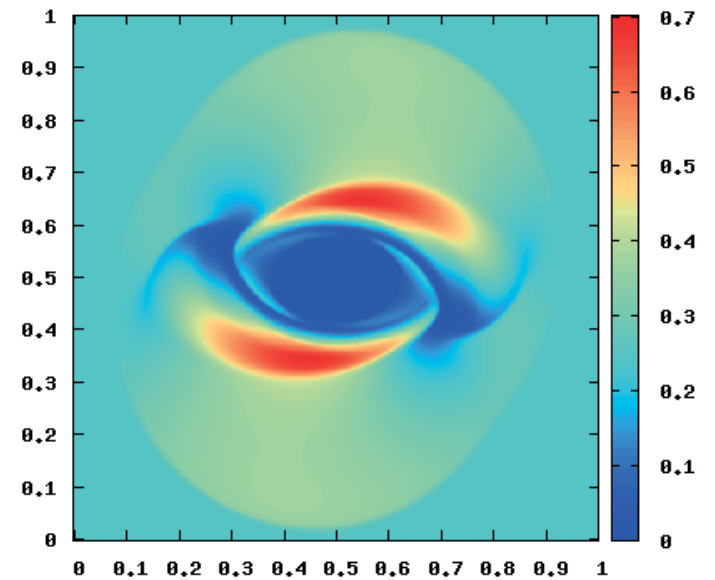


Fig. 15: Magnetic pressure distribution for second rotor problem

## 8. CONCLUSIONS

Here, we finally verify the higher order accuracy and calculate the discrete divergence.

### 8.1. Higher Order Accuracy

We now make a comparison between the 1<sup>st</sup> order scheme (without any reconstruction) assuming a constant cell-averaged value and the second order scheme that we have used. Our code was run for the rotor problem a second time without employing the reconstruction to see the first order results for the purpose of comparison. The colored contour plots for the pressure distribution using the 1<sup>st</sup> order scheme is shown in Fig. 16. The corresponding plot using the 2<sup>nd</sup> order reconstruction is shown in Fig. 18.

We magnify these plots to view individual grid cells in the region of the Alfvén wave in order to see the accuracy of the scheme. The marked square region in the pressure plots indicates the magnified portion.

These magnified plots are shown in Figs. 17 and 19 respectively. We notice that the Alfvén wave is dispersed over many, namely fifteen to sixteen grid cells in the 1<sup>st</sup> order simulation. In the 2<sup>nd</sup> order simulation, the Alfvén wave discontinuity is captured over just five to six cells, reflecting the high order accuracy of our scheme.

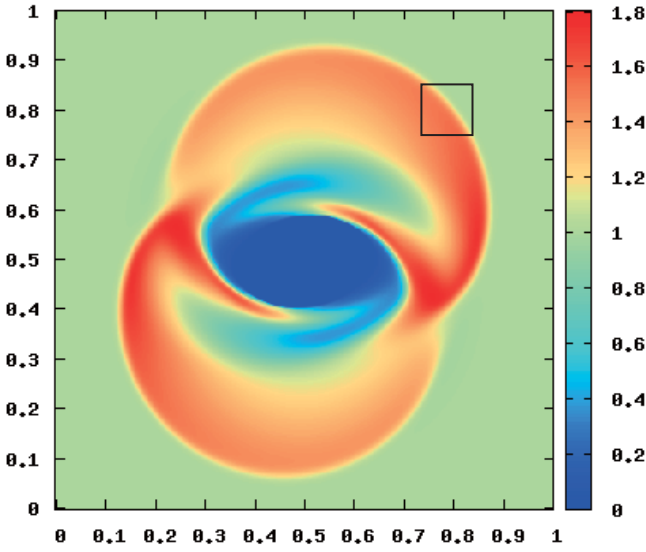


Fig. 16: Pressure distribution for first rotor problem using 1<sup>st</sup> order scheme

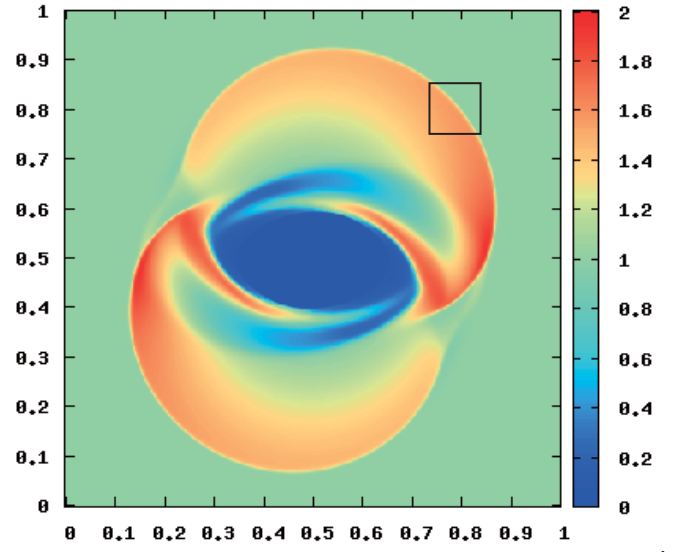


Fig. 18: Pressure distribution for first rotor problem using 2<sup>nd</sup> order scheme

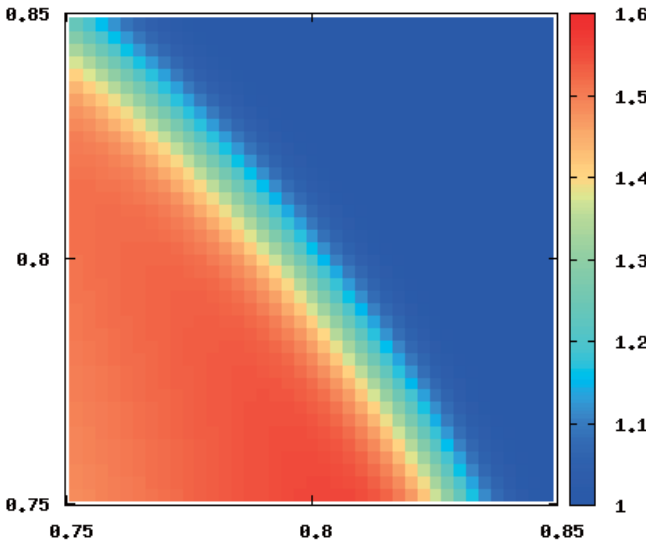


Fig. 17: Magnified pixelated image showing pressure distribution across Alfvén wave using 1<sup>st</sup> order scheme

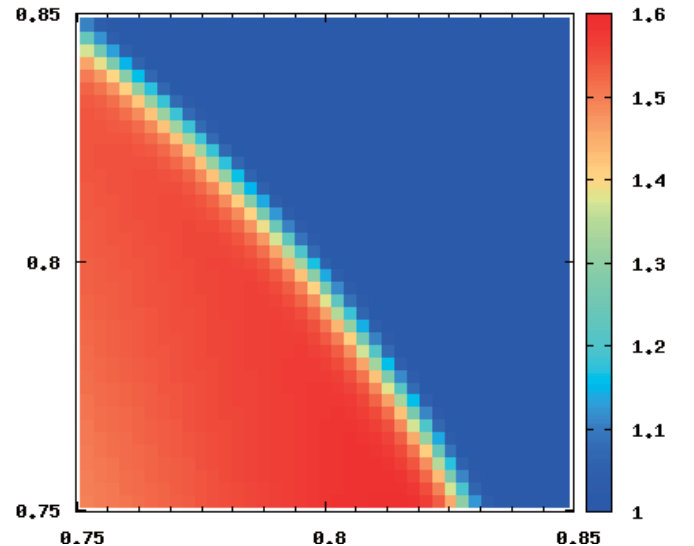


Fig. 19: Magnified pixelated image showing pressure distribution across Alfvén wave using 2<sup>nd</sup> order scheme

## 8.2. The Discrete Divergence

We now try to verify whether our staggered mesh algorithm for divergence-free evolution of magnetic fields has produced the desired results. The discrete divergence for a cell is given by :

$$\text{div}^c((B_x, B_y)_{ij}) = \frac{\delta_x(B_x)_{ij}}{\Delta x} + \frac{\delta_y(B_y)_{ij}}{\Delta y} \quad (36)$$

The  $\delta_x$  operator indicates differencing in the x-direction and the  $\delta_y$  operator indicates differencing in the y-direction.

The superscript 'c' denotes central differencing used here to obtain the discrete divergence. The divergence should ideally be zero according to the staggered mesh divergence-free evolution of the magnetic field. We calculate the  $L_2$  norm of the discrete divergence for the cases we have solved here. These divergence errors are tabulated in Fig. 20.

As expected, the discrete divergence errors are very close to zero and for the simulations run using double precision, they are almost negligible. These errors show an increasing trend with increasing number of cells which is more or less the trend observed in the calculation done by Mishra and Tadmor[8].

Number of cells	Cloud-Shock Interaction Problem		Magnetized Blast Problem		First Rotor Problem	Second Rotor Problem
	Single Precision	Double Precision	Single Precision	Double Precision	Single Precision	Single Precision
50x50	$3.83 \times 10^{-5}$	$7.28 \times 10^{-14}$	$6.56 \times 10^{-5}$	$1.46 \times 10^{-13}$	$1.18 \times 10^{-5}$	$6.76 \times 10^{-6}$
100x100	$1.17 \times 10^{-4}$	$2.02 \times 10^{-13}$	$1.74 \times 10^{-4}$	$3.74 \times 10^{-13}$	$2.88 \times 10^{-5}$	$1.69 \times 10^{-5}$
200x200	$3.97 \times 10^{-4}$	$5.86 \times 10^{-13}$	$4.75 \times 10^{-4}$	$9.70 \times 10^{-13}$	$7.88 \times 10^{-5}$	$4.53 \times 10^{-5}$
400x400	$1.01 \times 10^{-3}$	$1.73 \times 10^{-12}$	$1.36 \times 10^{-3}$	$2.62 \times 10^{-12}$	$2.23 \times 10^{-4}$	$1.26 \times 10^{-4}$

Fig. 20: Table showing  $L_2$  norm of discrete divergence errors for different test cases

### 8.3. Comparison With Other Numerical Fluxes

The simulations were run using other numerical fluxes too, namely HLLC[2], HLLC[2,3] and AUSM[4]. In terms of numerical diffusion, the HLLC flux proved to be extremely diffusive. All other schemes proved to be much sharper in capturing discontinuities and were almost comparable to each other. In terms of robustness, i.e. maintaining positivity of density and gas pressure, only the HLLC and SLAU2 fluxes worked well for all five cases in the 1<sup>st</sup> order case. SLAU2 2<sup>nd</sup> order worked well for the Orszag-Tang case handling low pressure regions robustly. This proves the superiority of SLAU2 applied to MHD. The results are tabulated in Fig. 21 for the 1<sup>st</sup> order results and Fig. 22 for the 2<sup>nd</sup> order results. The cases that failed are marked with a cross and those that worked robustly are shown with a tick.

	HLLC	HLLC	AUSM	AUSM <sup>+</sup>	SLAU2
Orszag-Tang Vortex	✓	✗	✓	✓	✓
Magnetized Blast	✓	✓	✓	✗	✓
Cloud-Shock Interaction	✓	✗	✗	✓	✓
Rotor 1	✓	✓	✗	✓	✓
Rotor 2	✓	✗	✗	✓	✓

Fig. 21: Table showing robustness characteristics of fluxes

	HLLC	HLLC	AUSM	AUSM <sup>+</sup>	SLAU2
Orszag-Tang Vortex	✓	✗	✗	✗	✓
Magnetized Blast	✓	✓	✓	✗	✗
Cloud-Shock Interaction	✓	✗	✗	✓	✓
Rotor 1	✓	✓	✗	✓	✗
Rotor 2	✓	✗	✗	✓	✓

Fig. 22: Table showing robustness characteristics of fluxes

### REFERENCES

- [1] D.S. Balsara, Second Order Accurate Schemes for Magnetohydrodynamics with Divergence-free Reconstruction, *The Astrophysical Journal* **151** (2004) 149.
- [2] T. Miyoshi, K. Kusano, A Multi-State HLL Approximate Riemann Solver for Ideal Magnetohydrodynamics, *Journal of Computational Physics* **208** (2005) 315.
- [3] S. Li, An HLLC Riemann Solver for Magnetohydrodynamics, *Journal of Computational Physics* **203** (2005) 344.
- [4] R. Agarwal, J. Augustinus, A Comparative Study of Advection Upwind Split(AUSM) and Wave/Particle Split(WPS) Scheme for Fluid and MHD Flows, *AIAA 99-3613*(1999).
- [5] M. Brio, C.C. Wu, An Upwind Differencing Scheme for the Equations of Ideal Magnetohydrodynamics, *Journal of Computational Physics* **75** (1988) 400.
- [6] Meng-Sing Liou, A Sequel to AUSM: AUSM<sup>+</sup>, *Journal of Computational Physics* **129** (1996) 364.
- [7] K. Kitamura, E. Shima, Towards Shock-Stable and Accurate Hypersonic Heating Computations: A New Pressure flux for AUSM-family schemes, *Journal of Computational Physics* **245** (2013) 62.
- [8] S. Mishra, E. Tadmor, Constraint Preserving Scheme using Potential-based Fluxes III: Genuinely Multi-Dimensional Schemes for MHD Equations, *ESAIM:M2AN* **46** (2012) 661.
- [9] Gabor Toth, The  $\nabla \cdot \mathbf{B} = 0$  Constraint in Shock-Capturing Magnetohydrodynamic Codes, *Journal of Computational Physics* **161** (2000) 605.
- [10] T.A. Gardiner, J.M. Stone, An Unsplit Godunov Method for Ideal MHD via Constrained Transport, *Journal of Computational Physics* **205** (2005) 509.
- [11] D.S. Balsara, D.S. Spicer, A Staggered Mesh Algorithm Using High Order Godunov Fluxes to Ensure Solenoidal Magnetic Fields in Magnetohydrodynamic Simulations, *Journal of Computational Physics* **149** (1999) 270.
- [12] T. Mouschovias, E. Paleologou, Magnetic Braking of an Aligned Rotator During Star Formation: An Exact, Time-Dependent Solution, *The Astrophysical Journal* **237** (1980) 877.

# VISUAL FEEDBACK CONTROL FOR TABLE TENNIS ROBOT

Yi-Kai Wang

Department of Mechanical Engineering, Graduate School of University of Michigan  
ykewang@umich.edu

Supervisor: Yoshikazu Hayakawa

Graduate School of Engineering, Nagoya University  
hayakawa@nuem.nagoya-u.ac.jp

## ABSTRACT

With the development of science technology over the past thirty years, computer vision and robot applications step into a new age. Now, the name “robot” cannot be limited as industrial facility anymore. Instead, more practical robots have been invented including disability robot, which is designed help people who have physical disabilities that impede with daily tasks and haptic interface robots, which allow touch-enabled user interaction with real and virtual environments. Most robots work in a dynamic environment and have to collect surrounding information by using external sensor such as force sensor, visual sensor and so on. In this paper, visual-based feedback control will be utilized on table tennis robot system. The basic idea for the control process is to get the ball information, position and velocity, by two high speed cameras and then use computer to predict the trajectory of the ball and control the movement of the racket. This research will focus on serving the ball.

## 1. SYSTEM CONFIGURATION

In order to complete the action of playing table tennis, three tasks are necessary. These are how to know what direction the ball is will move in, how to predict the hitting position and how to move the robot to hit the ball. Summarizing the requirement, the system should consist of three basic subsystems: vision system, control system and mechanical system. The relationship is just like human’s eye, brain and hand. The mechanism can be expressed in following figure 1.

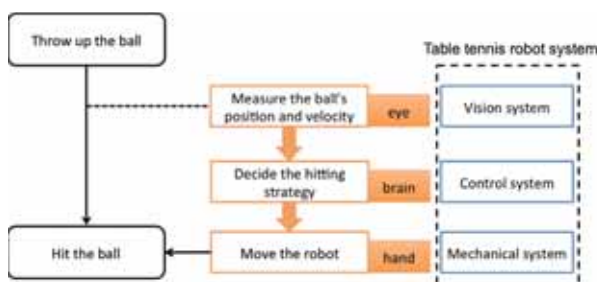


Figure 1: Construction of table tennis system

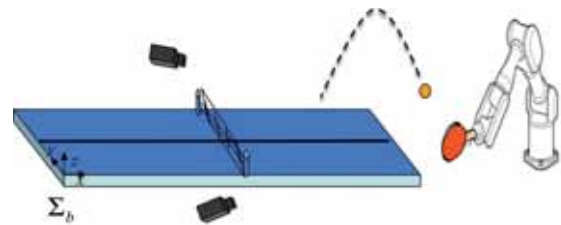


Figure 2: table tennis system

Figure 2 shows the whole system configuration. The origin of the base coordinate is at the left side corner and we throw up the ball behind the table.

### 1.1 VISION SYSTEM

Two cameras are used in our robot system for detecting the position and velocity of the ball. Each camera is put on each side of the table and a 3D space could be built. Those two cameras will detect the color of the ball and this information will be used to calculate the flying trajectory of the ball and predict the position where the arm robot will hit the ball. Therefore, vision system is quite significant since it directly affect the following predicting task and hitting performance.

The ball’s state includes three basic factors: position, translational velocity and rotational velocity. However, the goal of this research is to serve the ball so rotational velocity would not be concerned in the calculation. The speed of the camera we use is 150fps. Too fast camera needs more light resource and huge volumes of data will delay the speed of the program. On the contrary, too slow camera is not enough for predicting the precise hitting position. Thus, 150fps camera is relatively appropriate for the vision system.

### 1.2 CONTROL SYSTEM

Control system has some tasks: (1) Predict the flying trajectory of the ball and decide the hitting position to serve the ball. (2) Determine velocity and angle at hitting moment for the racket. (3) Plan a moving trajectory to abide by the

requirement in 2). (4) Control the robot according to the motion plan in 3). The control process is shown in figure 3.

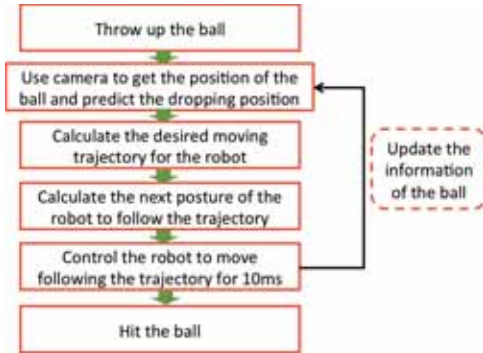


Figure 3: Control process for the racket

After the robot hits the ball, the control system will automatically stop the robot and then move the robot back to original position.

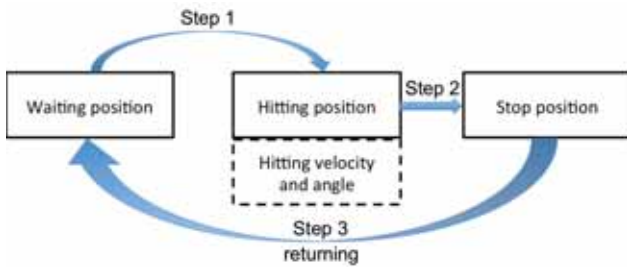


Figure 4: Motion plan

Figure 4 shows the three steps of racket movement. Once the racket hits the ball, it will reduce its velocity within 0.2 seconds. Then the system will calculate a new trajectory to return the robot.

### 1.3 MECHANICAL SYSTEM

Many kinds of table tennis system for previous research have been used in the past. Different structures were invented to realize the manipulator part. In this research, we adopt a 7-DOF robot to serve the Ping-Pong.



Figure 5: 7-DOF robot

## 2. PHYSICAL MODEL

Predicting the ball's motion trajectory is the first essential task for the control system since the robot has to know the hitting position in advance. Necessary physical

models for the table tennis robot system have been well established in previous research [1,2], in which aerodynamic model and racket rebound model will be discussed in this part.

### 2.1 AERODYNAMIC MODEL

Three forces mainly affect the ball's motion in the air: gravity, drag and Magnus force. The following is the equation of motion.

$$\ddot{p} = -g - \frac{1}{2} C_D \pi \frac{\rho}{m} r^2 \|\dot{p}\| \dot{p} + \frac{4}{3} C_M \pi \frac{\rho}{m} r^3 \omega \times \dot{p} \quad (1)$$

$\ddot{p}$ : acceleration,  $g$ : gravity constant,  $C_D$ : drag force coefficient,  $m$ : ball's mass,  $\rho$ : air density,  $\dot{p}$ : ball's velocity,  $r$ : ball's radius,  $C_M$ : magnus force coefficient,  $\omega$ : ball's angular velocity

Because in this research we throw the ball without rotating the ball, Magnus force can be ignored. Then, the equation can be modified as following.

$$\ddot{p} = -g - \frac{1}{2} C_D \pi \frac{\rho}{m} r^2 \|\dot{p}\| \dot{p} \quad (2)$$

Equation (2) can be written in state space form.

$$\begin{cases} \dot{x} = Ax + b_1 + \omega \\ y = C + v \end{cases} \quad (3)$$

where

$$x = \begin{bmatrix} p & \dot{p} \end{bmatrix}^T = \begin{bmatrix} {}^b p_x & {}^b p_y & {}^b p_z & {}^b \dot{p}_x & {}^b \dot{p}_y & {}^b \dot{p}_z \end{bmatrix}^T,$$

$$b_1 = \begin{bmatrix} 0 & 0 & 0 & 0 & 0 & -g \end{bmatrix}^T,$$

$$A = \begin{bmatrix} O_{3 \times 3} & I_3 \\ O_{3 \times 3} & -\frac{1}{2} C_D \pi \frac{\rho}{m} r^2 \|\dot{p}\| I_3 \end{bmatrix},$$

$$C = \begin{bmatrix} I_3 & O_{3 \times 3} \end{bmatrix}$$

Because the state space model is in continuous time system, it could be transferred into discrete time system represented in equation (4).

$$\begin{cases} x_{k+1} = A_d x_k + b_{1d} + \omega \\ y_k = C_D x_k + v \end{cases} \quad (4)$$

### 2.2 RACKET REBOUND MODEL

Figure 6 shows the rebound between the ball and the racket rubber, in which  $(v_b, w_b)$  and  $(v'_b, w'_b)$  represent the translational and rotational velocities of the ball's center before and after hitting.

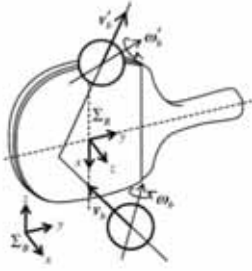


Figure 6: Racket rebound model [3]

When the racket hits the ball, the flying trajectory and direction of the ball will change at the same time. The following equation describes the relationship between before and after hitting.

$$\begin{bmatrix} v_1 - V \\ \omega_1 \end{bmatrix} = R_{RRM}(\alpha, \beta) \begin{bmatrix} v_0 - V \\ \omega_0 \end{bmatrix} \quad (5)$$

where

$$R_{RRM}(\alpha, \beta) = \begin{bmatrix} R_R & 0 \\ 0 & R_R \end{bmatrix} \begin{bmatrix} A_{vv} & A_{v\omega} \\ A_{\omega v} & A_{\omega\omega} \end{bmatrix} \begin{bmatrix} R_R & 0 \\ 0 & R_R \end{bmatrix}^T,$$

$$R_R = \begin{bmatrix} \cos \beta & \sin \beta \sin \alpha & \sin \beta \cos \alpha \\ 0 & \cos \alpha & -\sin \alpha \\ -\sin \beta & \cos \beta \sin \alpha & \cos \beta \cos \alpha \end{bmatrix},$$

$$A_{vv} = \text{diag}(1 - k_v, 1 - k_v, -e_r), \quad A_{v\omega} = k_v r S_{12},$$

$$A_{\omega v} = -k_\omega r S_{12}, \quad A_{\omega\omega} = \text{diag}(1 - k_\omega r^2, 1 - k_\omega r^2, 1),$$

$$S_{12} = \begin{bmatrix} 0 & 1 & 0 \\ -1 & 0 & 0 \\ 0 & 0 & 0 \end{bmatrix}$$

$R_R$  is the transfer matrix from base coordinate to racket coordinate with yaw angle  $\alpha$  and pitch angle  $\beta$ . The parameter  $r = 2 \times 10^{-2}$  (m) is the radius of the ball, and the parameters  $k_v = 6.15 \times 10^{-1}$ ,  $k_\omega = 2.57 \times 10^3$  and  $e_r = 7.3 \times 10^{-1}$  were obtained in previous research [3].

### 3. KALMAN FILTER [4,5]

When cameras track the trajectory of the ball, some noise influence the detection and estimation for on-line control is inevitable. Once the noise affects the camera detecting other object with similar color, it will cause incorrect estimation of hitting position. Therefore, Kalman filter would solve the problem since it uses a series of measurements observed over time and produces estimates that tend to be more precise than those based on a single measurement alone. More formally, Kalman filter operates recursively on streams of noisy input data to produce a statistically optimal estimate of the underlying system state.

State space model (4) is used to calculate the estimation. First, initial condition is set as  $\hat{x}_{0-1} = \bar{x}_0$  and

$P_{0-1} = P_{\bar{x}_0}$ . Then, Kalman gain  $K_k$  can be calculated by the following equation (6).

$$K_k = P_{k|k-1} C_k^T (V_k + C_k P_{k|k-1} C_k^T)^{-1} \quad (6)$$

After getting  $y_k$ , the estimate value  $\hat{x}_k$  and covariance of the estimate error  $P_{k|k}$  can be calculated in formula (7) and (8).

$$\hat{x}_{k|k} = \hat{x}_{k|k-1} + K_k (y_k - C_k \hat{x}_{k|k-1}) \quad (7)$$

$$P_{k|k} = P_{k|k-1} - K_k C_k P_{k|k-1} \quad (8)$$

Then, predicted value  $\hat{x}_{k+1|k}$  and estimate covariance  $P_{k+1|k}$  can be get by equation (9) and (10).

$$\hat{x}_{k+1|k} = A_k \hat{x}_{k|k} + B_k u_k \quad (9)$$

$$P_{k+1|k} = A_k P_{k|k} A_k^T + W_k \quad (10)$$

In (10),  $W_k$  is covariance of the process noise. Using (7), (9) and (6), (8), (10), we can get the following two equations.

$$\hat{x}_{k+1} = A(I - K_k C) \hat{x} + B_k u_k + A K_k y_k \quad (11)$$

$$P_{k+1} = A P_k A^T - A P_k C^T (C P_k C^T + V)^{-1} C P_k A^T + W \quad (12)$$

Because  $P_k$  and  $K_k$  converge very fast, they could be set as constant  $P$  and  $K$ . After solving  $P$  and  $K$ , the estimate value of position and velocity can be got by (11).

### 4. RACKET CONTROL STRATEGY

Although hitting position is predicted by the control system is calculated once the ball is thrown up, the environment will influence the ball's trajectory. Therefore, the method is adopted to update the trajectory of the racket every 1/150 seconds, which is the same with the camera speed.

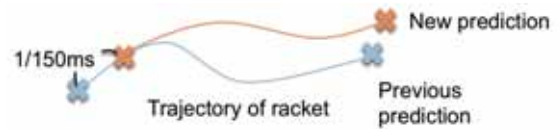


Figure 7: Updating racket trajectory

As shown in figure 7, the trajectory will change a little bit due to the influence from the environment. This method could increase the precision for the racket to hit the ball on its center. Also, in order to make the robot move more smoothly, we take the horizontal plane with the height of hitting position as plane symmetry and move the racket with the similar trajectory as the ball's motion.

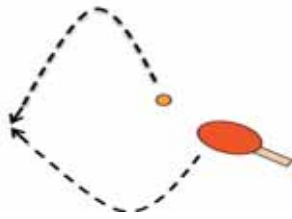


Figure 8: Racket trajectory

Figure 8 shows the racket moves along parabolic trajectory, which is similar with the ball's trajectory.

## 5. EXPERIMENTAL RESULTS

In the experiment, the ball is thrown up by a person who stands behind the table. The ball's position and velocity are measured by two high-speed cameras (150Hz). The following figure (9) and (10) show the position of the ball captured by the camera and the position processed by Kalman filter.

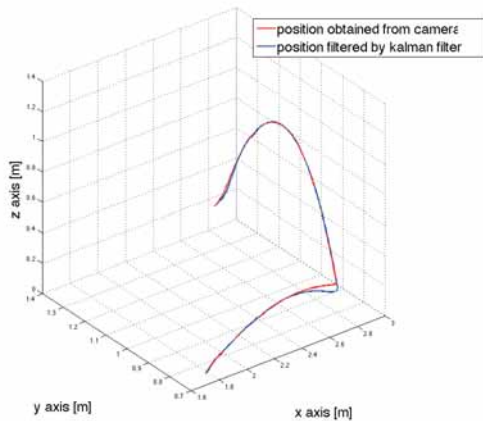


Figure 9: Ball's trajectory in 3D plot

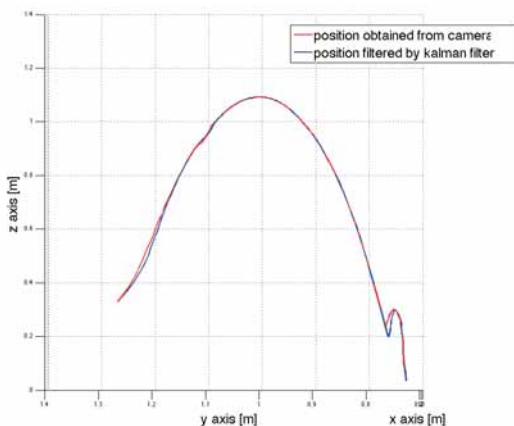


Figure 10: Ball's trajectory in 2D plot

Apparently, the information of the ball's position affected by some noise and the trajectory is not quite smooth. Kalman filter is able to avoid abrupt huge noise effect and control the information used in the program close to the ball's real trajectory.

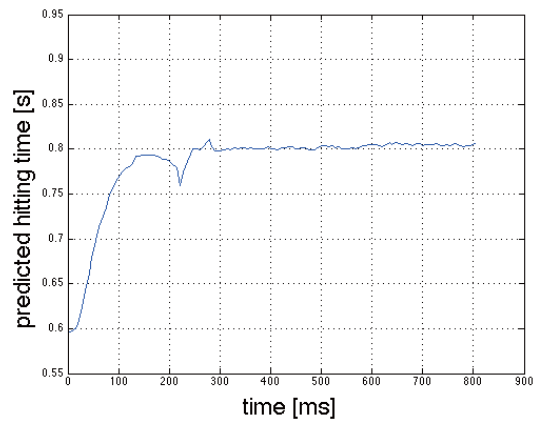


Figure 11: Predicted hitting time

As can be seen in figure 11, when the ball is thrown up, the predicted hitting time is ambiguous and during the flying there exists an obvious error. However, the system converges to correct value, around 0.8 seconds, quickly.

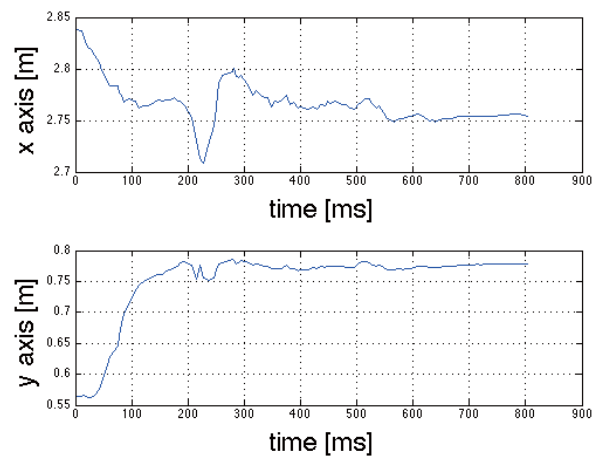


Figure 12: Predicted hitting position for x-axis and y-axis

From figure 12, it can be evaluated that the final hitting position is around (2.75, 0.78, 0.03), which is in robot coordinate. When the ball is flying in the air, the error occurs about 220ms for x-axis and y-axis. If there were no recursive calculation, the deviation would be more serious.

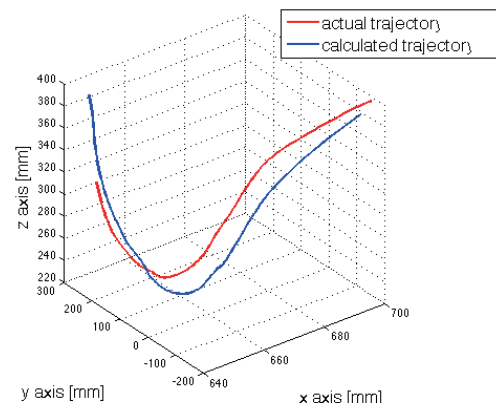


Figure 13: Racket moving trajectory in 3D plot

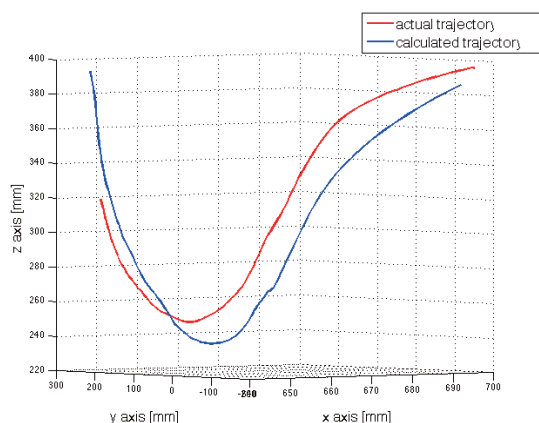


Figure 14: Racket moving trajectory in 2D plot

Finally, the most important part is to control the racket to hit the ball. In figure 13 and 14, the red line is the actual trajectory of the racket motion and the blue line is the desired moving trajectory calculated by the program. Apparently, blue line is always faster than red line, which means the robot has some signal delays. The designed hitting position is at (644, 253, 394); however, due to delay factor, the robot hits the ball at (643, 223, 320). Because the unit of the position is millimeter, the error is usually less than 3cm for most tests for x- and y-axis.

The experimental results above have almost the same trajectory as designed parabolic trajectory and the table tennis system is able to serve the ball to the other side of the table successfully. The hitting performance is correlated to several process variables including: the velocity of the ball, the position of the hitting position, the detection power of the camera, and inherent signal delay. Changes in these conditions will result in variation in the racket control. For the test discussed in this part, the ball is thrown up to the middle area of the table, which is the best area for the racket to hit the ball. For other test, even though the noise would affect the racket control, the robot could still follow the parabolic trajectory roughly and serve the ball. These results clearly indicate the ability of this new control strategy to optimize the hitting performance of typical method.

## 6. SUMMARY

This research has illustrated, and demonstrated the application, of table tennis system using 7-DOF robot. The key enablers were the precise predicted hitting position and time. The system used recursive calculation of Kalman filter algorithm to eliminate inevitable noise to enable very precise estimation. With effectiveness of the combination of prediction and control part, the robot could successfully serve the ball within a large area. However, for some special cases including that the ball is too close to the robot or too back from the table, which makes the robot does not have enough space to swing the racket and the ball could not be stroked to the other side. The major challenge is providing affordable program to control the racket. In some situations,

once the detection of the ball makes mistake, the posture of the robot would be weird and stop automatically. However, after modifying the program by using Cartesian coordinate to control the robot instead of joint space coordinate, the speed of the program gets great improvement; the calculation cycle is much less than 6.67ms, which is the speed of the camera. Therefore, the program is able to optimize the racket control once the noise influence occurs.

On-line control, especially visual feedback control, is not an easy task because of high demand for signal processing speed. The results from this research prove the feasibility of high-speed control for table tennis robot system.

## ACKNOWLEDGEMENTS

I am grateful for the guidance and assistance of this work provided by Prof. Hayakawa and Itoh Satoshi. Additionally, I would like to acknowledge the contribution and support of JUECEP office.

## REFERENCE

- [1] A. Nakashima, Y. Ogawa, Y. Kobayashi, and Y. Hayakawa: Modeling of rebound phenomenon of a rigid ball with friction and elastic effects, Shakouchi, T., Tsujimoto, K., Proc. of IEEE American Control Conference, pp. 1410–1415, 2010.
- [2] A. Nakashima, Y. Ogawa, C. Liu, and Y. Hayakawa: Robotic table tennis based on physical models of aerodynamics and rebounds, Proc. of the 2011 IEEE International Conference on Robotics and Biomimetics, pp. 2348–2354, 2011.
- [3] C. Liu, Y. Hayakawa, and A. Nakashima: Racket Control for a Table Tennis Robot to Return a Ball. SICE Journal of Control, Measurement, and System Integration, Vol. 4, No. 1, pp. 001–008, January 2011
- [4] 谷萩 隆嗣 : 「カルマンフィルタと適応信号処理」 コロナ社, 2005
- [5] 西山 清 : 「知識ベース」 電子情報通信学会, 1群-5 編-6章, 2009

# AUTOMATED STEERING SYSTEM FOR OBSTACLE AVOIDANCE BASED ON POTENTIAL FIELD METHOD

Yan Zhang

Department of Mechanical Engineering, College of Engineering, University of Michigan  
zhangyme@umich.edu

Supervisor: Professor Tatsuya Suzuki

Graduate School of Engineering, Nagoya University  
t\_suzuki@nuem.nagoya-u.ac.jp

## ABSTRACT

The main purpose of this research project is to utilize the Potential Field Method [1] and apply it in constructing an automated steering system for obstacle avoidance on a small electrical vehicle (COMS). A predetermined potential field representing a narrow road consisting of an obstacle in the middle and walls on both sides is used in the experiment. The reference path for the control program is calculated based on the potential field gradient. Based on the reference path and look-ahead point, distance and angle deviations are calculated and used as the inputs of control for the steering. The look-ahead distance and controller gains are tuned in the experiment so that the vehicle can follow the path in a smooth way.

## INTRODUCTION

Automated driving and steering assist systems are being studying in various institutes and automotive industry. With electrical power steering becomes popular nowadays, it provides an opportunity for automated steering or steering assist system to be implemented on modern vehicles. As a form of steering assist, Lane Keeping Assist system has already being offered on some luxurious vehicle to help keep the vehicle from drifting out of its lane. In such system, only small steering angle is needed to keep the vehicle in lane and out of danger. However, to avoid a sudden obstacle appears in front of a vehicle, large and quick maneuver is required. The automated steering system is aim to help the driver to avoid the collision with obstacle under this situation.

Only low speed experiments are done in this research to ensure safety because the control program is still in development. In the experiment, a small electric vehicle (COMS) is used. Digital encoders on rear wheels of COMS provide the position and yaw angle of the vehicle. Potentiometer on the steering column measures the steering angle. The tire angle is calculated by dividing the steering angle by the steering ratio. The main control program of

COMS has already been developed and works in hybrid with the automated steering control program developed in this research project.

## CONTROL ARCHITECTURE

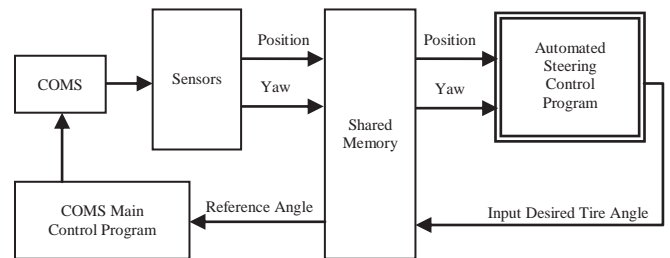


Figure 1: automated steering system block diagram

Figure 1 shows the information flow of the automated steering system control program. At first, the sensors provide the position and yaw angle information of the vehicle which is stored in the onboard memory shared by both the main control program and automated steering control program (double-lined box). Then, the automated steering control program reads the position and yaw angle from the shared memory, and calculates the desired tire angle from the reference path and potential gradient. The desired tire angle is then sent back to the shared memory as a reference for the main control program. Finally, the main control program drives the steering motor to the desire angle. This process is repeated every 0.02 second, meaning that the steering angle is updated in each time step.

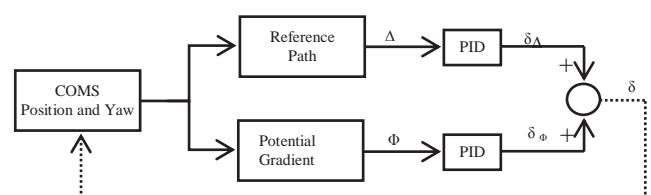


Figure 2: automated steering control program block diagram

The detail of automated steering control program (double-lined box in figure 1) is shown in figure 2. At first, a reference path (figure 3) is generated according to the given potential field of the driving environment shown in figure 4. The high potential on both side of the vehicle path represents the walls on the sides of a narrow street. The bump in the middle represents an obstacle in front. According to the potential field method, the heading direction of the vehicle should always point to the low potential at every time step. The reference path is then calculated as follows:

Given the potential function:

$$(x, y) \quad (1)$$

The heading direction vector of the vehicle at time  $t$  is:

$$[v_{x_t}, v_{y_t}]^T = -\nabla U(x_t, y_t) = \left[ \frac{\partial U(x, y)}{\partial x}, \frac{\partial U(x, y)}{\partial y} \right]_{x=x_t, y=y_t}^T \quad (2)$$

The vehicle location at time  $t+1$  is then:

$$x_{t+1} = x_t + d \cos \left( \tan^{-1} \left( \frac{v_{y_t}}{v_{x_t}} \right) \right) \quad (3)$$

$$y_{t+1} = y_t + d \sin \left( \tan^{-1} \left( \frac{v_{y_t}}{v_{x_t}} \right) \right) \quad (4)$$

, where  $d$  is a small distance interval.

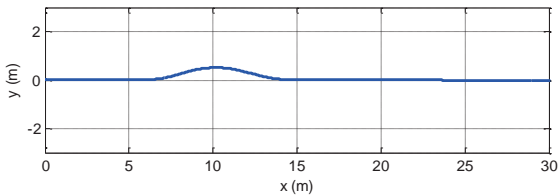


Figure 3: reference path calculated from potential field

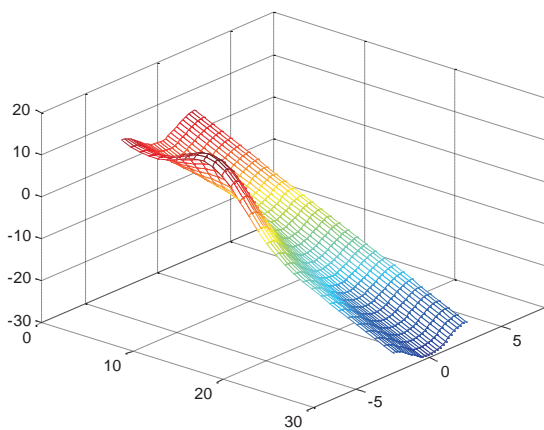


Figure 4: potential field of the driving environment

The steering angle (tire angle) is computed by the look-ahead observation (figure 5) and PID control. The look-ahead point, generated according to the vehicle speed, is a prediction of the vehicle position based on the current steering angle. The angle deviation ( $\Phi$ ) is the difference between the vehicle yaw angle and the potential gradient direction. The distance deviation ( $\Delta$ ) is the shortest distance from the look-ahead point to the reference path. The angle deviation and distance deviation are measured at each time step and sent to PID controllers as shown in figure 2. The steering angle is calculated by multiplying different gain values to the derivatives, integrals of  $\Delta$  and  $\Phi$  and to themselves, and then summing all up. First order backward difference quotient and trapezoidal rule are used to calculate derivatives and integrals in the program. The parameters of the PID controller gains are tuned in the experiment to let the vehicle follow a smooth path.

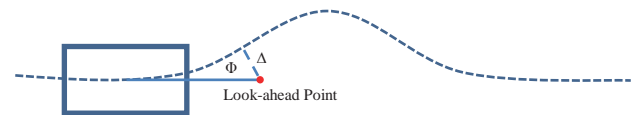


Figure 5: look-ahead observation

## SIMULATION

A simulation model is constructed in MATLAB (figure 6) to simulate the vehicle reaction to the steering input from the automated steering program. The linear bicycle model in a state space form [2] is used in the simulation, which simplifies the vehicle dynamics to only three degrees of freedom: longitudinal, lateral and yaw. The steering model is based on the actual response of the steering system on COMS (figure 7). A transportation delay and a second order delay are used in the steering model in the simulation. The look-ahead observation is not included in the simulation, so that the effect of steering delay can be studied.

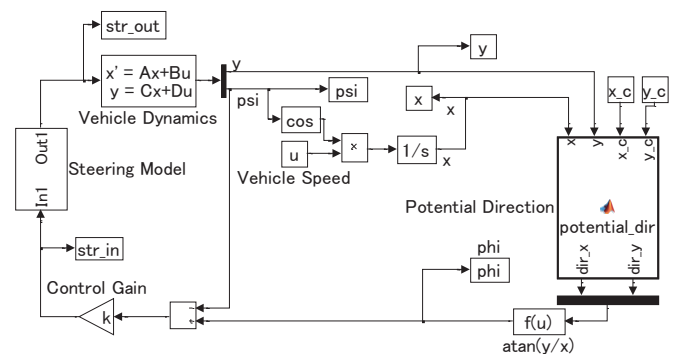


Figure 6: simulation model constructed in MATLAB

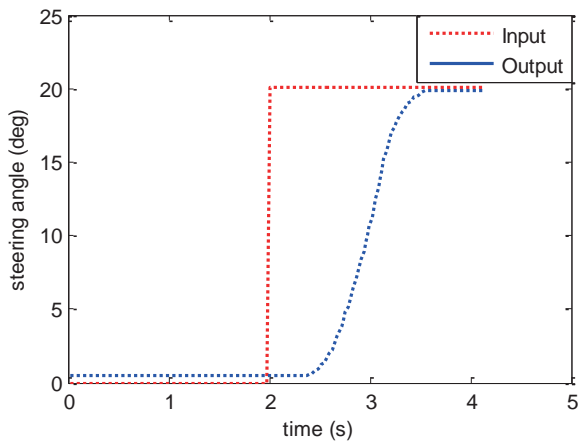


Figure 7: COMS steering system step response

Figure 7 shows the steering system response measured by a step input test inside the lab. A step input of 20 degrees is applied at time two seconds. As shown in the figure, the delay time of the steering system before it reaches to the final value is approximately 1.6 seconds. A transportation delay is also shown at the first 0.4 second when the input is applied. The simulation shows that these delays will lead to instability shown in the next few plots.

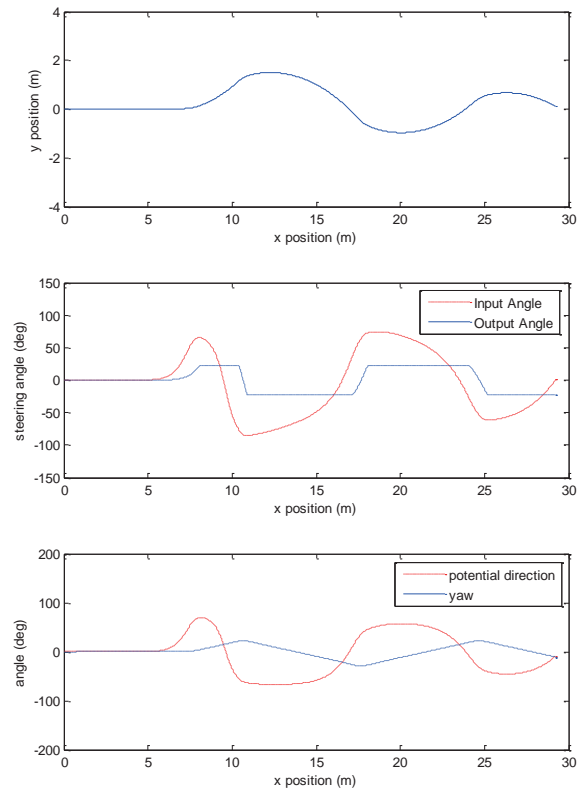


Figure 9: simulation result for medium speed (2 m/s)

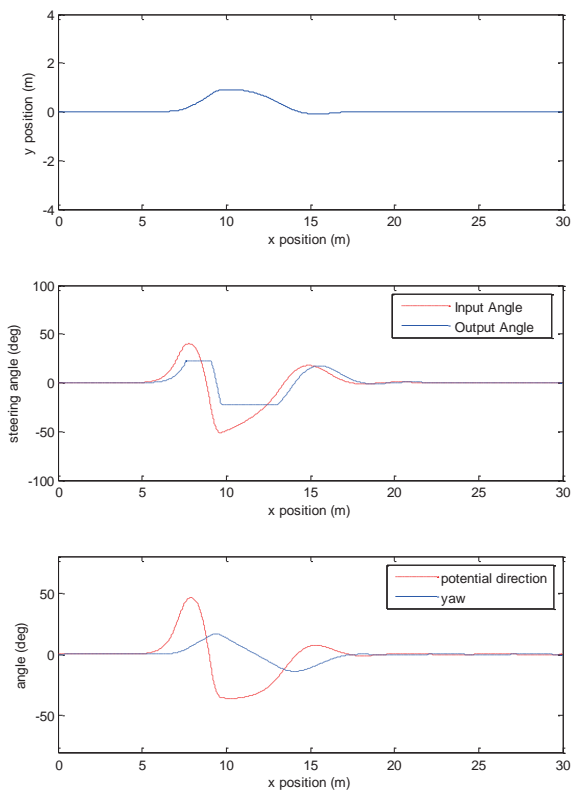


Figure 8: simulation result for low speed (1 m/s)

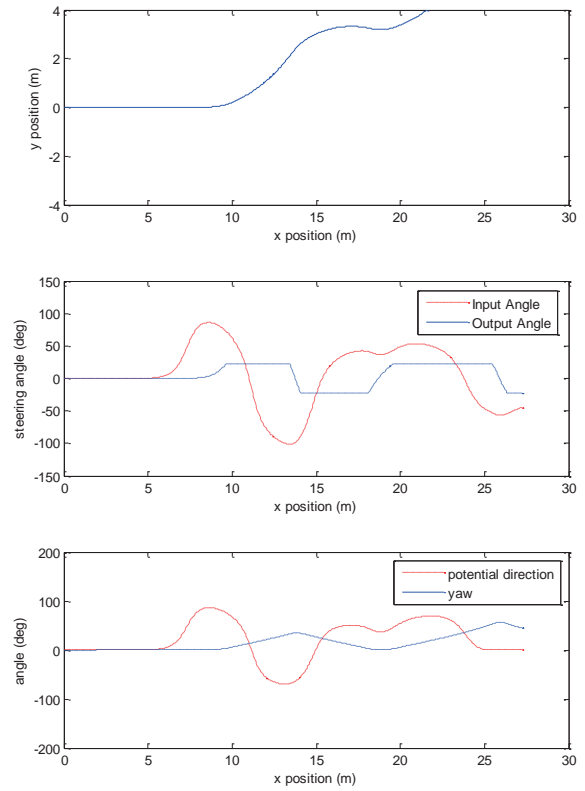


Figure 10: simulation result for high speed (4 m/s)

Figure 8, 9 and 10 show the simulation results of the vehicle behavior at low, medium and high speed separately. At low speed (figure 8), the vehicle can follow the desired path with a slight oscillation at the end. The steering delay does not affect the path tracking because there is enough time at low speed for the steering system to react to the input command. However, at medium speed (figure 9), the vehicle starts to oscillate severely around the reference path due to steering output lagging behind the input by a large amount. At even higher speed (figure 10), the vehicle becomes completely unstable and goes away from the reference path.

## EXPERIMENT

In the experiments, the testing speed is not as fast as the practical driving speed so that safety can be ensured. However, the results give a good indication of how the steering delay will affect the path tracking at different speeds and why look-ahead observation is required for controlling the vehicle.

At first, look-ahead point is not used so that the results can be compared with the simulation results. Figure 11, 12 and 13 are the experiment results for three different speeds. In these experiments, the tire reference angle is simply set to the angle deviation  $\Phi$  between COMS yaw angle and potential gradient angle. When comparing these results to the simulation results, the actual response of the vehicle agrees with the simulation results very closely.

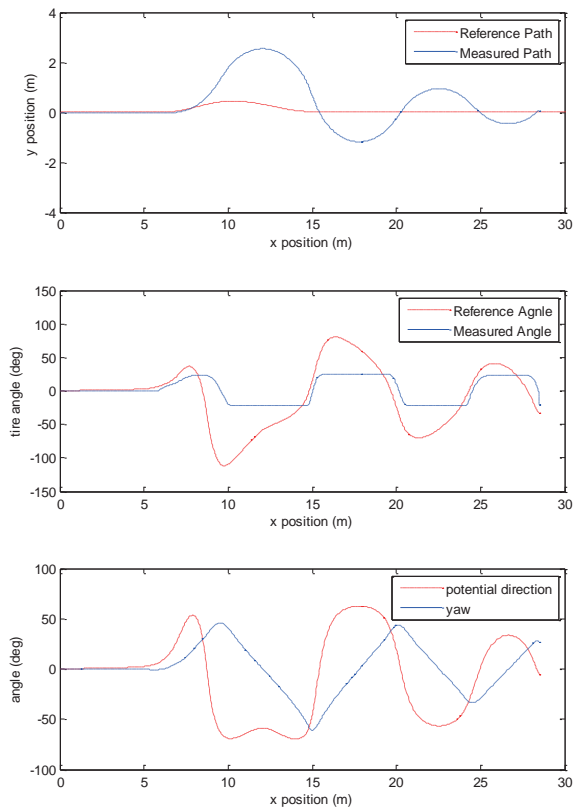


Figure 12: experiment result at medium speed (1 m/s)

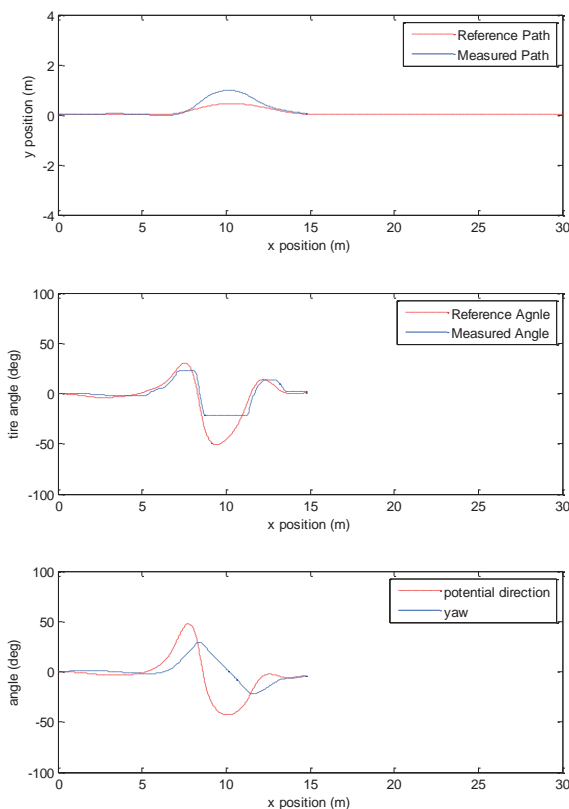


Figure 11: experiment result at low speed (0.5 m/s)

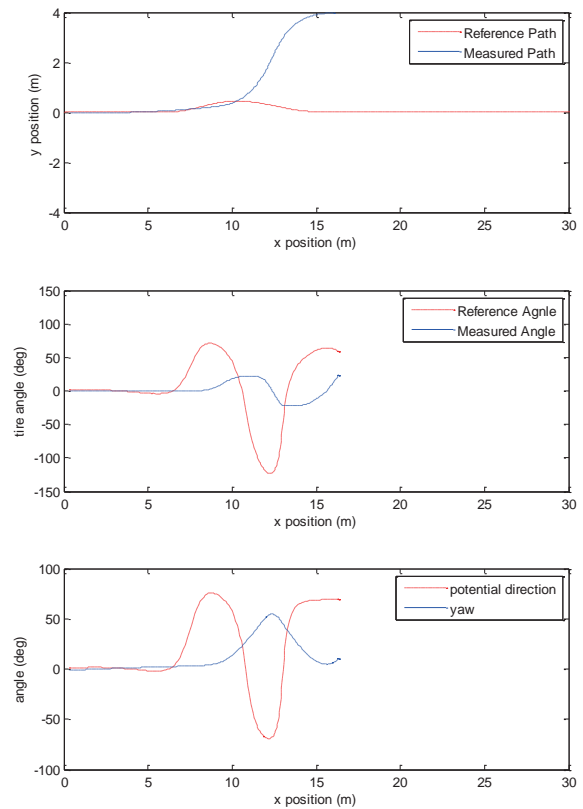


Figure 13: experiment result at high speed (3 m/s)

Since both the simulation and testing show that the vehicle cannot follow the reference very well without look-ahead control, then the program is tested again with look-ahead to compensate the steering delay. Only proportional control is used in the experiments at this time. The equation for the input tire reference angle is:

$$\delta = K * \Delta \quad (5)$$

Different look-ahead distances (L) and proportional gains (K) are chosen to in the tests to find the optimum values. Because the look-ahead distance is highly dependent on the vehicle speed, the tests are done with a constant speed of 1 m/s (3.6 km/h). The following figures show the experiment results with corresponding look-ahead distances and control gains. As shown in figure 16, when the control gain is equal to 0.4 and look-ahead distance is 3.35 m, COMS can track the reference path very accurately with only slightly oscillation at the end which needs more fine-tunes to eliminate.

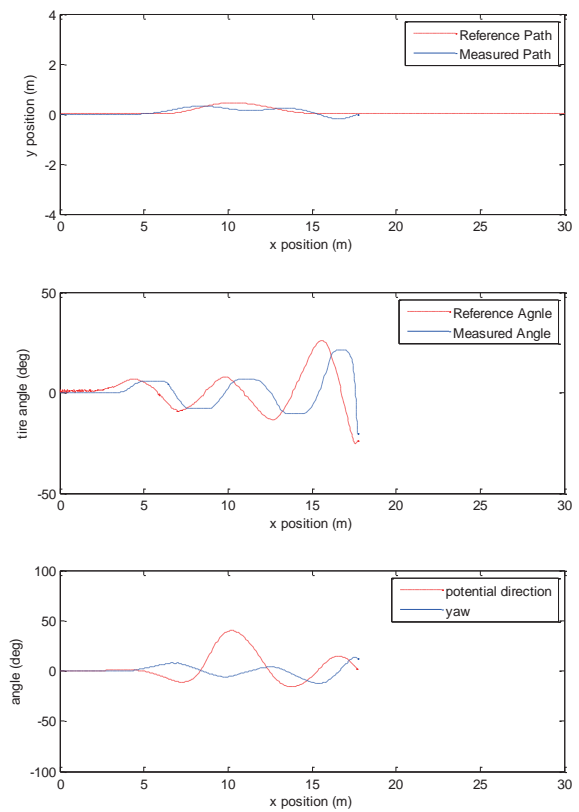


Figure 15: experiment result with K = 0.5, L = 4

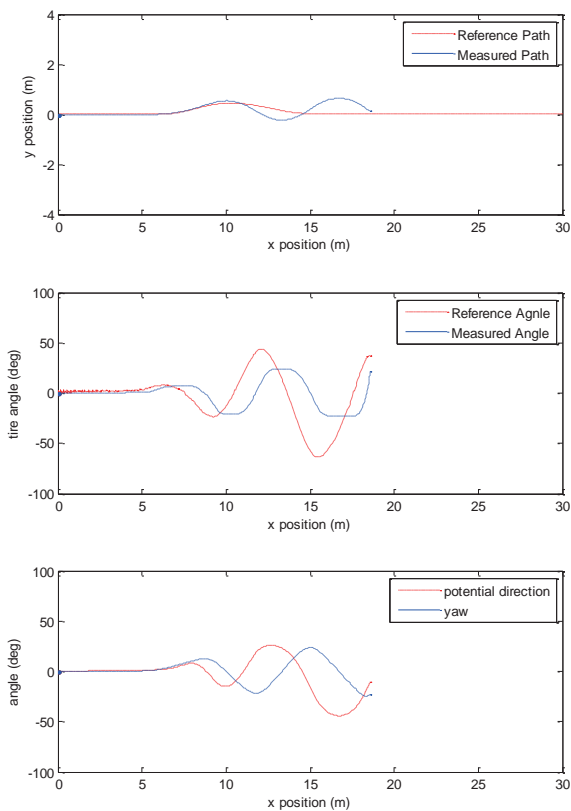


Figure 14: experiment result with K = 1, L = 2

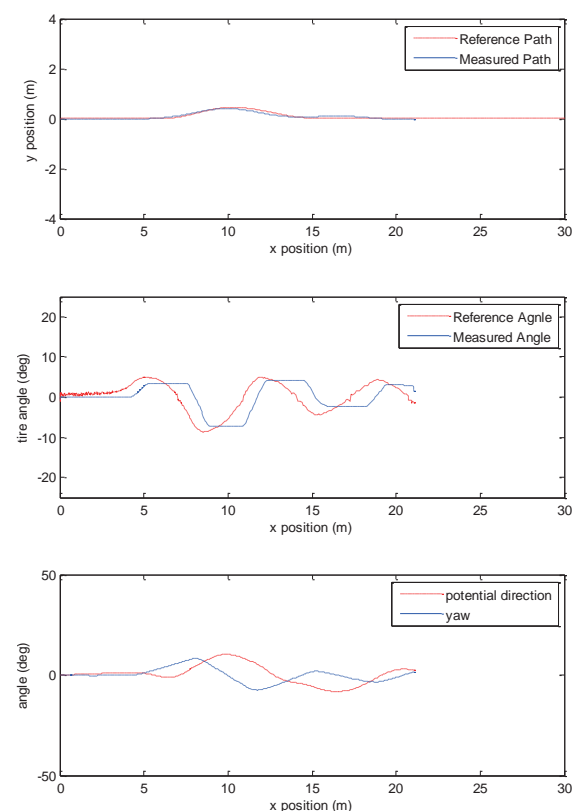


Figure 16: experiment result with K = 0.4, L = 3.35

## DISCUSSION

The main difficulty of controlling the vehicle to follow a desired path in this research project comes from the delay to steering. Possible reasons for the delay are: backlash of the gears inside the steering system, communication delay between the steering control program and the main control program, or steering motor controller delay.

The look-ahead observation is used to solve the problem of steering delay by predicting the steering angle required ahead of time. This method requires knowing exactly where the correct look-ahead point is. However, since the look-ahead point is also dependent on the speed of the vehicle, testing of different look-ahead points at various speeds is very important. Unfortunately, not enough testing has been done currently to find out a relationship between the vehicle speed and the correct look-ahead point. Thus the next step of this research is to experiment with different look-ahead points subject to different speeds.

Although the main structure of the automated steering control has been built, the program is still far away from being finished. The PID control gains are also not decided and should be tested for the optimum values. The relationship between the vehicle speed and control gains is unknown and requires more testing to find out.

The MATLAB model used in the research gives a relatively accurate result comparing to the actual testing result. The simulation can be used to test new control strategy for optimization of the path tracking. However, since the linear bicycle vehicle dynamics model is only valid at low speed, when moving to a higher speed, nonlinear model without more degrees of freedom will give a better prediction.

The vehicle speed is kept constant in the simulations and experiments. However, when the vehicle is traveling at high speed, sudden maneuver is very likely to make the vehicle completely losing control. Slowing down by applying braking before steering will help in such situations. Thus, automatic braking can also be considered in future development of the control program. Implementing vehicle stability control (VSC) to work in conjunction with the automated steering control program is also recommended at high speed.

## CONCLUSION

In the research project about the automated steering control, the theory of potential method has been implemented in constructing the reference path and tested in the control program. The program now has a basic structure and can work in parallel with the main control program on COMS. During experiments, problem caused by the steering delay has been found. Although the look-ahead observation is suggested to solve this problem, more testing and data are required for it to fully work, which should be the next step of this research project.

## REFERENCES

- [1] Noriyasu Noto, Hiroyuki Okuda, Yuichi Tazaki and Tatsuya Suzuki, Steering Assisting System for Obstacle Avoidance Based on Personalized Potential Field, 2012 15<sup>th</sup> International IEEE Conference on Intelligent Transportation Systems, Anchorage, Alaska, USA, September 16-19, 2012.
- [2] Hwei Peng, Handling of Ground Vehicles, lecture notes distributed in ME 542 Vehicle Dynamics at University of Michigan, winter 2013.

# BONE ANALOG MATERIAL FOR ORTHOPEDIC SURGICAL TRAINING

Yihao Zheng

Department of Mechanical Engineering, Graduate School of, University of Michigan  
yhzheng@umich.edu

Noritsugu Umehara

Graduate School of Engineering, Nagoya University  
ume@mech.nagoya-u.ac.jp

## ABSTRACT

In order to better fit the requirements of bone analogs for orthopaedic surgical training, in this study, 3D printed plaster soaked with epoxy was proposed as a novel type of material to simulate the human cortical bone. The validation of this bone mimicking material was carried out from the following three perspectives: mechanical properties, thermal conductivity, and machining responses. In this report, the comparisons between proposed material and bovine bone specimens with respect to the mechanical properties including hardness and friction coefficient were elaborated. The thermal and machining tests are ongoing in University of Michigan, and the experimental setups were demonstrated. Though regarding to friction coefficient, the proposed material manifested the similarity with bovine bone, its hardness was estimated to be less than half of the bone hardness. Problems were analyzed and future efforts were discussed.

## 1. INTRODUCTION

Many orthopedic surgeries involve cutting operations on bones including drilling, reaming, tapping, sawing, and milling which demand a high degree of precision regarding not only to the geometry and location of the cutting result, but also to the process that requires accurately controlled temperature and force. In most cases, these eminently precise operations rely on the surgeons' skills and experience which can only be obtained through repetitiously effective trainings and practices. Therefore, efficacious bone simulators for the orthopedic surgery training are highly demanded.

### 1.1 CURRENT BONE ANALOGS

The human cadaveric bone is one of the common choices for orthopedic surgical trainings. However, it is normally underprovided and very expensive; the properties of cadaveric specimens can vary largely due to age brackets, diseases, lifestyles and so on. And the storage and antiepidemic of human cadaver can also cause troubles. The bovine bone, although readily available, is also variable in

nature and different from human bone in lots of aspects including geometry, density, and hardness.

There are several synthetic bone simulator products in the market. Sawbones, one of the largest manufacturers of orthopedic models, makes bone models by molding the polyurethane foams into specific shapes. Similarly, some other companies chose to mold polymers such as Acetal copolymers, delrin, and UHMWPE. These products can offer precise geometric features, whereas their hardness, density, and melting point are too low to render any verisimilar experiences when the users practice surgical cutting operations on them. BoneSim™ 1800 series bone analog from BoneSim™ paid a special attention on the simulation of mechanical properties (hardness, density, and compressive strength) and the cutting tool interaction (screw insertion torque, and drilling toughness), however this product is typically offered in a shape of disk, thus failing to provide any geometric characters of bones, although customized molding is available. The cost of BoneSim™ 1800 is relatively high partially because the product is produced from the cortices of long bones from USDA approved cattle

To sum up, for orthopedic surgical trainings, few existing bone analogs simultaneously attend to both the geometric features and the mechanical machining properties. Accurate geometric features assist surgeons to practice cutting at proper positions; mechanical and machining properties that resemble the bones, render the surgeons verisimilar haptic feedbacks during the practices, which helps surgeons to accumulate experience upon which they rely to control the force and temperature during bone cutting operations.

### 1.2 3D PRINTING PLASTER SOAKED WITH EPOXY

In this study, 3D printed plaster soaked with epoxy was proposed as a novel type of material to simulate the human cortical bone. The 3D printing or additive manufacturing technology has been extensively applied in the industry for its capacity to achieve complex structures with relatively less time and cost. Various shapes of bone can be readily created at high accuracy by binding plaster powder layer by

layer. Epoxy, to some extent, has the mechanical and machining properties similar to the bone, and is subject to the adjustment of some properties by changing the ways of preparation, so is chosen to strengthen the printed plaster parts. Remarkably, via combining the flexibility of the 3D printing and the specialties of plaster and epoxy, both main aspects of bone features: shape and mechanical machining properties can be intentionally simulated.

The validation of the analog performance of the proposed bone mimicking material was conducted by the comparison between the bovine bone specimens and prepared treated plaster samples with regarding to three perspectives: mechanical properties including the hardness and friction coefficient, thermal conductivity, and machining responses.

### 1.3 COLLABORATION PROJECT

This project is under a close collaboration between the University of Michigan (UM) and the Nagoya University (NU), via the JUACEP program. Fumitake Nonoyama, first year Master student from the Umehara Laboratory of NU, is currently working in the S. M. Wu Manufacturing Research Center in UM as one of the participants of JUACEP, focusing on the machining property part. The thermal conductivity is tested by Rui Zhou, a visiting student from China in UM. Yihao Zheng, the author of the report, first year Master student of UM attending the JUACEP, formulated the material preparation procedures and finished the mechanical properties measurements in the past three months in the Umehara Laboratory at NU.

The following part of the report will first elaborate the sample preparation procedures, and then mainly present the test methods and results of mechanical properties, hardness and friction coefficient respectively. Experiment setups for thermal and machining tests in UM will also be briefly introduced.

## 2. SAMPLES PREPARATION

Four types of samples were prepared for tests: two types of bone mimicking material (distinguished for the treatment of two epoxy products) and two types of bovine femur samples (different in cutting directions). In this section, the preparation procedures of proposed material, as well as the bone specimens are specified. And the consistent surface polishing methods for all samples, ensuring the rationality of comparison of test results, are documented.

### 2.1 EPOXY TREATED PLASTER SAMPLE PREPARATION

#### 2.1.1 Plaster 3D Printing

Printed plaster disks ( $\Phi$  50mm  $\times$  5 mm) were fabricated by Spectrum Z1M510 printer using zp<sup>®</sup>150 powder from 3D Systems.

#### 2.1.2 Epoxy Treatment

In this study, two types of epoxy, RBC-3200/AB-312, and AeroMarine 300/21, were selected to strengthen the

printed plaster samples, because of their relatively lower viscosity, longer pot life, and higher hardness as shown in Table 1. Those properties ensure epoxy can soak into plaster easily and thoroughly, and the treated plaster material is more similar to the bone.

Table 1  
Properties of Selected Epoxy Products

Property \ Epoxy	RBC-3200/AB-312	AeroMarine 300/21
Viscosity (cps)	300	600
Pot life (hrs)	3	0.5
Hardness (Shore D)	90	85

Following steps were conducted in the epoxy strengthening process:

a. Epoxy preparation.

Epoxy products typically consist of two parts, resin and hardener, which are separately stored and supposed to be mixed together in a designed ratio in application. Abiding by the mix ratio of the epoxy product, resin and hardener were mixed in a glass beaker by stirring smoothly (to avoid generating air bubbles) for two minutes. Then the mixed epoxy was poured into another beaker for another two-minute stir, eliminating the negative effect of the liquids clinging to the sides and bottom of the beaker.

b. Soaking

Considering the porous structure of the printed plaster parts, the vacuum chamber was adopted to assist epoxy to fill the tiny clearances of the printed plaster samples, so that a thorough soaking process can be achieved. Vacuum pressure and time were settled as technical rules of this soaking process according to the pot life of the specific type of epoxy, as well as the printed sample geometry, which is shown in Table 2.

Table 2  
Vacuum Conditions of Epoxy Soaking Process

Condition \ Epoxy	RBC-3200/AB-312	AeroMarine 300/21
Pressure (kPa)	-90	-90
Time (minute)	60	25
Sample thickness (mm)	5	5

Printed plaster disks were put into the beaker containing the well-mixed epoxy. Then the beaker was put into a vacuum chamber applying the conditions mentioned above.

c. Cure

After the soaking process, the plaster disks impregnated with epoxy were taken out of the epoxy and the surface residual epoxy were wiped by tissue paper to maintain the original part dimension. The epoxy preserved in the plaster tends to seep and drip out because of the gravity, so the sample was grilled under an infrared heater at 80°C for 30 minutes to speed up the surface epoxy cure process, and rolled over frequently to avoid the effect of gravity. The sample was flipped over every 20 seconds for the first 10 minutes and every 2 minutes for the following 20 minutes. After that a shell of cured epoxy was formed to

maintain the inner epoxy which will take another time period (5.5 hrs for RBC-3200/AB-312 at 60°C, 24 hrs for AeroMarine 300/21 at room temperature) to cure completely.

## 2.2 BONE SAMPLE PREPARATION

Several fresh bone segments of the mid-shaft section of bovine femur were cut longitudinally into half cylinder pieces preserving the outer cylindrical surface of the bone on one side which was grinded and polished to get a flat surface for tests, called lengthwise bone sample. Considering the anisotropic property of bone, another type of bone samples called radial bone samples were processed by cutting the mid-shaft sections of bovine femur transversely to get bone ring pieces which were then grinded and polished. All the tests on bone samples were conducted within 6 hours after preparations, ensuring the bone samples were fresh enough to represent the properties in living condition.

## 2.3 SURFACE POLISHING

All samples including two types of epoxy treated printed plaster disks and two types of bovine femur pieces followed the same surface polishing procedures, so that the friction tests' results are independent from the sample surface conditions. Test surfaces of the samples were polished on a lapping machine using a series of sandpapers: 800, 1500, 2500, and 3000 grit, then washed in ultrasonic bath, rinsed by distilled water and dried by tissue papers and the air blower.

## 3. HARDNESS TEST

Regarding to the epoxy soaking effect, from the micro perspective, epoxy fills the tiny clearances of bound plaster powders, which indicates, epoxy and plaster, though mixed, are mutually independent, maintaining their own properties. It is the integrated performance of the material that is utilized to simulate the bone. Therefore, micro scale hardness testers are not applicable for this material. Shore durometer and Rockwell tester were selected to measure the hardness.

### 3.1 SHORE DUROMETER

Shore durometer is typically used as a measure of hardness in polymers, elastomers, and rubbers. The durometers of bone has been extensively tested and reported as Shore D 85-95, and the durometer of cured epoxy is typically included in the data sheet of product. The durometer of cured RBC-3200/AB-312 is estimated at Shore D 90, and AeroMarine 300/21's is Shore D 80-95, which makes it promising for plaster with epoxy material to achieve the hardness similar to bone in Shore D scale. However, Shore durometer indicates a rough estimation of hardness. It is less accurate, comparing with some other hardness test methods, like Rockwell test.

## 3.2 ROCKWELL SUPERFICIAL HARDNESS TEST

The Rockwell test determines the hardness by measuring the depth of penetration of an indenter under a large load compared to the penetration made by a preload [1]. Rockwell superficial 15-T scale adopts 1/16-inch-diameter (1.588 mm) steel sphere as the indenter and a total load of 15 kgf.

### 3.2.1 Bone Sample Hardness

Hardness tests were performed on radial bone samples and lengthwise bone samples respectively, though the results turned out to be approximately uniform. Radial bone samples have a mean hardness of 64.3 HR 15-T with a standard deviation(STD) of 7.0, except for the part where the blood vessel went into the bone as marked in a red circle in Fig. 1. The marked part consisted of relatively spongy structure, and therefore had a lower hardness of 41.3 HR 15-T with a standard deviation of 5.5. Almost the same hardness distribution can be observed on the lengthwise bone samples. The mean value of compact part hardness was estimated at 63.1 HR 15-T (STD: 1.5), while for the spongy part connecting with the vessel as marked with blue line in Fig. 1 (b), the mean hardness was 55.0 HR 15-T (STD: 2.2).

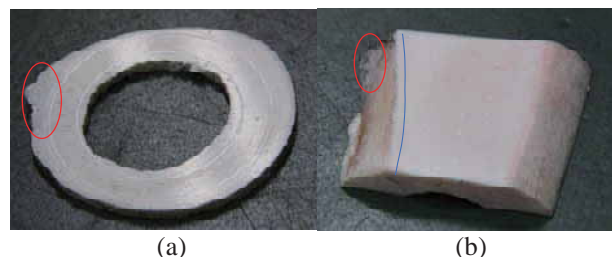


Fig. 1 Hardness test bone samples. (a) Radial bone sample. (b) Lengthwise bone sample. The red circle indicates the part where blood vessel went in to the bone. Indentations in red circle in (a) and along the blue curve in (b) gave lower hardness values, for the relatively spongy structure.

### 3.2.2 Plaster with Epoxy Sample Hardness

The results of both types of plaster with epoxy samples turned out to be undesirable. For RBC-3200/AB-312 epoxy treated plaster sample (RBC plaster sample), the mean hardness was 31.1 HR 15-T (STD: 3.3). However, AeroMarine 300/21 epoxy treated plaster sample (AM plaster sample) was too soft to gain any applicable hardness values on the Rockwell superficial 15-T scale which is an appropriate standard scale for soft material among Rockwell test scales.

To sum up, the RBC plaster sample's hardness in HR 15-T scale was found to be half of that of bovine compact bone, while the AM plaster was proved to be too soft to mimic the bone. The RBC plaster, though also softer than expected, still stood some chance to simulate the bone in

friction coefficient and thermal, machining properties. Albeit, the AM plaster was decided to be abandoned. The main reason for its weakness was its pot life, 30 minutes, during which, epoxy can hardly soak thoroughly into plaster. The negative effect of deficient soaking was actually noticed during the surface polishing process. By following the same polishing procedures, AM plaster can not achieve the same smooth surface as RBC plaster, because some tiny plaster powders without wrapping with cured epoxy dropped as a whole during polishing, leaving pitting on the surface.

## 4. FRICTION TEST

### 4.1 SETUP

A friction wear tester with a pin-on-disk apparatus was carried out as shown in Fig. 2 to measure the friction coefficient between steel and prepared samples (bovine femur, and epoxy treated plaster). Tests were performed on steel/epoxy treated plaster sample, steel/bovine femur piece tribopair. Polished 8mm diameter AISI 52 100 steel balls with the surface roughness of  $R_z$  30 nm were used as pins. The epoxy treated plaster plates and the bovine bone pieces were mounted as disks.

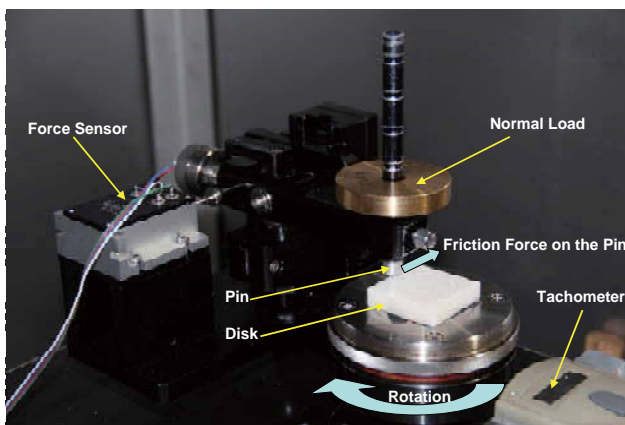


Fig. 2 Friction Wear Tester with a Pin-on-disk Apparatus.

## 4.2 Methods

### 4.2.1 Sliding Speed

In orthopedics surgeries, medical bone drill bits typically have diameters ranging from 0.5mm to several millimeters [2], and the rotational speed is commonly around 1000 r/min. So the drilling surface linear speed typically ranges from 50mm/s to 200mm/s. The friction test sliding speed was selected at 100mm/s accordingly.

### 4.2.2 Normal Load

The thrust force applied when drilling on the cortical bone was mentioned in several historical researches about bone drilling, however it varies enormously, from less than 10 N[3][4] to over 100 N[5]. Therefore, bone drilling thrust

force measurements were conducted, with the help of two experienced orthopedic surgeons from the department of orthopedic surgery of University of Michigan. The surgeons were asked to drill the bovine cortical bone samples as they normally operate in surgeries, and the thrust forces were measured by a dynamometer mounted under the tested bone samples, which can yield a real concept of the thrust force magnitude in bone drilling operations. Consequently, the thrust force was confirmed in a range of 40-80N. Considering the geometry of the most commonly used medical 2-fluted drill bits with point angle of  $90^\circ$ [2], the normal load generating the friction during drilling process was roughly estimated at 15-25N. Applying a high load will wear the sample rapidly, which impedes getting sufficient friction coefficient data during the test, so the normal loads for the friction test were selected as 200gf, 400gf, and 700gf. Friction coefficient in higher load scenarios will be inferred.

## 4.3 RESULT

### 4.3.1 Bone Sample

Because of the anisotropic and inhomogeneous properties of bones, the friction coefficient is supposed to be different for different orientations and can vary a lot even on a same sliding track. However, the trends can be observed from the test results shown in Fig. 3 and Fig. 4. For radial bone samples, the friction coefficient tended to be 0.33 with a variation about 0.1. For lengthwise bone samples, the friction coefficient tended to be 0.56, with a variation about 0.15. And importantly, the friction coefficient of bone samples rarely changed due to the change of normal load.

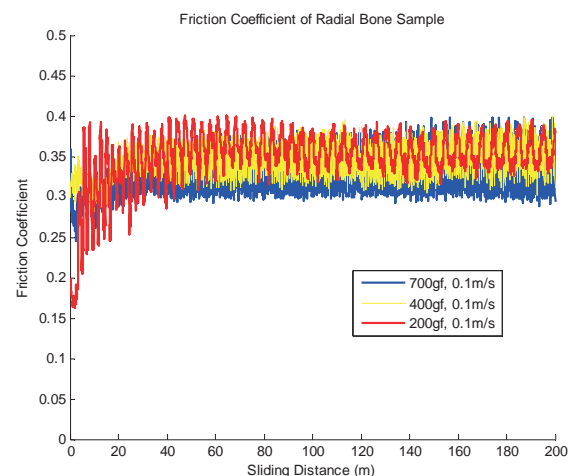


Fig. 3 Friction Test Result of Radial Bone Samples.

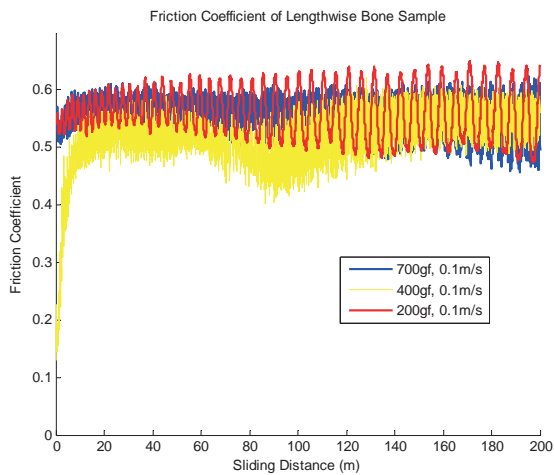


Fig. 4 Friction Test Result of Lengthwise Bone Samples.

### 4.3.2 Epoxy Treated Plaster Sample

The friction test result of RBC plaster samples was shown in Fig. 5. The friction coefficient tended to be 0.56 with a variation about 0.05.

Comparing with the friction coefficient of lengthwise bone samples, the friction coefficient of the proposed material demonstrated a very similar trend, though the variation was smaller. The friction coefficient of the radial bone samples was lower, whereas it is obviously that there are no operations involving the friction with the normal load vertical to the bone's cross section. It is reasonable to expect a lower friction coefficient than that of lengthwise bone samples (0.56), when the orientation of friction plane deflects. However, the proposed material still can be taken as a qualified analog of bone with regarding to the friction coefficient.

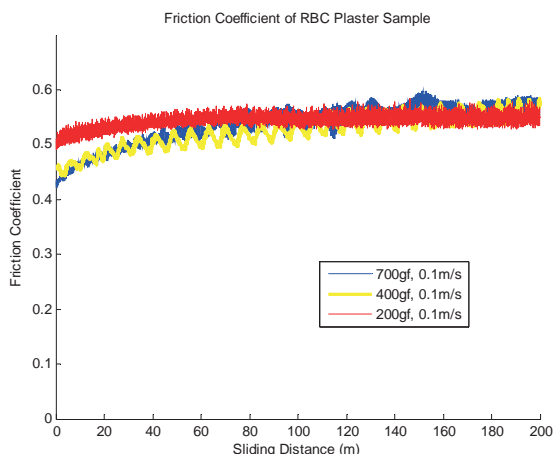


Fig. 5 Friction Test Result of RBC Plaster Samples.

### 4.3.3 Conformity to State of Drilling Chip

The friction coefficient of the drilling chip with the tool rake face has effects on the chip thickness and the cutting force [6]. The friction coefficients of the samples with the steel, according to the friction tests, were almost equal. Therefore, the state of chip of drilling the proposed samples

is supposed to be similar with that of dilling bones. Drilling experiments in Umich confirmed this hypothesis. As shown in Fig. 6, a similarity of the shape of drilling chip can be observed between the bone samples and the epoxy treated plaster samples.

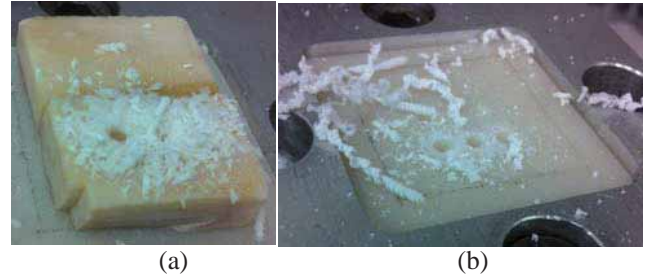


Fig. 6 State of Drilling Chip. (a) Cortical bovine bone sample. (b) RBC plaster sample.

## 5. THE EXPERIMENTS IN UM

As to the other two aspects of the validation of the proposed material, thermal conductivity and machining property, the experiments are ongoing in the S. M. Wu Manufacturing Center of UM. A brief introduction will be given in this part.

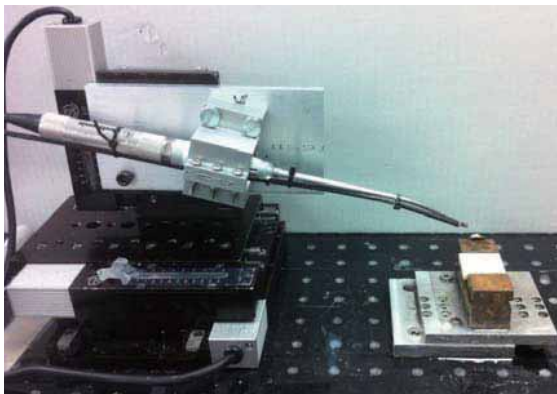
A thermal insulation box with cavities fitting the shape of the samples was created for thermal conductivity test, as shown in Fig. 7 Thermal couples were adopted to measure the temperature change.

The machining tests were conducted with three types of commonly used medical devices for bone cutting: Kwire, drill, and burr; accordingly the three experiment setups were built respectively as shown in Fig. 8.

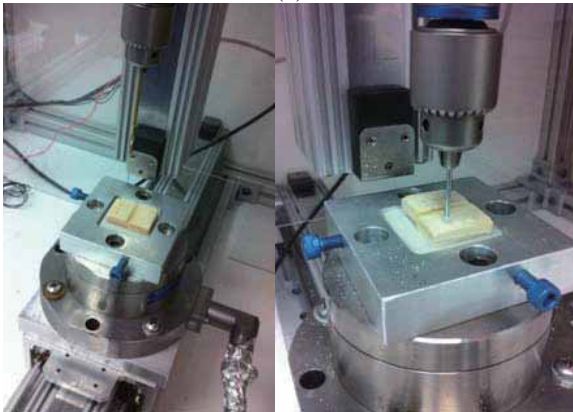
In order to make sure the consistency between the samples made in Umich and here in Nagoya, the epoxy treated plaster samples made in Umich were mailed to the Nagoya University. Both Rockwell hardness tests and friction tests were conducted on the Umich made samples by the same procedures, which confirmed the samples made in Nagoya and those made in Umich were identical.



Fig. 7 Thermal Insulation Box for Thermal Conductivity Test.



(a)



(b)

(c)

Fig. 8 Machining Test Setups. (a) Burr. (b) Drill. (c) Kwire.

## 6. FUTURE WORK

The current results are under expectation, mainly due to the weak haptic feedback in machining tests. Several factors may contribute to this situation. Firstly, the hardness of the epoxy treated plaster is less than half of the bone's hardness, which may be caused by the epoxy property and the soaking process. Secondly, according to the comparison of the thrust force curves recorded during the drilling test, the first 2mm period, epoxy treated plaster generated almost the same force feedback as the bone sample did. The desired consistency disappeared for the last 3mm process during which the thrust force of the bone drilling kept on rising while that of epoxy treated plaster sample stayed at a constant value. It is suggested that the heat generated on the tip of drill softens the epoxy.

However, as mentioned in the introduction, epoxy was chosen to strengthen the printed plaster because its property can be adjusted via various methods. Several alternative steps may be taken in the future work. Firstly, a new type of epoxy product has been recommended and offered by RBC INDUSTRIES Inc. This new product has a higher distortion temperature, which may assist to avoid the negative effect of drilling heat. Moreover, some additives like glass fibers can be added into epoxy to achieve a higher hardness. Secondly, the current printed plaster powder, zp<sup>®</sup>150, may be switched to improve the proposed material. Thirdly, several factors in the material preparation procedures, for instance, the

vacuum time, the vacuum pressure, and the curing temperature, can be further optimized.

## ACKNOWLEDGEMENTS

This project owes much to the JUACEP program, the collaboration between the Nagoya University and the University of Michigan. I would express my heartfelt gratitude to Prof. Noritsugu Umehara, the leader of JUACEP, my advisor in Nagoya University, Prof. Albert Shih, my advisor in the University of Michigan, Dr. Li-Jung Tai who coordinates this project, the JUACEP office staffs in the Nagoya University, and the group members in my laboratory. The support from the RBC INDUSTRIES Inc is considerably appreciated.

## REFERENCES

- [1] Tobolski, E.L., Fee, A., Macroindentation Hardness Testing, ASM Handbook, Volume 8: Mechanical Testing and Evaluation, ASM International, 2000, p 203-211, ISBN 0-87170-389-0.
- [2] Bertollo, N., Walsh, W.R., Drilling of Bone: Practicality, Limitations and Complications Associated with Surgical Drill-Bits, Biomechanics in Applications, Dr Vaclav Klika (Ed.), ISBN: 978-953-307-969-1, InTech, DOI: 10.5772/20931.
- [3] Abouzgia, M.B., Sumington, J.M., Effect of drill speed on bone temperature, Biomechanics in Applications, Int J Oral Maxillofac Surg 1996;25:394-9.
- [4] Abouzgia, M.B., James, D.F., Temperature rise during drilling through bone, Int J Oral Maxillofac Impl 1997;12:342-53.
- [5] Matthews, L.S., Hirsch, C., Temperatures measured in human cortical bone when drilling, J Bone Joint Surg Am 1972;54A:297-308.
- [6] Ke, F., Ni, J., Stephenson, D.A., Chip thickening in deep-hole drilling, International Journal of Machine Tools and Manufacture, Volume 46, Issues 12-13, October 2006, Pages 1500-1507, ISSN 0890-6955.

# SIMULATION OF RC STRUCTURES UNDER CYCLIC LOADING

Chung-Wen CHUANG

Department of Civil and Environmental Engineering, UCLA, USA  
rainmos@ucla.edu

Supervisor: Professor Hikaru NAKAMURA

Department of Civil Engineering, Nagoya University, Japan  
hikaru@cc.nagoya-u.ac.jp

## ABSTRACT

In this study, the degradation of the shear strength after flexural yielding of RC structures subjected to cyclic loading was simulated numerically using three-dimensional Rigid-Body-Spring Model (3D RBSM). The investigation of illustrative results of stress distributions and crack patterns is the key objective of this study. Firstly, through the cyclic loading, the phenomenon of the flexural behavior gradually replaced by the shear behavior was found based on the compressive stress distribution; in the meantime, the applicability of 3D RBSM was confirmed. Then, a comparison of two RC structures under between cyclic loading and monotonic loading was executed to demonstrate different degradation mechanisms of the shear strength after flexural yielding.

**Keywords:** Rigid-Body-Spring Model, Cyclic Loading, Stress Distribution, Crack Pattern, Flexural Behavior, Shear Behavior, Failure Mode

## 1. INTRODUCTION

It was investigated that the shear failure after flexural yielding occurs under cyclic loading [1]. The typical explanation is that the shear failure mode occurs under cyclic loading due to the degradation of the shear strength subjected to cyclic loading after flexural yielding based on the increase of the displacement, although the shear strength originally is higher than the flexural strength in the initial stage, as shown in Fig 1. According to the explanation, curves for the shear strength degradation were proposed by statistical procedures of many testing results [2, 3]. However, the mechanism of the shear failure under cyclic loading has not been clarified, as well as the degradation of the shear strength has not been evaluated determinately.

In this study, the shear failure after flexural yielding of RC beams subjected to cyclic loading was simulated using 3D Rigid-Body-Spring Model (3D RBSM) with the constitutive model; meanwhile, the applicability of this method was confirmed. Moreover, by investigating illustrative results of compressive stress distributions and

crack patterns, the degradation mechanism of the shear strength according to the increase of the displacement, as well as the failure mode, was evaluated numerically.

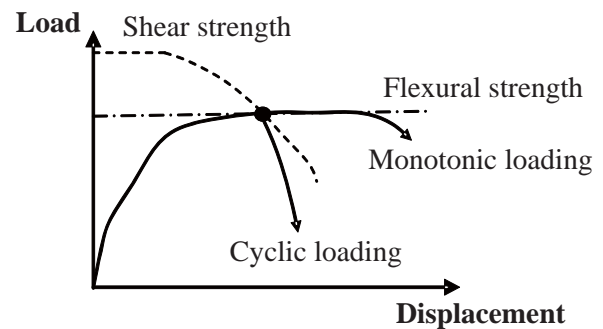


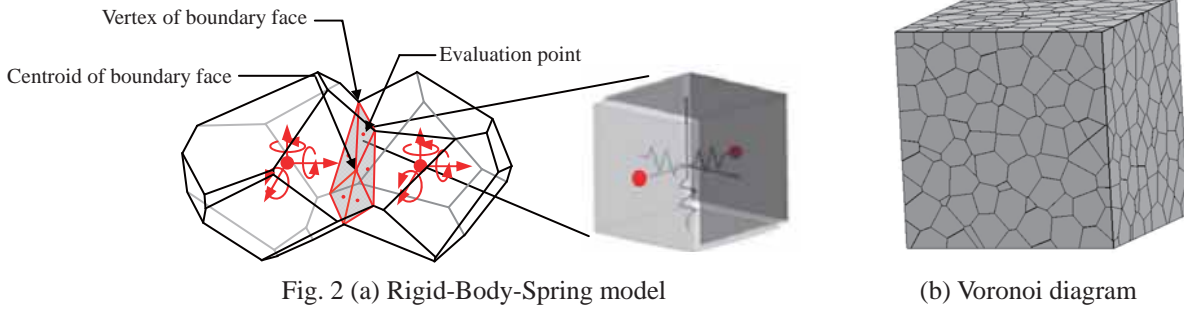
Fig. 1 Shear failure after flexural yielding

## 2. NUMERICAL MODEL

### 2.1 THREE-DIMENSIONAL RIGID-BODY-SPRING MODEL (3D RBSM)

In RBSM, concrete is modeled as an assemblage of rigid particles interconnected by springs along their boundary surfaces, shown in Fig. 2 (a), which is easy to simulate concrete cracking process and its effects. The crack pattern is strongly affected by the mesh design as the cracks initiate and propagate through the interface boundaries of particles. Therefore, a random geometry of rigid particles is generated by a Voronoi diagram, as seen in Fig. 2 (b), which reduces mesh bias on the initiation and propagation of potential cracks.

The response of the spring model provides an insight into the interaction among the particles, which is different from models based on continuum mechanics. In this model, each rigid particle has three translational and three rotational degrees of freedom defined at the nuclei (or nodal points) that define the particles according to the Voronoi diagram, as shown in Fig. 2 (a). The boundary surface of two particles is



divided into several triangles with a center of gravity and vertices of the surface. One normal and two shear springs are set at the center of each triangle. By distributing the springs in this way, over the Voronoi facet common to two neighboring nodal points, this model accounts for the effects of bending and torsional moment without the need to set any rotational springs [4].

## 2.2 CONCRETE MATERIAL MODEL

The constitutive models for tension, compression and shear that are used in 3D RBSM are shown in Fig. 3 [5]. The tensile model for normal springs is shown in Fig. 3 (a). Up to tensile strength, the tensile behavior of concrete is modeled as linear elastic and, after cracking, a bilinear softening branch according to 1/4 model is assumed. In the model,  $\sigma_t$ ,  $g_f$  and  $h$  represent tensile strength, tensile fracture energy, and distance between nuclei, respectively. Fig. 3 (b) shows the stress-strain relationship for compression of normal springs that was modeled as a S-shape curve combining two quadratic functions. The parameters of  $\sigma_c$ ,  $\epsilon_{c2}$ ,  $\alpha_{c1}$  and  $\alpha_{c2}$  shown in Fig. 3b are material parameters

which controlled the nonlinearity of the compression behavior of the normal spring under hydrostatic pressure.

The shear stress-strain relationship represents the combination of two shear springs. The envelope of the stress-strain relationship for shear is given in Fig. 3 (c). The stress elastically increases up to the shear strength with the slope of shear modulus  $G$  and softening behavior is also assumed.  $\beta$  is the shear-softening coefficient. It is assumed that the shear softening coefficient  $\beta$  depends upon the stress of the normal spring as represented in Figure 3 (d), where,  $\beta_0$ ,  $\beta_{max}$  and  $\chi$  are the parameters of dependency on the normal spring for the shear-softening coefficient. The Mohr-Coulomb criterion is assumed as the failure criteria for the shear spring, as shown in Fig. 3(e), where  $c$  and  $\phi$  are cohesion and the angle of internal friction, respectively. Moreover, it is assumed that the shear stress decreases with an increase in crack width at the cracked surface, which is similar to Saito's model [6]. The calibrated parameters are shown in Table 1.

Fig. 4 (a) shows the typical hysteresis loop of the normal spring [5]. The unloading paths in the tension zone

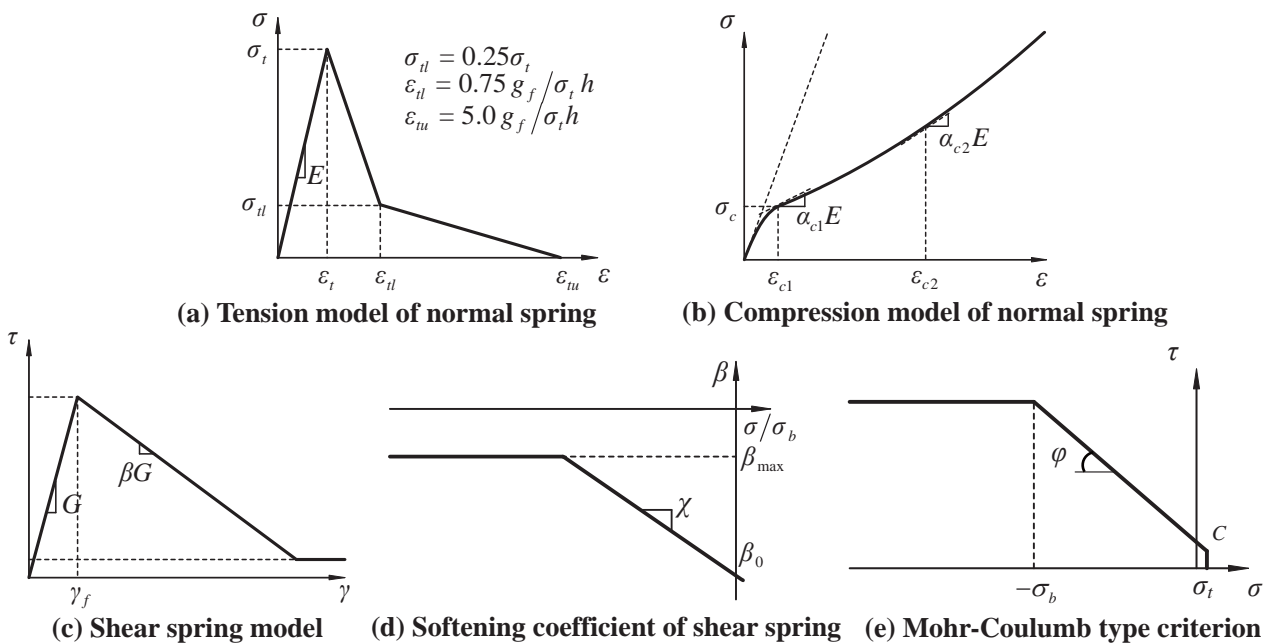


Fig. 3 Constitutive model for concrete

Table 1 Model parameters

Normal spring							Shear spring							
Elastic modulus	Tensile response		Compressive response				Elastic modulus	Fracture criterion			Softening behavior			
$E$ N/mm <sup>2</sup>	$\sigma_t$ N/mm <sup>2</sup>	$g_f$ N/mm <sup>2</sup>	$\sigma_c$ N/mm <sup>2</sup>	$\epsilon_{c2}$	$\alpha_{c1}$	$\alpha_{c2}$	$\eta = G/E$	$c$ N/mm <sup>2</sup>	$\varphi$ degree	$\sigma_b$ N/mm <sup>2</sup>	$\beta_0$	$\beta_{max}$	$\chi$	$\kappa$
$1.4E^*$	$0.8f_t^*$	$0.5G_f^*$	$1.5f_c'^*$	-0.015	0.15	0.25	0.35	$0.14f_c'^*$	37	$0.65f_c'^*$	-0.05	-0.02	-0.01	-0.3

\* The macroscopic material parameters obtained from the concrete specimens tests

$E^*$  : Young's modulus,  $f_t^*$  : Tensile strength,  $G_f^*$  : Fracture energy,  $f_c'^*$  : Compressive strength

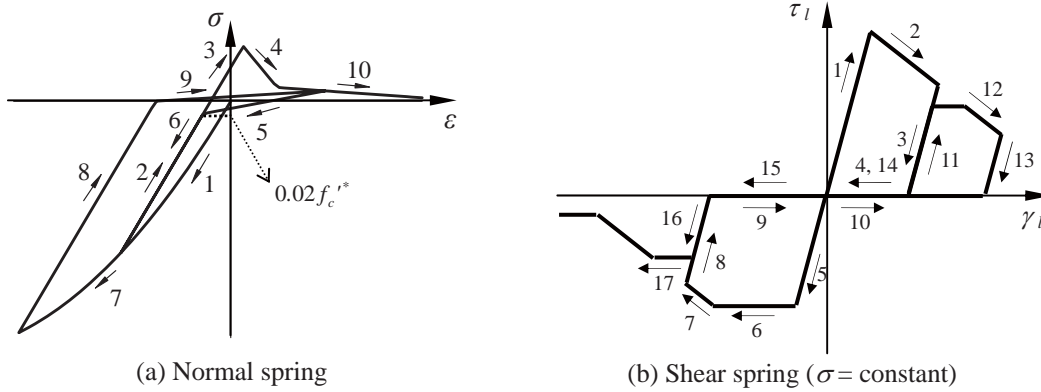


Fig. 4 Hysteresis of stress-strain relation

pass toward the point of stress  $\sigma = -0.02f_c'$  on the compression loading path. The reloading paths in the tension zone pass toward the start point of the unloading. The stiffness of the unloading in the compression zone is initial elastic modulus  $E$ . Fig. 4 (b) shows the typical hysteresis loop of the shear spring. The stiffness of the unloading and reloading is initial elastic modulus  $G$ . In addition, after the stress reaches to zero on the unloading path, the stress keeps zero until the strain reaches to the residual strain of the opposite sign.

### 2.3 REINFORCEMENT MODEL

Reinforcement is modeled as a series of regular beam elements (Fig. 5) that can be freely located within the structure, regardless of the concrete mesh design. Three translational and three rotational degrees of freedom are defined at each beam node. The reinforcement is attached to

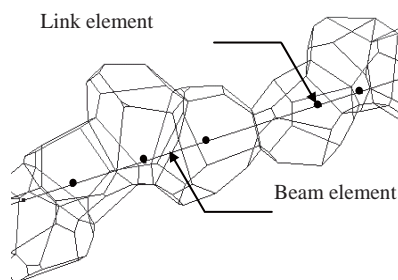


Figure 5 Reinforcement models

the concrete particles by means of zero-size link elements that provide a load-transfer mechanism between the beam node and the concrete particles. For the reinforcing bar, the bilinear kinematic hardening model is applied. The hardening coefficient is 1/100. Crack development is strongly affected by the bond interaction between concrete and reinforcement. The bond stress-slip relationship is provided in the spring parallel to the reinforcement of linked element as shown in Fig. 6.

### 3. ANALYTICAL MODEL

#### 3.1 GENERATION OF ANALYTICAL MODEL

The cantilever type of a RC beam, as shown in Fig. 7, was simulated. The specimen has the uniform cross-section of  $150 \times 200$  mm<sup>2</sup> and shear span of 640 mm. Two

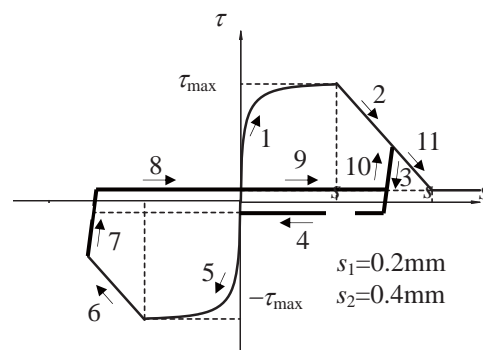


Figure 6 Bond - slip relationship

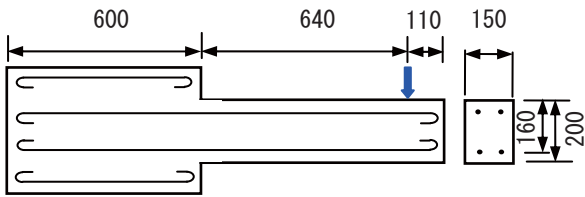


Figure 7 Dimension of specimen

longitudinal reinforcements of D13 were arranged at upper and lower sides with the cover thickness of 40 mm, and web reinforcements were not arranged. This specimen was tested by Machida et al. [7] and the shear failure after flexural yielding under cyclic loading was observed when the displacement is 20 mm ( $4\delta_y$ ).

Fig. 8 shows analytical model which was modeled by Voronoi diagram. The average element size is about 20mm. The analytical model was modeled as a uniform cross-sectional member, and the plate element was modeled in the footing part to restrain the deformation. All reinforcements were modeled as beam elements. It is assumed that the compressive strength of the concrete is  $40.5 \text{ N/mm}^2$ , and the yielding stress of longitudinal reinforcements is  $380 \text{ N/mm}^2$ .

In the analysis, the displacement of the loading plate element was controlled and alternative cyclic loading with an incremental deformation of  $\delta_y$  (5mm) was applied. Monotonic loading analysis was also conducted in order to compare with the results under cyclic loading.

### 3.2 APPLICABILITY OF 3D RBSM TO SHEAR FAILURE AFTER FLEXURAL YIELDING

Fig. 9 shows the load-displacement relationship

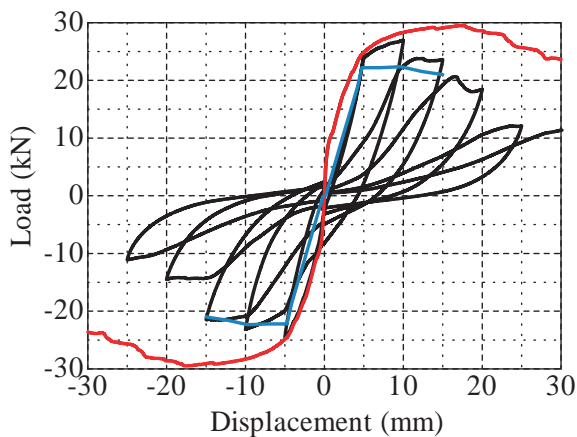


Figure 9 Load-displacement relationship

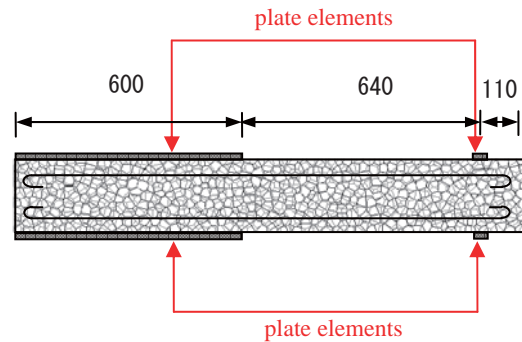


Figure 8 Analytical model

obtained by the analysis. The black line shows the result of cyclic loading analysis, the red line shows the result of monotonic loading analysis and the blue line shows the experimental results [7]. The envelopes for load-displacement curves of cyclic and monotonic loading are almost same until  $2\delta_y$  (10 mm). However, the load carrying capacity under cyclic loading decreases after  $3\delta_y$ . At  $4\delta_y$ , the shear failure occurs in the test, the load carrying capacity decreases rapidly, and the shape of the hysteresis loop changes to S-shape remarkably. This type of the behavior is usually observed in the test of the shear failure of RC columns. The difference between the results of cyclic and monotonic loading analysis increases with the increase of the displacement.

Fig. 10 and Fig. 11 show the deformations at 20 mm ( $4\delta_y$ ) obtained from the monotonic and cyclic loading analysis, respectively. It is understood that the flexural behavior is dominant in the monotonic loading case. On the other hand, in the cyclic loading case, the diagonal crack is dominant and the flexure crack does not develop. Moreover, it is observed that the deformation extends to lateral direction and X-shape cracks occur. This result is clearly different from the monotonic one and shows typical shear failure behavior. The applicability of 3D RBSM to the shear failure after flexural yielding under cyclic loading is



Figure 10 Deformation under monotonic loading at 20mm ( $4\delta_y$ )

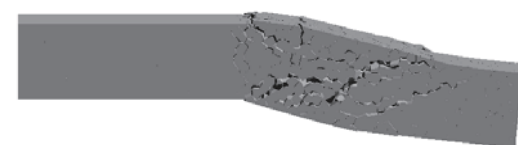


Figure 11 Deformation under cyclic loading at 20mm ( $4\delta_y$ )

Chung-Wen CHUANG

confirmed.

### 3.3 EVALUATION OF SHEAR STRENGTH DEGRADATION

As described in Introduction, the reason why the shear failure after flexural yielding occurs is that the shear strength degrades under cyclic loading, although the shear strength ( $V_c$  in Fig. 12) is higher than the flexural strength ( $P_u$  in Fig. 12) in the initial stage. Therefore, the degradation mechanism of the shear strength should be clarified quantitatively in order to evaluate the shear failure after flexural yielding. However, it is difficult to understand the degradation behavior in the test, since the degraded shear strength in the test is given by only a point on load-displacement relationship (Point A in Fig. 12). In order to obtain the shear strength degradation behavior, an analytical method was proposed. Fig. 12 shows a concept of the proposed method [1], and the detail of this method is explained in the following.

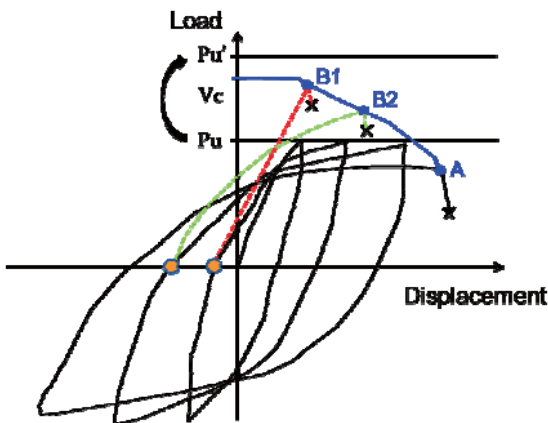


Figure 12 Concept of method

It is supposed that shear failure after yielding occur due to the degradation of the shear strength as the blue line in Fig. 12. The values of the shear strength on blue line, such as B1 and B2, after the increase of the displacement under cyclic loading can not be obtained, because the load does not increase over  $P_u$  which corresponds to the flexural strength. However, if the flexural strength at each cycle is changed over the blue line in the analysis, the shear strength can be obtained. In order to achieve the requirement, it was proposed that the yielding stress of longitudinal reinforcements is replaced by the higher values at orange points in each cycle in Fig. 12, which results in an increase of the flexural strength to  $P_u'$ . Then, the shear strength of the blue line less than increased flexural strength  $P_u'$  is calculated. The proposed method is based on fact that the yielding stress of longitudinal reinforcements increase only on the flexural strength and does not influence on the shear strength. This method utilizes the merit of numerical analysis which can consider the virtual situation.

The proposed method explained is applied to RC members. The yield stress of the longitudinal reinforcement

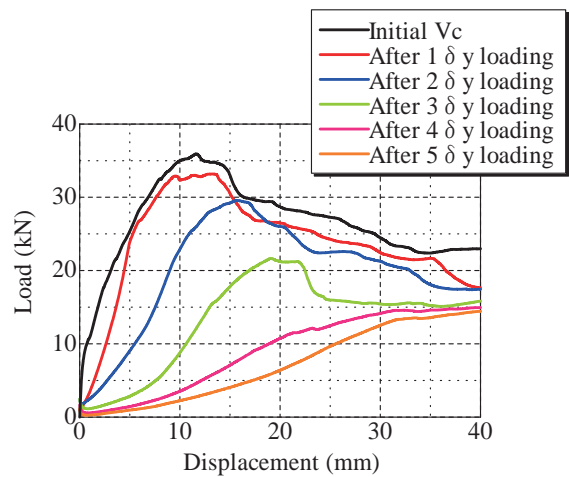


Figure 13 Load-displacement relationship for RC member under cyclic loading

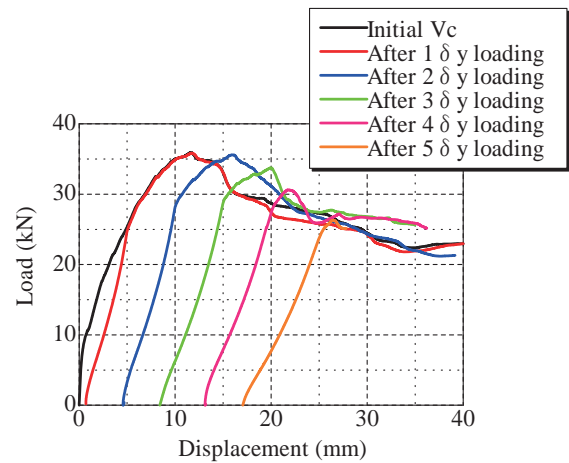


Figure 14 Load-displacement relationship for RC member under monotonic loading

is increased from 380 to 900  $N/mm^2$  at each cycle, when the load is zero after unloading in negative loadings.

Fig. 13 shows load-displacement relationship obtained from the proposed method. The shear strength obviously degrades with the increase of displacement. The shear strength after 1 $\delta$ y loading degrades little from the initial strength and the strength is higher from the flexural strength. Therefore, the shear failure does not occur at the stage in the test. On the other hand, the shear strength after 3 $\delta$ y degrades remarkably. Because the degraded shear strength is lower than the flexural strength in Fig. 9, the shear failure occurs independently on increasing the yield stress of the longitudinal reinforcement.

The shear strength degradation under monotonic loading is evaluated using the same method. The yield stress of the longitudinal reinforcement is increased after unloading until zero load at each displacement under monotonic loading. Fig. 14 shows load-displacement relationship to obtain the shear strength after flexural yielding. The shear strength

Chung-Wen CHUANG

hardly degrades until  $3\delta y$  loading. The shear strength gradually decreases after  $3\delta y$  loading, and the each post-peak behavior coincides. This result shows obviously different from the result under cyclic loading.

## 4. RESULTS DISCUSSION

### 4.1 STRESS DISTRIBUTION AND CRACK PROPAGATION OF RC STRUCTURES UNDER CYCLIC LOAD

In order to better observe the variation of the stress behavior and clearly recognize the degradation of the shear strength in the proposed RC cantilever beam subjected to cyclic loading, several illustrations of stress distributions in sequence for the middle longitudinal cross-section of the beam were developed using 3D RBSM programming. In the meanwhile, a series of illustrations of crack patterns corresponding to the stress distributions was also produced so as to reveal distinct crack types during different cycles of the loading. The load-displacement relationship for the applied cyclic loading is shown in Fig. 15. The feature of load-displacement relationship is that the hysteresis loops change from the spindle-shape to the S-shape with the increasing displacement.

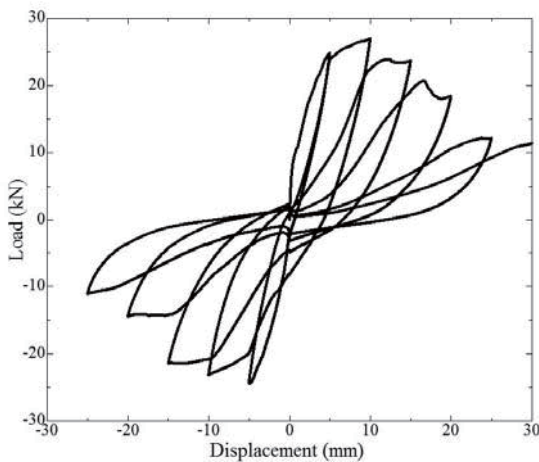


Fig. 15 Load-displacement relationship of the applied cyclic loading

#### 4.1.1 Stress Distribution

Two distinct cycles, in which the shapes of hysteresis loops are changed and maximum loads decrease, were implemented to display the distinct behavior of stress-distributions. The executive manner of the two cycles is illustrated in Fig. 16. The first cycle starts from point A to point B through point A', while the second cycle is from point B to point C via point B'. At each cycle, four points were picked for the purpose of investigating and comparing distinct stress distributions. For example, for the first cycle, A1, A2, A3 and A4 are selected; on the other hand, B1, B2, B3 and B4 are chosen for the second cycle. The results of the stress distributions under the first and second cycle,

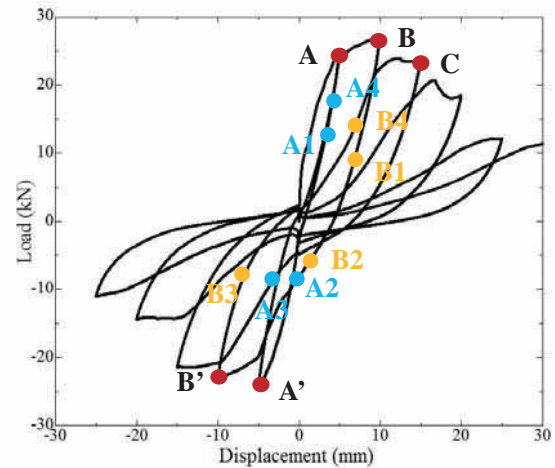


Fig. 16 Illustration of two distinct cycles

executed by means of 3D RBSM programming, are shown in Fig. 17 (a) and Fig. 18 (a), respectively. In the meantime, Fig. 17 (b) and Fig. 18 (b) represent the corresponding crack pattern to the stress distribution at each point generated for the assistance in understanding of correlative deformation of the beam at each point. In addition, Fig. 17 (b) and Fig. 18 (b) are further used to interpret the crack propagation in the following section.

In Fig. 17 (a) and Fig. 18 (a), the largest to smallest quantity of the compression is exhibited as colors of red, orange, and yellow in order, and the green color represents the zero compressive stress.

From Fig. 17 (a), it is discovered that in this cycle, the stress behavior is almost dominated by the compression behavior at upper and lower part of cross section. The distribution is usually observed in flexural behavior. Even after a full first cycle, the stress distribution at point A does not much differ from the stress distribution at point B. The only notice of interest is expansion to middle part of cross section.. This implies that the stress behavior is going to change.

From Fig. 18 (a), it is found that the stress behavior gradually converts from the flexural behavior to the shear behavior during the second cycle. Specifically, after half of the second cycle, the stress distribution of the compression behavior becomes diagonal. This means that the shear behavior forms progressively, as shown from the stress distribution at point B' toward point C. Eventually, at point C, it is obvious that the shear behavior is dominant at this moment.

Consequently, it is concluded that the shear behavior would take over the compression behavior gradually with the increasing number of the cycles of the loading. As a result, a RC structure under more cyclic loading tends to perform a severer shear failure with the more remarkable shear behavior.

Chung-Wen CHUANG

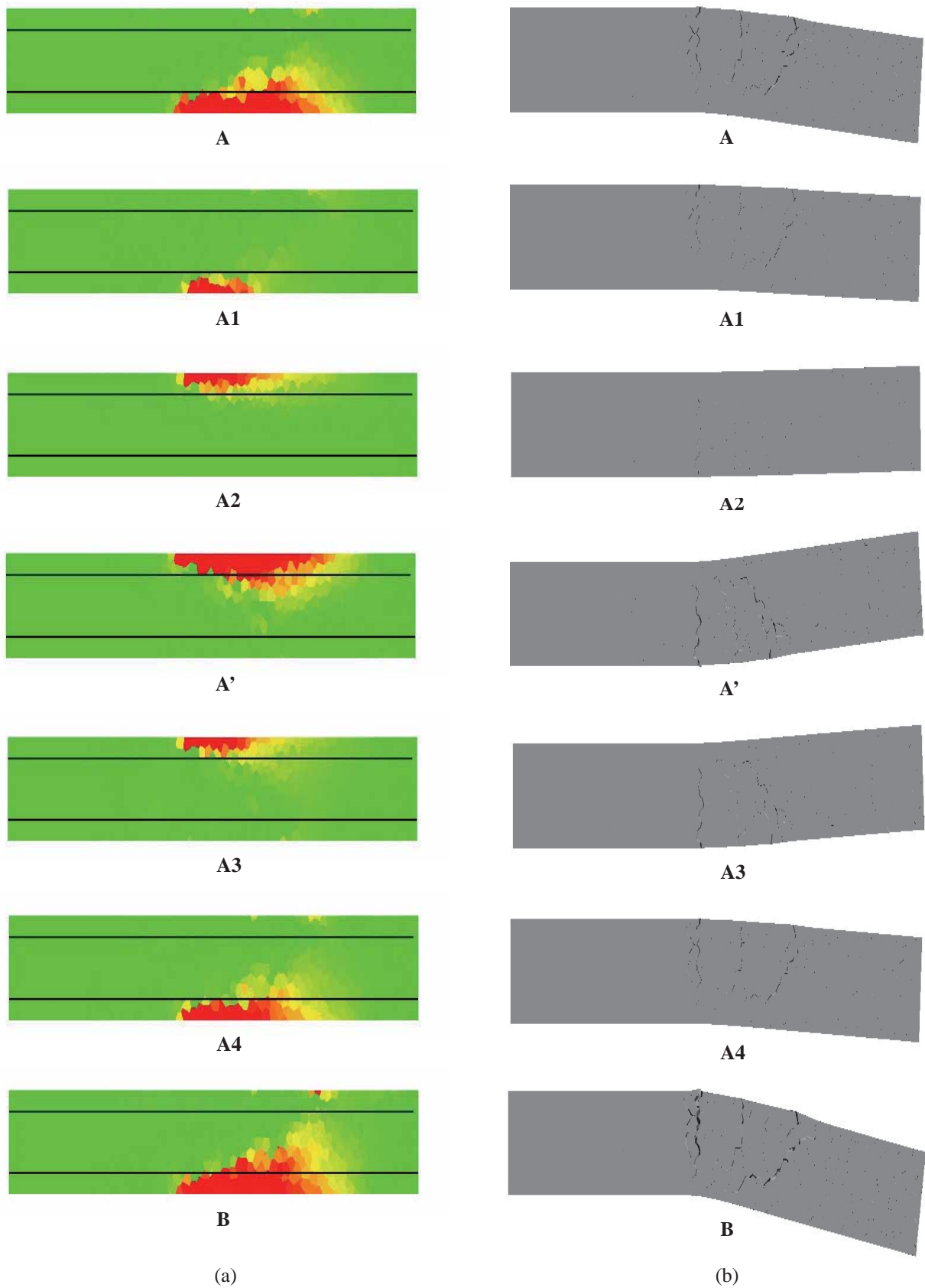


Fig. 17 (a) Stress distributions at different points of the first cycle of the loading; (b) Crack patterns at different points of the first cycle of the loading

Chung-Wen CHUANG

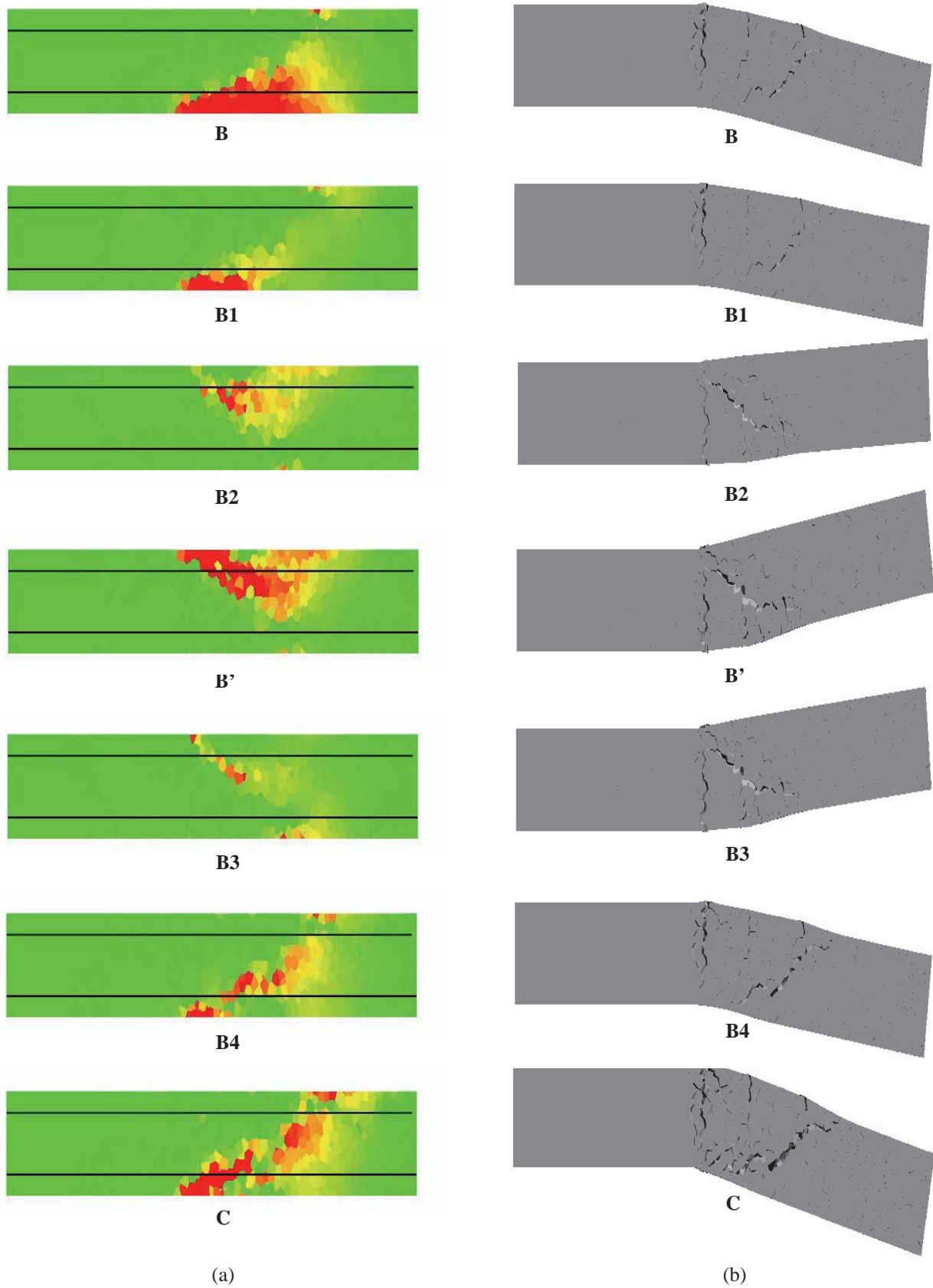


Fig. 18 (a) Stress distributions at different points of the second cycle of the loading; (b) Crack patterns at different points of the second cycle of the loading

Chung-Wen CHUANG

Furthermore, the simulated results obtained from 3D RBSM programming agree with the explanation of that the shear failure occurs due to the severe degradation of the shear strength under cyclic loading after flexural yielding as described in Introduction.

#### 4.1.2 Crack Propagation

In Fig. 17 (b) and Fig. 18 (b), the magnification factor of 10 is used consistently throughout all the illustrations of crack patterns in order for the clear and accurate identifying the difference among the cracks and deformations at different points.

From Fig. 17 (b), it can be seen that within the first cycle of the loading, only the flexural cracks occur at each point, except that there begins a slight shear crack appearing at the last point (i.e. Point B). This phenomenon agrees with the description in Section 4.1.1 of the stress distribution. That is, the flexural behavior is dominant during this cycle in either the positive or negative deformation. In addition, from the observation of Point B in Fig. 17 (a), a distinct stress distribution begins to occur at the top of the beam at Point B; accordingly, this result agrees with the initial appearance of the stress crack at Point B, as shown at Point B in Fig. 17 (b).

Fig. 18 (b) demonstrates that the behavior of stress distributions changes from the flexural behavior to the shear behavior, as illustrated in Fig 18 (a). In other words, more and more shear cracks are appeared within the second cycle of the loading, whereas the flexural cracks don't have outstanding variations of the width and amount at this stage. Eventually, at the last point (i.e. Point C), it is found that a remarkable shear crack is going to penetrate the lateral cross-section. The distinct shear cracks appear at B2 between the flexural cracks, though load value is small. The behavior from positive to negative deformation in cyclic loading may influence to initiation of the shear crack. Thus, the illustrations of the crack pattern during the second cycle of the loading confirms that the eventually damage of this proposed RC cantilever beam subjected to cyclic loading results from the shear failure mode.

## 4.2 COMPARISON OF STRESS DISTRIBUTION AND FAILURE MODE AT PEAK LOAD BETWEEN CYCLIC AND MONOTONIC LOADING

In order to study how significant the cyclic loading influences the RC structure on stress distributions and crack patterns, as well as failure modes, in this section, a contrast is induced for the comparison. That is, this contrast is an identical RC structure with the same properties and arrangements of both concrete and steel materials compared to the analytical model, except the applied loading conditions. To be specific, the monotonic loading is applied to the contrast. In this section, only three cycles/loops of loading conditions are developed and compared as it is quite time-consuming to simulate the entire load-displacement

curves up to peak loads for the last two models under cyclic loading. However, from the results of RC structures subjected to the first three cycles/loops of either the cyclic loading or the monotonic loading, the data obtained from the 3D RBSM programming are much enough to investigate obviously the big difference between two RC structures under different loading conditions.

Two identical RC structures with the same material properties and arrangements, but different loading conditions applied, are simulated in this section. Fig. 19 (a) and Fig. 19 (b) show the stress distributions at individual peak load for the first three cycles of the cyclic loading and the first three loops of the monotonic loading, respectively. In the figure, the colourful patches have the same definition with the Section 4.1.1.

From the stress distributions illustrated in Fig. 19, it is found that the range of the stress distribution at each peak load decreases extraordinarily from the first cycle to the third cycle under cyclic loading, as shown in Fig. 19 (a). On the contrary, the range of the stress distribution at each peak load slightly decreases from the first loop to the third loop of the monotonic loading, as shown in Fig. 19 (b). The difference is observed at the compression stress zone due to the bending moment. Under cyclic loading, the compression stress due to the bending moment is lost and flexural behavior does not contribute to the load carrying capacity. This phenomenon implies that the cyclic loading greatly affects the strength of RC structures. This strength should belong to the shear strength of RC structures as mentioned in Introduction so that the shear strength of RC structures degrades much while subjected to cyclic loading.

## 5. CONCLUSIONS

(1) 3D RBSM can simulate the shear failure after flexural yielding under cyclic loading. Accurate cracks and illustrative stress distribution can be developed and investigated using 3D RBSM programming.

(2) Curves for the degradation of the shear strength obtained by 3D RBSM analytical model show similar behavior with the proposed formula which obtained by statistical procedures, so that the possibility to evaluate the degraded shear strength using numerical analysis is confirmed.

(3) It is found that the shear behavior would take over the flexural behavior gradually with the increasing number of the cycles of the loading. As a result, a RC structure under more cyclic loading tends to perform a severer shear failure with the more remarkable shear behavior.

(4) It is discovered that within the cyclic loading, the shear cracks on RC structures become larger after a cycle, whereas the flexural cracks don't grow a lot. That is, the shear cracks on RC structures under cyclic loading apparently develop in width, length and number after every cycle, but there is not much change for the flexural cracks in width, length and number. This phenomenon agrees with the

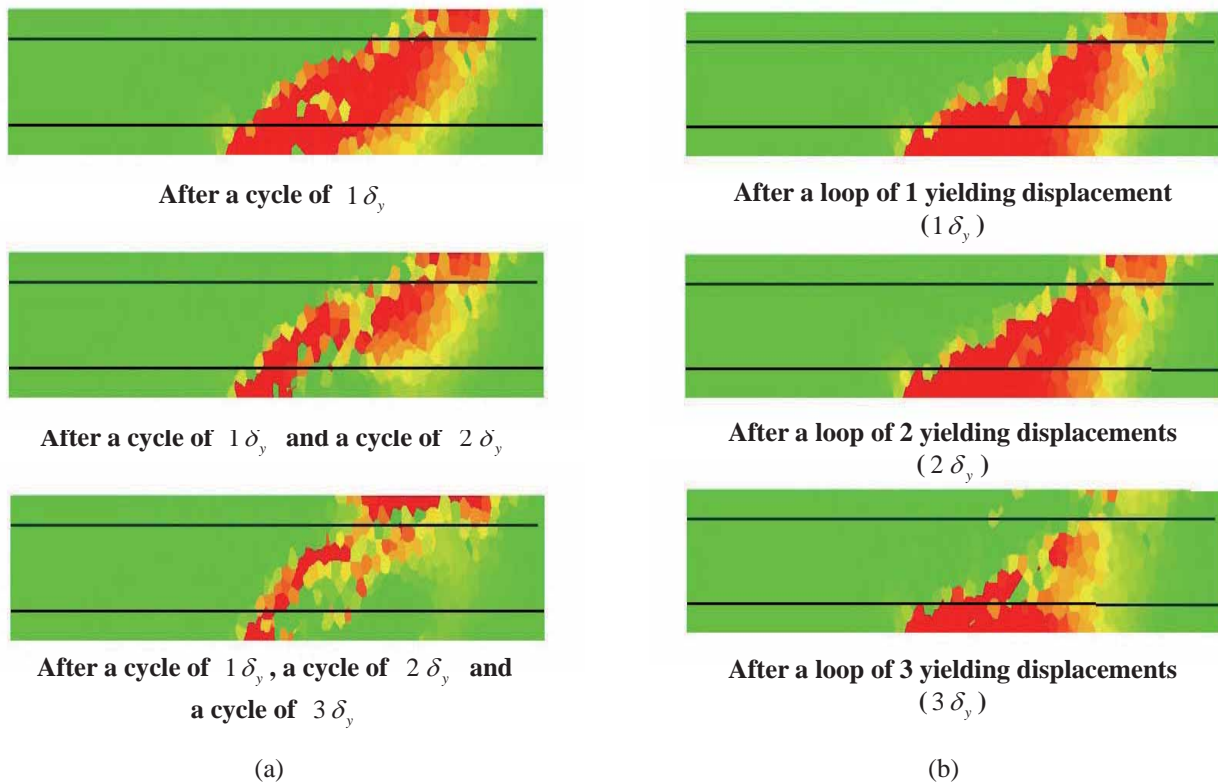


Fig. 19 Stress distributions at the peak load of each cycle/loop condition for two identical RC cantilever beams under (a) the cyclic loading; (b) the monotonic loading, respectively

concept that the shear behavior eventually dominates the failure mode when RC structures are subjected to cyclic loading.

## 6. ACKNOWLEDGEMENTS

This study is supported by JUACEP Summer Program 2013 at Nagoya University.

## 7. REFERENCES

- [1] Furuhashi, H., Nakamura, H., Yamamoto, Y., Numerical Study on Shear Strength Degradation after Flexural Yielding of RC Member Subjected to Cyclic Loading, EASEC-13 (2013).
- [2] Priestley, M. J. N., Seible, F., Carvi, G. M., Seismic Design of Retrofit of Bridges, A Wiley-Interscience Publication (1996).
- [3] Ohe, R., Yoshikawa, H., Study on shear strength degradation of single reinforced concrete columns under repeated large deformation, Doboku Gakkai Ronbunshuu E. V-56, No. 711, pp. 59–71 (2002).
- [4] Gedik, Y. H., Nakamura, H., Yamamoto, Y., Kunieda, M., Evaluation of Three-Dimensional Effects in Short Deep Beams using a Rigid-Body-Spring-Model, Cement and Concrete Composites, 33(9), pp. 978-991 (2011).
- [5] Yamamoto, Y., Nakamura, H., Kuroda, I., Furuya, N., Simulation of Crack Propagation in RC Shear Wall Using a 3D Rigid-Body-Spring Model with Random Geometry, FraMCoS-8 (2013).

- [6] Saito, S., Hikosaka, H., Numerical Analysis of Reinforced Concrete Structures Using Spring Network Model, Journal of Materials, Concrete Structures and Pavements, Vol. 44, No. 627, pp. 289-303 (1999).
- [7] Machida, A., Mutsuyoshi, H., Toyoda, K., Evaluation of the Ductility of Reinforced Concrete Members, Annual Journal of Japan Concrete Institute, Vol. 7, No. 1, pp. 629-632 (1985).

## TWO POINT PROBE RESISTIVITY MEASUREMENT OF CARBON NANOTUBES

Owen Suyuan Liang

Department of Materials Science and Engineering, Henry Samueli School of Engineering, UCLA  
owenliang@ucla.edu

Supervisor: Yahachi Saito

Quantum Engineering, Graduate School of Engineering, Nagoya University  
ysaito@nagoya-u.ac.jp

### ABSTRACT

Two point probe measurement was performed in-situ on various CNT samples inside a SEM equipped with nanomanipulators. The diameter of the MWCNTs were 16.67 [nm] and most CNTs were at least 1 [μm] in length and probed from 1-2 [V]. Many trials were done but only one data set had positive contact resistance. An extrapolation of the contact resistance gave 3 [MΩ] and a resistivity of  $3.49 \times 10^{-2}$  [Ω-m]. CNTs could prove to be the next material choice in replacing the metallic interconnects of modern technology.

### Introduction

As technology pushes forward, limitations of materials get reached. An example of such can be seen in the semiconductor industry where the transistor cannot simply be made smaller to make a silicon chip more powerful. Processors chips become more powerful with increasing number of transistors that can fit on a limited area. However, as the transistor becomes smaller, undesirable quantum effects occur that essentially render the device useless. One of the various issues with smaller transistors is the interconnect technology.

Interconnects are metallic wires that connect the various transistors together to allow communication. This is a relatively trivial task if it only involves connecting several transistors together; however, with modern technology pushing the transistor amount to billions, a complex architecture is necessary for complete communication. Thus, modern interconnect technology consist of extremely small two-dimensional metallic patterns with multiple out-of-plane layers that interweave to form a complex network. Nevertheless, as hinted earlier, smaller structures lead to other undesirable effects and for interconnect technology, this is electromigration.

Electromigration is the mass transport of ions under the influence of a large electric current (1). The free-electron model states that electrons flow freely in a metal under the assumption of a perfect lattice of ions. However, phonon vibrations can cause scattering interactions with the electrons and this will eventually lead to electrical resistance and Joule heating. When current densities are low, there is no net effect on the diffusion of the ion; however, for current density above  $10^4$  [A/cm<sup>2</sup>], atomic displacement occurs with the flow of electrons bombarding the ions out of equilibrium. With continual bombard, the lifetime of the interconnect decreases and eventually the wire becomes an open circuit. For nano-sized devices, the cross sectional area is very small thus the phenomenon of electromigration is more prevalent as the current density increases inversely with area. Therefore, a new material needs to be found to continue pushing technology to fit Moore's law.

Within the past couple decades, a new type of nano-material was discovered that could possibly solve the impending road block of silicon technology. This new material had very tough constraints on its properties and needed parameters such as, high conductivity, high strength, and low cost. Surprisingly enough, this new material is not made out of a newly discovered heavy element, but the light, abundant element carbon. This new area of carbon nano-materials include: Fullerenes (2), Carbon NanoTubes (CNTs) (3) and Graphene (4). The focus of this paper will be on the electronic properties of CNTs and their application to the semiconductor interconnect technology.

With the discovery of CNTs just a little over a decade ago, a vast amount of effort has been put in to determining the various properties of CNTs. Although the CNTs' mechanical properties will not be explained in this paper, there are major

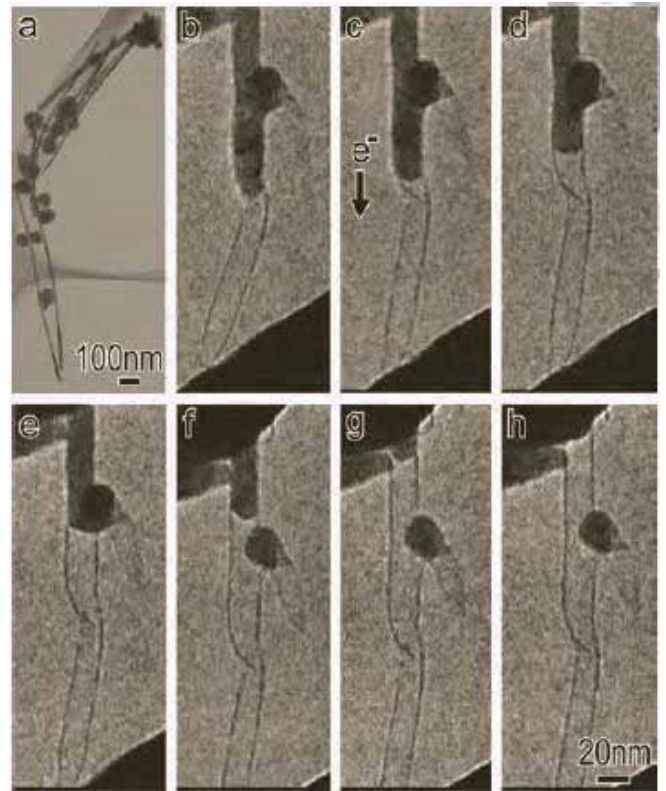
potential applications utilizing its tensile strength that should not be taken lightly. Electronic-wise, for Single-Walled Carbon NanoTubes (SWCNTs), its structural shape will determine its electrical property. An example of the structural influence can be seen at the edges of the CNT where an armchair pattern will give a metallic CNT and a zigzag pattern will give a semiconductor-like CNT (5). If it is a chiral pattern, it can be either semiconducting or metallic depending on the chirality. It is also interesting to note that for the same chirality semiconducting nanotubes, the band gap will be inversely proportional to its diameter (6). Thus for the samples used in this paper, since they are Multi-Walled Carbon NanoTubes (MWCNTs) and have large diameters, their electronic property is assumed to be metallic.

The application of these MWCNTs is to replace the interconnecting wires of either Al or Cu. As mentioned before, due to electromigration, these wires have a shorter lifetime when compared to large devices created a decade ago. However, it was recently proved that CNTs can withstand the electromigration while the Cu ions will diffuse away as seen in Figure 1. As seen in Figure 1, (b) to (h) show a time-lapse of a Transmission Electron Microscope (TEM) image of a Cu filled CNT where Cu ions migrate from a nano-rod to a nano-sphere. Yet after the mass transport, the shell of the CNT is still intact proving that CNTs are not affected by the high current density. However, the resistivity of CNTs is not well known since its electronic property depends on the structural shape. Of course, there are some papers on the resistivity of CNTs (7) and the maximum current density, which was as high as  $6 \times 10^6$  [A-cm<sup>-2</sup>]. However, inspection of the table can easily conclude a range from  $10^{-5}$  to 1 so the standard deviation is too large. Thus, the purpose of this study is to help alleviate this discrepancy with more data points on the resistivity of MWCNTs.

Resistivity of any material can be calculated by Ohm's Law. This variant of Ohm's law is true for bulk materials and relates resistivity to resistance, cross-sectional area, and length (8).

$$\rho = \frac{RA}{L} \quad (1)$$

$\rho$  is the resistivity of the material,  $R$  is the electrical resistance at a certain voltage and current,  $A$  is the cross-sectional area, and  $L$  is the length of the CNT. The area of the CNT was assumed to be constant at a diameter of 16.67 [nm] measured from a TEM image similar to Figure 1. Thus the cross-sectional area is assumed to be  $8.73 \times 10^{-16}$  [m<sup>2</sup>] for all the CNTs. Rearranging the equation to:



$$\left(\frac{\rho}{A}\right) \times L = R \quad (2)$$

will give me a relationship where the slope of the graph can relate to resistivity, the X-coordinates

**Figure 1 – TEM image of an enclosed Cu nano-rod inside a CNT. (a) shows Cu nano-particles that are attached to the CNT, (b) – (h) show a time-lapse of the electron migration of the Cu nano-rod to the Cu nano-particle. An outline can still be seen showing no effect done on the CNT. (13)**

are the measured lengths from the Scanning Electron Microscope (SEM) images, and the Y-coordinates are the resistance calculated from the measured voltage and current from a standard digital multimeter. If a trendline is extended from the plot to a theoretical length of zero meters, that y-intercept value can be assumed to be the contact resistance of the measuring probes. Since resistivity is also temperature dependent, room temperature is assumed for all measurements. The author also notes that as materials get smaller, quantum effects such as electron surface scattering and grain boundary scattering (9) can take place that will deviate Ohm's law from its linear relationship. However, there was not enough time to measure different sized CNTs to determine this

relationship so a linear relationship is assumed with a big sign of caution.

## Experimental

A FEI Quanta SEM system is used to image the CNTs and allow in-situ two-point probe resistivity measurement. Firstly, MWCNTS were made via the arc-discharge method (10) and then transferred to an insulating substrate like SiO<sub>2</sub>.

To probe the CNT, tungsten Scanning Tunneling Microscopy (STM) tips were made using NaOH and 0.15 [mm] tungsten wire. The wire was hooked up to an apparatus that would trigger and remove the tungsten wire from the etching solution when the measuring current would fall below 10 [mA]. It was found that 2.5 – 2.6 [V] gave a good variance of sharp W tips from 50 – 150 [nm]. Smaller voltages would give shaper but thinner tips that would break easily in the SEM. Although the CNTs were less than 20 [nm] in diameter, a larger tip would make contacting much easier. Tips were then immediately washed in De-Ionized (DI) water and then in ethanol and were examined via the SEM for tip integrity.

In the beginning, W tips were made a couple days before usage and were stored in a vacuum box; however, after some trial and error, it was found that thick W oxide layers prevented measurements at 1-2 [V]. Thus, it was found that made-to-order tips were more effective at providing a good contact with the CNT.

The SEM had two Kleindiek MM3A-EM micromanipulators that could hold the W tips and provide fine movement to probe the CNTs in-situ. Each micromanipulator was controlled via a piezoelectric that had two rotational axis ( $\theta$  and  $\phi$  in spherical coordinates) and one linear axis ( $r$  in spherical coordinates). The micromanipulator can be controlled via a Nanocontroller with rotary knobs or a Playstation joystick depending on the user preference. The coarse steps had a range of 12 [mm] in  $r$  and 240° in  $\theta$  and in  $\phi$ . Each coarse step moved the manipulator 40 [nm] in the  $r$  and 400 [nm] in a rotational arc length. The fine steps allowed a range of 1 [μm] in  $r$  with 0.25 [nm] per step and a range of 20 [μm] in rotation with 5 [nm] per step (11).

After the W tips are installed into the micromanipulator and the CNT sample is also in the SEM, probing can begin. Probing requires a certain finesse and there is a steep learning curve to fully understand the difficulty in probing CNTs. The various speeds between coarse and fine steps

need to be switched constantly to freely move the W tips to any CNT located on the sample. To measure the resistivity of one CNT, hours must be spent to find a completely isolated CNT from the various CNT forests. If difficulty arises and the W tip accidentally crashed into the surface, then a technique can be utilized to intentionally swipe the area of the CNT forest to separate an individual CNT. Other techniques include shorting the W probes together to evaporate some oxide and vibration of the W tips for further verification of surface touching.

After the W probes are contacting a CNT from both sides, an Advantest R8340A Ultra High Resistance Meter was used to supply a voltage and measure the resulting current. SEM images were taken to measure the length of the CNT and an average current was taken after a stabilization of 5 seconds. 1 and 2 volts were used to measure the CNTs with varying distances. After the initial successful measurement, one of the probes needs to be relocated for a new distance and current on the same CNT.

## Results and Discussion

Although this experiment sounds relatively simple, there was much difficulty in probing enough samples for a good statistical data analysis. As bad as it sounds, luck is a key factor in producing enough data points. Of course, initially there will be difficulty as the user needs to acquire a skill level; however this author found many seemingly uncontrollable events. There were cases when the piezoelectric manipulators would move after a current measurement; most likely due to some charge up however, all the equipment was isolated correctly. This would cause movement during measurement where after 1 minute, the current would drop because one of the tungsten probes has moved off of the CNTs. Figure 2 is an example of a before and after SEM image and it shows movement of the probe after just a minute. The red line is a reference line centered on the middle of the tip and it shows that the W tip moved off center right after the 2 [V] measurement. It should be noted that the high voltage of the SEM was deliberately turned off during the current measurement so any sort of charging must have come from the voltage source.

The data collected for various CNTs is listed in Table 1. All lengths were measured with their respective SEM image and resistances were calculated from their respective voltage and average current. CNTs were selected to be greater than 1 [μm], however data collection would sometimes damage the tubes and result in a smaller distance measured. As mentioned

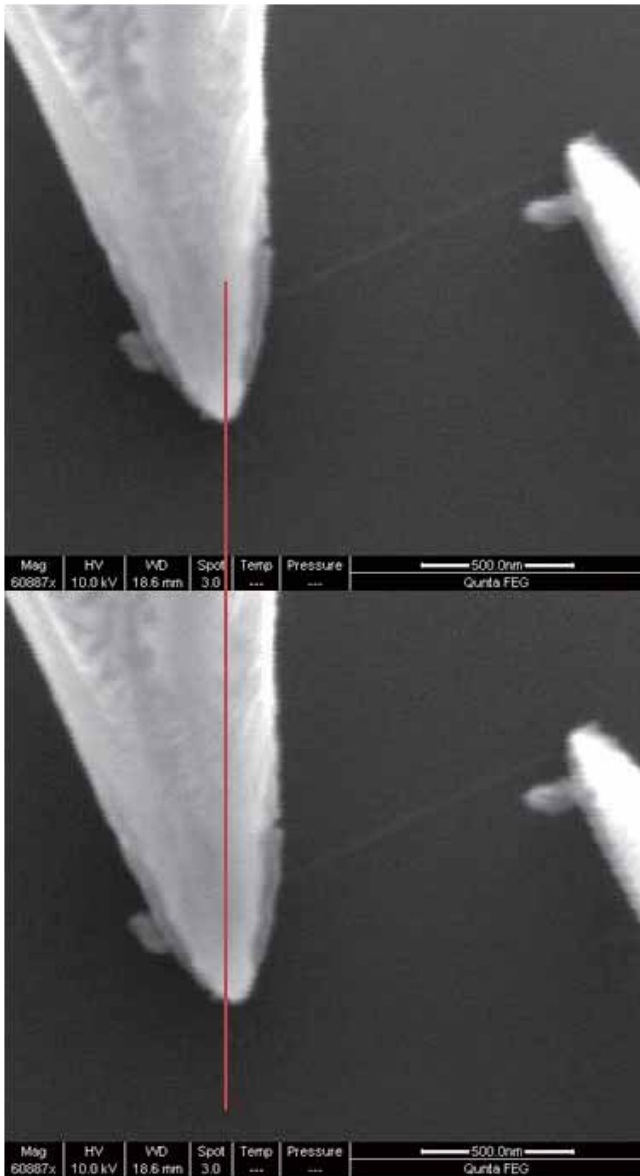


**Figure 2 - An SEM image showing the movement of the tungsten probe after a successful measurement. The top insert is before the 2 V measurement and the bottom insert is taken right after. The red line is a reference line which intersects the middle of the probe in the top insert but not the middle in the bottom insert.**

**Table 1 – Data collected from various CNTs and grouped into the same voltage.**

before, current had to be averaged out and the

Sample Name	Length [m]	Resistance [ $\Omega$ ]
<b>1 volt</b>		
CNT#2	4.00E-07	8.98E+07
CNT#3_1	5.51E-07	2.50E+07
CNT#3_2	1.38E-06	4.47E+07
CNT#4	1.34E-06	9.24E+06
	1.34E-06	8.28E+06
CNT#8	8.97E-07	1.31E+07
	3.15E-07	1.00E+08
	3.12E-07	1.11E+08
CNT#12	4.23E-06	1.25E+06
	4.23E-06	8.00E+05
<b>2 volt</b>		
CNT#2	4.00E-07	5.35E+07
	4.00E-07	5.03E+07
CNT#4	1.34E-06	2.02E+06
	1.34E-06	2.47E+06
	1.99E-06	6.67E+07
CNT#6	1.86E-06	2.45E+07
	1.63E-06	4.84E+07
	1.53E-06	5.95E+06
	1.53E-06	6.30E+06
CNT#8	8.97E-07	5.19E+06
	8.49E-07	3.64E+07
	3.15E-07	1.40E+07
	3.12E-07	1.64E+07
CNT#12	4.23E-06	8.33E+05
	4.23E-06	6.67E+05
	2.80E-06	3.33E+07
	2.80E-06	4.44E+07
<b>4 volt</b>		
CNT#2	8.94E-07	1.33E+08
	4.00E-07	3.56E+07
CNT#6	1.64E-06	2.91E+07

range was taken about 5 seconds afterwards. Ideally, three distance measurements are minimal for a trendline approximation; however, the difficulty in maintaining the integrity of a CNT and collecting a current meant only two data points for some measurements. If there were more time, more attempts could have made this plot better. Figure , Figure , Figure , Figure are the plots for all the data listed in Table 1. The various trendline that gave negative y-intercepts or negative slope were ignored as labeled as non-physical data. Thus the only acceptable data point can be seen in Figure and Figure which highlight CNT #8. An extrapolation of the trendline revealed a large contact resistance of 10 M $\Omega$  and if the outlier point was removed, the contact resistance can be calculated to be 3 M $\Omega$ . This clearly shows that contact resistance is a major issue in probing CNTs. Although, W oxide cannot be the only issue because some measurements, like CNT #12, had their W probe

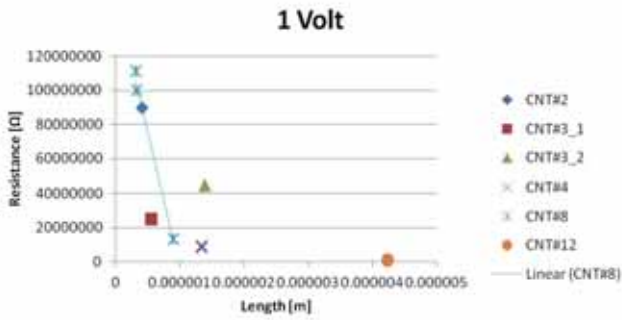


Figure 3 – A plot of the length vs. resistance for all CNTs taken at 1 voltage. Certain measurements could not be taken because 1 voltage was not enough to overcome the contact resistance.

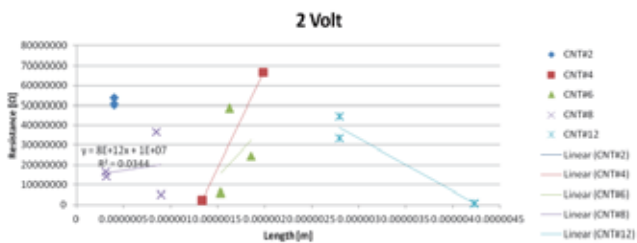


Figure 4 – A plot of the length vs. resistance for all CNTs taken at 2 voltage. Although most CNTs had various points, the trendline for most CNTs gave negative y-intercepts. This is not physically possible so only CNT#8 could be accepted as usable.

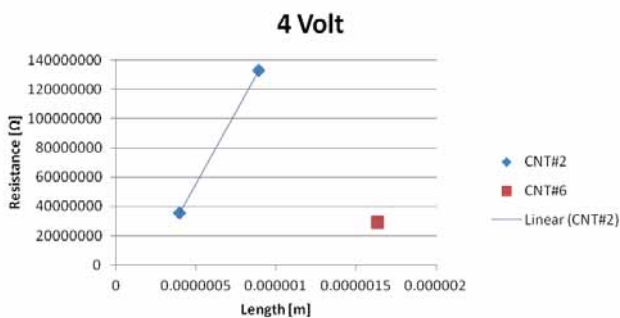


Figure 5 – The resistance vs. length plot for 4 voltage. This data set was not done very often in fear of damaging the CNT, however, some contact resistances were extremely high and 4 volts was necessary to get a current measurement.

burned off. This was done by crossing the probes together and maintaining a large current to remove the oxide. Yet, the data clearly shows unphysical data even if outlier points could be removed.

The resistivity of CNT #8 was calculated to be  $6.98 \times 10^{-3} \text{ } [\Omega\text{-m}]$  for all the data points included

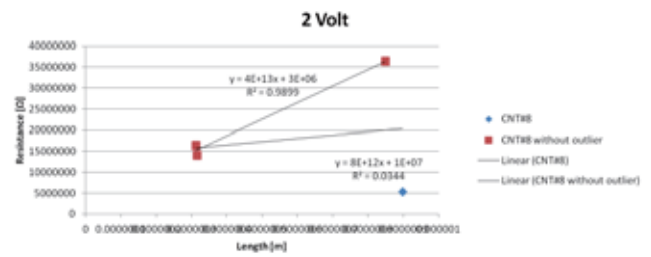


Figure 6 – A zoomed in plot of CNT #8 which was the only successful trendline plot. The initial plot in Figure showed CNT#8 with four data points however the trendline approximation gave a low  $R^2$  value. If the outlier point is removed, we see an increase in the  $R^2$  value from 0.0344 to 0.9899. This accuracy cannot be overlooked, so this plot shows covers the difference between the two. Equations for the plots are given to show the calculations for resistivity done for CNT#8.

and  $3.49 \times 10^{-2} \text{ } [\Omega\text{-m}]$  with the one outlier point removed. These numbers show that the CNTs measured could have been semiconducting because in general, metals have resistivity in the  $10^{-8} \text{ } [\Omega\text{-m}]$ . A quick search of the resistivity of graphite showed  $10^{-6} \text{ } [\Omega\text{-m}]$  for in-plane conduction and  $10^{-5} \text{ } [\Omega\text{-m}]$  for out-of-plane conduction. This unfortunately shows that even the data for CNT #8 might not be true as an out-of-plane conduction between graphitic layers is more conductive than the CNT and that cannot be true.

## Conclusion

The goal of this study is to gather more statistical data in understanding the electrical properties of CNTs. Understanding their resistivity is essential if CNTs will be used to replace metallic interconnects of modern technology. However, measuring the resistivity requires probing the sample with extremely sharp STM tips and this contains a very difficult learning curve. Even if the user can bring the probes to the sample safely, other issues can occur such as contact resistance, unwanted piezoelectric movement, and unnecessary charging of the sample. As such, there are not many papers listing the resistivity of CNTs because of this difficulty. It is clear to this author that more time is needed for a successful result. A literature search shows that other groups are also attempting to invent various methods to improve this low yielding data collection. One such group suggested putting the sample stage on the manipulator and on a tilt (12). This will allow for a safer probe contact to the surface approach but difficulty in probe movement throughout the sample; this is because the SEM has a high depth of field and will not give much information

parallel to the electron beam. However, these are all ideas that can be exploited. If more time was given to this author, then some of the more unorthodox procedures would have been attempted; these include: forced melting of the tungsten tips for zero oxide interference, deliberate charging of the CNT with a positive potential on a tip for CNT attraction, melting of a CNT to the tungsten probe, and many more. The hope is for an automatic process that would streamline these measurements and prove to the world the potential of CNTs as a viable replacement of metallic interconnects.

## ACKNOWLEDGEMENTS

I would like to thank the JUACEP for giving me this opportunity to visit Japan and do some interesting research. I would also like to thank my advisor, Professor Yahachi Saito, for his guidance and concern when I was sick. Mr. Chenxing Wang for teaching me the skills needed to probe the CNTs and how to make STM tips. Mr. Motofumi Karita for guiding me on the project and planning out logistics for my sample. And finally, Mr. Keita Yamaguchi for attempting to fix the furnace to grow my insulating substrate on time and making tips with me at the very beginning.

xxxxxxx.

## REFERENCES

1. *Recent advances on electromigration in very-large-scale-integration of interconnects.* **Tu, K. N.** 9, 2003, Journal of Applied Physics, Vol. 94, pp. 5451-5473.
2. **Dresselhaus, M.S., Dresselhaus, G. and Eklund, P.C.** *Science of fullerenes and carbon nanotubes.* 1st. San Diego : Elsevier Science Imprint, 1996.
3. *Helical microtubules of graphitic carbon.* **Sumio, Iijima.** 1991, Letters to Nature, Vol. 354, pp. 56-58.
4. *The Rise of Graphene.* **Geim, A.K. and Novoselov, K. S.** 3, 2007, Nature Materials, Vol. 6, pp. 183-191.
5. *Atomic structure and electronic properties of single-walled carbon nanotubes.* **Odom, Teri Wang, et al.** 1998, Letters to Nature, Vol. 391, pp. 62-64.
6. *Carbon Nanotubes: Synthesis, Integration, and Properties.* **Dai, Hongjie.** 2002, Acc. Chem. Res., Vol. 35, pp. 1035-104.
7. *Electrical Conductivity of Individual Carbon Nanotubes.* **Ebbesen, T.W., et al.** 1996, Nature, Vol. 382, pp. 54-56.
8. *Copper-Filled Carbon Nanotubes: Rheostatlike Behavior and Femtogram Copper Mass Transport.* **Golberg, Dmitri, et al.** 2007, Advanced Materials, Vol. 19, pp. 1937-1942.
9. **Iniewski, Krzysztof.** *Nanoelectronics: Nanowires, Molecular Electronics, and Nanodevices.* 1st. New York : McGraw-Hill, 2010.
10. *Large-scale synthesis of carbon nanotubes.* **Ebbesen, T.W. and Ajayan, P.M.** 1992, Letters to Nature, Vol. 358, pp. 220-222.
11. **Reuter, Piet.** *Probing Inside a Scanning Electron Microscope.* Graz : Graz University of Technology, 2010.

12. *Depth-detection methods for microgripper based CNT manipulation in a scanning electron microscope.* **Eichhorn, Volkmar, et al.** 2008, J. Micro-Nano Mech., Vol. 4, pp. 27-36.

13. *Electric and Mass Transport of a Carbon Nanotube Encapsulating a Copper Nano-Rod Studied by In-Situ Transmission Electron Microscopy.* **Kimura, F., et al.** 2010, Journal of Nanoscience and Nanotechnology, Vol. 10, pp. 3907-3909.

## Low Temperature Development of Metal Matrix Composites through Compression Torsion Process

Jonathan Quan

(Ph.D. Student) Department Materials Science and Engineering, UCLA  
jonquan@ucla.edu

Naoyuki Kanetake

Graduate School of Engineering, Nagoya University  
kanetake@numse.nagoya-u.ac.jp

### ABSTRACT

Compression Torsion Process (CTP) was used to create a metal matrix composite (MMC) at room temperature composed of  $\alpha$ -iron particles (3-5 $\mu$ m) sandwiched by 1050 aluminum discs (0.5cm in thickness and 4 cm in diameter). CTP is a useful, efficient process that combines grain refinement, solid-state welding, and powder compaction. When dissimilar materials are brought together to form MMC, there is a chance that undesirable intermetallics or compounds are formed if the process was conducted at high temperatures. However, CTP can hopefully eliminate this problem by creating the composite at room temperature, well below most fusion temperatures. Different conditions of this MMC were varied such as iron content, Al discs' surface roughness, and initial process temperature. Afterwards, the specimens' longitudinal cross section was characterized. Slight variations in the construction of the MMC helped develop more uniform microstructure and improved properties. Though XRD showed inconclusive results, Al-Fe intermetallic compounds were not identified.

### 1. INTRODUCTION

Metal Matrix Composites have become a popular topic amongst aerospace and automobile manufacturers because they offer an alternative to traditional metal and metal alloy components with reduced density and weight while experiencing an increase in strength and modulus<sup>1</sup>. By definition, metal matrix composites are composed of a metal matrix that encases reinforcement, which can be in either particulate or fibrous form. Two particular metals of great interest include aluminum and iron (steel). Joining these two materials have been quite difficult while also obtaining favorable property enhancements. Ideally, metal matrix composites experience increase strengthening when an applied load is transferred from the weaker matrix material to the higher strength reinforcements materials.

Metal matrices material selection criteria generally include: low density, easily processing, and good ductility. Aluminum usually fits these criteria and is a common matrix material. It has a density of 2.70 g·cm<sup>-3</sup>, low melting temperature of 933.3K, and a ductility of 42%. In addition, studies have been made about wettability with other materials. These criteria are important to help provide easy processing and integration with reinforcement materials<sup>2</sup>.

Reinforcement materials are chosen on a variety of

criteria, which includes, but not limited to cost, elastic modulus, density, melting temperature, strength, and compatibility with matrix material. Very often these reinforcement materials are ceramic materials because they generally have higher elastic modulus and also have very good thermal stability because of a high melting temperature<sup>3</sup>.

One of the major attractions of metal matrix composites is the variety of different processing routes to reproduce desirable microstructures and properties. Major routes include liquid phase, solid state, and a combination of a two-phase (solid-liquid) process. In any of these cases, it is important that there is good wetting of the two different materials to create a good interfacial bond, which is stronger than the surface tension of the metal matrix. Intuitively, the liquid phase processes is the most common of the process routes for metal matrix composites because it is easier to have molten matrix materials to encase over the reinforcements. Aluminum, a common matrix material has a relatively low melting temperature at 933.3K in comparison with common ceramic reinforcements. However, more process options have opened up because there have been recent solid-state process gains through severe plastic deformation (SPD) processes. Severe plastic deformation (SPD) has been a useful technique for grain refinement and solid-state welding<sup>1-3</sup>.

Grain refinement has been an important mechanical strengthening technique. The famous Hall-Petch equation shown in equation 1 shows that at the tensile strength ( $\sigma_y$ ) of the material is inversely proportionate to the grain size:

$$\sigma_y = \sigma_i + \frac{k}{\sqrt{D}} \quad (1)$$

where  $\sigma_i$  is the frictional stress,  $k_y$  is a material constant, and  $D$  is the dimension of the grain size. As the grain size decreases, the strength increases due to the dislocation density pile up. However, when the grain size is reduced below the 20nm range, the Hall-Petch equation breaks down where the strength decreases due to the inability of the grain to prevent dislocation movement<sup>4</sup>. Fortunately, SPD hits a threshold when it comes to grain refinement to ~100nm. Thus the breakdown of the Hall-Petch equation is rarely applicable for SPD<sup>5-6</sup>.

Solid-state welding is method of joining of metals that does not require the materials to reach a molten stage in order to form a bond. Instead, it uses mechanical pressure or

vibration to bring two materials together. Very often solid-state welding is used for dissimilar metals because of variety of incompatibilities make it difficult to weld for traditional fusion welding. These incompatibilities include differences in melting temperature, Thermal conductivity, and Coefficient of Thermal Expansion (CTE). Most importantly, fusion welding often leads to the undesirable development of brittle intermetallic or compound interfaces which can overall lead to diminished material properties<sup>7</sup>.

One particular SPD process, Compression Torsion Process (CTP), shown in figure 1, has presented itself as a useful, efficient method for grain refinement, solid-state welding, and powder compaction<sup>8-10</sup>.

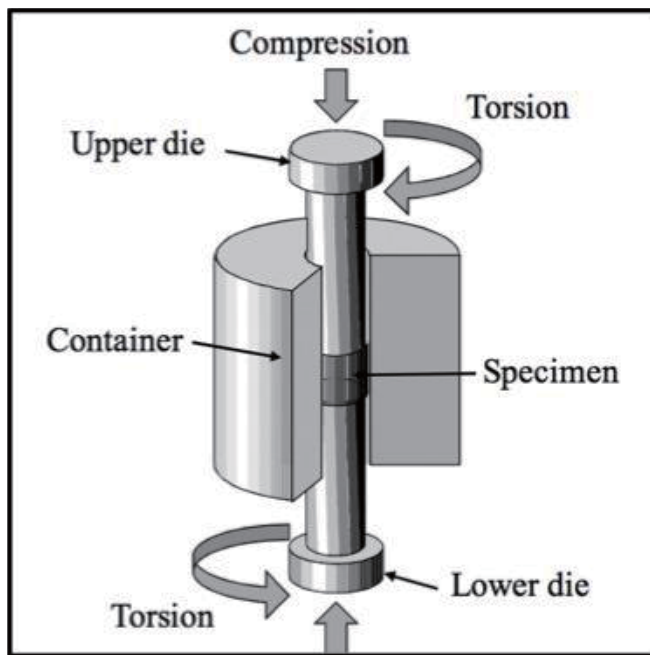


Fig.1 This shows the diagram of the CTP<sup>8</sup> (Courtesy of Kanetake)

The diagram shows two dies that compress and torque the material. To prevent outward expansion, a container is used. Often in literature, CTP is labeled as high-pressure torsion. In this process, bulk material can undergo grain refinement through a top-down process. With the combination of the torque, the material can undergo substantially more plastic deformation. For CTP, the shear strain  $\gamma$  is govern by equation 2:

$$\gamma = 2 \cdot N \frac{\pi \cdot r}{h} \quad (2)$$

where  $2\pi$  is the cylindrical constant,  $r$  is the radius of the cylinder,  $N$  is the number of rotations, and  $h$  is the height from the center of the cylinder. The shear strain can be related the effective strain  $\epsilon_{eff}$  (Von-Mises strain) is given by equation 3:

$$\epsilon_{eff} = \frac{\gamma}{\sqrt{3}} = N \frac{2 \pi \cdot r}{\sqrt{3} \cdot h} \quad (3)$$

In addition to the grain refinement, these equations help

explain the flow of the material during CTP. Recent attempts have been made to model the flow of different materials and alloys while being mixed together (limits). Additional modeling is needed to help predict the future microstructure outcomes<sup>11</sup>. For the joining of dissimilar materials, CTP uses high-pressure to plasticize the materials and have them deform to mechanically and chemically bond to each other. As far as powder compaction, CTP can effectively sinter powders together while also eliminating a substantial amount of porosity. In terms of environmentally friendly processing, this is an effective step because it can recycle scrap components without heat treatment<sup>12</sup>.

During CTP, a few parameters can be controlled and monitored: temperature, pressure, rotation speed, and torque. Usually, temperature is not a stable due to the heat generated by friction. It is important to monitor the heat to detect sudden jumps in temperature generated from chemical reaction, especially the development of intermetallics. The initial temperature can also be adjusted through heating elements. Generally for pressure and rotation speed, they are initially programmed and monitored for any fluctuations. Finally, the torque is monitored during CTP. The torque varies depending on the geometry and the material selection of the specimen.

CTP also presents itself as a good candidate for developing metal matrix composites through solid state welding. In a few recent papers, it has shown that under correct conditions certain combinations can create desirable intermetallics<sup>13-14</sup>. In many cases, intermetallics offer many significant advantages. These include higher modulus and greater melting temperature. However, in some cases, intermetallics are not desirable. The most classic case is aluminum iron intermetallics. The intermetallic compounds  $Fe_3Al$ ,  $FeAl$ ,  $FeAl_2$ ,  $Fe_2Al_5$ ,  $FeAl_3$  tend to be brittle, potentially causing areas of potential fracture<sup>15</sup>. If the two materials did not form these intermetallics, but still held strong chemical or mechanical bonds, this would help alleviate many critical weight issues for aerospace and automobile manufacturers. Unfortunately, many of these manufacturers have not yet made the transition to solid-state welding because they do not yet bring economical advantages over traditional fusion welding techniques.

In this study, the goal is to develop a metal matrix composite through CTP at low temperatures to minimize intermetallic development. The metal matrix composite will be comprised of a 1050 aluminum matrix with  $\alpha$ -phase iron powders (3-5 $\mu$ m) reinforcement. Three different conditions were carried out to observe how the iron would integrate into the aluminum: iron content, aluminum surface roughness, and temperature.

## 2. EXPERIMENT

The basic construction of the metal matrix composite samples consisted of an iron powder (3-5 $\mu$ m in particle diameter) layer sandwiched by two solid pure aluminum discs, as shown in figure 2a. The Al discs were 0.5 cm thick and 4cm in diameter. The iron powder were weighed in 10, 20, and 40 gram quantities to produce respective 1, 2, or 4 mm thick and 4cm in diameter disc layer. The purpose for

variant thicknesses would allow effective observation of mixing of the iron powder into the Al discs.

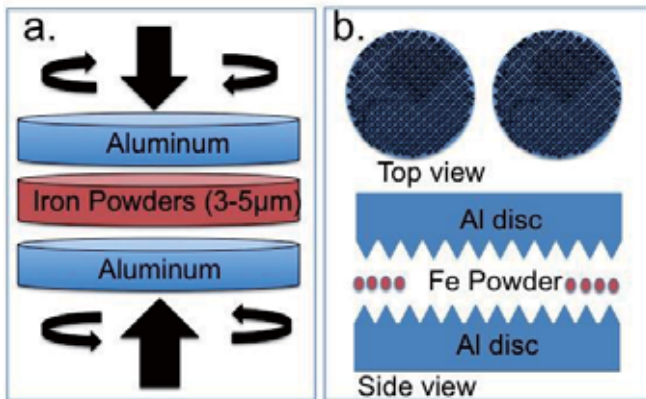


Fig.2. The metal matrix composite construction for CTP. 2a shows polished Al disc version of the CTP. 2b Shows shows an interpretation of the surface treatment of the Al disc before CTP

The CTP parameters included a compression stress of 100MPa, 30 turns, and 5rpm. These conditions were chosen because previous reports of Aluminum and alloys have shown good grain refinement distribution. During the process the temperature and the torque of both the bottom and the top surfaces of the sample were monitored. Unless specified, the initial temperatures of each sample construction was at room temperature ~300K.

In addition to the variation of iron content, a variation of the Al disc' surface roughness was observed. The objective of this variation would show how the surface roughness could play a role in the mixing of the iron powders in the Al matrix. There are two sets of samples of the respective 1, 2, and 4 gram iron powder batches were prepared. The first set features polished Al discs shown in figure 2a. The second set would include surface treated (ST), through periodic indentation of the Al's disc surface shown in figure 2b. The indentations were inverted 2x2 mm<sup>2</sup> pyramids spaced with no gap or overlap between them.

Afterwards, CTP was performed three more separate times of the sample with 20g of iron powder and Al surface treated discs were made at different initial temperatures: 373K, 523K and 623K. The higher temperature would change the way the iron powder would mix into the sample. Also, the higher temperature would increase the reactivity between Al and Fe. At 623K, Al becomes more soft because the temperature more than half the matrix melting temperature.

After developing these metal matrix composites through CTP under these different iron content, surface treatment, and temperature conditions, each sample was characterized. Before each characterization, each sample was cut in half along the longitudinal axis. They were then mechanically polished to mirror like surfaces. Optical images were taken to observe the flow of the iron particles. Using optical and scanning electron microscopy (SEM) the samples' microstructure was observed. The SEM was also equipped with Energy Dispersive Spectroscopy (EDS) to help determine the composition of different microstructures. The specimens were then analyzed under X-ray Diffraction

(XRD) using monochromatic Cu<sub>k</sub>α radiation to determine if any intermetallics were formed during the CTP process. Finally, microhardness testing was performed using a Vickers tip. Twelve spots in one of the quadrants of the specimen were tested under microhardness to help determine the strength distribution based on the flow of the iron particles.

### 3. RESULTS AND DISCUSSION

Under optical observation, shown in figure 3, all of the specimens show a vortex trend in metallic flow. The aluminum has a lighter tone compared with the iron particles. From this, gauge how the iron particles moved in the aluminum matrix. There are regions of light areas indicating that the matrix material is void of iron powders. In other areas, there are dark spots on the specimens indicating some of the iron did not mix with the aluminum matrix. Finally, there are areas of medium contrast possibly indicating that the iron particles mixed in the aluminum matrix.

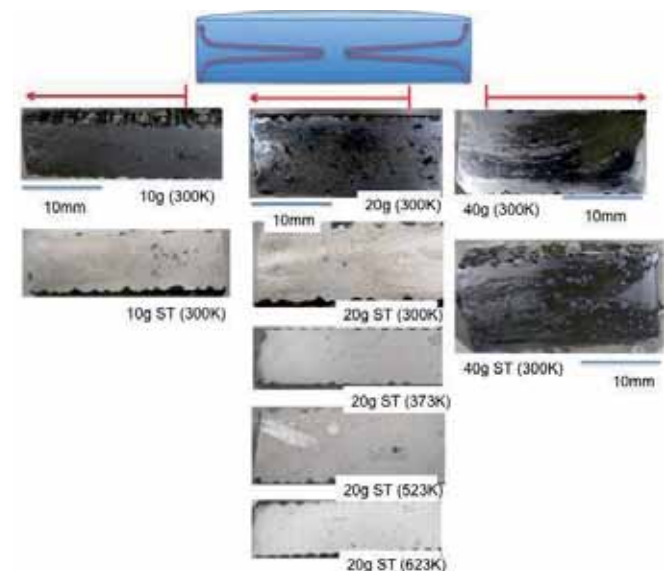


Fig. 3. This shows the nine samples developed through CTP. Differences in iron content, aluminum disc surface roughness, and process temperature were altered to better understand the distribution of iron particles in the aluminum matrix.

For the specimens with the surface treatment: 10g ST, 20g ST, and 40g ST; there was better uniform distribution with smaller iron concentration. Similar to the trend of the previous set the more iron content had harder time integrating the iron powder with the aluminum flow. The overall iron powder is the least uniform the 40g ST in comparison with the 10g ST and 20g ST samples. However, it is more important to point out that the surface treatment to the Al disc prior to CTP help provided better iron particle circulation and overall more uniform iron distribution. In comparison with the smooth disc samples, these surface treated samples showed much fewer areas of conglomerations of powders in the aluminum matrix. The thicker samples had less uniform distribution, which could be attributed to lower strain values. The experimental results

favorably agree with equation 2. The shorter the sample, the more strain it will receive, which helps increase the flow of the particles.

When comparing the 20g surface treated specimens at different initial temperature, there were two trends. The first trend showed that a slight increase in mobility for the Fe particles to move into the Al matrix when the temperature was slightly increased to 373K. The second trend showed a decrease in individual particle mobility when temperature was raised above 523K. Instead, large conglomerates of particles were more mobile. This led to disproportional mixing and less uniform microstructure. From figure 3, it also appears that the 20g ST 623K sample has less height than originally anticipated. During CTP, some of the aluminum matrix was lost because the material became soft and squeezed outside the container.

Using the SEM, the cross sections of each specimen were analyzed under higher magnification. Despite using just the secondary electron mode, there was distinct contrast between the matrix and the particles. In figure 4, coming from sample 40g, it shows three different types of microstructure regions found in all of the samples. The first microstructure region is the matrix showing a rough morphology with some pitting. The second microstructure region showed a conglomeration of particles (3-5mm in diameter). The third microstructure region showed well dispersed particles (3-5mm in diameter) in the rough matrix. In some areas, there were greater concentrations of these particles than others. These mixed regions also appeared to be harder because they were smoother than the matrix region and had visibly less scratches.

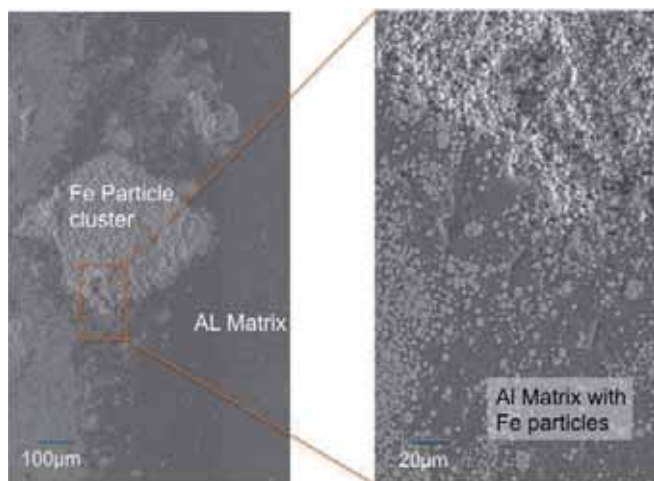


Fig. 4. This SEM image shows a region where all three microstructures are present: Fe particle cluster, Al matrix, and Fe particles distributed in the Al matrix

The flow of the particles was also much more clear using SEM. From the optical image in figure 5a, from sample 40g ST, we can clearly see that the flow of the particles beginning to split towards the upper corners. Under higher magnification using SEM in figure 5b, we can clearly see the flow of the iron particles beginning to shift upwards in a vortex form. Upon greater magnification in figure 5c, we can see that the lines of the flow are simply made up of

3-5mm particles. The aluminum area is quite interesting because the iron particles displaced the aluminum matrix that was originally in the right and left corners. Further study is needed to help provide an explanation for this. Many have reported that the end regions near the container is considered the dead space because the container inherently has some friction and holds back the material. The pitting of the matrix is also more visible. Figure 6 shows another example of the flow of particles in another region of the same specimen. Again we see similar flows by the particles. Large conglomeration of particles are not seen in sample 40g ST.

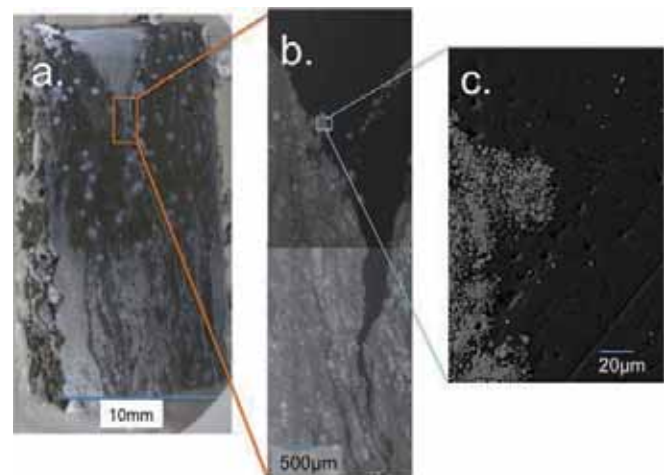


Fig. 5. In this image of sample 40g ST, it highlights the area where the iron particles are moving in a vortex shape.

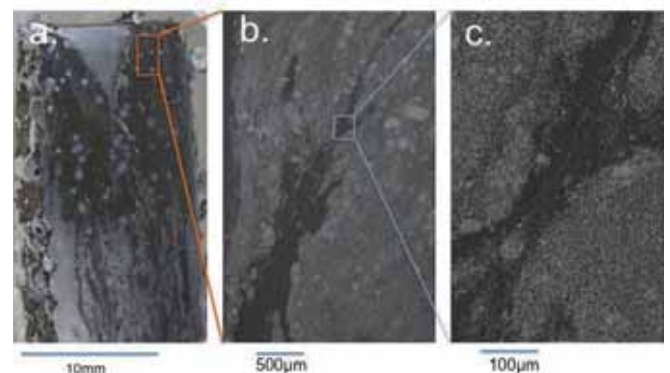


Fig. 6. Another area was analyzed from the sample 40g ST, it highlights the area where there is clearly flow of the particles.

Using EDS, an SEM image of a mixed microstructure was analyzed and is shown in figure 7. Chemical mapping both 1D and 2D were performed to help confirm the composition of the observed regions. The matrix material showed a dominant aluminum signal while also showing trace elements of molybdenum, silver, and silicon. The EDS map of the particles showed only iron signals. From EDS analysis, aluminum signals dominated the matrix region while iron signals dominated the particle regions and the conglomeration of the particle regions. From the SEM-EDS analysis, an intermetallic region between the Al matrix and the Fe particle could not be determined.

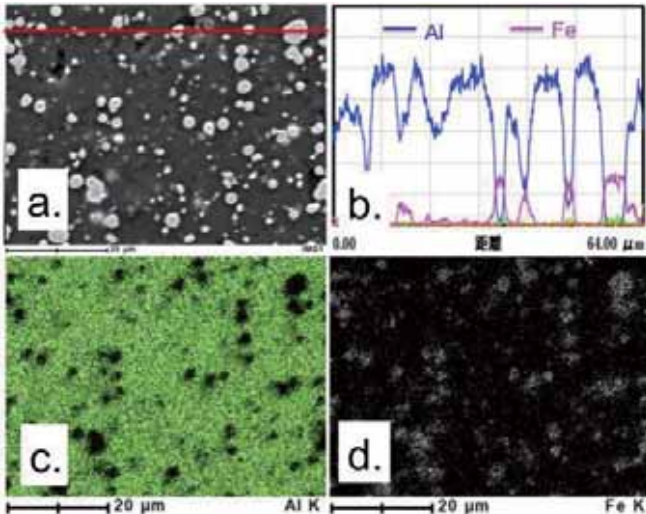


Fig. 7. The SEM image shows a region of iron particles mixed in with the aluminum matrix. 7b shows the 1D readings. 7c shows the Al K shell emissions. 7d shows the iron K shell emissions.

To help determine if intermetallics were formed and present, XRD was performed. The XRD patterns (figure 8) showed interesting results. As expected, strong aluminum and iron ( $\alpha$ -phase) diffraction peaks were identified. However, there appeared to be many unidentified smaller peaks. Fortunately, these peaks did not match the common XRD reference labels for the common  $\text{Fe}_3\text{Al}$ ,  $\text{FeAl}$ ,  $\text{FeAl}_2$ ,  $\text{Fe}_2\text{Al}_5$ , and  $\text{FeAl}_3$  intermetallics. In addition, the clay used to help mount the sample was also scanned but showed no peaks that were similar to the unidentified peaks. The peaks could have been generated from colloidal silica, which was used during mechanical polishing. This would explain the strong peak at  $34^\circ$ , which was common in all of the samples. However, the Si characteristic signal should have been much stronger from SEM-EDS analysis. Nevertheless, this XRD data provides some assurance that the CTP did not produce Al-Fe intermetallics while creating the metal matrix composite. However, until the smaller peaks are identified, there will always be some speculation on the byproducts that were produced in this process.

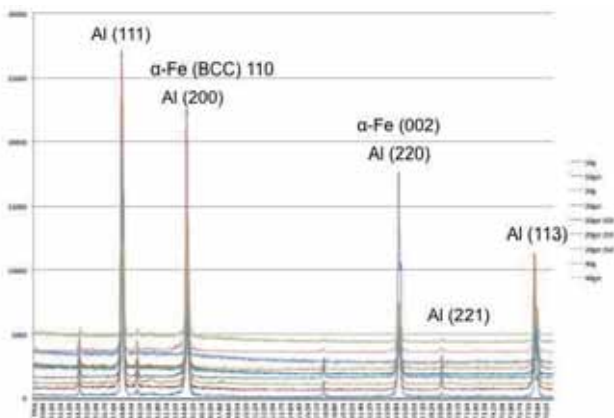


Fig 8. The XRD shows strong Al and Fe peaks. The smaller peaks were not identified, but they were confirmed to not match common Al-Fe intermetallic compounds.

In the microhardness testing, all the specimens showed similar results for the three microstructures. The first microstructure, the Al matrix, showed a statistical average of 29 Hv. This value is a 50% improvement compared to common 1050 Al and statistically the same with other severe plastically deformed aluminum. In the regions of concentrated iron powders, the microhardness was statistically 400Hv. It shows that the iron powder held well together and possibly encountered some sintering where chemically or mechanically. In the regions that showed iron powders mixed with Al matrix, the statistical value ranged from 40-140 Hv. The values depend on how many iron powders were mixed. Figure 9a shows an area where all three microstructures are present. As expected, areas where there were higher concentrations of iron powders were harder according to the microhardness reading. Evidence for this is shown in figure 9b where the diamond shaped indent has a disfigured shape due to the high concentration of iron powders in the lower left region.

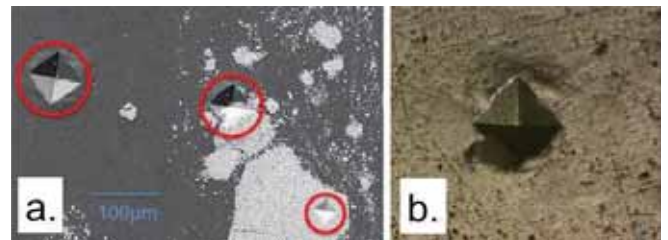


Fig. 9. Shows the indents created by the Vickers Hardness. One can see that the three different microstructures are present in 9a. The hardness of those three regions vary. In figure b, a small Fe cluster adds hardness to the surface and makes it difficult for the indenter to make a clean cut in the sample.

#### 4. CONCLUSION

In this experiment,  $\alpha$ -iron reinforcement particles ( $3\text{-}5\mu\text{m}$ ), sandwiched by 1050 aluminum discs, were successfully developed into metal matrix composites through CTP. This process was performed at low temperatures to prevent Al-Fe intermetallic reaction. In this work, different samples were made with different iron content, Al surface treatments, and initial processing temperatures. Each played a role in ability and inability for Fe reinforcement particles to integrate with the Al matrix. Microscopy showed three different microstructures, a rough Al matrix, a dense conglomeration of Fe particles, and a region of mixed iron particles in the Al matrix. EDS was able to help verify the chemical content of these microstructures while XRD was able to identify no Fe-Al intermetallics were developed. Finally, the hardness of the sample was shown some proportionality to the density of iron particles.

#### 5. REFERENCES

1. Ibrahim, I. A., F. A. Mohamed, and E. J. Lavernia. "Particulate reinforced metal matrix composites—a review." *Journal of materials science* 26.5 (1991): 1137-1156.

2. Singh, Harpreet, and Brij Kumar Dhindaw. "Metal Matrix Composites: Aluminum." *Wiley Encyclopedia of Composites* (2012).
3. Chawla, Nikhilesh, and Yu-Lin Shen. "Mechanical behavior of particle reinforced metal matrix composites." *Advanced engineering materials* 3.6 (2001): 357-370.
4. Estrin, Y., and A. Vinogradov. "Extreme grain refinement by severe plastic deformation: A wealth of challenging science." *Acta Materialia* 61.3 (2013): 782-817
5. Lowe, T. C., and R. Z. Valiev. "Producing nanoscale microstructures through severe plastic deformation." *JOM Journal of the Minerals, Metals and Materials Society* 52.4 (2000): 27-28.
6. El-Danaf, E. A., et al. "Enhancement of mechanical properties and grain size refinement of commercial purity aluminum 1050 processed by ECAP." *Materials Science and Engineering: A* 458.1 (2007): 226-234.
7. Chen, C. M., and R. Kovacevic. "Joining of Al 6061 alloy to AISI 1018 steel by combined effects of fusion and solid state welding." *International journal of machine tools and manufacture* 44.11 (2004): 1205-1214.
8. Kume, Yuji, et al. "Visualization and Quantification of Severe Internal Deformation on Compressive Torsion Process." *Materials Science Forum*. Vol. 654. 2010.
9. Kume, Yuji, et al. "Influence of Compressive Torsion Processing Temperature on Microstructure Refinement and Property of Aluminum Alloy." *Advanced Materials Research* 26 (2007): 133-136.
10. Tsuda, Satoshi, Makoto Kobashi, and Naoyuki Kanetake. "Producing technology of aluminum foam from machined chip waste." *Materials transactions* 47.9 (2006): 2125.
11. Zhilyaev, Alexander P., and Terence G. Langdon. "Using high-pressure torsion for metal processing: Fundamentals and applications." *Progress in Materials Science* 53.6 (2008): 893-979.
12. Inoue, Tadanobu, et al. "Distributions of Hardness and Strain during Compression in Pure Aluminum Processed with Equal-Channel Angular Pressing and Subsequent Annealing." *Materials transactions* 50.1 (2009): 27.
13. Edalati, Kaveh, et al. "In situ production of bulk intermetallic-based nanocomposites and nanostructured intermetallics by high-pressure torsion." *Scripta Materialia* 66.6 (2012): 386-389.
14. Oh-ishi, Keiichiro, et al. "High-pressure torsion for enhanced atomic diffusion and promoting solid-state reactions in the aluminum–copper system." *Acta Materialia* (2013).
15. Kobayashi, Shigeaki, and Takao Yakou. "Control of intermetallic compound layers at interface between steel and aluminum by diffusion-treatment." *Materials Science and Engineering: A* 338.1 (2002): 44-53.

## Acknowledgments:

Professor N. Kanetake  
Assistant Professor Y. Kume  
Kei Uchida  
Shohei Miyake  
Wataru Kimura  
JUACEP  
UCLA's Hybrid Materials Lab

## III-NITRIDE LEDS ON PATTERNED SILICON SUBSTRATES FABRICATION OF BACKSIDE CONTACTS VIA WET ETCHING

Christopher Roberts

Department of Materials Science and Engineering, UC Los Angeles  
ccroberts@ucla.edu

Supervisor: Hiroshi Amano

Graduate School of Engineering, Nagoya University  
amano@nuee.nagoya-u.ac.jp

### ABSTRACT

III-Nitride materials are useful in high power, high frequency, and lighting applications. Their built-in polarization fields can be varied based on growth orientation, allowing for rich device physics. The high cost of traditional substrates often limits the commercial application of III-N devices. As such, silicon substrates have been presented as a viable alternative by utilizing advanced epitaxial layer overgrowth techniques. However, the AlN buffer layer used between GaN and the Si substrate is highly resistive, and hinders the use of directly deposited backside contact methods. Here we investigate the feasibility of manufacturing backside contacts via wet etching through the Si substrate and AlN buffer layer to the underlying GaN layer.

### INTRODUCTION

Nitride based III-V semiconductor materials (III-N) have many advantageous electrical characteristics. For example, the bandgap of indium, aluminum, and gallium nitride (InN, AlN, GaN) can theoretically be engineered from 0.7-6.2 eV, however typical wavelengths run from the near UV to visible green.<sup>1,2</sup> Besides excellent potential for lighting applications, the large electron mobility and critical breakdown field make GaN based devices ideal for both high-speed and high-power applications such as high electron mobility transistors (HEMTS). GaN also boasts a thermal conductivity three times that of GaAs. GaN has a direct energy bandgap with all other valleys lying at least 2 eV

above the conduction band minima. Therefore, only the dispersion around the gamma point is usually considered, without concern for overshoot effects. Due to the anisotropic nature of the arrangement of III and N atoms (fig. 1a) in the polar  $\langle 0001 \rangle$  direction (fig. 1b), III-N materials contain a built-in electric fields stemming from their pyro- and piezoelectric polarizations. These fields vary with orientation from the polar c-plane (fig. 1b) to the nonpolar a-plane (fig. 1c). Polarization fields can act to localize carriers for high mobility transport. When GaN is epitaxially grown on commonly available substrates the lattice mismatch can introduce up to five times the density of dislocations found in other compound semiconductors, reducing mobility and acting as non-radiative recombination centers. Further complicating matters is the fact that the GaN material system lacks an efficient p-type dopant. Upon deposition, magnesium dopants form a hydrogen complex, which requires electron irradiation or an annealing treatment to separate, allowing for an activated Mg acceptor. The activation yield is limited to ~10%, putting an upper limit on p-type doping an order of magnitude below the solubility limit.<sup>3</sup>

Despite these challenges, the benefits of III-Nitride based devices have fueled a growing commercial industry for direct bandgap polar materials. III-N integration on silicon substrates has also been of interest for a number of reasons. Si substrates would reduce the manufacturing cost when compared to traditional substrates, especially SiC. Since Si wafer sizes are significantly larger than other substrates, a higher yield of devices per fabrication step could be achieved. Si substrates have ideal thermal and

electrical properties for integration with GaN. However, growth on Si results in a large dislocation density due to the greater thermal mismatch as compared to sapphire. Even more serious is the crack formation or delamination resulting from the relaxation of thick films. These problems demonstrate the importance of strain engineering for sufficient crystal quality. Si atoms on GaN reside on Ga-sites, with energy levels that are 22-42 meV below the conduction band, thus acting as donors.<sup>4,5</sup> Al rich AlN barriers must be present which are thick enough to prevent Si diffusion, further complicating the electronic and strain profile of the heterostructure. Nonetheless, III-N devices on Si substrates have proven economically viable in a number of applications.

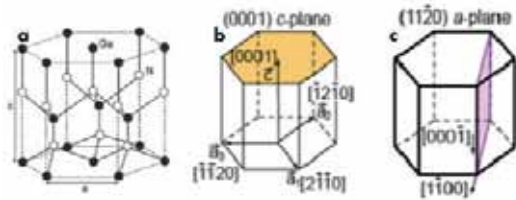


**Fig. 1) Wurtzite crystal structure**  
Position of Ga (black) and N (white) species (a). Devices grown in the (0001) c-plane orientation (b) will exhibit a polarization field, while the (11-20) a-plane (c) is free from such fields.<sup>6</sup>

In light emitting structures, carriers are confined such that wavefunction overlap enables electron transitions resulting in light emission. The polarization fields present in polar III-N materials cause the electron densities to be localized close to the surface at the Ga-terminated face, while the hole densities are confined to the N-terminated face, each within a triangular well. The wavefunction overlap is reduced and becomes a function of the well width. This so-called quantum confined Stark effect (QCSE) is detrimental to the carrier recombination efficiency. As a result, wider wells require an engineered staggered configuration to increase wavefunction overlap.<sup>7,8,9,10</sup> The emission spectra of polar materials has also been shown to be blueshifted at higher current injection.<sup>11,12</sup> However, some aspects of the polar geometry are beneficial. The valence subband character of polar and semipolar InGaN/GaN quantum wells have shown to be polarized themselves, leading to polarized light emission.<sup>13,14</sup> This holds potential applications in photonics and displays. However, in general III-N LEDs and laser diodes

would benefit greatly from the reduction of the QCSE that is afforded by the semipolar or nonpolar orientation. Reduction of the blueshift at high current injection has been reported for nonpolar structures,<sup>15</sup> as well as a reduction of turn-on voltage<sup>16</sup> and large light polarization.<sup>13</sup>

While using silicon as a growth substrate has many benefits, one key challenge is the integration of the n-type contact. The AlN buffer layer between the Si substrate and epitaxially grown GaN layers is highly resistant. As such, novel contact geometries must be explored to overcome this limitation.

## THEORY

The most common growth orientation for growth of polar c-plane GaN on Si is the Si(111) orientation, with a ~17% lattice mismatch, much greater than that of Si/SiC.<sup>6</sup> Thermal mismatch is also a concern, since the CTE of GaN is 5.59 ppm/°C, while that of Si is 3.59 ppm/°C.<sup>17</sup> Such large mismatch (~56%) causes cracks in the epilayer upon cooling, and a number of strain engineering techniques have been suggested. Utilizing wafer curvature prior to growth can help mitigate stress upon cooling. Using AlN buffer layers, fully coalesced, crack free GaN has been grown on Si(001) substrates.<sup>18</sup> Nitrogen implantation has also been shown to reduce the stress at the Si/AlN layer.<sup>19</sup> Most ingenious are the patterned substrates which allow for epitaxial layer overgrowth (ELO), which hinder the propagation of dislocations by directing their propagation away from the active surface.<sup>20,21</sup> Most of these techniques rely on a buffer layer between the Si substrate and GaN film in order to reduce strain and also block diffusion of Si into GaN.

Although a number of buffer layers have been studied for the Si/GaN system, AlN/AlGaIn has been shown to give the best quality, with films up to two microns thick.<sup>22</sup> AlN's CTE is between that of Si and GaN, making it an ideal material. Furthermore, AlN can limit diffusion of Si in GaN. A few monolayers of Al are deposited prior to protect the Si substrate from nitridation, as Si<sub>x</sub>N<sub>y</sub>, prevents planar growth of the AlN layer.<sup>19</sup> A multilayer high/low temperature AlN stack followed by a graded AlGaIn buffer layer has shown to inhibit Si diffusion into GaN while also greatly reducing strain.<sup>23</sup> The low temperature AlN acts as a diffusion barrier, while the graded AlGaIn is thought to partially block dislocations.

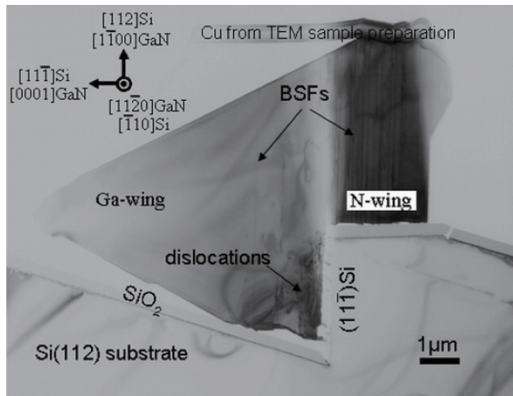


**Fig. 2) TEM cross-section of GaN on Si(112)** Threading dislocations from the Si(111) surface are restricted to the bottom of the GaN structure. Stacking faults can be seen in the N wing above the oxide mask, while the Ga wing is relatively defect free.<sup>26</sup>

Epitaxial layer overgrowth, coupled with graded buffer layers, has allowed high quality GaN films of varying polarities to be grown on Si substrates. Semipolar (1-101) and (11-22) films have been grown on Si(001) and Si(113) substrates, respectively.<sup>24,25</sup> These semipolar films have a reduction of the polarization field. Nonpolar m-plane (1-100) films, with zero polarization field, have also been demonstrated on Si(112).<sup>26</sup> ELO is achieved by first etching trenches into the silicon substrate, revealing (111) faces. First, a stripe oxide mask pattern is prepared and the Si allowed to be preferentially etched by potassium hydroxide. All but one of the exposed (111) faces is masked to inhibit growth. An exception to this masking process is growth using a Si(113) substrate, where the geometry of the crystallographic orientation only allows one face to grow.<sup>27</sup> One key difference in ELO versus planar growth lies with the strain management. While planar growth relies on graded buffer layers to relieve the elastic strain and hinder dislocation propagation, ELO utilizes a different active surface than that of the growth front, allowing the dislocations to propagate away from the active layer, as shown in figure 2.<sup>26</sup> Stacking faults are observed over the SiO<sub>2</sub> mask, however much of the Ga wing is defect free, allowing for high quality device growth. Interestingly, Sawaki and coworkers observed carbon and/or its complex act as a shallow acceptor in (1-101) N-face terminated ELO films grown on Si(001), as opposed to films grown in the (0001) or (11-22) orientations.<sup>24</sup> Besides decreasing the defect densities associated with

planar GaN growth, the ELO method offers access to the nonpolar and semipolar planes which previously required bulk substrate cutting. Therefore, precise control over the built-in polarization fields and possible novel doping techniques can be utilized for different device performance and characteristics.

Semipolar (1-101) LEDs have been grown on Si(001) substrates.<sup>27,28,29</sup> Semipolar structures have a reduced polarization field and thus reduced QCSE. Current droop, a phenomena caused by the Auger recombination process,<sup>30</sup> usually hinders the EQE, and thus light output, at high carrier injection. However, these semipolar devices show a reduction of the droop phenomena as well, as can be seen as an increase in EQE at high current densities.<sup>31</sup> The thick u-GaN and n-GaN layer acts to prevent absorption by the Si substrate. The reduced QCSE allows for greater carrier overlap and thus larger radiative recombination rates, additionally raising the IQE and thus EQE. Increasing the exposed active area by using the back n-contact geometry can additionally increase the EQE.

Lasers have also been demonstrated using the ELO technique. Semipolar (1-101) was grown on 8° offcut Si(100).<sup>32</sup> The structure utilized an AlGaIn cladding layer and multiple InGaIn/GaN quantum wells. At low excitation, the photoluminescence (PL) spectra of a single stripe is broad, but narrows markedly at higher excitation. However, even when lasing the spectra is broad due to exciting multiple laser stripes at once. The ELO method results in a reduction of dislocation density, which can be seen in the increase in IQE.<sup>32</sup>

A major drawback is the low electrical conductivity of the AlN layer for conductive substrate applications. AlN has been shown to be difficult to dope n-type, with maximum doping concentrations around 10<sup>16</sup>/cm<sup>3</sup>.<sup>23</sup> The optimal case would include an AlN layer thin enough for tunneling, however such dimensions no longer impede Si diffusion or act as a sufficient buffer layer. One way to avoid the AlN layer is to etch through the active layer to the underlying n-type layer, as shown in figure 3. This method is disadvantageous in that it reduces the device area used for light emission. In order to maximize the surface area while still providing an ohmic contact to the n-type GaN layer, vias etched from the bottom of the Si substrate through the AlN layer to the n-type GaN layer have been proposed. This vertical structure would also help to spread the current for more radiative recombination.

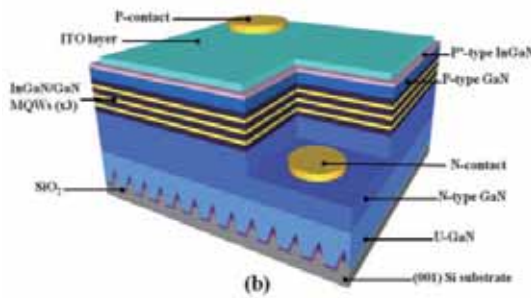


**Fig. 3) GaN MQW on patterned Si substrate**  
N-type contact is fashioned by etching through the active layer ( $\sim 1\mu\text{m}$ ) to the n-GaN layer.<sup>29</sup>

Traditionally, high aspect ratio vias have been fabricated using a number of techniques<sup>33</sup>, including wet etching,<sup>34</sup> plasma etching,<sup>35</sup> and laser drilling.<sup>36</sup> Laser drilling involves nanosecond bursts of laser energy, usually in to UV range, that bombard and ablate the target surface. Through silicon vias (TSV) have been fabricated using a multi-burst pulse train that enable smooth via walls with a 5:1 entrance to exit diameter ratio.<sup>37</sup> Deep reactive ion etching (DRIE) using the Bosch method has been readily adapted in the silicon industry due to its high aspect ratio ability and control over via dimensions.<sup>33</sup> Wet etching provides the simplest and least expensive method of via fabrication since it forgoes complicated machinery and instead relies on techniques already ubiquitous in the silicon industry and fabrication labs. However, wet etching is disadvantageous due to the difficulty reproducing the etching rates,<sup>38</sup> and anisotropic dependence on the crystallographic planes.<sup>39,40,41</sup>

The Bosch process is a combination of dry etching and surface passivation that enables high aspect ratios.<sup>42</sup> After the initial etch, the vias are polymerized, using gases such as  $\text{CHF}_3$  and Ar. Next, the Teflon-like bottom layer and some of the sidewall layer are etched using an etch gas such as  $\text{SF}_6$ ,  $\text{NF}_3$  or  $\text{CF}_4$ . The process is repeated, allowing the sidewall layer to be protected from the etching gas until the desired depth is reached. If the vias need to be isolated further to reduce crosstalk, a dielectric layer can be deposited.  $\text{SiO}_2$  has been used to act as both the dielectric layer and also a Cu diffusion barrier.<sup>43</sup>

Because of the alternative step behavior of the Bosch process, the sidewall profile develops a scallop pattern (fig. 4). Such a profile adds to the difficulty of uniform dielectric/seed deposition after etching. Electrodeposition of the seed layer has been suggested as a solution to

the coverage problem.<sup>44,45</sup> Another issue is the reliability of the TSVs after copper filling. Because of the thermal mismatch between copper (CTE 17.5 ppm/ $^\circ\text{C}$ ) and silicon (3.59 ppm/ $^\circ\text{C}$ ) thermal reliability is a concern.<sup>46</sup> Cracking of the polymerization layer can lead to problems such as Cu diffusion into the surrounding silicon. Further complicating matters is the dependence of the passivation on the gas flow, pressure, and rf power.<sup>47</sup>

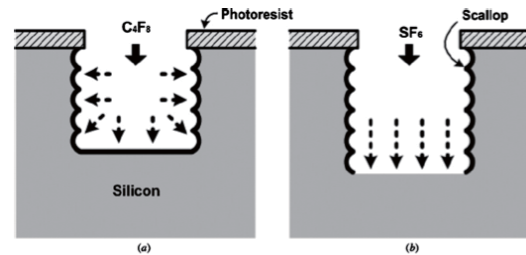
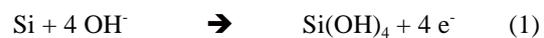


**Fig. 4) The Bosch Process**

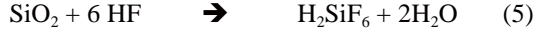
$\text{C}_4\text{F}_6$  gas polymerizes the surface (a).  $\text{SF}_6$  gas etches away the bottom layer (b).<sup>33</sup>

Wet etching is advantageous due to its low cost and simplicity. However, proper masking material and environmental factors have to be carefully considered. Commonly used etchants in the silicon industry include potassium hydroxide (KOH), tetra-methyl ammonium hydroxide (TMAH), and mixtures of hydrofluoric and nitric acid ( $\text{HF}:\text{HNO}_3$ ).<sup>33</sup> Common masks employed include silicon dioxide, silicon nitride, photoresist, and sputtered metal.<sup>48</sup> Both TMAH and KOH are reaction-limited etchants, demonstrating a linear relation between etch depth and time. The general etching reaction mechanism for basic solution etchants such as these is shown in equation 1 below.<sup>49</sup>



When etching with the  $\text{HF}:\text{HNO}_3$  system,  $\text{H}_2\text{O}$  is oftentimes substituted by acidic acid to increase the wettability of the Si surface. As such, this etchant system is commonly abbreviated HNA. The lack of acidic acid does not affect the etching mechanism. This system becomes diffusion limited with lower  $\text{HF}:\text{HNO}_3$  ratios, while decreasing the temperature dependence. As it is a diffusion limited reaction, there is an expected  $\sqrt{t}$  dependence of the etch depth. The general reaction for this system involves nitric acid oxidizing the silicon surface

(equations 2-4) and then the removal of oxidized silicon by HF (equation 5).<sup>50</sup>



KOH etchant results in smooth sidewalls due to the anisotropic selectivity of crystallographic facets, however its use is limited in the silicon industry due to the detrimental potassium ion. HF:HNO<sub>3</sub> is primarily used in back wafer thinning to remove the subsurface damage induced by mechanical lapping.<sup>51</sup> Wet etching has also been combined with other techniques such as laser drilling to improve the sidewall profile.<sup>52</sup> However, wet etching for high aspect ratios is disadvantageous due to the lack of control over etch depth since the rate of etching is difficult to reproduce consistently. As such, etch-stop layers are often employed. AlN and GaN have been shown to be highly resilient to many common etchants, especially at room temperature.<sup>53</sup> This opens the possibility of using the AlN and GaN materials as etch-stop layers.<sup>54</sup> The AlN layer in the Si/AlN/GaN system can be selectively etched by either KOH or NaOH.<sup>55</sup>

## EXPERIMENT

Commercially available, pre-patterned silicon substrates were diced into 10x14 mm dies. The received wafer was offcut by 8° towards the [-110] direction as indicated by the major flat. The pattern consisted of 1 μm wide SiO<sub>2</sub> stripes between 2 μm wide windows running perpendicular to the tilt direction. After dicing, dies were placed in an ultrasonic bath of acetone (10 min.) and methanol (5 min.) to remove particle contamination. After drying in N<sub>2</sub>, the dies were subjected to a 15 second HF (1:15) dip to remove the native oxide. Following the wash in DI H<sub>2</sub>O, dies were dried again in N<sub>2</sub> prior to etching. Dies were placed in a 35% wt. KOH bath at 42°C for 150 sec. to reveal ~300 nm of the Si (111) faces. Finally, a quick 3 second dip in HF (1:15) was used to passivate the surface.

In order to promote GaN growth along only the Si (111) facet with the proper 8° tilt, ~80 nm of SiO<sub>2</sub> was deposited on the other exposed facets using e-beam deposition. Afterwards, III-N material was grown via MOCVD using trimethyl aluminum (TMA), tri-methyl gallium (TMG), tri-methyl indium (TMI), and NH<sub>3</sub>. H<sub>2</sub> and N<sub>2</sub> were used as the carrier gases. Si and Mg

were used as the n- and p-type doping, respectively. First, an Al pretreatment was done immediately prior to AlN growth for 12 seconds to guard against the formation of Si<sub>x</sub>N<sub>y</sub>. Then the AlN buffer layer was epitaxially grown at 1420°C for 15 minutes to promote the planar growth of GaN and to prevent Si diffusion into the active layer. Unintentionally doped GaN was grown at 1230°C for 20 minutes, followed immediately by Si doped n-GaN layer grown at 1170°C for 20 minutes. Next, 5x InGa<sub>x</sub>N/GaN quantum wells were grown at 930°C for 30 minutes to form the MQW active region, followed by a GaN cap grown for 5 minutes. A p-AlGa<sub>x</sub>N electron blocking layer was then grown at 1020°C for 20 minutes. Finally, a Mg doped p-GaN layer was grown at 1020°C for 15 minutes, followed by a 3 minute p+Ga<sub>x</sub>N growth for the top contact layer. Dopant concentrations for the n- and p-type layers were nominally 5x10<sup>19</sup>/cm<sup>3</sup> and 1x10<sup>18</sup>/cm<sup>3</sup>, respectively.

Next, the dies were mounted onto a lapping fixture using wax adhesive, with the Si substrate exposed for mechanical lapping. Diamond slurry (3 μm) was used in free abrasive lapping in combination with a copper lapping plate. Two angular velocities were investigated, 15 and 30 rpm, while the use of additional air pressure was investigated in the range of 20-90 KPa.

After lapping to a thickness of 100 μm, dies were etched for variable times with a 1:5:2 HF:HNO<sub>3</sub>:H<sub>2</sub>O etchant with AlN acting as an etch-stop layer. This was followed by a 60 second HF (1:15) etch to remove any remaining SiO<sub>2</sub> layer the HF:HNO<sub>3</sub>:H<sub>2</sub>O etchant might have missed. Then the dies were etched for 60 seconds in 44% KOH at 85°C in an effort to selectively etch the ~70 nm AlN layer, with GaN acting as an etch-stop layer. After etching, an n-contact layer (Ti/Al, 20/100 nm) was deposited using e-beam deposition and annealed in an N<sub>2</sub> environment at 650°C for 5 minutes, followed by deposition of transparent p-contacts (Ni/Au, 5/5 nm) and annealing at 525°C for 5 minutes.

## RESULTS

Evaluation of the substrate preparation and epitaxial growth were done with an optical microscope and SEM. The defects in figure 5 illustrate GaN meltback etching, which occurs when Si reacts with Ga, and results from insufficient AlN coverage or high growth temperature. In general the epitaxial samples exhibited very little meltback. A SE SEM cross-sectional view of the Si substrate with epitaxial GaN layer on top reveals the 80 nm SiO<sub>2</sub>

masking layer, the 70 nm AlN buffer layer, the 1.5  $\mu\text{m}$  coalesced GaN layer, the MQW active region, and the 0.3  $\mu\text{m}$  p-GaN layer (fig. 6). The BSE SEM cross-sectional view of the active area clearly shows the n-GaN layer, MQW active region consisting of 5x InGaN/GaN quantum wells (10/30nm), a 50 nm GaN cap, 20 nm p-AlGaIn electron-blocking layer, and the top 0.3  $\mu\text{m}$  p-GaN layer (fig. 7).



**Fig. 5) Optical plan view of epitaxial u-GaN surface**

GaN meltback etching occurring for higher temperature growth or insufficient AlN coverage.

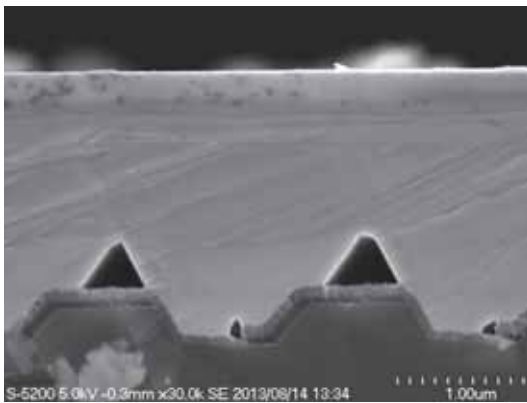


**Fig. 6) SE SEM cross-section of LED structure**

The darker SiO<sub>2</sub> and AlN seed layer are clearly visible between the Si substrate and epitaxial GaN, along with voids from the noncoalesced regions.

Lapping rates were measured for a variety of pressures and angular velocities (fig. 8). It was observed that the ratio to fixture to plate angular velocity was not as important for removal uniformity, possibly due to the small die sizes in comparison to the fixture and plate radii. Higher air pressures resulted in higher removal rates, but

also detrimental chipping of the die sides. Higher removal rates were also achieved by increasing the angular velocity, but at the cost of a higher standard deviation of the removal rate. Removal rate trends can be seen in fig. 9.



**Fig. 7) BSE SEM cross-section of LED structure**

From bottom to top: n-GaN, 5x InGaN/GaN quantum wells, p-AlGaIn electron blocking layer, and p-GaN with p+ top layer for contacts.

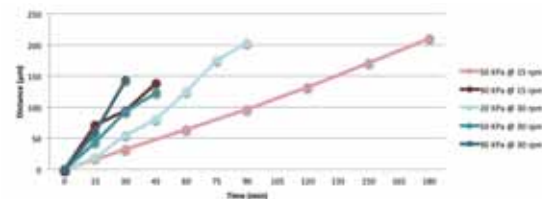


**Fig. 8) Reduced thickness vs. lapping time**

Higher pressures resulted in catastrophic die chipping prior to reaching ~200  $\mu\text{m}$  removed thickness.

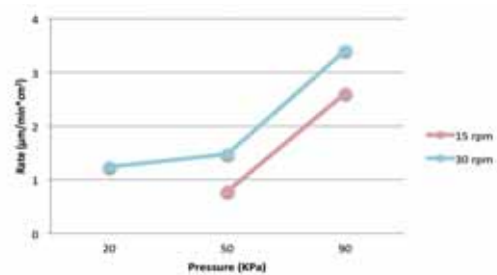


**Fig. 9) Removal rate vs. applied air pressure**

Dies were successfully lapped down to ~75  $\mu\text{m}$  thicknesses (fig. 10a) without chipping by applying lower pressures (20-50 KPa). Dies with larger thicknesses up to ~150  $\mu\text{m}$  (fig. 10b) were also investigated for greater mechanical strength. Since thinning of the dies increased the chances of brittle fracture during processing, the high-temperature tape that was to be used for the

etching mask was directly applied before removing the dies from the lapping fixture. Afterwards, the temperature was brought to 100°C to bring the fixture adhesive close to its melting point, and the dies removed.

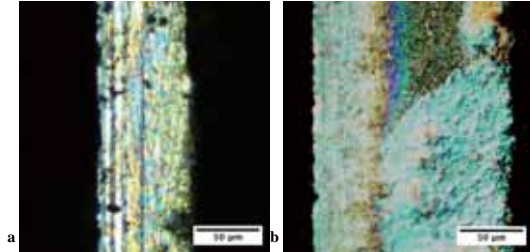


**Fig. 10) Optical cross-section of lapped wafers**  
Thicknesses of  $\sim 75 \mu\text{m}$  (a) were achieved using low applied pressures. In order to maintain mechanical strength, dies as thick as  $\sim 150 \mu\text{m}$  (b) were also investigated.

In order to wet etch vias through the Si substrate for n-contact deposition, a variety of etchants and masks were investigated. First, etch rates for TMAH, KOH, and HF:HNO<sub>3</sub>:H<sub>2</sub>O were investigated. Both TMAH and KOH are reaction-limited etchants, demonstrating a linear relation between etch depth and time. TMAH (2.38% at 90°C) was found to have an insufficiently low etch rate for practical via etching at  $60 \pm 30 \text{ nm/min}$  (fig. 11), although this etch rate was an order of magnitude lower than that found in literature.<sup>56</sup> KOH (44% @ 85°C) was found to be an order of magnitude higher, at  $560 \pm 120 \text{ nm/min}$  (fig. 12), however this rate was 2-3 times lower than that reported in literature.<sup>49,57</sup> The isotropic nature of this etch was also of concern, as the etching might terminate in an inverse pyramid of (111) facets before reaching the AlN layer.

The HNA system becomes diffusion limited with lower HF:HNO<sub>3</sub> ratios, while decreasing the temperature dependence. As it is a diffusion limited reaction, there is an expected  $\sqrt{t}$  dependence of the etch depth. The HF:HNO<sub>3</sub>:H<sub>2</sub>O (1:5:4 at 35°C) etchant, which was comprised of 1 part HF (50%), 5 parts NHO<sub>3</sub> (60%), and 4 parts DI H<sub>2</sub>O, displayed an insufficient etch rate of  $160 \pm 40 \text{ nm/min}$  (fig. 13). However, the higher concentration (1:5:2) displayed a sufficiently high etch rate at  $5.67 \mu\text{m/min}$ , also accompanied by a much higher standard deviation of  $1.18 \mu\text{m}$  (fig. 14). This etchant showed promise for etching sufficiently deep vias in an anisotropic manner.

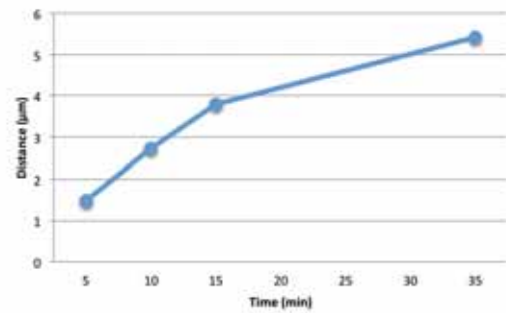


**Fig. 11) Etch depth as a function of time**  
TMAH (2.38% 90°C):  $60 \pm 30 \text{ nm/min}$ .

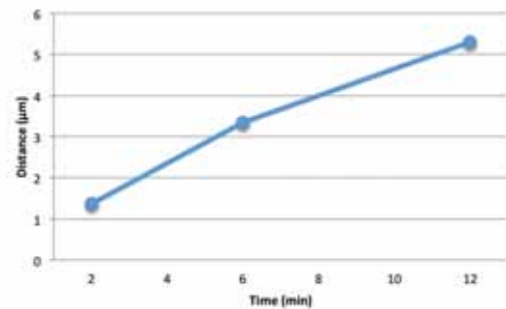


**Fig. 12) Etch depth as a function of time**  
KOH (44% @ 85°C):  $560 \pm 120 \text{ nm/min}$ .

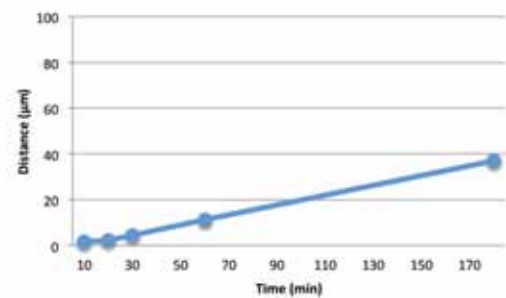


**Fig. 13) Etch depth as a function of time**  
HF:HNO<sub>3</sub>:H<sub>2</sub>O (1:5:4 35°C):  $160 \pm 40 \text{ nm/min}$ .

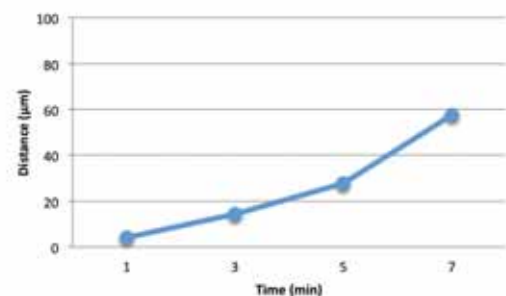


**Fig. 14) Etch depth as a function of time**  
HF:HNO<sub>3</sub>:H<sub>2</sub>O (1:5:2 35°C):  $5.7 \pm 1.2 \mu\text{m/min}$ .

KOH and HF:HNO<sub>3</sub>:H<sub>2</sub>O were used to investigate possible masking material for longer etches. Five different mask materials were tested; e-beam evaporated SiO<sub>2</sub>, rf sputtered SiN<sub>x</sub>, photoresist, dicing tape and high-temperature tape. The relative robustness of each material can be found in table 1. The etchant mechanism for HF:HNO<sub>3</sub>:H<sub>2</sub>O involves the oxidation of silicon by the nitric acid, which is then etched by the hydrofluoric acid. As such, SiO<sub>2</sub> was an ineffective mask for this etchant. However SiO<sub>2</sub> showed moderate resilience to etching in KOH. Sputtered ~250 nm thick SiN<sub>x</sub> masks were easily etched by both etchants in under 2 minutes.

**Table 1) Relative mask resilience vs. etchant**

Mask	HF:HNO <sub>3</sub> :H <sub>2</sub> O	KOH
E-beam SiO <sub>2</sub>	Low	Moderate
Sputtered SiN <sub>x</sub>	Low	Low
Photoresist	Low	Moderate
Dicing tape	Moderate	Moderate
High T tape	High	Moderate

Photoresist and dicing tape both showed moderate to low resilience against both etchants, with dicing tape detrimentally dissolving in both etchants around 10 minutes, and the high-temperature tape dissolving in KOH around 20 minutes. The dicing tape also showed signs of delamination around the mask openings, allowing for a greater amount of undercutting.

The most promising masking material was proven to be the high-temperature tape. In KOH, the upper tape material delaminated quickly, but the residual adhesive residue served as a mask for up to 5 minutes. Eventually KOH would etch ridges as the adhesive residue dissolved, detrimentally affecting the LED surface (fig. 15). The high-temperature tape was very resilient in the HF:HNO<sub>3</sub>:H<sub>2</sub>O etchant, showing no delamination and very mild undercutting even after 180 minutes. Because of anisotropic nature of the HF:HNO<sub>3</sub>:H<sub>2</sub>O etchant and the superiority of the high-temperature tape mask, this combination was chosen for the via etching through silicon.

Openings were made periodically in the high-temperature masking tape by piercing the tape with a uniform stylus ~200-300 μm in diameter. The tape was then attached to the lapped silicon substrate surface directly after lapping to allow for easy removal from the

lapping fixture. Once separated, the remaining surfaces of the die were covered in tape as well to protect the LED surface and die sides. Initially, etching times were calculated from the previously determined etch rates, however it was found that the etch rate for the masked samples was retarded by an order of magnitude. This was attributed to gas formation and bubble trapping at the entrance of the mask opening, so new etch rates were calculated using masked substrates. As shown in fig. 16, the fitting of a constant etch rate (~190 ±120 nm/min) was poor, and even among the same etch times the standard deviation of etch depth was on average ~20 μm.

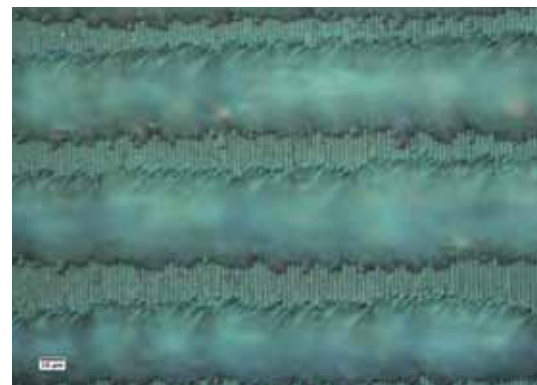


**Fig. 15) Optical plan view of KOH etched nitride layer**

Etched ridges under the tape mask after 20 minute KOH etch.

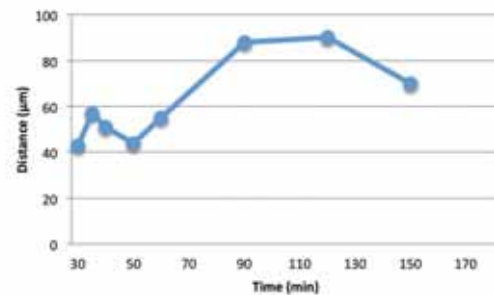


**Fig. 16) Etch depth as a function of time**  
HF:HNO<sub>3</sub>:H<sub>2</sub>O (1:5:2 35°C): 190 ±120 nm/min.

Samples were etched for 120 minutes in 1:5:2 HF:HNO<sub>3</sub>:H<sub>2</sub>O at 35°C utilizing the AlN material as an etch-stop layer. After etching, light could clearly be seen through the vias, indicating that the etchant had reached the nitride layers. Next, a 60 sec. etch in HF at 35°C was applied to remove any remaining SiO<sub>2</sub>. Then, a 60 sec. etch in 44% KOH at 85°C was applied to remove the resistive AlN layer. Finally, the high-temperature tape was carefully removed in

an acetone environment to help loosen the adhesive. The resulting via contact area ranges from 0.1~0.15 mm<sup>2</sup> (fig. 17 & 18). Deposition of the n-contact showed sufficient coverage (fig 19). The I-V characteristics show rectifying behavior, however the turn-on voltage was greater than 20 V (fig. 20). Although the intensity was too low to quantify, the emitted light appeared white, contrasted against the 780 nm peak resulting from photoluminescence data.

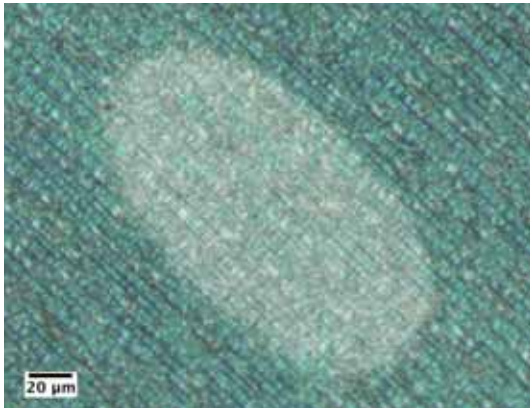


**Fig. 17) Optical plan view of the top (p-GaN) nitride layer**

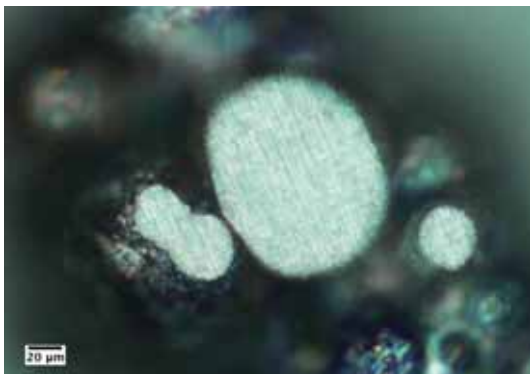


**Fig. 18) Optical plan view of the bottom nitride layer**



**Fig. 19) Optical plan view after n-contact deposition**

## DISCUSSION

The mechanical strength of the thinned Si substrate is critical to maintaining the device area. Chipping of the substrate during lapping occurred for pressures above 50 KPa. Substrates thinned below 100 μm were easily broken during handling even when supported by the tape mask. Substrates that were greater than 100 μm were difficult to etch down to the nitride layer, even with increased etching time.

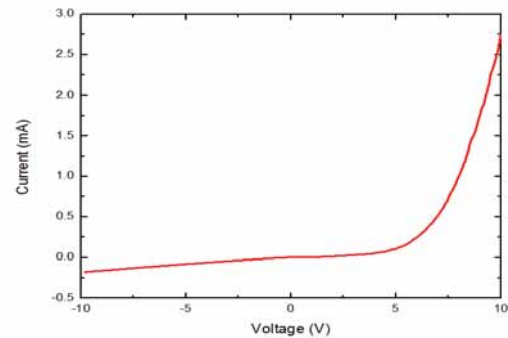


**Fig. 20) I-V Characteristics of the LED**

The high-temperature tape adhesive was also difficult to remove. Soaking in acetone for greater than 10 hours did not remove the adhesive, and sonication resulted in fracturing the dies. Physical removal in an acetone environment provided the best results, but this was also prone to fracturing the dies. Especially difficult was removal of the adhesive from the GaN surface without fracturing the nitride layers along the <111> directions (fig. 21). Such holes within the active layer provide a possible pathway for electrical shorting of the device. Future work should include a chemical based method for removing the tape adhesive without damaging the nitride layers.



**Fig. 21) Optical plan view of the top nitride layer**

Fracturing of the nitride layer along the <111> directions with tape removal.

It has not been shown that the AlN layer was fully etched by the KOH etchant, however the high-temperature tape should act as a sufficient mask for short additional etching if needed. The e-beam deposition provided sufficient coverage of the n-contact material on the backside nitride layer through the silicon substrate. When placed under bias, the LED structure succeeded in emitting light, although the intensity was small. Possible sources of resistance could be non-ohmic contacts, any remaining AlN layer, or resistive solder paste. Nevertheless, the reported procedure provides a method of via etching for back contact fabrication. By utilizing two different nitride materials for etch-stop layers, sufficiently large vias can be etched using commonly available wet etchants, and standard contact deposition techniques can be applied.

## CONCLUSION

The feasibility of using wet etchants for back-contact fabrication for III-N LEDs on patterned Si substrates has been investigated. Semipolar (1-101) InGaN/GaN LEDs were grown via MOCVD on patterned Si substrates. The nitride materials were used as etch-stop layers for etching through the 100  $\mu\text{m}$  lapped Si substrate and 70 nm AlN layer. Backside n-type contacts were deposited via e-beam evaporation and annealed at 650°C, followed by deposition of transparent p-type contacts. The structure LED structure succeeded in emitting light, although the intensity was too small to quantify. This method demonstrates a viable alternative for creating n-type contacts that maximize the surface area of the exposed active region.

## ACKNOWLEDGEMENTS

The author would like to thank the Amano laboratory of Nagoya University for their helpful guidance and training. This work was supported by the JASSO scholarship through the JUACEP summer 2013 program.

## REFERENCES

- <sup>1</sup> Kneissl, M. et al. Phys. Stat. Sol. A **200**, 118 (2003)
- <sup>2</sup> Neubert, B. et al. Appl. Phys. Lett. **87**, 182111 (2005)
- <sup>3</sup> Amano, H et al. Jpn. J. Appl. Phys. **28** p. 2112 (1989)
- <sup>4</sup> Wang H. et al. J. Appl. Phys., **87** p. 7859 (2000)
- <sup>5</sup> Götz, W. et al. Appl. Phys. Lett., **68** p. 3144 (1996)
- <sup>6</sup> Izyumskaya, N. et al. Proc. SPIE 7939, Gallium Nitride Materials and Devices VI, 79391 (2011)
- <sup>7</sup> Ibbetson, J.P. et al, Applied Physics Letters, **77** 2 (2000)
- <sup>8</sup> Wong, L. W. et al. Appl. Phys. Lett., **73** 139 (1998)
- <sup>9</sup> Dimitrov, R. et al. Phys. Stat. Sol.(a), **168** 7 (1998)
- <sup>10</sup> Arif, R.A. et al. IEEE Journal of Quantum Electronics, **44** 6 p. 573 (2008)

- <sup>11</sup> Liao, C. et al. Journal of Applied Physics, **108** 6 p. 063107 (2010)
- <sup>12</sup> Park, S. et al. Applied Physics Letters, **94** 4 p. 041109 (2009)
- <sup>13</sup> Hongping Z. et al. IEEE Journal of Selected Topics in Quantum Electronics, **15** 4 p. 1104 (2009)
- <sup>14</sup> Chang, S.J. et al. IEEE Journal of Selected Topics in Quantum Electronics, **8** 2 p. 278 (2002)
- <sup>15</sup> Gardner, N.F. et al. Applied Physics Letters, **86** 11 pp.111101 (2005)
- <sup>16</sup> Schubert, M. et al. Appl. Phys. Lett. **91**, 051117 (2007)
- <sup>17</sup> Li, T, Mastro, M and A. Dadrgar, III-V Compound Semiconductors. CRC Press (2011)
- <sup>18</sup> Dagar, A. et al. Japanese Journal of Applied Physics, **39** L1183 (2000)
- <sup>19</sup> Jamil, M. et al. Applied Physics Letters **87** 082103 (2005)
- <sup>20</sup> Li T. K and S.T. Hsu, US patent 7358160 (2008)
- <sup>21</sup> Lei L. Appl. Phys. Express **5** 051001 (2012)
- <sup>22</sup> Lin, K. L.. et al. Applied Physics Letters, **91** 222111 (2007)
- <sup>23</sup> Izyumskaya, N. et al. Proc. SPIE 7939, Gallium Nitride Materials and Devices VI, 79391 (2011)
- <sup>24</sup> Sawaki, N. et al. Journal of Crystal Growth, **311** 10 p. 2867 (2009)
- <sup>25</sup> Suzuki, N et al. Journal of Crystal Growth **311** 10 p. 2875 (2009)
- <sup>26</sup> Izyumskaya, N. et al. Journal of Crystal Growth, **314** 1 p. 129 (2011)
- <sup>27</sup> Chiu, C. et al. J. of Crystal Growth **318** p.500 (2011)
- <sup>28</sup> Hikosaka, T. et al. phys. stat. sol. (c) **5**, 6 p. 2234 (2008)
- <sup>29</sup> Chiu, C. et al. Proc. SPIE 7939, Gallium Nitride Materials and Devices VI, 79391 (2011)
- <sup>30</sup> Kioupakis, E. et al. Appl. Phys. Lett. **101** 231107 (2012)
- <sup>31</sup> Chiu, C. et al. Proc. SPIE 7939, Gallium Nitride Materials and Devices VI, 79391 (2011)
- <sup>32</sup> Murase, T. et al. Physica Status Solidi (c) **8** 7-8 p. 2160 (2011)
- <sup>33</sup> Wu, B et al. Jour. Appl. Phys. **108**, 051101 (2010)
- <sup>34</sup> Meerakker, J. et al. J. of the Electromec. Soc. **147** 7 p. 2757 (2002)
- <sup>35</sup> Takizawa, T. et al. IEEE Electronic Components and Technology Conference 2002
- <sup>36</sup> X. Li, T. Abe, Y. Liu, t al. Microelectromech. Syst. **11**, 625 (2002)
- <sup>37</sup> Tan, B. J. Micromech. Microeng. **16** p. 109 (2006)
- <sup>38</sup> Burns, D. MEMS Materials and Processes Handbook (Ghodssi & Lin, 2011)
- <sup>39</sup> Kim, S. et al. Sixth IEEE International Conference on Emerging Technologies and Factory Automation Proceedings, p. 248, IEEE, New York, NY. (1997)
- <sup>40</sup> Bassous, E. IEEE Trans. Electron Devices **25**, 1178 (1978)
- Kim, S et al. Technical Digest of the 15th Sensor Symposium, p. 193, The Institute of Electrical Engineers of Japan IEEJ
- <sup>41</sup> Charlton, M. and Parker, G. J. Micromech. Microeng. **7**, 155(1997)
- <sup>42</sup> Laermer and A. Schilp, "Method of anisotropically etching silicon," U.S. Patent No. 5501893 (1996)
- <sup>43</sup> Sage, S. Microelectronic Engineering **107** p.61 (2013)
- <sup>44</sup> Shen, S. et al. Microelectronic Engineering **105** p.25 (2013)
- <sup>45</sup> Defforge, T. Microelectronic Engineering **106** p160 (2013)
- <sup>46</sup> Lui, X. et al. IEEE Electronic Components and Technology Conference (2009)
- <sup>47</sup> Ayón, A. et al. J. Electrochem. Soc. **146** 339 (1999)
- <sup>48</sup> Powell, O. et al. Device and Process Technologies for MEMS, Microelectronics, and Photonics III Proceedings of SPIE **5276** (2004)
- <sup>49</sup> [www.microchemicals.eu/technical\\_information](http://www.microchemicals.eu/technical_information)
- <sup>50</sup> Yamamura, K & Mitani, T. Surf. Interface Anal. **40** p.1011 (2008)

- <sup>51</sup> Yoshikawa, K et al. ECS Trans. **45** 6 p. 141 (2012)
- <sup>52</sup> Tang, C. et al. Micro & Nano Letters **7** 7 p 693 (2012)
- <sup>53</sup> Zhuang, D & Edgar, J. Mat Sci. and Eng. R **48** 1-46 (2005)
- <sup>54</sup> Mileham, J. et al. J. Vac. Sci. Technol. A **14** 3 p. 836 (1996)
- <sup>55</sup> Mileham, J et al. Appl. Phys. Lett. **67**, 8 (1995)
- <sup>56</sup> Schnakenberg, U et al. Proc. 1991 Int. Conf. Solid-State Sensors and Actuators (Tansducers '91) San Fransisco, USA p.815 (1991)
- <sup>57</sup> Seidel, H. et al. J. Electrochem. Soc. (USA) **137** p 3626-32, 1990

# Hand Layup Fabrication with Vacuum Bagging and Compression Testing of Cross-ply Carbon Fiber Pre-Preg Tubes

Justin Wang

Department of Materials Science and Engineering, Henry Samueli School of Engineering, UCLA  
justinwangsj@ucla.edu

Supervisor: Dr. Takashi Ishikawa

Department of Aerospace Engineering, Graduate School of Engineering, Nagoya University  
ishikawa@nae.nagoya-u.ac.jp

## Abstract

Carbon fiber tubes in 0/90 and  $\pm 45$  degree orientations were fabricated from cross-ply pre-preg sheets and compressed until failure to observe buckling behaviors. Due to the limited time available to complete the project, only one sample of each orientation was fabricated and tested. Aluminum support pieces for testing are normally required, but were not developed also due to limited time and machine availability. Compression testing resulted in failure at the tube ends, with only the  $\pm 45$  tube showing buckling failure. This experiment was an exercise in hand fabrication of carbon fiber pre-preg sheets cured using vacuum bagging in an autoclave. Testing results demonstrated that the lack of proper end supports gives unsatisfactory buckling results.

## Introduction

The use of carbon fiber pre-preg sheet laminates in forming structural parts has been increasingly prevalent, especially in the aerospace field. Pre-pregs are Fiber Reinforced Polymers (FRP) that have epoxy resin already pre-impregnated with the fibers.

Pre-pregs have the advantage of being easier to use and less messy than a traditional composite wet layup. As a sufficient amount of resin is already infused with the fibers, there is no need to prepare resin separately and apply it on fiber laminates.

There are two types of resin: thermoplastic and thermoset, the latter of which is more common. This experiment will use thermoset pre-preg. Unlike thermoplastic resin, thermoset resin has a limited shelf life since it cures slowly at room temperature. To extend the usability of thermoset pre-pregs, the material is kept frozen to slow the curing process prior to use. Elevated temperatures in an oven or autoclave will speed up the resin cure, typically in a few hours.

Fabrication of composite tubes is common in rocketry projects, whether at home or in school clubs. The high specific strength of composites such as glass fiber (GFRP) or carbon fiber (CFRP) composites are highly desirable for rocket structures, where weight savings are of great importance.

The author of this paper worked two years in the UCLA Rocket Project club fabricating large carbon fiber body tubes for the club's experimental hybrid-fueled rocket. The pre-preg sheets used for the project were unidirectional: the fibers in the composite are all aligned in a single direction. The overall design of the rocket was over 400 cm (13 feet) tall, 20 cm (8 inches) wide, and wet weight of about 80 kg (180 pounds). In order to obtain good structural rigidity for such a large and heavy rocket, all tubes were 8-ply in 0/90 orientation. The main body tubes were about 20 cm (8 inches) in diameter, and about 61 cm (24 inches) long.

Tube layup was performed carefully by hand with several team members, since the large tubes

had a lot of area to cover and required many skilled hands to align and secure films and plies properly. Each layer was made using a single ply with exact dimensions calculated based upon the circumference at the layer. Each subsequent layer had to be larger due to the slight increase in circumference from the previous layers' thickness. Each carefully-fabricated tube took many hours to prepare, since poorly applied films and plies would create strength-weakening flaws or wrinkles that would take more time to smoothen out. Since the rocket club lacked access to an autoclave for pressurized curing, heat shrink tape was used in order to consolidate CFRP layers and eliminate air bubbles. Due to the lack of student availability and project schedule constraints, the mechanical strength of the tubes was not assessed experimentally.

This study was an experiment in fabricating tubes out of carbon fiber pre-preg with a 0/90 cross-ply weave, as opposed to a unidirectional lamina. Based on the tools available in Dr. Takashi Ishikawa's lab, it was decided to attempt tube fabrication using a vacuum bagging method in an autoclave. With an autoclave, external pressure could be applied on a vacuum bagged tube to better consolidate the CFRP plies while curing. For testing, the tubes were compressed axially. The buckling behavior of the tubes was observed and the failure strength of the tubes was calculated.

The compression testing machine used has a load limit of 200 kN, so optimal thickness and dimensions of the tube had to be calculated to prevent overloading the machine. The mechanical properties of the cross-ply CFRP are given in Table 1. Equation 1, obtained from Bengoichi's text, describes the critical strength of a composite tube as a function of thickness (h), radius (r), and Young's modulus (E). When combined with the general uniaxial stress formula (Eq. 2), and the cross-sectional area of the tube (Eq. 3), equation 4 was obtained.

$$\sigma_{cr} = 0.6 \frac{Eh}{r} \quad (1)$$

$$\sigma = \frac{F}{A} \quad (2)$$

$$\begin{aligned} A &= \pi(r+h)^2 - \pi r^2 \\ &= 2\pi rh + \pi h^2 \end{aligned} \quad (3)$$

$$F = 0.6 \frac{Eh}{r} (2\pi rh - \pi h^2) \quad (4)$$

Equation 4 was used to calculate the maximum thickness possible, with a chosen tube diameter of 10 cm. It was determined that a thickness of 1 mm or less was allowed. Each CFRP ply is 0.24 mm thick, so a four layer thick tube would provide optimal testing results without overloading the machine.

## Experiment

Two carbon fiber tubes in different orientations were formed by hand and cured using a vacuum bagging method and an autoclave. The pre-preg CFRP used was W3101/Q112J made by Toho Tenax Co., Ltd. Due to the size constraints of the carbon fiber roll, which is only in the 0/90 orientation, the four layer thick cylinders were produced by using two sized pre-preg sheets. Each sheet is long enough to form two full layers thickness when wrapped in a spiral fashion around an aluminum bar or mandrel. By using this two-sheet method, it's possible to cut out sheets in both the 0/90 and  $\pm 45$  orientations with the same size, thereby allowing both tubes to be produced in the same way.

The dimensions of the tube desired were 10 cm diameter with a length of 15 cm. During fabrication, a tube of 20 cm length was designed in order to allow trimming for smoother ends.

In order to properly seal the vacuum bag around the carbon fiber tube, the vacuum cup needs to rest on a flat surface. The bagging assembly was designed using a flat aluminum plate and the carbon fiber on an aluminum cylinder. By placing the cylinder on the plate, a proper vacuum bag can be prepared along with room for the vacuum cup assembly.

For the plastic films that are wrapped around the tube underneath and over the carbon fiber layup, extra length was provided so that the films can overlap themselves to ensure proper

coverage. Each of the carbon fiber sheets was measured to form two layers precisely. The minor increase in length of the second sheet necessitated due to the change in circumference from the thickness of the first sheet was neglected; both first and second sheets were cut to the same dimensions.

It was of utmost importance that each film and carbon fiber layer placed on the cylinder was as tightly packed and smoothed out as possible. Any slack or trapped air would cause the cured tube to have wrinkles, which is less optimal for testing. Rubber paint rollers and attention to detail greatly helped in ensuring a smooth wrapping.

The 20 cm long tubes were trimmed down to 15 cm using a band saw. The band saw, while effective at cutting through carbon fiber, was difficult to align such that the ends cut cleanly. The tubes were placed around a 15 cm long Al cylinder of the same diameter as the mandrel used for tube layup, and the tubes were filed down to ensure smooth and parallel ends.

The procedure for the fabrication of the tube is as follows:

1. Prepare aluminum plate by drawing out a 25 cm x 40 cm box, and a 25 cm line for cylinder alignment.
2. Cut out 25 cm x 40 cm release film and place onto Al plate. Secure and seal release film with sealant tape
3. Prepare aluminum cylinder by marking out placement lines for the outer bagging (25 cm apart), and for the carbon fiber layup (20 cm apart) between the bagging lines.
4. Cut 25 cm x 35 cm release film and place onto Al cylinder. Secure and seal release film with sealant tape.
5. Cut 1 cm slit in film to allow air to escape.
6. Take out roll of carbon fiber and wipe away frost. Cut out carbon fiber in double length dimensions: 20 cm x 64 cm. Cut out two pieces in both 0/90 and  $\pm 45$  orientations.
7. Wrap first CF layer on cylinder. Take care that the sheet is properly aligned and is tightly wrapped. (Fig. 1)
8. Wrap second CF layer on top of the first. Begin wrapping on the opposite side (180°) away from the end of the first.
9. Wrap with a layer of porous plastic film. Film should fully cover carbon fiber.
10. Wrap breather cloth around tube.
11. Place a layer of breather cloth on top of the release film on the aluminum plate. Add an extra layer where the cylinder will rest, as well as a small patch where the vacuum cup will sit.
12. Place Al cylinder with CF tube on the Al plate. Ensure proper alignment and proper bonding of the sealant.
13. Wrap neck of vacuum cup with a strip of sealant tape and place on the plate breather cloth.
14. Cut out a sufficiently sized sheet of vacuum bagging film and cover cylinder/plate assembly. Before placing, cut out a small hole for the vacuum cup neck. Start the seal from the center of the cylinder and work outwards. Take extra care when covering the acute angle between the cylinder and plate – additional sealant may be necessary. (Fig. 2)
15. Cure in autoclave for 6 hours. Use a compression pressure of 0.59 MPa and chamber temperature of 130°C.
16. Remove from autoclave, unwrap bagging, and remove CF tube from Al cylinder. (Fig. 3)
17. Trim both ends of CF tube down to a length of 15 cm. Use filing or sanding to smooth and flatten the ends. (Fig. 4)

For compression testing, each tube was placed under a compression machine without end supports. While measuring the force load, the

tube was compressed axially until failure, or when a decrease in loading force was observed.

## Results

The first tube, in 0/90 orientation, cured into a very smooth tube. The  $\pm 45$  tube cured with many wrinkles, despite the care taken during layup. Two people worked together to put together the first tube while only one person made the second, so the reason for the higher quality first tube may be that multiple people working as team produces better results – as was the case in the UCLA rocket project.

Tube cutting and filing was not much of an issue, and the trimmed tubes were satisfactory. However, cutting the tubes produced a lot of carbon fiber dust that needed to be cleaned up with a vacuum cleaner.

Tube testing was quick and produced unsatisfactory results, as was expected without the use of metal support pieces. The  $\pm 45$  failed with noticeable buckling behavior near one end of the tube (Fig. 5), while the 0/90 tube was simply crushed at one end of the tube before the load decreased (Fig. 6). Aluminum support pieces placed the ends would have prevented failure near the ends, and would have been more likely to produce buckling failure near the center of the tubes.

The failure strength is shown in Table 2. The much lower strength of the 0/90 tube may be due to the early crushing failure of the tubes at one end. It should be noted that the  $\pm 45$  tubes had a significantly larger amount of wrinkles, which may have contributed to the higher failure strength and buckling failure.

## Conclusion

While the compression tests were a failure, it demonstrated the need for proper tube end supports. If more time was available, more tubes could be fabricated for testing which can be of higher quality through user practice and experience. The use of the vacuum bagging method proved the viability of the manufacturing method as shown by the first tube made. Quality of the tubes may be improved if two people work together to lay up the tube. Overall, this

experiment demonstrated that production of tubes is greatly dependent on the tools available, and the skill and care of the producers.

## Acknowledgements

Dr. Takashi Ishikawa  
Dr. Jenn-Ming Yang  
Daiki Yamagami  
JUACEP Staff

## References

- [1] Johnson, Todd. "What Are Prepregs." Composites / Plastics. About.com, n.d. Web. 17 Aug. 2013.
- [2] Bengoichi, Shingo; Ishikawa, Takashi. "Advanced Composite Materials Engineering." Baifukan. May, 2005.

## Figures and Tables



Fig. 1: CFRP plies wrapped around Al cylinder.

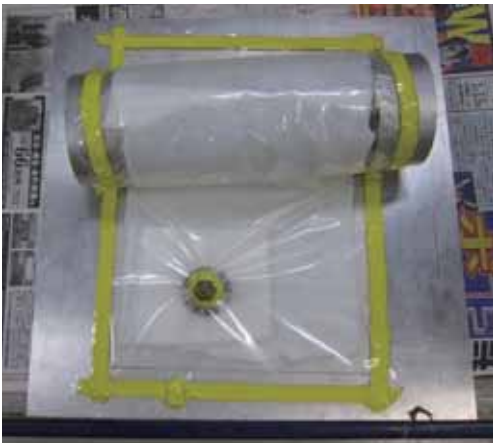


Fig. 2: A complete vacuum bagged tube. Note that this cylinder was poorly aligned with the aluminum plate.



Fig. 3: Vacuum bagged tube after curing in autoclave. Note the resin that has been absorbed by the breather cloth.

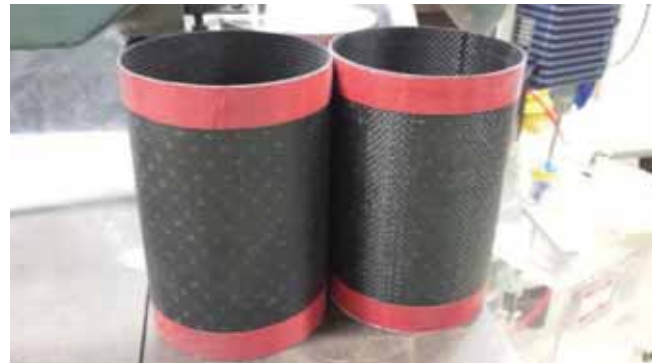


Fig. 4: Trimmed tubes. Red tape was used as guidance for cutting.

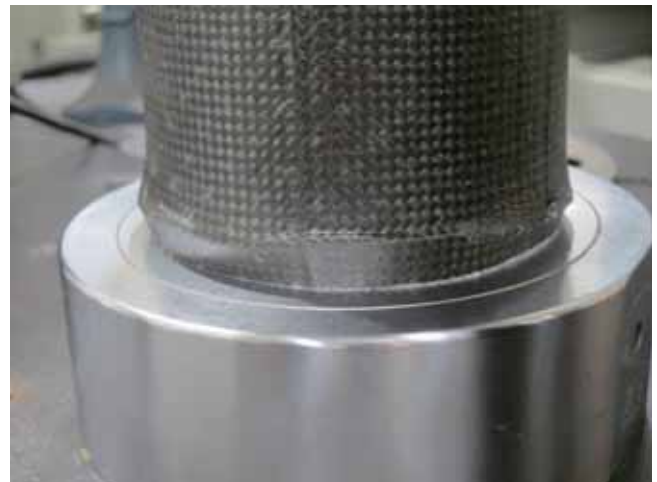


Fig. 5: Buckling failure near one end of the  $\pm 45$  tube.



Fig. 6: Crushed end of 0/90 tube.

Table 1, mechanical properties of W3101/Q112J:

$E_{1,2}$ (GPa)	G (GPa)	$\nu_{12}$
60	4.1	0.12

Table 2, failure strength results:

	$\sigma_{\text{failure}}$ (GPa)
0/90	47
$\pm 45$	73

# EFFECT OF ADDING SOLVENT ELEMENT ON 4H-SiC BY USING TOP SEED SOLUTION GROWTH

Yaodong Wang

Department of Materials Science and Engineering, University of California, Los Angeles  
yaodongwang1@gmail.com

Supervisor: Toru Ujihara

Graduate School of Engineering, Nagoya University  
ujihara@nagoya-u.jp

## ABSTRACT

Top seeded solution growth of 4H-SiC was performed for Pure-Si, Si-Ti-C, and Si-Cr-C solution. Ti and Cr concentration were varied to study the effect on the surface morphology of epitaxial layer. Differential interference contrast microscope with Namarski type prism and laser microscope were used to investigate the terrace width and step height. Pure-Si and Si-20Cr-C with large macrostep were considered to be the candidate to observe threading screw dislocation conversion. Si-18Ti-C solution with extremely smooth C-face and thick epitaxial layer was considered to be promising candidate to fabricate high-quality 4H-SiC for long-time growth.

## Introduction

Silicon carbide (SiC) is wide bandgap semiconductor, which has high thermal conductivity, high saturated electron drift velocity and potentially used in high frequency and high power electronic devices. As Moore's law approaches to the end of era, SiC is considered to be possible candidate to compete with conventional semiconductor such as Si and GaAs. SiC is also known as its excellent physical strength and high resistance to chemical attack

Although SiC-based devices have attracted widespread interest for high-voltage power applications due to the material's high breakdown field and long minority carrier lifetimes, it is notoriously known that SiC has suffered with a variety of issues such as polytype stability and large dislocation density and multiple types of dislocation. For example, the performance of SiC-based bipolar devices has been reported to degrade under forward-bias conditions due to the expansion of Shockley-type stacking faults (SF).

Stacking fault is a one or two layer interruption in the stacking sequence of the crystal structure. These interruption carry a certain stacking fault energy. Due to low stacking fault energy, SiC is known to exist in a larger number of different polytypes. The most commonly found polytypes in

SiC are 3C, 4H and 6H. The main crystal structures of SiC are cubic and hexagonal. Ramsdell notation is used to describe the polytypes. The number of this notation system indicates the number of repeating layers in a unit cell and a latter represents crystal symmetry. For example, for 3C SiC, stacking sequence repeats per three layer in ABCAC periodic stacking. And C indicates cubic crystal symmetry. For commercially used 4H SiC, stacking sequence is ABCBACB with hexagonal crystal symmetry. For 6H SiC, stacking sequence repeats per every six layer in ABCACBACB with hexagonal crystal symmetry.

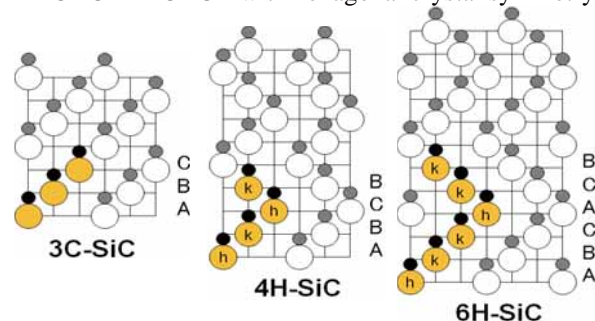


Fig. 1. Crystal structure and stacking sequence of 3C-, 4H-, and 6H-SiC

SiC crystallizes in close-packed structures consisting of bi-layer of Si and C atoms. Each layer of atoms along c-axis can occupy three different positions A, B and C. Each bi-layer Si-C pair should be considered one unit in close-packed stacking. Due to low stacking fault energy, however, stacking can be changed along c-axis, which results in hundreds of polytypes exist in SiC.



Fig. 2. Schematic diagram of bilayer of SiC

*C-face and Si-face*

SiC is a polar material. If cutting perpendicular to the *c*-axis it exhibits polar surfaces, where the top most layer is covered by either Si or C atoms. By convention, outermost face in [0001] direction are referred to Si-face whereas the [000 $\bar{1}$ ] direction C-face. Due to the different free surface energies, the growth is different on these faces. The lower surface free energy corresponding to C-face causes more uniform nucleation and growth. The nature of the nucleation and growth of SiC on C-face (000 $\bar{1}$ ) is different than Si face (0001).

#### Dislocation Conversion

SiC is suffered with large number of dislocation density and multiple types of dislocation including micropipe, threading screw dislocation (TSD) and threading edge dislocation (TED), basal plane dislocation (BPD), stacking fault (Perfect and partial dislocations: Shockly-type stacking fault etc) and low angle grain boundaries; triangular depressions, carrot-like grooves on the surface. There are three major types of dislocation in SiC crystals. Among them, TSD/TED and BPD are commonly observed types of dislocation, which are harmful to device quality. The amount of dislocation density can be performed by etch pit density measurement (EPD) on Si face by using molten KOH etching at 500 °C. Due to isotropic etching on C-face, however, KOH etching is hardly effective. Tilt polishing and new etching approach are required. Another effective way to investigate dislocation density is using reflection Synchrotron X-ray topography, which is non-destructive measurement and able to obtain high contrast dislocation image.

#### Growth mode

##### Growth modes

There are three classically epitaxial growth modes. Volmer-Weber (VW) is 3D island growth mode. Adatoms-adatoms interactions are stronger than those to the surface, which results in the formation of three-dimensional adatoms clusters or islands.

In Frank-van der Merve (FV) growth is characterized by layer-by-layer growth mode, and also known as 2D layer growth. Adatoms preferentially attach to the sites on surface resulting in atomically smooth layers.

The third epitaxial growth mode is known as Stranski-Krastanov (SK) growth mode. SK growth mode is a combination of both 2D layer growth and 3D island growth.



Fig. 3. Volmer-Weber, Frank-van der Merve and Stranski-Krastanov growth modes

The growth mode and the film morphology are strongly related. Surface morphology strongly determines the structural properties such as perfection, flatness, smoothness and interface abruptness (Epitaxial growth of thin films).

In addition to the three well-known growth modes mentioned above, there are another three distinct growth modes: step flow, step bunching and spiral growth modes.

##### Step flow

Step flow growth is often found in the epitaxial growth on misoriented cut substrate. In this mode, unidirectional step flow is induced by substrate misorientation, or off-cut angle  $\theta$ . Step height  $h$  and terrace width  $w$  obey simple trigonometric relation:

$$\tan \theta = \frac{h}{w}$$



Fig. 4. Schematic diagram of step flow

##### Step bunching

During step flow, step bunching is often observed when multiple steps move with same speed. In general, macrosteps form and has thickness of hundreds to thousands of microsteps.

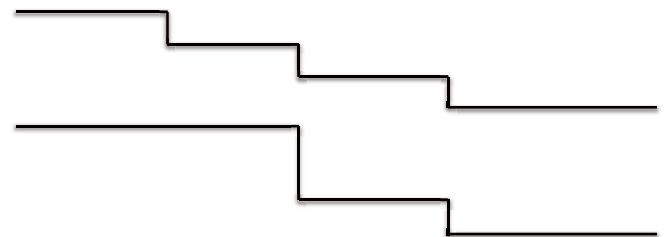


Fig. 4. Schematic diagram of the formation of multiple steps to form step bunching

##### Spiral Growth

Spiral growth initiates on screw dislocation on the substrate.

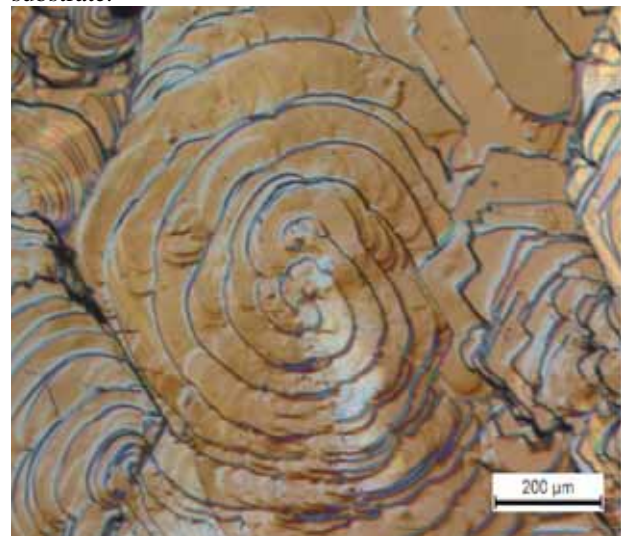


Fig. 5. Spiral growth of Si-10V-C grown for 5h at 1650 °C formed along *c* axis parallel to [0001]

The 2D nucleation arises on a perfect surface. However, real crystals contain defects such as screw dislocations which are typically present in hexagonal SiC substrates. Due

to a screw dislocation on the surface a step is formed. The adatoms arrive and are incorporated into the step which is moving forward, but it does not disappear. Thus the new step do not need to appear for the growth to continue and the 2D nucleation is suppressed.

#### TSSG growth of off-axis 4H-SiC

In growth from solutions, the components (the solute) for the crystal growth are dissolved in a solvent. The concentration of crystalizing species is often low and depends on the solubility of the components at the growth temperature. The solute species have to diffuse from the bulk of the solution to the growth. A gradient of the solute concentration exists at the interface due to the depletion of the growth species close to the interface.

Advantages of using TSSG:

1. low cost
2. high-quality crystal obtained due to near to thermodynamic equilibrium

Disadvantages of using TSSG:

1. low growth rate
2. difficult to find a suitable solvent with sufficient solubility and low incorporation of its constituent into the crystal

#### Substrate wetting

During solution growth, uniform wetting with small wetting angle is expected. A larger wetting angle results in a bad wetting, i.e., the liquid does not cover the solid to a desirable extent. As the wetting angle decreases the covered area of the solid increases. This is preferred in liquid phase growth since the properties of the grown material will be more uniform. The solution and substrate are brought into contact and kept at the same temperature until growth is terminated.

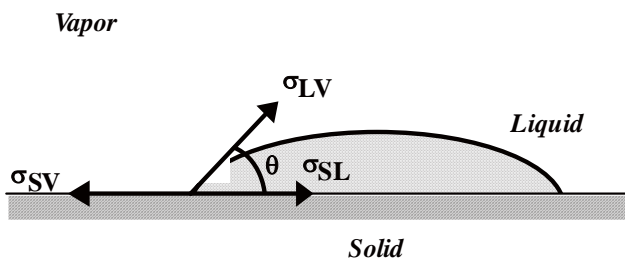


Fig. 6. Wetting between a liquid and a solid with surface/interfacial energies

$$\sigma_{SV} = \sigma_{LV} \cos \theta + \sigma_{SL}$$

In previous study, threading dislocations were reported to be converted into the defects in the basal plane on Si face during the solution growth of 4H-SiC. This conversion is related with the macrosteps (height above 100  $\mu\text{m}$ ) on the crystal surface, which provide the imaging force for the conversion of threading dislocation. By using this conversion mechanism, high quality crystals can be obtained on the Si face. However, the dislocation conversion of

threading dislocation on C-face has not been observed because of the smooth surface on the C-face. We try to grow SiC crystal on the C face by adding the third elements in silicon containing solution. By controlling the surface morphologies on the C-face, high conversion ratio of threading dislocation on the C-face is expected.

In this study, 4H-SiC crystals will be grown on off-axis seed crystals by top seeded solution growth (TSSG) method. Different third elements X will be added into the silicon solution (Si-X-C) to investigate their effect on surface morphology. After growth, Nomarski microscope and laser microscope were mainly used to evaluate surface morphology and step height.

#### Experimental Procedure

LPE growth experiments were performed by a dipping method in an induction furnace. High purity Si chips (11N) were melted in high-purity graphite crucible at atmospheric pressure of 6N grade He ( $2.2 \times 10^5$ ). Substrates were PVT-grown 4H-SiC (000-1) C-face with misorientation ( $2^\circ$  tilt seed crystal). The size of the substrate used for this study was  $10 \times 10 \text{ mm}^2$ . Si melt was kept under  $1450^\circ\text{C}$  for 2 hrs until Si was fully melted and Carbon fully dissolved. The temperature gradient was  $11.42^\circ\text{C}/\text{cm}$ , which was measured by W-Re thermocouple. The high-purity graphite crucibles were used as a container for the pure-Si melt and third element solvent and as a carbon source. Before growth, wafers of n-type 4H SiC with  $2^\circ$  off-axis with respect to [0001] direction were used in the study. The samples were cleaned ultrasonically using deionized water ( $18.2 \text{ M}\Omega\text{cm}$ ), methanol, acetone and HF. And the basic solution was prepared by melting high-purity Si chunks, Cr chips and Ti pellets 3-mol in total.

#### Introduction of interior of LPE furnace

The interior of TSSG furnace uses RF-heating. The coils induce current in a graphite container to provide heat. Directly inside the coil there is a quartz tube that houses insulation. The schematic diagram of TSSG is shown in Fig. x. SiX mixture were melted in the crucible in the inert He atmosphere. High purity graphite crucible both act as solution container and C source. High-purity He gas was used to maintain the inner growth environment.

The  $10 \times 10 \text{ mm}$   $2^\circ$ -tilt 4H-SiC substrates with c-axis toward  $[1\bar{1}20]$  and C-face upwards were dipped into the Si-C, Si-18at%Ti-C, Si-23at%Ti-C, Si-28at%Ti-C, Si-20at%Cr-C, Si-25at%Cr-C, Si-30at%Cr-C, Si-10%V solution at the same growth condition for 5 hour. The heating profile was illustrated in Fig. 8. The substrate was immediately deposited at a relatively higher temperature region in the solution to achieve a slight meltback of the substrate surface. After that the substrate was moved to a growth position where the solution was supersaturated with SiC. The growth temperature was set at  $1650^\circ\text{C}$  for 5h. After the growth, the substrate was removed from the solution by pulling out. The solidified Si on the substrate was eliminated by HF- $2\text{HNO}_3$  in volume ratio. Surface

morphology was investigated by using differential interference-contrast microscope (DIC) with Nomarski prism and Confocal Laser Microscope. Epi-layer thickness was investigated by cleavage and polishing method and further studied by transparent optical microscope..

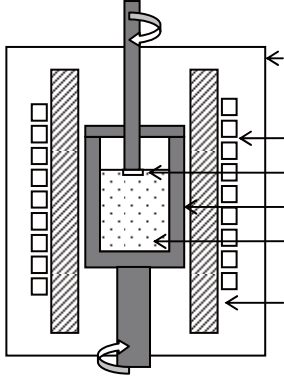


Fig. 7. Schematic diagram of top seeded solution growth (TSSG)

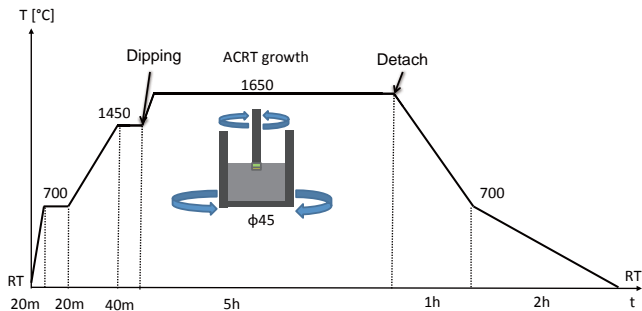


Fig. 8. Heating profile of 4H-SiC by Top Seeded Solution Growth

Accelerated crucible rotation technique (ACRT) was performed during the growth under relatively low temperature comparing to vapor phase epitaxy. In the ACRT growth, the crucible and seed crystal were counter rotating with alternating direction (clockwise and counter clockwise).

## Results

Solution growth on the 2° tilt off-axis 4H-SiC substrate. The homogeneous liquid phase epitaxy was carried out on 2° tilt off-axis 4H-SiC substrate with C-face placed upwards and Si-face downwards. The temperature gradient was kept around 11.24 °C/cm.

Considering 4H-SiC is mainly used for electronic power device such as bipolar junction transistor (BJT) and MSOFET, reduction of dislocation density and particularly the type of dislocation is critically important. Among various types of dislocation, basal plane dislocation should be reduced because they induced forward voltage instability for bipolar devices. It was reported that BPD in the substrate is converted to TD in the epilayer, which is less harmful to bipolar device, by etch-pit density measurement on Si-face.

### *TSD to Frank-type stacking fault conversion*

It is known that the conversion ratio of TSD to Frank-type stacking fault is highly influenced by the surface polarity of the seed crystal and step height. After conversion, the stacking faults laterally propagate towards the outside of the crystal, which can be removed to left with high-quality part of crystal.

TSD conversion occurs due to image force of large macrosteps on Si-face. However, due to lower surface energy, C-face behaves smooth and macrosteps is normally smaller than that of Si-face. In order to expect similar dislocation conversion to occur, third solvent was added to study the surface morphology, i.e., step height, terrace width, step angle, surface roughness.

In the experiment, Pure-Si, Si-Ti-C, and Si-Cr-C solution have been employed to grow 4H-SiC by TSSG method.

### Pure-Si

Fig. 9a. shows the DIC image of C-face of Pure-Si grown for 5h at 1650 °C with large macrosteps on C-face. Comparing to C-face, Si-face behaves conventional zigzag-shape step flow.

### Si-Ti-C

Ti with 18, 23 and 28 atomic percent were added into the Pure-Si mel. It has shown from DIC image that C-face behaved very smooth while Si-face is significantly rough and also more attractive for poly-Si deposition.

### Si-Cr-C

Furthermore, Cr with 20, 30 and 40 atomic percent was added into Pure-Si melt. Fig 13 shows the step flow of C-face of Si-20Cr-C. Zigzag step flow has also been found in its Si-face. However, with increasing Cr concentration, C-face wettability reduces dramatically when Cr reaches 30 at%. Fig. 14b shows the C-face surface morphology image with rarely grown layer with lower-face Si-face morphology due to transparent light. When further increasing Cr concentration to 40 at%, growth mode changes from step flow to spiral growth on C-face.

### Si-V-C

Fig 16 shows the C-face of V, it has been found that C-face of Si-10V-C has been covered by spiral growth while step flow growth mode occurs on its Si-face with less terrace width.



Fig. 9a. C-face of Pure-Si grown for 5h

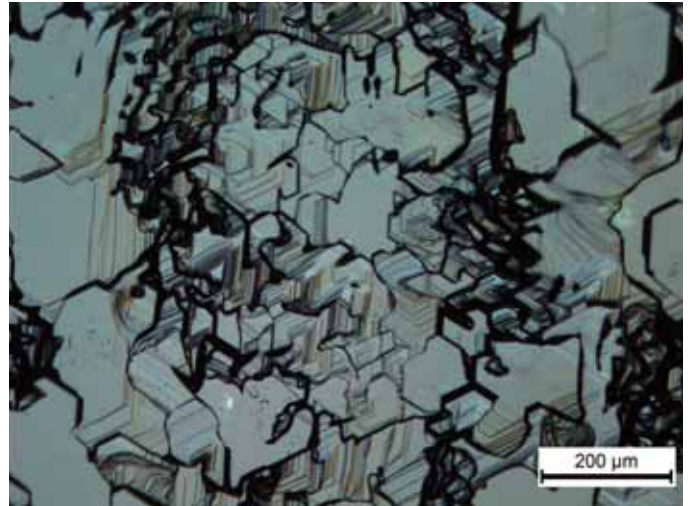


Fig. 10b. Si-face of Si-18Ti-C grown for 5h



Fig. 9a. Si-face of Pure-Si grown for 5h

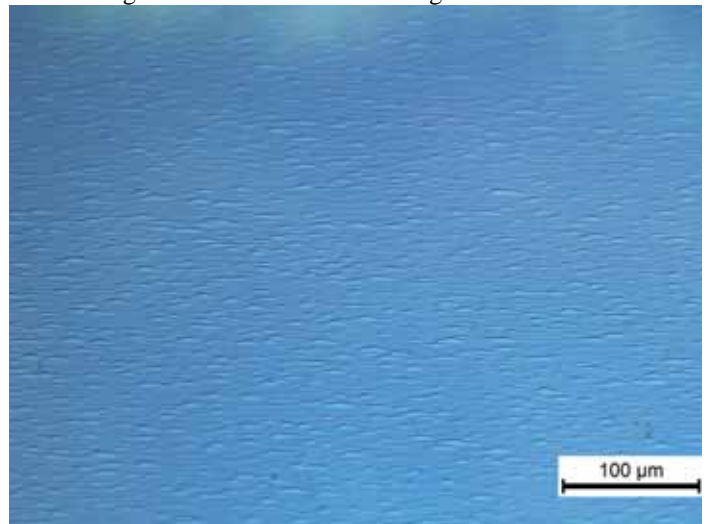


Fig. 11a. C-face of Si-23Ti-C grown for 5h



Fig. 10a. C-face of Si-18Ti-C grown for 5h

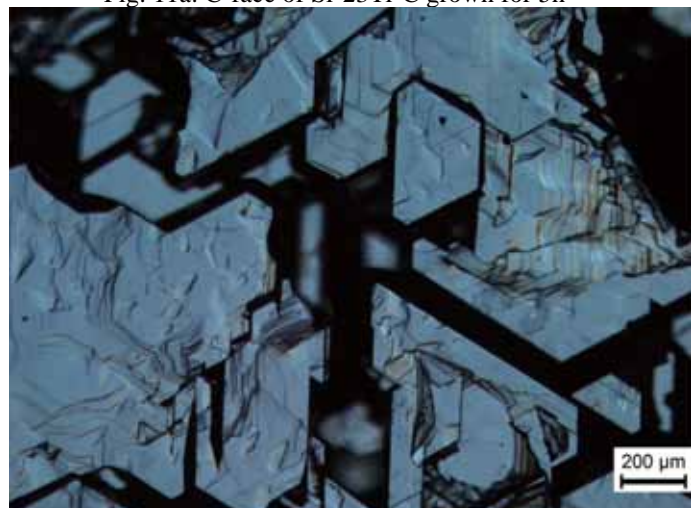


Fig. 11b. Si-face of Si-23Ti-C grown for 5h

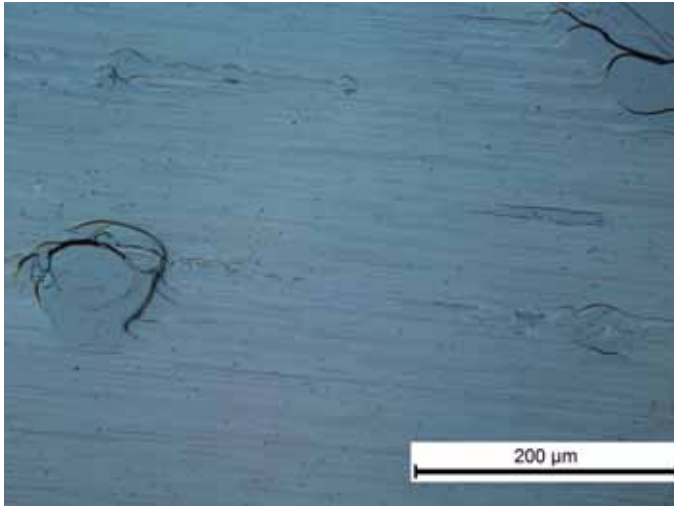


Fig. 12a. C-face of Si-28Ti-C grown for 5h

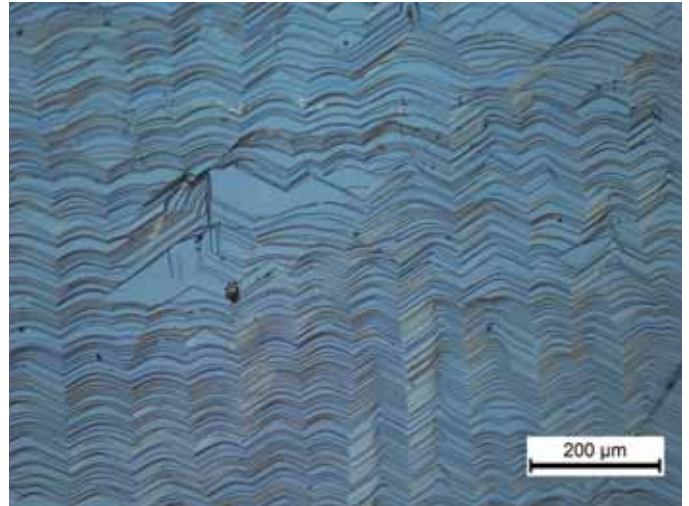


Fig. 13b. Si-face of Si-20Cr-C

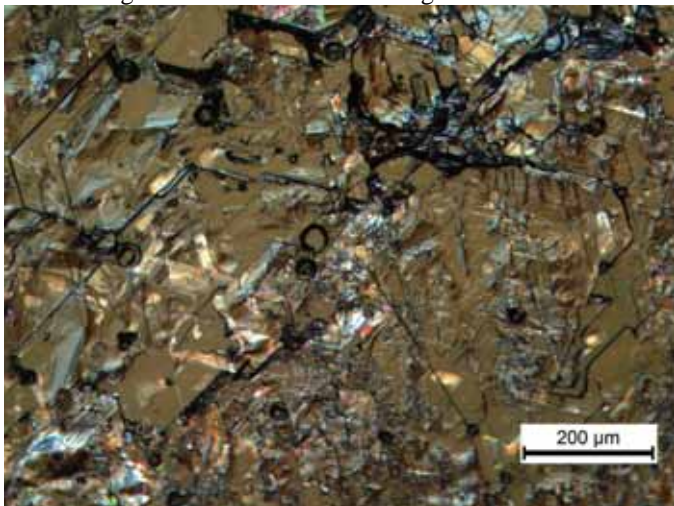


Fig. 12b. Si-face of Si-28Ti-C grown for 5h

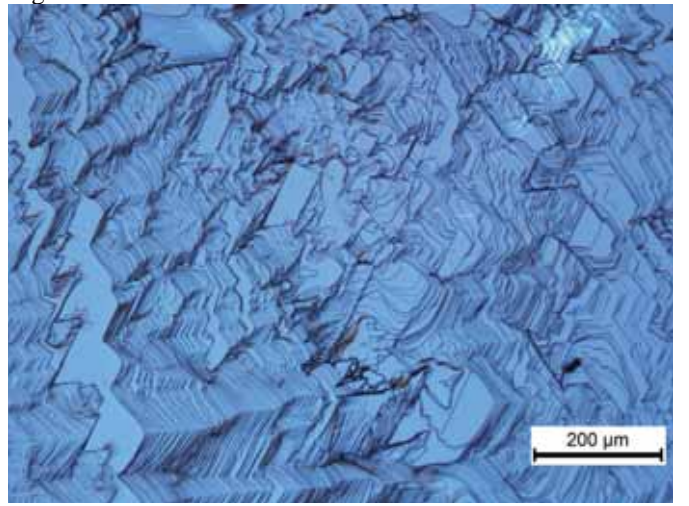


Fig. 14a. Si-face of Si-30Cr-C

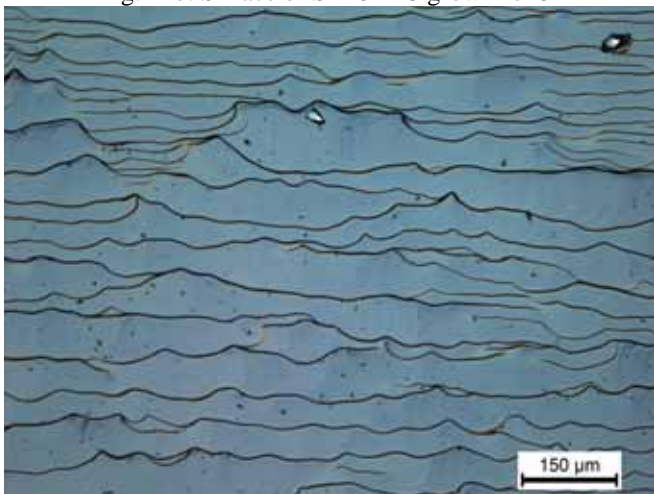


Fig. 13a. C-face of Si-20Cr-C

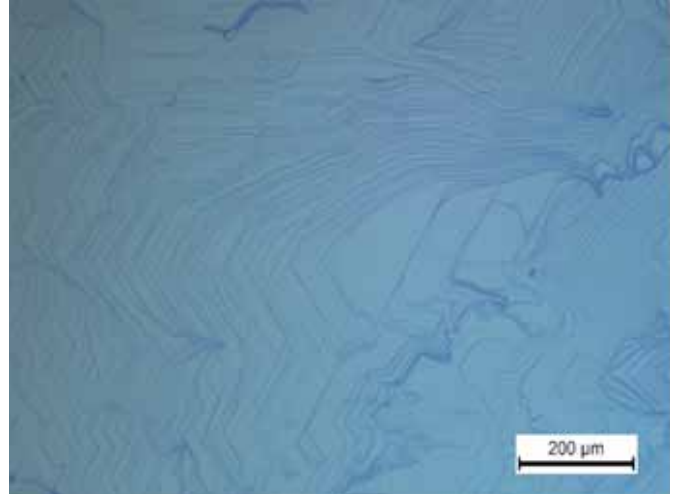


Fig. 14b. C-face of Si-30Cr-C

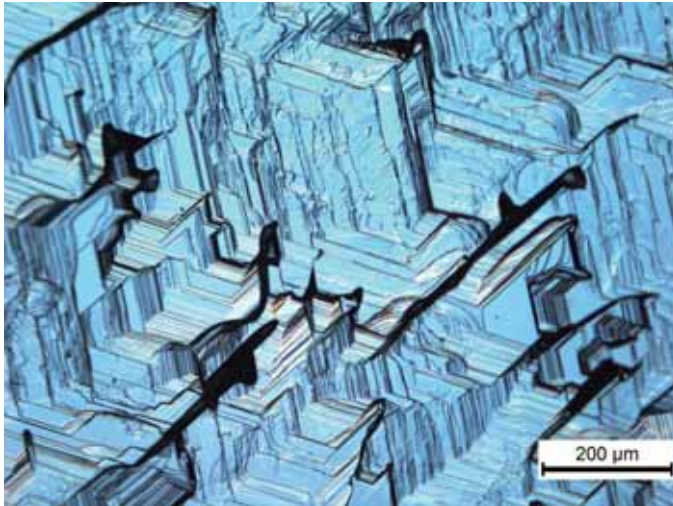


Fig. 15. C-face of Si-40Cr-C

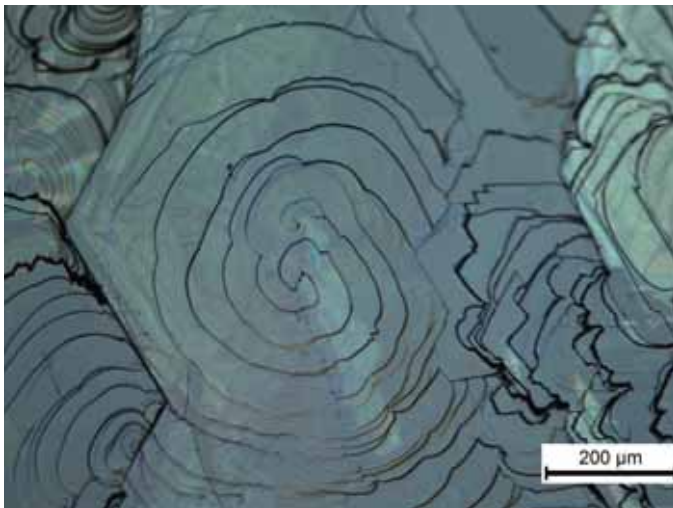


Fig. 16a. C-face of Si-10V-C solution

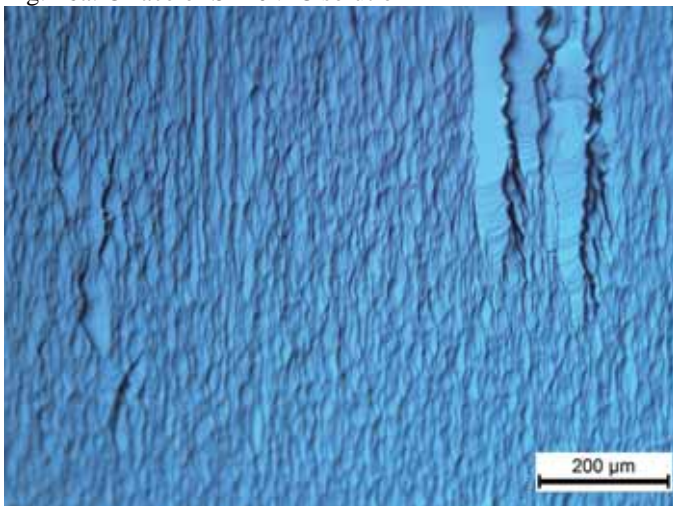


Fig. 16b. Si-face of Si-10V-C solution

## Discussion

Step height of Pure-Si, Si-Ti-C, and Si-Cr-C with varying atomic concentration was investigated by Laser Microscope (Keyence).

It has been shown in laser 3D image that steeply-changed macrostep height and large terrace width have been found in Pure-Si grown for 5h in Fig. 9a. C-face of Si-20Ti-C so smooth that step flow is hardly found. For Si-20Cr-C shown in Fig.13a, large terrace width and steep step height occurred in C-face. And step height of various samples has been summarized in Table 1.

Table 1. Summary of terrace width and step height of 4H-SiC grown from Pure-Si-5H, Si-18Ti-C and Si-20Cr-C solution

Sample	Pure-Si-5h C-face	Si-18Ti-C C-face	Si-20Cr-C C-face
Terrace width	Wide	small	Upper intermediate
Step height	High	low	Upper intermediate

Pure-Si grown for 5h and Si-20Cr-C with large step height and terrace width suggest them promising candidates to observe TSD conversion. Further reflection X-ray topography will be carried out to measure dislocation density and dislocation type.

### *tan(2 deg) evaluation*

As substrate was off-cut 2° with [0001] direction, step height and terrace width can be approximately evaluated by simple tangent trigonometric function as shown in Fig. 17.



Fig. 17. Off-cut 2° substrate with step height h and terrace width w

Table 2. tan θ evaluation

tan θ	Pure-Si-5h	Si-18atTi-C	Si-23atTi-C	Si-28atTi-C	Si-20atCr-C	Si-30atCr-C	Si-40atCr-C
C-face	0.035	0.005	0.007	0.031	0.023	NA	NA
Si-face	0.067	NA	NA	NA	0.022	0.082	0.028

The above tan θ shows good fitting with tan (2deg)=0.035 except for Si-Ti-C samples. This further indicates that step flow is hardly observed in Si-Ti-C samples and their C-face behaves extremely smooth.

Growth rate of epilayer grown for 5h was summarized in Fig.18. It shows that growth rate can be significantly increased with addition of Ti and Cr.

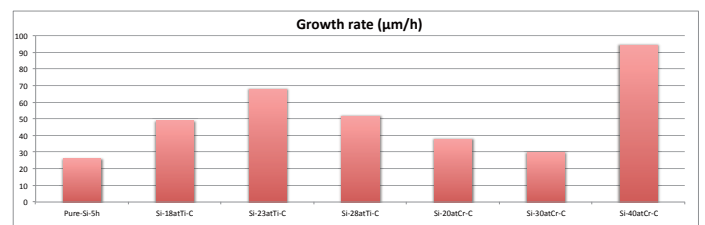


Fig. 18. Growth rate of Pure-Si, Si

Fig. 19 shows the grown epilayer thickness. It shows that both Ti and Cr can increase the epilayer thickness significantly comparing to pure-Si melt.

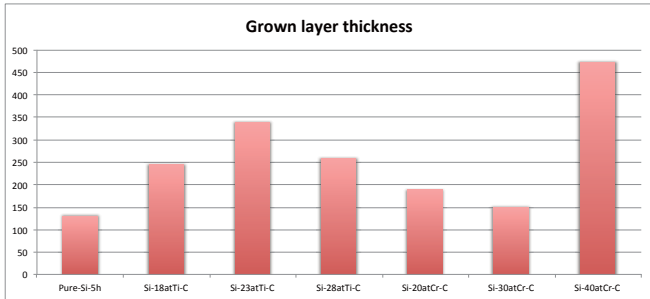


Fig. 19. Grown layer thickness

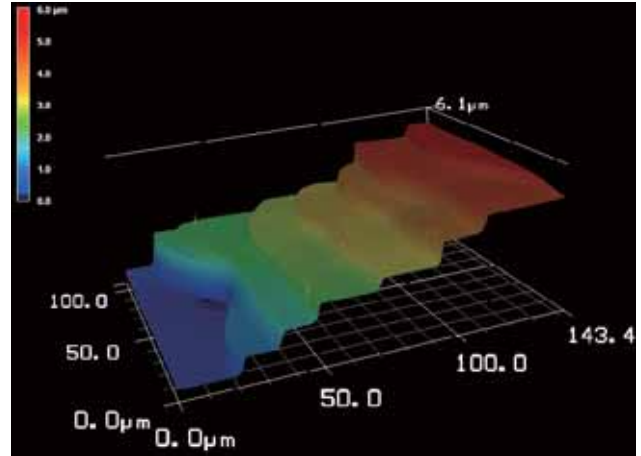


Fig. 20c. Laser microscope image of C-face of Si-20Cr-C solution

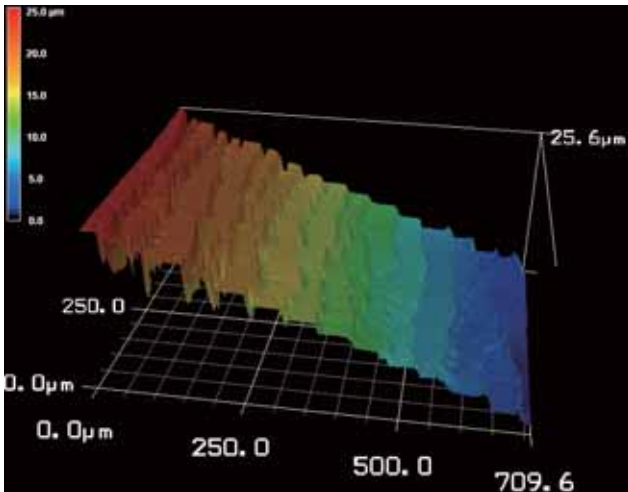


Fig. 20a. Laser microscope image of C-face of Pure-Si grown for 5h

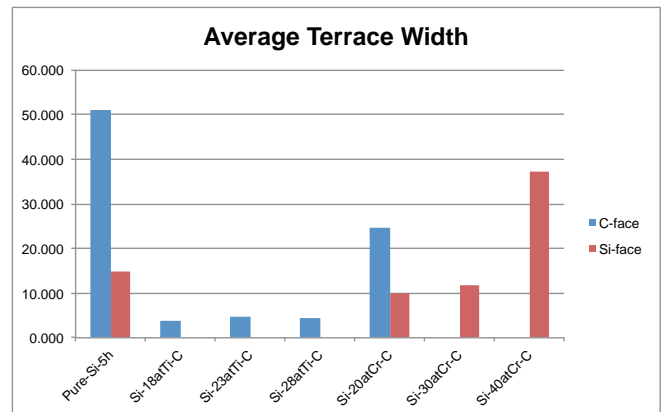


Fig. 21 Average terrace width of 4H-SiC grown from Pure-Si, Si-Ti-C and Si-Cr-C solution

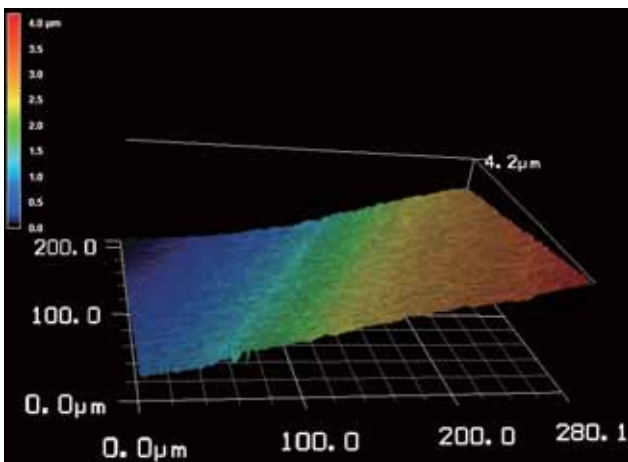


Fig. 20b. Laser microscope image of C-face of Si-18Ti-C

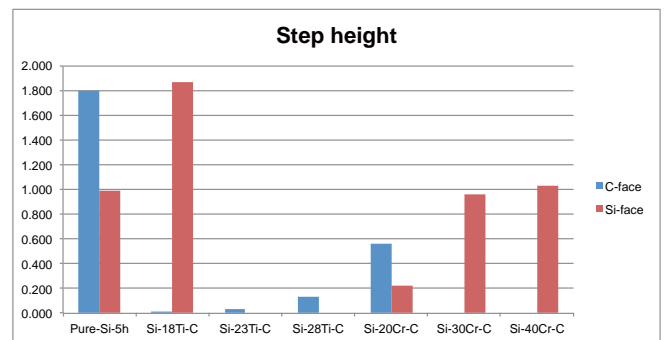


Fig. 22. Average step height of 4H-SiC grown from Pure-Si, Si-Ti-C and Si-Cr-C solution

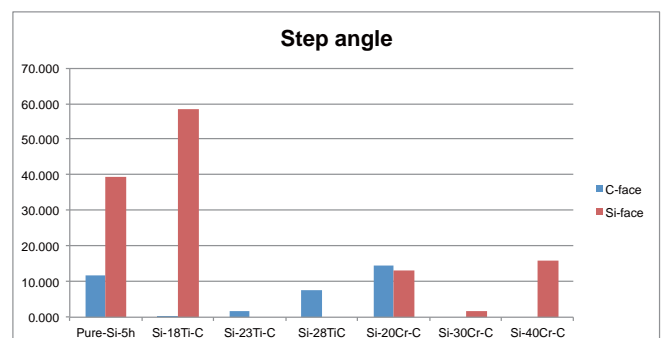


Fig. 23. Average step angle of 4H-SiC grown from Pure-Si, Si-Ti-C and Si-Cr-C solution

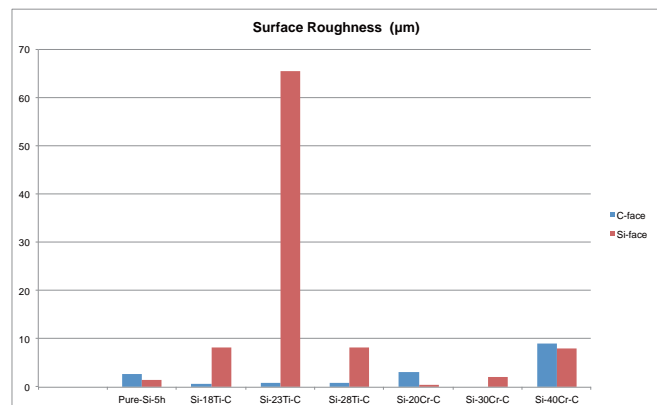


Fig. 24. Average surface roughness of 4H-SiC grown from Pure-Si, Si-Ti-C and Si-Cr-C solution

## Conclusions

Top seeded solution growth was performed to grow 4H-SiC from Pure-Si, Si-Ti-C, and Si-Cr-C solution. By using DIC microscope and laser microscope to measure surface morphology and step height, Pure-Si grown for 5h and Si-20Cr-C SiC sample with large macrosteps were considered a promising candidate to observe dislocation conversion to occur. Si-20Cr-C with large macrosteps on C-face and smooth Si-surface worth further AFM and cross-sectional TEM study for detailed step structure and dislocation conversion phenomenon. Furthermore, C-face from Si-18Ti-C SiC sample is extremely smooth which is suitable to grow high-quality SiC substrate.

## Future work

Detailed step structure shall be further studied by AFM. The characterization of cross-sectional detail will be investigated by cross-sectional TEM. And reflection Synchrotron X-ray topography will be performed to study the dislocation density and dislocation conversion phenomena.

## Acknowledgement

This work was supported by Prof. Ujihara's lab. During the experiments, I received considerable help from all of students from Prof. Ujihara's lab. I would like to especially thank Prof Ujihara, Prof Harada, Mr Yamamoto, Mr Koike, Mr Mutou, Mr Horio, Mr Nagaya Mr Kenji. Without their support and understanding, I could not finish my experiments.

## REFERENCES

1. Mikael Syvajarvi, high growth rate epitaxy of SiC growth process and structural quality

2. Y. Yamamoto et al, High efficiency conversion of threading screw dislocations in 4H-SiC by solution growth
3. J. Palisaitis, Epitaxial growth of thin films
4. H. Daikoku et al., Top-seeded solution growth of 4H-SiC bulk crystal using Si-Cr based melt
5. K. Kamei et al., Solution growth of single crystalline 6H, 4H-SiC using Si-Ti-C melt
6. R Hattori et al., LPE growth of low doped n-type 4H-SiC layer on on-axis substrate for power device application
7. S. Chung et al., Direct observation of basal-plane to threading-edge dislocation conversion in 4H-SiC epitaxy
8. M. Syvajarvi et al., Liquid phase epitaxial growth of SiC
9. R. Hattori et al., Solution growth of off-axis 4H-SiC for power device application

More than one hundred of references have been studied during the research and report writing. Due to the limited amount of time, I could not be able to make reference for all of them. Apologies were made for any absent citation

## 2-e. Workshop

### *The 5th JUACEP Workshop*

**Date:** Thu., August 8

**Venue:** Room 103, ES Building, Nagoya University

**Timetable:**

13:00            Opening ~Address from Prof. Ju~  
13:10 - 17:10   Presentations by UM students  
                  (14 mins. presentation + 5 mins. Q&A each)  
17:10 - 17:40   Award Ceremony  
18:00 -           Farewell Banquet

~Presentation Title~

**1. Michael Bigang Ding (p.144)**

“NC-AFM Characterization of Au-Glass and Au-Si”

**2. Hao Wang (N/A)**

“Theoretical Analysis and Experiment Verification of Self-sensing Magnetic Levitation Using Hall Signal”

**3. Yan Zhang (p.147)**

“Automated Steering System for Obstacle Avoidance based on Potential Field Method”

**4. Nishant Mayur Narechania (p.150)**

“AUSM Family 2nd Order Schemes for Ideal Magnetohydrodynamics with Divergence-free Reconstruction”

**5. Yihao Zheng (p.155)**

“Bone Analog Material for Orthopedic Surgical Training”

**6. Ambarish Krishnanand Desai (p.159)**

“Linear and Nonlinear Optimal Control of Furuta Pendulum”

**7. Yi-Kai Wang (p.163)**

“Visual Feedback Control for Table Tennis Robot”

**8. Weiyu Cao (p.167)**

“Study on the Loop Heat Pipe with New Type of Evaporator for Mass Production”

**9. Sriram Ganesan (p.169)**

“Monte-Carlo Simulation of Polycrystal Plasticity using Discrete Dislocation Plasticity Approach for Lamellar Materials”

**10. Yu-Shiuan Chu (N/A)**

“Design Accuracy Improving Methods in Human Activity Sensing Consortium Project”

**11. Zhenyu Gan (p.173)**

“Application of Momentum-exchange-impact-damper on Vehicle Collision”

# Michael Bigang Ding

## NC-AFM CHARACTERIZATION OF AU-GLASS AND AU-SI

Michael Ding  
University of Michigan, Ann Arbor

Prof. Yang Ju  
Laboratory  
Nagoya University

### WHAT IS AFM ?

- AFM stands for *atomic force microscopy*. It forms an integral part of *scanning probe microscopy*, abbreviated as SPM
- Like all other SPMs, AFM works by analyzing the interaction between the probe and the material substrate.
- AFM instruments allow us to characterize materials at very small lengths scales (~nm).
- STM, EFM are other examples of SPMs.

### MOTIVATION BEHIND AFM

Our Interests

NEW Microwave AFM

Microwave Interaction with Material Substrate

### OPERATIONAL PRINCIPLES OF AFM (1/2)

- Two main types of AFM : non-contact AFM and contact AFM. Our focus is on **non-contact AFM** [abbrev. NC-AFM]
- NC-AFM operates at a constant vibrational amplitude but allows for the modulation of frequency.
- The AFM instrument measures the interaction force between the cantilever-tip structure and material substrate. Hence, the reasoning behind the name *atomic force microscopy*.
- Interactions forces experienced by the AFM probe are **van der Waals forces**. Therefore, these forces are fundamentally electromagnetic.

### OPERATIONAL PRINCIPLES OF AFM (2/2)

- Interaction between cantilever and substrate is characterized by a single parameter:  $V_{ts}$ , tip-surface interaction potential .
- Mechanical behavior of cantilever can be described by two parameters: (1) **frequency shift** and (2) **amplitude** . No need to concern ourselves with the cantilever's vibrational amplitude in NC-AFM.
- Frequency shift is defined by  $\Delta f = f - f_0$ , where  $f_0$  is the natural resonant frequency of the cantilever. The value of  $f_0$  is obtained a process called **tuning**.
- Fundamental Relations<sup>3</sup> linking  $V_{ts}$  and  $\Delta f$ :

Important!

$$\Delta f = (V_{ts} \cdot V_0) \times 200 \text{ [Hz/V]} \quad (1)$$

$$dV / dz = - 2 k (\Delta f / f_0) \quad (2)$$

### FABRICATION OF SUBSTRATES

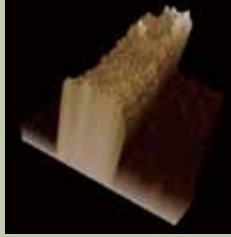
- Standard photolithographic techniques and E-Beam
- 2, 4, and 6  $\mu\text{m}$  thick Au lines on glass and silicon substrates were fabricated. ~ 110 nm in height.

# Michael Bigang Ding

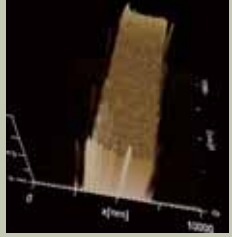
### TOPOGRAPHIES OF SUBSTRATES

During topographic mode, cantilever is kept vibrating at the same frequency. In order to do this, distance between tip and surface must change. This gives the topography.

Au-glass



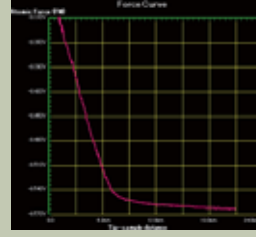
Au-Si



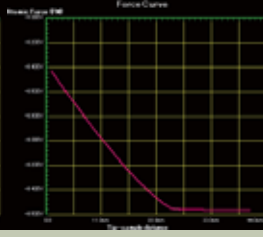
### SURFACE-TIP INTERACTION DATA

$V_{1s}$  vs. tip-sample distance (z) of Au-Si substrate

Au portion

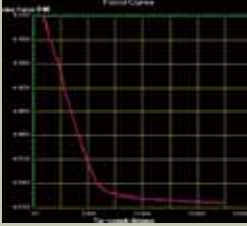


Si portion

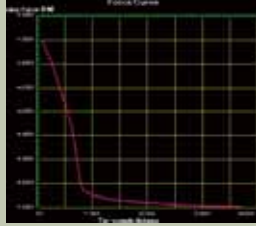


### INTERESTING SUBSTRATE EFFECT

Au portion of Au-Si

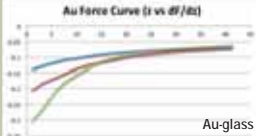


Au portion of Au-glass



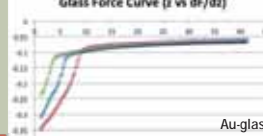
### FORCE DERIVATE CURVE ANALYSIS

Au Force Curve (z vs dF/dz)



Au-glass

Glass Force Curve (z vs dF/dz)



Au-glass

AuSi Substrate. Au Force Curve

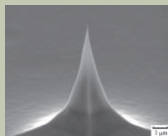
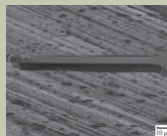
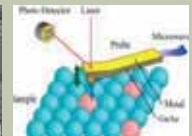
Au-Si

Si Force Curve (z vs dF/dz)

Au-Si

### MICROWAVE-BASED AFM

- Microwave-based AFM is a special type of NC-AFM where microwaves are propagated through the a new tip-cantilever mechanism.
- Follows the same operating principles as classical non-contact AFM. Equations (1) and (2) are still applicable!
- Generated microwaves had frequency of 94.00 GHz and corresponding amplitudes of: 0, 10, 20, 25 dBm.

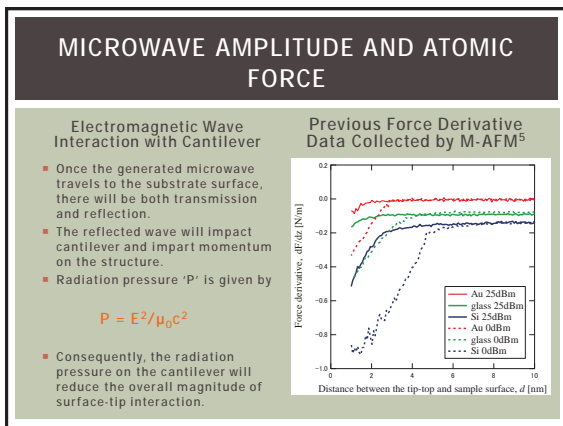
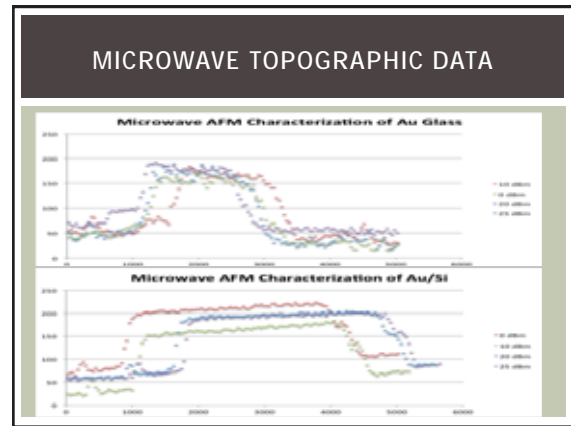
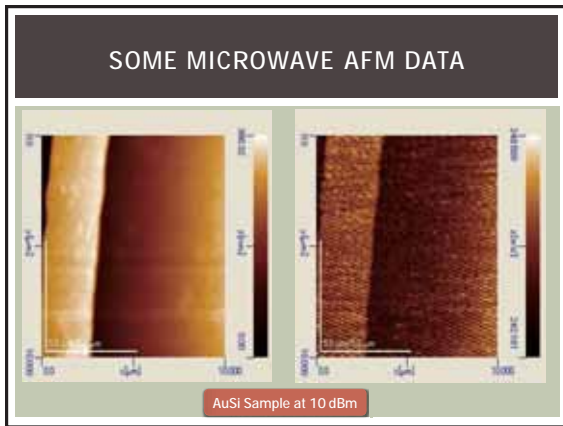




### BENEFITS OF MICROWAVE-BASED AFM

Classical NC-AFM → Microwave-based NC-AFM

- No tip deformation.
- No need to take into consideration of frictional forces
- No need to worry about tip sticking onto the substrate's surface.
- Non-destructive testing.
- Simultaneously obtain topographic and electrical properties of materials.
- We can find values for  $\epsilon$ ,  $\mu$ , and  $\Omega$ .

# Michael Bigang Ding



### CONCLUSION

- The experiments demonstrate the versatility of non-contact AFM in analyzing physical properties of different material substrates.
- Found the threshold distance is not only dependent on the surface material but also the bulk substrate.
- Substrate also plays an important role in determining dF/dz.
- Microwave-based AFM produces accurate topography of substrates. There does not seem to be an experimental correlation between topographic heights and strength of the generated microwave.
- Increased microwave amplitudes may negate surface-tip interaction forces.

I would like to thank Professor Ju, Professor Hosoi, and everyone else in the Ju laboratory for helping me and making my stay in Japan feel very enjoyable. A special thanks goes out to Takahiro Nakashima [M2 student in Ju laboratory]. Also, this wonderful research opportunity would not have been possible without the kind and generous financial support given by the JASSO organization.

**Thank You!**

**THE END**

### REFERENCES

1. AFM (atomic force microscope), Angewandte Physiks, <http://www3.physik.uni-greifswald.de/method/afm/eafm.htm>
2. Cantilever Sensor, Microscopy Laboratory at University of Colima, <http://fejer.ucof.mx/meb/img/punta.JPG>
3. R. Garcia, R. Perez, *Surface Science Reports* 47, 197 (2002)
4. L. Zhang, Y. Ju, A. Hosoi, A. Fujimoto, *Review of Scientific Instruments* 81, 123708 (2010)
5. Courtesy of Takahiro Nakashima (M2 student In Ju Lab)



## Automated Steering System for Obstacle Avoidance based on Potential Field Method

---

Yan Zhang



## Introduction

- ▣ Driver assist systems becomes popular on modern vehicles.
- ▣ They provide safety and convenience to the driver and passengers.



Lane Keep Assist



Parking Assist

- ▣ They only work when steering angle is small or speed is low.



## Motivation

- ▣ The goal of the automated steering system is to avoid a sudden obstacle appears in front of the vehicle.
- ▣ Thus large and quick maneuver is required when the speed is high.
- ▣ A small electric vehicle (COMS) is used in the research. Only low speed experiments are done to ensure safety.

PC, PLC, Control Programs

Steering Angle Sensor:  
Steering Angle

Odometry:  
Position, Yaw Angle

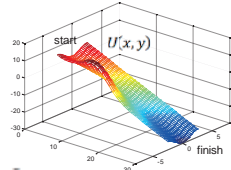
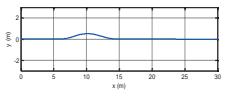




## Basic Idea

- ▣ Assuming knowing the location of the obstacle and width of the road, the potential field function of the driving environment is determined.
- ▣ The reference path is calculated as:
  - Given the potential function:  $U(x, y)$
  - The direction vector at time  $t$  is:
 
$$[v_{x_t}, v_{y_t}]^T = -\nabla U(x_t, y_t) = \left[ \frac{\partial U(x, y)}{\partial x}, \frac{\partial U(x, y)}{\partial y} \right]^T_{x=x_t, y=y_t}$$
  - The vehicle location at time  $t+1$  is then:
 
$$x_{t+1} = x_t + d \cos \left( \tan^{-1} \left( \frac{v_{y_t}}{v_{x_t}} \right) \right)$$

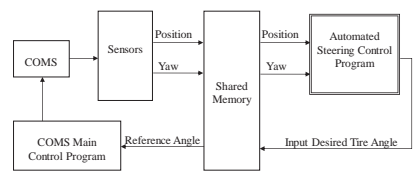
$$y_{t+1} = y_t + d \sin \left( \tan^{-1} \left( \frac{v_{y_t}}{v_{x_t}} \right) \right)$$
- where  $d$  is a small distance interval.



## Control Architecture (1)

- ▣ The automated steering control program works in hybrid with COMS main control program.



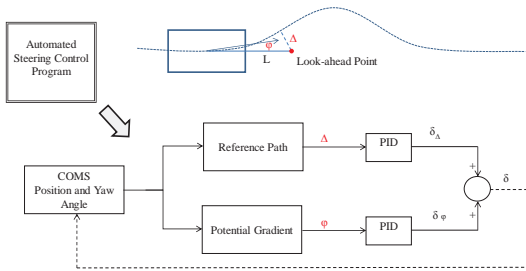
```

    graph LR
      COMS[COMS] --> Sensors[Sensors]
      COMS --> COMS_Main[COMS Main Control Program]
      Sensors -- Position --> Shared_Memory[Shared Memory]
      Sensors -- Yaw --> Shared_Memory
      Shared_Memory -- Position --> Auto_Steering[Automated Steering Control Program]
      Shared_Memory -- Yaw --> Auto_Steering
      COMS_Main -- Reference Angle --> Shared_Memory
      Input[Input Desired Tire Angle] --> Shared_Memory
  
```



## Control Architecture (2)

- ▣ The automated steering control program takes the position and yaw angle inputs and outputs the desired steering angle.



```

    graph TD
      Auto_Steering[Automated Steering Program] --> Ref_Path[Reference Path]
      Auto_Steering --> Pot_Grad[Potential Gradient]
      COMS_Pos[COMS Position and Yaw Angle] --> Ref_Path
      COMS_Pos --> Pot_Grad
      Ref_Path -- Δ --> PID1[PID]
      Pot_Grad -- φ --> PID2[PID]
      PID1 -- δ_Δ --> Sum((+))
      PID2 -- δ_φ --> Sum
      Sum -- δ --> Output[Desired Steering Angle]
  
```

### Control Law

- Look-ahead observation is used to predict the steering angle required for COMS to follow the reference path.
- The total tire reference angle is calculated as:
 
$$\delta = \left( K_{p1} \delta_d + K_{i1} \int_{t_{i-1}}^t \delta_d dt + K_{d1} \frac{d\delta_d}{dt} \right) + \left( K_{p2} \delta_\psi + K_{i2} \int_{t_{i-1}}^t \delta_\psi dt + K_{d2} \frac{d\delta_\psi}{dt} \right)$$
 ,where Kp, Ki and Kd are adjustable in the program.
- The look-ahead distance  $L$  is also adjustable to compensate different vehicle speeds.

### Interface

- Automated Steering Control Program GUI (C#)
  - User adjustable parameters:
    - PID control gains
    - obstacle location
    - look-ahead distance
    - time step size
    - vehicle speed
  - Position display
  - Tire angle display
  - Yaw angle display

### Experiments

- At first, the responsiveness of the steering system is tested by a step input.
- The output shows a transportation delay and a second order delay.

- The look-ahead control is needed to compensate the delay.

### Experiments

- Test results without look-ahead control show the effect of steering delay.  $\delta = K * \phi$
- At very low speed, the vehicle can follow the path. But oscillation starts to occur very quickly when speed increases.

### Experiments

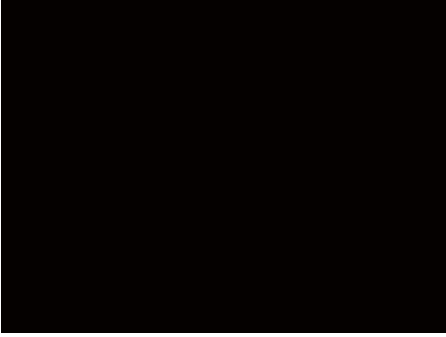
- Look-ahead control predicts the steering angle needed ahead of time so that effect of the delay can be eliminated.
- Testing speed is approximately 1 m/s.

### Experiments

- Compare the two methods.



## Experiments



## Discussion and Conclusion

- The main structure of the automated steering control program has been developed but it is far away from being finished.
- The main difficulty of controlling the vehicle in this research comes from the delay of the steering system. This delay may be caused by the backlash of the steering system, steering motor controller or the communication between the automated steering program and main control program.
- Look-ahead control can be used to solve this problem. More testing need to be done to find the look-ahead distances and control gains for higher speeds.
- Obstacle detection function can be realized by using the laser scanner on COMS.
- As the speed goes higher, the vehicle can be unstable due to the nature of vehicle dynamics. Stability control algorithm needs to be added at high speed. Automatic braking can also be considered to work in conjunction with the program.



## Q&A



# Nishant Mayur Narechania

**AUSM FAMILY 2<sup>ND</sup> ORDER SCHEMES FOR IDEAL  
MAGNETOHYDRODYNAMICS WITH  
DIVERGENCE-FREE RECONSTRUCTION**

NISHANT NARECHANIA  
AEROSPACE ENGINEERING, UNIVERSITY OF  
MICHIGAN, USA

ASSISTANT PROFESSOR KEIICHI KITAMURA  
AEROSPACE ENGINEERING, NAGOYA  
UNIVERSITY, JAPAN

8<sup>TH</sup> AUGUST 2013

STRUCTURE OF THIS PRESENTATION

- ◆ What is MHD?
- ◆ AUSM Numerical Flux and Motivation
- ◆ Details of Computation
- ◆ Results and Conclusion

**MAGNETOHYDRODYNAMICS(MHD)**

Earth-Sun Interaction :  
Solar Wind, CMEs

Earth's Space  
Environment :  
Magnetosphere,  
Bow Shock, Aurora

Astrophysics : Galactic  
Jets, Black Holes

Geophysics : Earth's  
Core



**INVISCID EULER EQUATIONS**

$\frac{\partial \rho}{\partial t} + \nabla \cdot (\rho \mathbf{u}) = 0$	Conservation of Mass
$\frac{\partial (\rho \mathbf{u})}{\partial t} + \nabla \cdot (\rho \mathbf{u} \otimes \mathbf{u}) + \nabla p = 0$	Conservation of Momentum
$\frac{\partial E}{\partial t} + \nabla \cdot (\mathbf{u}(E + p)) = 0$	Conservation of Energy

**MAXWELL'S EQUATIONS**

$\nabla \cdot \mathbf{E} = \frac{\rho}{\epsilon_0}$	Gauss's Law
$\nabla \cdot \mathbf{B} = 0$	Gauss's Law for Magnetism
$\nabla \times \mathbf{E} = -\frac{\partial \mathbf{B}}{\partial t}$	Faraday's Law of Induction
$\nabla \times \mathbf{B} = \epsilon_0 \mu_0 \left( \mathbf{J} + \epsilon_0 \frac{\partial \mathbf{E}}{\partial t} \right)$	Ampere's Law

STRUCTURE OF THIS PRESENTATION

- ◆ What is MHD?
- ◆ **AUSM Numerical Flux and Motivation**
- ◆ Details of Computation
- ◆ Results and Conclusion

THE AUSM FAMILY NUMERICAL FLUX

*Advection Upstream Splitting Method*

- ◆ Originally developed for Gas Dynamics
- ◆ Types : AUSM, AUSM+, AUSM+-UP, SLAU, SLAU2
- ◆ WHAT AM I DOING ?  
Extension of AUSM+ and SLAU2 to MHD



6

THE AUSM FAMILY NUMERICAL FLUX

Total Numerical Flux = Advection Flux + Pressure Flux

$$\begin{pmatrix} \bar{v}_x \\ \bar{v}_x v_x \\ \bar{v}_x v_y \\ \bar{v}_x v_z \\ (\bar{v}_x p_{gas} + 1/2 B^2 \bar{v}_x B_x) v_x \\ 0 \\ v_x B_y \\ v_x B_z \end{pmatrix} + \begin{pmatrix} 0 \\ p_{gas} + 1/2 B^2 \bar{v}_x B_x \\ \bar{v}_x B_y \\ \bar{v}_x B_z \\ \bar{v}_x (v_y B_y + v_z B_z) \\ 0 \\ \bar{v}_y B_x \\ \bar{v}_z B_x \end{pmatrix}$$


7

THE AUSM FAMILY NUMERICAL FLUX

- ◆ Upwinding performed on Advective Flux
- ◆ Interface Mach No./ Velocity/ Mass flux determines upwinding direction
- ◆ Interface Pressure found by polynomial interpolation



8

STRUCTURE OF THIS PRESENTATION

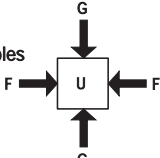
- ◆ What is MHD?
- ◆ AUSM Numerical Flux and Motivation
- ◆ Details of Computation
- ◆ Results and Conclusion



9

CONSERVATIVE FORM OF EQUATIONS

- ◆ Conservative Form of Equations
- ◆ Required for Computational Techniques after Discretization
- ◆ Finite Volume Method
- ◆ Cell-Averaged Zone-Centered Variables



$\frac{\partial U}{\partial t} + \frac{\partial F}{\partial x} + \frac{\partial G}{\partial y} = 0$



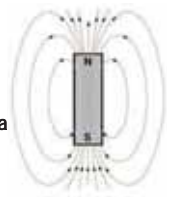
10

THE DIVERGENCE CONSTRAINT

Gauss's Law for Magnetism  
Non-existence of magnetic monopoles  
Not satisfied by usual FVM  
Discrete divergence  $\neq 0$   
Leads to unphysical solutions and instabilities

Special treatment required

$\nabla \cdot B = 0$



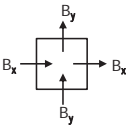

11

# Nishant Mayur Narechania

**STAGGERED GRID**

Face-centered magnetic fields Instead of zone-centered

Try to ensure discrete divergence = 0

$$\text{div}(B_x, B_y) = \frac{B_{x,\text{right}} - B_{x,\text{left}}}{\Delta x} + \frac{B_{y,\text{top}} - B_{y,\text{bottom}}}{\Delta y}$$


12

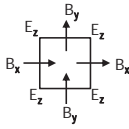
**SOLENOIDAL UPDATE OF MAGNETIC FIELDS**

Faraday's Law of Induction :

$$\nabla \times E = -\frac{\partial B}{\partial t}$$

Discrete time update :

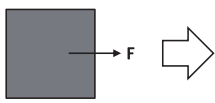
Zone-cornered electric fields

$$\frac{B_{x,\text{right}}^{n+1} - B_{x,\text{right}}^n}{\Delta t} = \frac{E_{z,\text{bottom\_right}} - E_{z,\text{top\_right}}}{\Delta y}$$


13

**SECOND ORDER RECONSTRUCTION**

Constant cell-averaged profile      Polynomial to represent variation throughout grid-cell



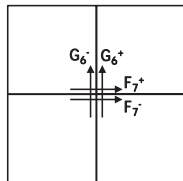
Simpson's Rule to calculate Flux  $F = \frac{F_1 + 4F_2 + F_3}{6}$

14

**ELECTRIC FIELDS FROM FLUXES**

$$E_z = -F_7 = G_6$$

$E_z$  is located at cell corners  
Hence averaged from fluxes calculated at cell corners by reconstruction from all 4 cells sharing the corner

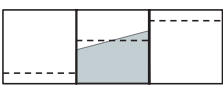


15

**SECOND ORDER RECONSTRUCTION PROFILE**

Cell-averaged Variables :      Face-centered Solenoidal Magnetic Fields :

Linear Profile Using Minimum Undivided Differences

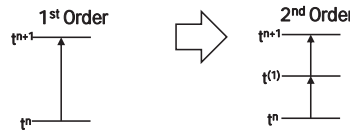


Divergence Constraint exactly satisfied inside each cell  
Linear Variation on each face

16

**TWO-STEP RUNGE-KUTTA TIME MARCHING**

First Order : Error ~  $\Delta t$       Second Order : Error ~  $\Delta t^2$   
 $U^{n+1} = U^n + \Delta t L(U^n)$        $U^{(1)} = U^n + \frac{1}{2} \Delta t L(U^n)$   
 $U^{n+1} = U^n + \Delta t L(U^{(1)})$



$$\frac{\partial U}{\partial t} = L(U)$$

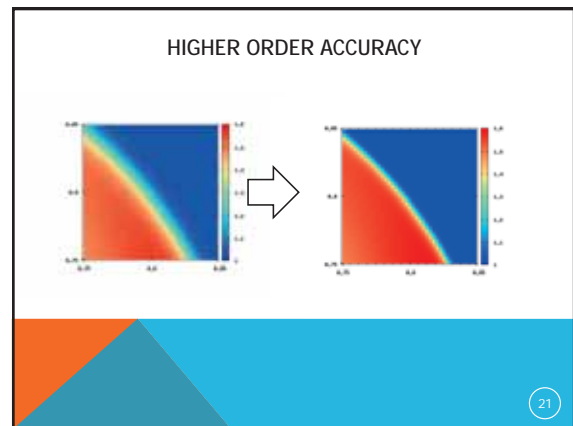
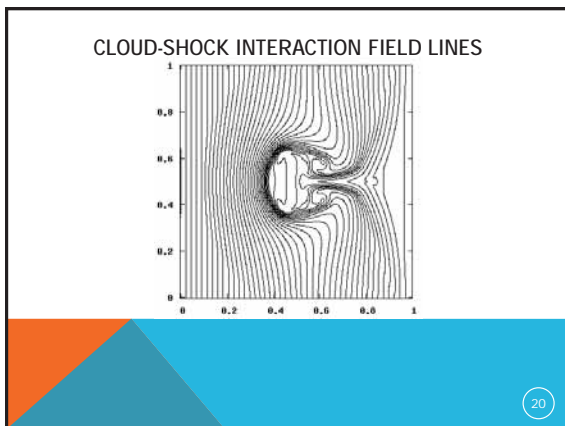
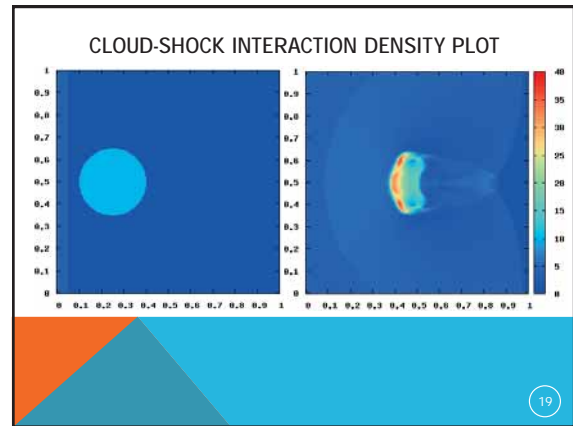
17

STRUCTURE OF THIS PRESENTATION

- ◆ What is MHD?
- ◆ AUSM Numerical Flux and Motivation
- ◆ Details of Computation
- ◆ Results and Conclusion



18



COMPARISON WITH OTHER NUMERICAL FLUXES

**HLLC :**  
 Very diffusive  
 Extremely robust

**AUSM, HLLC, SLAU2, AUSM\* :**  
 Low diffusion  
 Robustness ??



22

COMPARISON WITH OTHER NUMERICAL FLUXES  
 IN TERMS OF ROBUSTNESS (1<sup>ST</sup> ORDER)

	HLLC	HLLC	AUSM	AUSM*	SLAU2
Orszag-Tang Vortex	✓	✗	✓	✓	✓
Magnetized Blast	✓	✓	✓	✗	✓
Cloud-Shock Interaction	✓	✗	✗	✓	✓
Rotor 1	✓	✓	✗	✓	✓
Rotor 2	✓	✗	✗	✓	✓



23

## Nishant Mayur Narechania

### COMPARISON WITH OTHER NUMERICAL FLUXES IN TERMS OF ROBUSTNESS (2<sup>ND</sup> ORDER)

	HLLC	HLLC	AUSM	AUSM <sup>+</sup>	SLAU2
Orszag-Tang Vortex	✓	X	X	X	✓
Magnetized Blast	✓	✓	✓	X	X
Cloud-Shock Interaction	✓	X	X	✓	✓
Rotor 1	✓	✓	X	✓	X
Rotor 2	✓	X	X	✓	✓

24

### SUMMARY AND CONCLUSION

◆ SLAU2 proves to be superior and robust

◆ Future Work :  
Better AUSM-type numerical flux  
3<sup>rd</sup> order accuracy  
Incorporation of General Relativity

25

# Yihao Zheng

JUACEP Michigan Engineering

## Bone Analog Material for Orthopedic Surgical Training

Yihao Zheng

Advisors: Prof. Noritsugu Umehara  
Prof. Albert Shih

2013-8-8

JUACEP Michigan Engineering

## Content

- Background
  - Market Demand
  - Current Options
- Proposal
  - 3D Printed Plaster with Epoxy Treatment
- Validation
  - Sample Preparation
  - Collabration
  - Hardness Test
  - Friction Test
  - Thermal and Machining Tests in UM
- Future Work

2013-8-8 2

JUACEP Michigan Engineering

## Background

- Orthopedic Surgery



2013-8-8 3

JUACEP Michigan Engineering

## Background

- Orthopedic Surgery---Practice Makes Perfect!

- Threaded Holes
  - Drilling
  - Reaming
  - Tapping
- Precision
- Position & Form
- Force & Heat



2013-8-8 3

JUACEP Michigan Engineering

## Background

- Current Options for Bone Cutting Praticce



- Human Cadaveric Bone**
  - "Gold Standard"
  - Underprovided
  - Expensive
  - High Variability
  - Antiepidemic

2013-8-8 4

JUACEP Michigan Engineering

## Background

- Current Options for Bone Cutting Praticce



- Bovine Bone**
  - Available
  - Similar
  - Poor Geometric Features
  - Different from Human's
  - High Variability

2013-8-8 4

**Background**

- Current Options for Bone Cutting Practice



Sawbones Products

**Polymer Molding**

- Polyurethane Foams
- Acetal Copolymers
- Delrin
- UHMWPE

Precise Geometric Features

Poor Machining Responses

- Low Hardness
- Low Melting Point

2013-8-8 5

**Background**

- Current Options for Bone Cutting Practice



Sawbones Products



BoneSim™ 1800

**Biomechanical Test Blocks**

- Polyurethane Foams
- Epoxy
- Cattle Bone

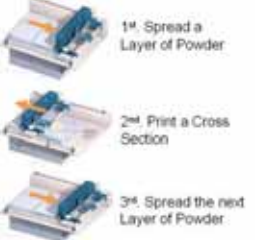
Similar Mechanical Properties

No Geometric Features

2013-8-8 6

**Proposal**

- 3D Printed Plaster
- Epoxy Treatment



- 1<sup>st</sup>. Spread a Layer of Powder
- 2<sup>nd</sup>. Print a Cross Section
- 3<sup>rd</sup>. Spread the next Layer of Powder

2013-8-8 7

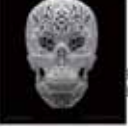
**Proposal**

- 3D Printed Plaster
- Epoxy Treatment



Complex Structures

Low Cost in Time and Money



Printed Plaster

Low Strength



Hard

Waterproof

Adjustable

Biomechanical Property

2013-8-8 7

**Proposal**

- 3D Printed Plaster
- Epoxy Treatment

Flexibility

Strength

Geometric Feature

Mechanical Property

Effective Training

2013-8-8 7

**Validation**

- Sample Preparation



Middle Shafts of Fresh Bovine Femur

0.25 Mix 0.25

60 mins Vacuum 25 mins

85°C 4 hrs Cure 20°C 24 hrs

2<sup>nd</sup> 810 printer  
zpl: 150 powder  
© 50mm x 3 mm disk

Polishing #800 1500 2500 3000 Sandpaper

Lengthwise Bone Sample

Radial Bone Sample

RBC Plaster Sample

AM Plaster Sample

2013-8-8 8

**Validation**

- Collaboration

S. M. Wu  
Manufacturing Research Center

Yihao Zheng  
Mechanical Property Tests  
Hardness & Friction Coefficient

Fumitake Nonoyama  
Machining Property Tests  
Thermal Conductivity

2013-8-8 9

**Validation**

- Hardness Test

**Rockwell Superficial Test**  
15-T Scale Indenter: 1/16-inch (1.588 mm) diameter steel sphere  
Total load: 15 kgf

**Result**

Longitwise Bone Sample	Radial Bone Sample	RBC Plaster Sample	AM Plaster Sample
Mean: 63.1	Mean: 64.3	Mean: 31.3	Mean: N.A.
STD: 1.5	STD: 7.0	STD: 3.3	STD: N.A.

2013-8-8 10

**Validation**

- Friction Test Setup

Pin-on-disk Apparatus  
Pin: AISI 52 100 Steel Ball  
φ6mm, Rz 30nm  
Disk: Prepared Samples  
Sliding Speed: 100mm/s  
Normal Load: 200, 400, 700 gf

2013-8-8 11

**Validation**

- Friction Test Result

Radial Bone Sample

Longitwise Bone Sample

2013-8-8 12

**Validation**

- Friction Test Result

Bone Sample

RBC Plaster Sample

2013-8-8 12

**Validation**

- Friction Test Conformity

Drilling Chip of Bovine Bone

Drilling Chip of RBC Plaster

2013-8-8 13

**JUACEP** Michigan **Engineering**

### Validation

- Thermal and Machining Tests in UM  
Thermal Conductivity Test



Thermal Insulation Box

2013-8-8 14

**JUACEP** Michigan **Engineering**

### Validation

- Thermal and Machining Tests in UM  
Machining Response Test



Bar Drill Knife

2013-8-8 14

**JUACEP** Michigan **Engineering**

### Future Work

- Hardness Improvement  
Epoxy Adjustment  
Preparation Optimization
- Finish Machining Test
- Publication

2013-8-8 15

**JUACEP** Michigan **Engineering**

### Bone Analog Material for Orthopedic Surgical Training



- Questions
- Thank you very much for your attention!

2013-8-8 16

# Amarish Krishnanand Desai

**LINEAR AND NONLINEAR OPTIMAL CONTROL OF FURUTA PENDULUM**

**AMBARISH DESAI**  
MSE, Aerospace Engineering, University of Michigan, Ann Arbor

**Supervisor: Dr. Noboru Sakamoto**  
Dept. Aerospace Engineering, Nagoya University

**Overview**

- Furuta Pendulum System
  - Rotary single inverted pendulum (RSIP)
  - Rotary double inverted pendulum (RDIP)
- Linear Optimal Control - LQR
- Stabilization using LQR
  - Experiment and Simulations
- Nonlinear Optimal Control
  - Stable Manifold Theory
  - Stable Manifold Algorithm
- Results and Simulation
- Conclusion

**Furuta Pendulum**

- First introduced by Dr. Furuta
- Mechanically simple yet strong nonlinear system dynamics
- Significant underactuated system to test control laws
- Rotary single inverted pendulum (RSIP)
- Rotary double inverted pendulum (RDIP)



**System Dynamics**

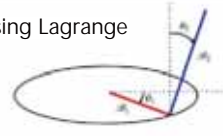
Derive equations of motion using Lagrange equation

$$\frac{d}{dt} \frac{\partial L}{\partial \dot{\theta}} - \frac{\partial L}{\partial \theta} = Q$$

RSIP:

$$I_1 \ddot{\theta}_1 + I_2 \ddot{\theta}_1 \sin^2(\theta_2) + 2 I_2 \dot{\theta}_1 \dot{\theta}_2 \cos(\theta_2) \sin(\theta_2) + m_2 \ddot{\theta}_2 L_1 l_2 \cos(\theta_2) - m_2 \dot{\theta}_2^2 L_1 l_2 \sin(\theta_2) + m_2 \dot{\theta}_1 L_1^2 = n(KDC u + \mu_0 \dot{\theta}_1)$$

(torque)  $\tau$

$$I_2 \ddot{\theta}_2 + m_2 \dot{\theta}_1 L_1 l_2 \cos(\theta_2) - I_2 \dot{\theta}_1^2 \cos(\theta_2) \sin(\theta_2) - m_2 g l_2 \sin(\theta_2) = 0$$


**State Space Representation**

- Introduce state vector for RSIP

$$X = \begin{bmatrix} x_1 \\ x_2 \\ x_3 \\ x_4 \end{bmatrix} = \begin{bmatrix} \theta_1 \\ \dot{\theta}_1 \\ \theta_2 \\ \dot{\theta}_2 \end{bmatrix}$$

$$\dot{X} = f(X) + g(X)u$$

- Linearize about X=0
- State Space Representation

$$\dot{X} = AX + Bu$$

$$A = \left. \frac{\partial f}{\partial X} \right|_{X=0} \quad B = g(0)$$

**Linear Optimal Control**

- Linear Quadratic Regulator (LQR)

For a system:

$$\dot{x} = Ax + Bu$$

with a cost function:

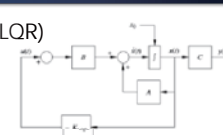
$$J = \int_0^{\infty} (x^T Q x + u^T R u) dt$$

with Q symmetric, positive semi-definite and R a symmetric positive definite matrix

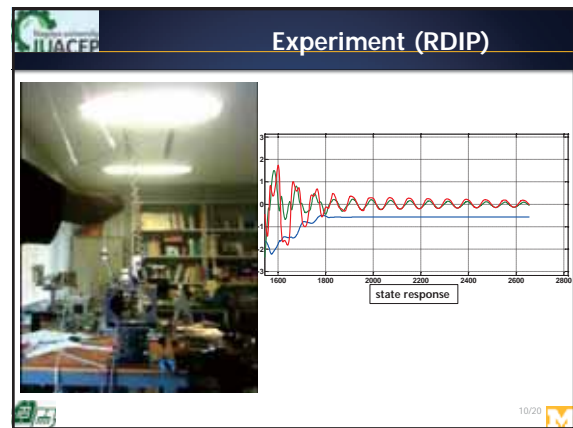
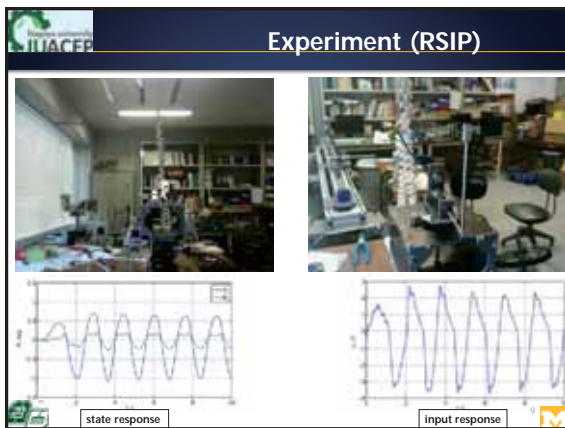
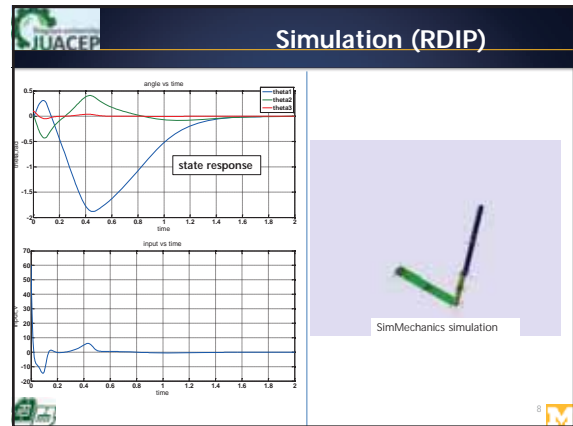
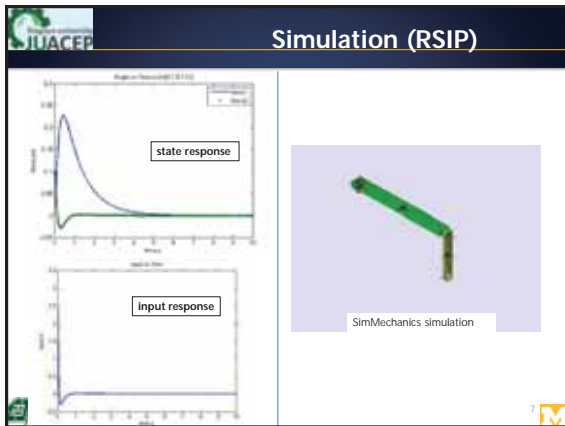
Optimal feedback is given by:

$$u = Kx = -(R^{-1} B^T P)x$$

where P is the solution of algebraic Riccati equation:

$$A^T P + PA + Q - PBR^{-1}B^T P = 0$$


# Amarish Krishnanand Desai



### Nonlinear Optimal Control

- Problem definition:
  - For a system:  $\dot{x} = f(x) + g(x)u$
  - with a cost function:  $J = \int_0^\infty (x^T Q x + u^T R u) dt$
  - optimal feedback is given by:  $u = -\frac{1}{2} R^{-1} g(x)^T p(x)$
  - where  $P$  is the solution of Hamilton-Jacobi (HJ) equation:  $p^T f(x) - \frac{1}{2} p^T g(x) R^{-1} g(x)^T p + q(x) = 0$
  - where  $p = \frac{\partial V}{\partial x}$ ,  $V$  is an unknown function

**How to find  $p(x)$ ?**

### Stable Manifold theory

For a system:  $\dot{x} = Ax$

- Invariant stable, center and unstable subspace associated with eigenvalues  $Re(\lambda) < 0$ ,  $Re(\lambda) = 0$  and  $Re(\lambda) > 0$

Similarly for a dynamical system:  $\dot{x} = f(x)$ ,  $x \in R^n$

a manifold  $M \subset R^n$  such that if  $x \in M$ , then  $M$  is an invariant manifold if  $\phi(x, t) \in M, \forall t \in R$

Separating linear and nonlinear terms:  $\dot{x} = Ax + F(x)$

the system will have invariant stable  $\rightarrow Re(\lambda_i) < 0$ ; center  $\rightarrow Re(\lambda_i) = 0$  and unstable  $\rightarrow Re(\lambda_i) > 0$  manifolds

# Amarish Krishnanand Desai

### Stable Manifold theory (2)

Consider a dynamical system :

$$\dot{x} = Ax + F(x)$$

having  $k \leq n$  eigenvalues with  $Re(\lambda_i) < 0$

then there exists a  $k$ -dimensional stable manifold  $S$  such that

$$\forall t \geq 0, \phi(S, t) \subset S \quad \text{and} \quad \forall x \in S$$

$$\lim_{t \rightarrow \infty} \phi(x, t) = 0$$

### Stable Manifold theory (3)

Consider the Hamilton-Jacobi (HJ) equation:

$$H(x, p) = p^T f(x) - \frac{1}{4} p^T R(x) p + q(x) = 0$$

where  $p = \frac{\partial V}{\partial x}$ ;  $f(x) = Ax + F(x)$ ;  $q(x) = x^T Q x$

with  $R$  symmetric and  $Q$  positive semidefinite matrix and  $f(0)=0$ , then  $V(x)$  is a solution if  $\Lambda = \left\{ (x, p) \mid p = \frac{\partial V}{\partial x}(x) \right\}$

is invariant under the space associated with the Hamilton system

$$\dot{x} = f(x) - \frac{1}{2} R(x) p$$

$$\dot{p} = -\frac{\partial f}{\partial x}(x)^T p + \frac{1}{4} \frac{\partial (p^T R(x) p)^T}{\partial x} - \frac{\partial q^T}{\partial x}(x)$$

### Stable Manifold theory (4)

$$A^T P + PA + Q - PR(0)P = 0$$

A solution  $P$  to above Riccati equation is called a stabilizing if  $A - R(0)P$  is stable. LQ control implies such  $P$  exists.

Then a stabilizing solution to HJ equation also exist locally around origin [N. Sakamoto and A. J. van der Schaft, IEEE TAC, 2008]

using a transformation  $\tilde{x} = \begin{bmatrix} I & S \\ \Gamma & \Gamma S - I \end{bmatrix}$

where  $\Gamma$  is the stabilizing solution and  $S$  is a solution of Lyapunov equation

$$(A - R(0)\Gamma)S + S(A - R(0)\Gamma)^T = -R(0)$$

the Hamilton system can be written as

$$\begin{pmatrix} \dot{x} \\ \dot{p} \end{pmatrix} = \begin{pmatrix} A - R(0)\Gamma & 0 \\ 0 & -(A - R(0)\Gamma)^T \end{pmatrix} \begin{pmatrix} x \\ p \end{pmatrix} + H.O.T$$

### Stable Manifold algorithm

Consider the system:  $\dot{x} = Fx + n_s(t, x, y)$

$$\dot{y} = -F^T y + n_o(t, x, y)$$

where  $F$  is asymptotically stable and  $n_s, n_o$  are higher order terms

Define sequences

$$x_{k+1} = e^{Ft} \xi + \int_0^t e^{F(t-s)} n_s(s, x_k(s), y_k(s)) ds$$

$$y_{k+1} = - \int_t^\infty e^{-F^T(t-s)} n_o(s, x_k(s), y_k(s)) ds$$

for  $k=0, 1, 2, \dots$  with  $x_0 = e^{Ft} \xi, \xi \in \mathbb{R}^n$

then as  $k \rightarrow \infty, x_{k+1}, y_{k+1}$  approach a limit function such that [Ryu Fujimoto and N. Sakamoto, IFAC, 2011]

$$\lim_{k \rightarrow \infty} \{x(t, \xi), \{y(t, \xi)\} = \zeta$$

implying that it lies on the stable manifold and is the solution of the above system.

### Problem setup

- RSIP simplified into 2D dimension

$$X = \begin{bmatrix} x_1 \\ x_2 \\ x_3 \\ x_4 \end{bmatrix} = \begin{bmatrix} \theta_1 \\ \dot{\theta}_1 \\ \theta_2 \\ \dot{\theta}_2 \end{bmatrix} \rightarrow X = \begin{bmatrix} x_1 \\ x_2 \end{bmatrix} = \begin{bmatrix} \theta_2 \\ \dot{\theta}_2 \end{bmatrix}$$

$$\dot{X} = f(X) + g(X)u \quad \text{with} \quad \begin{matrix} AX = f(X) - H.O.T \\ B = g(0) \end{matrix}$$

- Hamilton matrix for the system

$$H = \begin{pmatrix} A & -\frac{1}{2} B R^{-1} B^T \\ -2Q & -A^T \end{pmatrix}$$

- Initial condition  $X_0 = \begin{bmatrix} \pi \\ 0 \end{bmatrix}$
- Compute nonlinear optimal control for swing up and stabilization.

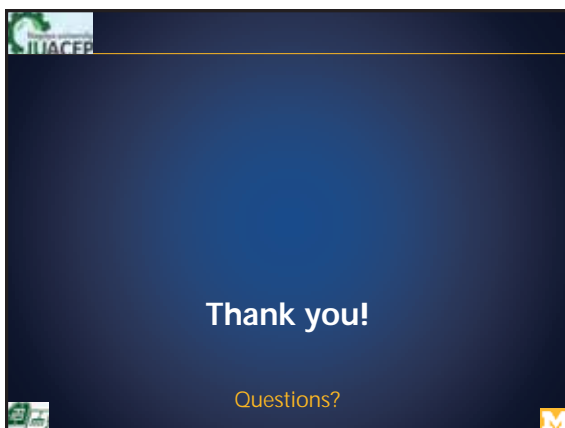
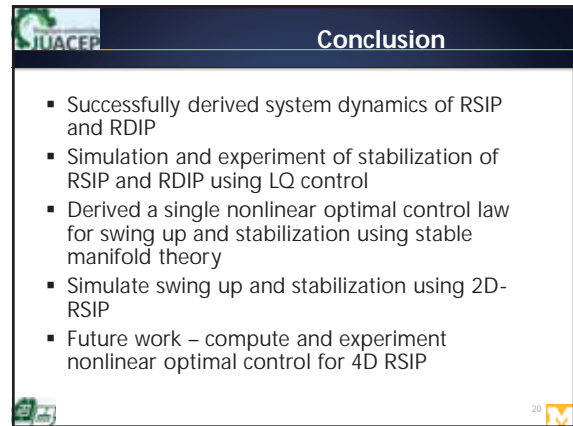
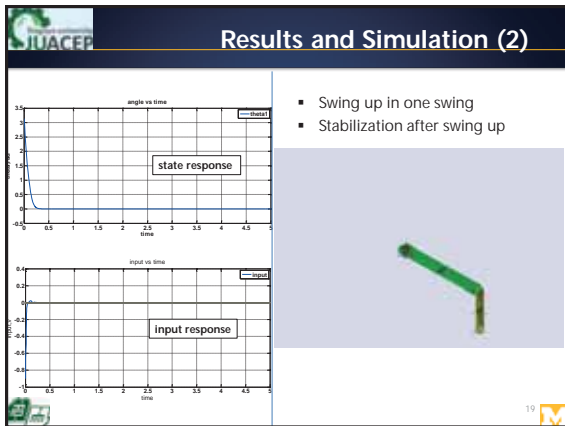
### Results and Simulation

- Iterations for many values of  $\xi$  to get state trajectory to pass through initial condition

- Calculate approximate value of  $\rho(x)$  using polynomial fit
- Calculate feedback control law

$$u = -\frac{1}{2} R^{-1} g(x)^T p(x)$$

## Amarish Krishnanand Desai



# VISUAL FEEDBACK CONTROL FOR TABLE TENNIS ROBOT

Hayakawa Lab

8.8.2013 Yi-Kai Wang

## Introduction

- In the past, the human labor and the aid of domesticated animals, both gave the efforts to build the society.
- When the machines were invented to perform repetitive tasks, the our life quality gets great improvement.



## Introduction

- Electronics is a major technological advance that lead to the creation of the “autonomous robot” by William Grey in 1948.
- Recently, different kinds of sensor are invented for various robot applications.



## System configuration

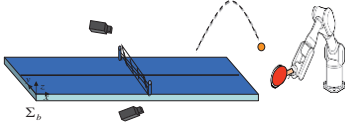


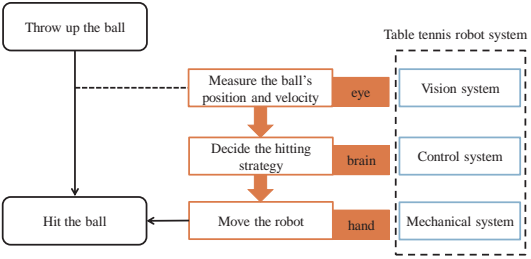
Table tennis system

- Two high speed cameras with 150fps speed
- 7-DOF arm manipulator
- Throw up the ball near the table by human

## Example video



## Construction of the system



```

    graph TD
      A[Throw up the ball] --> B[Hit the ball]
      A -.-> C[Measure the ball's position and velocity]
      C --> D[Decide the hitting strategy]
      D --> E[Move the robot]
      E --> B
      subgraph "Table tennis robot system"
        C --- C1[Vision system]
        D --- D1[Control system]
        E --- E1[Mechanical system]
      end
      C --- eye[eye]
      D --- brain[brain]
      E --- hand[hand]
  
```

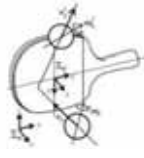
### Racket Rebound Model

□ The relationship between before and after hitting

$$\begin{bmatrix} v'_x \\ v'_y \\ v'_z \end{bmatrix} = R_{RRM}(\alpha, \beta) \begin{bmatrix} v_x \\ v_y \\ v_z \end{bmatrix}$$

$\alpha$ : yaw angle,  $\beta$ : pitch angle

$$R_{RRM}(\alpha, \beta) = \begin{bmatrix} R_R & 0 \\ 0 & R_R \end{bmatrix} \begin{bmatrix} A_{xy} & A_{yz} \\ A_{xy} & A_{yz} \end{bmatrix} \begin{bmatrix} R_R & 0 \\ 0 & R_R \end{bmatrix}^T$$

$$R_R = \begin{bmatrix} \cos \alpha & \sin \alpha \sin \beta & \sin \alpha \cos \beta \\ 0 & \cos \alpha & \sin \alpha \\ \sin \alpha & \cos \alpha \sin \beta & \cos \alpha \cos \beta \end{bmatrix}$$


### Aerodynamic Model

□ The equation describes motion of the ball in the air

$$\ddot{\mathbf{p}} = \underbrace{-g}_{\text{gravity}} \mathbf{e}_z + \underbrace{\frac{1}{2} C_D \frac{\rho}{m} r^2 \|\dot{\mathbf{p}}\| \dot{\mathbf{p}}}_{\text{drag force}} + \underbrace{\frac{4}{3} C_M \frac{\rho}{m} r^3 \dot{\mathbf{p}} \times \hat{\mathbf{p}}}_{\text{magnus force}}$$

$$\ddot{\mathbf{p}} = \frac{1}{2} C_D \frac{\rho}{m} r^2 \|\dot{\mathbf{p}}\| \dot{\mathbf{p}}$$

$$\mathbf{x} = \begin{bmatrix} p & \dot{p} \end{bmatrix}^T = \begin{bmatrix} {}^b p_x & {}^b p_y & {}^b p_z & {}^b \dot{p}_x & {}^b \dot{p}_y & {}^b \dot{p}_z \end{bmatrix}^T$$

$$\begin{cases} \dot{\mathbf{x}} = A_c \mathbf{x} + b_{c1} + b_{c2}(x) + \dot{\mathbf{c}}_c \\ \mathbf{y} = C_c \mathbf{x} + \dot{\mathbf{c}}_c \end{cases} \quad A_c = \begin{bmatrix} 0_{3 \times 3} & I_3 \\ 0_{3 \times 3} & 0_{3 \times 3} \end{bmatrix} \quad b_{c2}(x) = \begin{bmatrix} 0_{3 \times 1} \\ -\frac{1}{2} C_D \frac{\rho}{m} r^2 \|\dot{\mathbf{p}}(x)\| \dot{\mathbf{p}}(x) \end{bmatrix}$$

$$b_{c1} = \begin{bmatrix} 0 & 0 & 0 & 0 & 0 & g \end{bmatrix}^T \quad C_c = \begin{bmatrix} I_3 & 0_{3 \times 3} \end{bmatrix}$$

### Discretized system

□ Continuous system is not compatible for digital control

$$\begin{cases} \dot{\mathbf{x}} = A_c \mathbf{x} + b_{c1} + b_{c2}(x) + \dot{\mathbf{c}}_c \\ \mathbf{y} = C_c \mathbf{x} + \dot{\mathbf{c}}_c \end{cases} \rightarrow \begin{cases} \mathbf{x}_{k+1} = A \mathbf{x}_k + b_1 + b_2(x_k) + \dot{\mathbf{c}}_k \\ \mathbf{y}_k = C \mathbf{x}_k + \dot{\mathbf{c}}_k \end{cases}$$

$$A = e^{A_c h} \quad b_1 = \int_0^h e^{A_c(h-\tau)} b_{c1} d\tau \quad E\{\dot{\mathbf{c}}_k \dot{\mathbf{c}}_j^T\} = W \delta_{kj}$$

$$C = C_c \quad b_2 = \int_0^h e^{A_c(h-\tau)} b_{c2}(x_k) d\tau \quad E\{\dot{\mathbf{c}}_k \dot{\mathbf{c}}_j^T\} = V \delta_{kj}$$

### Current Limitation

□ Noise comes from the visual system.

- The ambient light will affect the detection power of the camera.
- Inherent signal noise of the visual system.

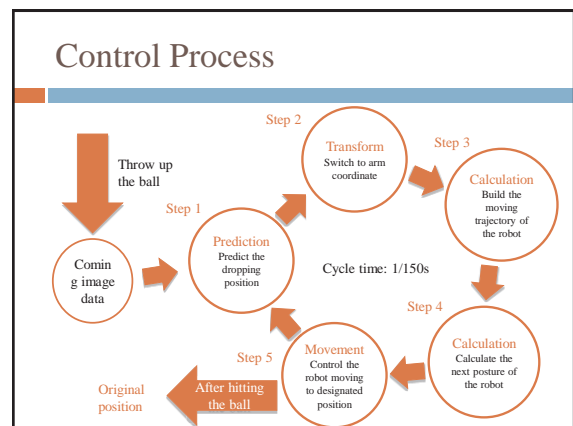
□ Imprecise prediction for the trajectory of the robot

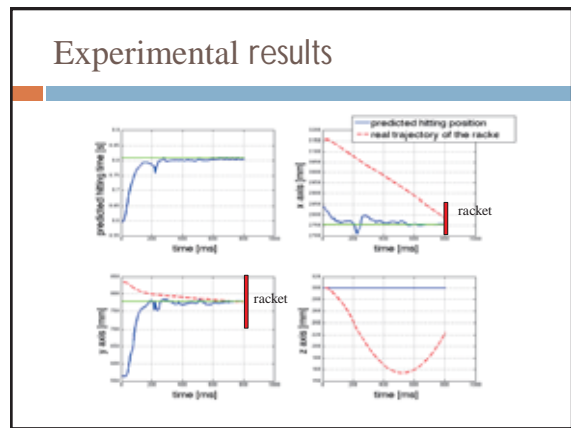
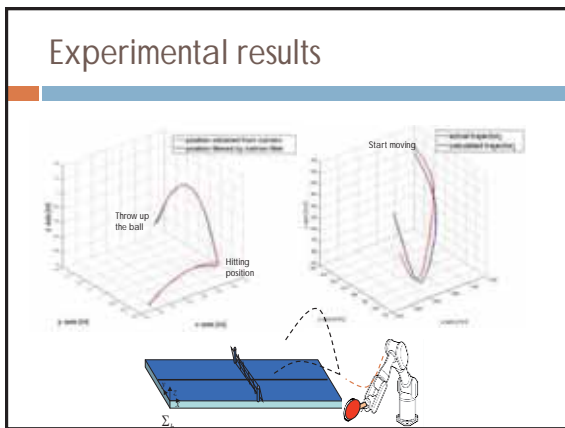
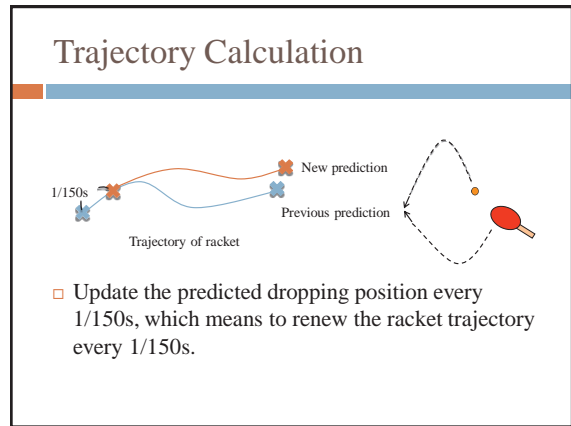
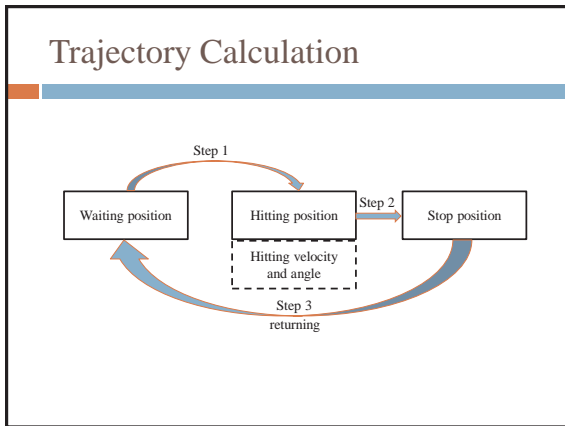
- While the ball is flying in the air, its surrounding will influence the trajectory.
- Inherent signal delay for robot control

### Kalman filter

□ Kalman filter uses a series of measurements observed over time and produces estimates that tend to be more precise than those based on a single measurement alone.

$$\text{offline} \begin{cases} P = A P A^T - A P C^T (C P C^T + V)^{-1} C P A^T + W \\ K = P C^T (V + C P C^T)^{-1} \end{cases}$$

$$\hat{\mathbf{x}}_{k+1} = A(I - KC)\hat{\mathbf{x}}_k + b_1 + b_2(\hat{\mathbf{x}}_k) + AKy_k$$




## Yi-Kai Wang

Video 3



Video 4



Video 5



### Future work

- Optimize the situation if the ball is thrown up too far away and too close to the robot
- Concern the rotation of the ball
- Solve the problem of the robot delay

Thanks for listening

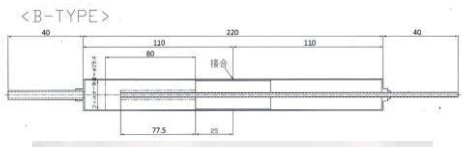
### Study on the Loop Heat Pipe with New Type of Evaporator for Mass Production

- Student: Weiyu Cao
- Instructor: Hosei Nagano



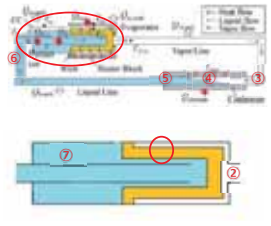
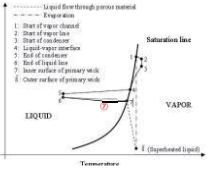
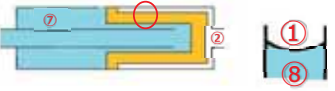
### Introduction

- Loop Heat Pipes (LHPs) are effective and efficient two-phase heat transfer devices
- The terrestrial application of LHPs was popular currently
- The production of the evaporator in LHPs used to cost a lot




### Introduction

- Operating Mechanism of LHPs


### Mathematical Model

- Modeling of the pipe flows

- Single phase flow:
  - $-mC_p \frac{dT}{dx} = \left(\frac{UA}{L}\right)_{p-a} (T - T_{amb})$
  - $-\frac{dp}{dx} = f \times \frac{1}{2} \rho u^2 \times \frac{4}{d_i}$
- Two phase flow:
  - $-\frac{dX}{dx} = \frac{1}{m\lambda} \left[ \left(\frac{UA}{L}\right)_{C-S} (T_{SAT} - T_{sink}) \right]$
  - $\Delta P_{TP} = \Phi_1^2 \times \Delta P_I$
  - $\Phi_1 = 1 + \frac{c}{X} + \frac{1}{X^2}$
  - $\chi = \Delta p_l / \Delta p_v$

The flows inside the vapor groove, vapor line, condenser and liquid line were all considered as pipe flow

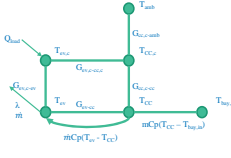
Lockhart Martinelli model was applied to gain the pressure drop of the two phase flow



### Mathematical Model

- Modeling of the Evaporator-CC Integral and Solving Algorithm

Heat Transport network in Evaporator-CC Integral



Flow chart for solving algorithm

```

    graph TD
      Start([start]) --> Input[Input parameters]
      Input --> Assume[Assume Evaporating Temperature]
      Assume --> Calculate[Calculate the properties along the LHP]
      Calculate --> Check{Energy conservation in CC satisfied}
      Check -- No --> Assume
      Check -- Yes --> End([end])
    
```



### Experiment Set Up

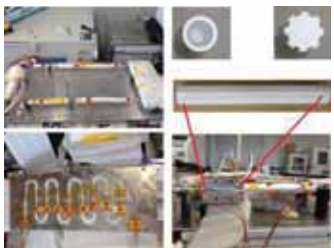
- Configuration of the Test LHP

Heater Block		Evaporator Case		CC	
Length [mm]	70	Length [mm]	75	Length [mm]	135
Width [mm]	50	O. D. [mm]	21	O. D. [mm]	21
Height [mm]	40	I. D. [mm]	19.4	I. D. [mm]	19.4
Vapor Line		Condenser		Liquid Line	
Length [m]	1	Length [m]	1.4	Length [m]	1
O. D. [mm]	6.4	O. D. [mm]	6.4	O. D. [mm]	3.2
I. D. [mm]	4.6	I. D. [mm]	4.6	I. D. [mm]	1.8



### Experiment Set Up

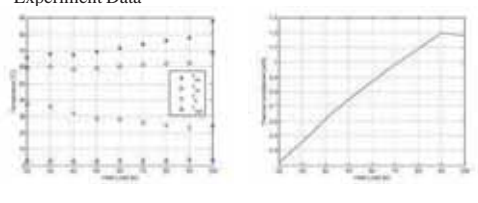
- Thermocouple positions along the test LHP



Nagoya University 7

### Results

- Experiment Data

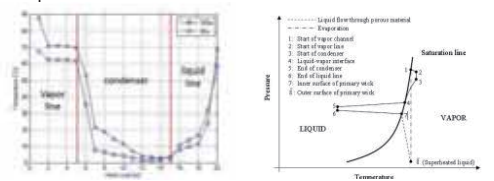


Characteristic temperature profiles of test LHP      Heat Conductance of the LHP varying with heat load

Nagoya University 8

### Results

- Experiment Data

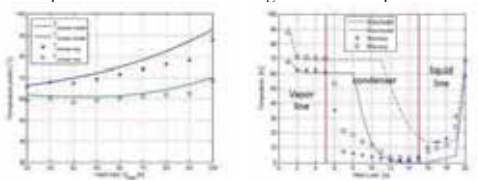


Temperature profile at different parts of LHP

Nagoya University 9

### Results

- Comparison between the modeling results and experiment data

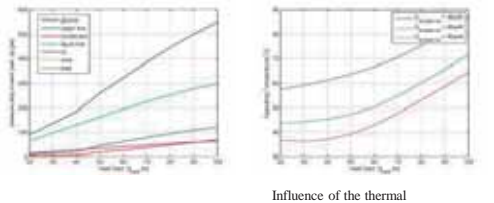


Characteristic temperature profiles of test LHP      Temperature profile at different parts of LHP

Nagoya University 10

### Results

- Parametric Study based on mathematical model



Pressure drop in different parts in LHP      Influence of the thermal conductance between the evaporator case and evaporator on operating temperature profile

Nagoya University 11

### Discussion

- Limitations of the new type evaporator
  - The connection of the liquid line connector and the CC body was weak and easy to break
  - Possible vapor leak from the vapor channel in evaporator to CC
  - High axial heat leak



Nagoya University 12

# Sriram Ganesan




## Monte-Carlo Simulation of Polycrystal Plasticity using Discrete Dislocation Plasticity Approach for Lamellar Materials

Sriram Ganesan  
Dr. Dai Okumura

Department of Computational Science and Engineering  
Nagoya University




## Presentation Outline

- Motivations
- Discrete Dislocation Plasticity
- Hall-Petch Effect
- Lamellar Material Analysis
- Results
- Conclusions

Aug 08, 2013
JUACEP, Nagoya University
2




## Motivations

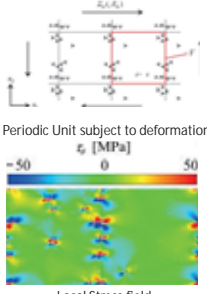
- Dislocation and microstructure-interplay
- Dislocation-grain boundary arrangement
- Microstructure optimization
- Hall-Petch effect dependence

Aug 08, 2013
JUACEP, Nagoya University
3




## Discrete Dislocation Plasticity

- Crystalline materials-dislocation motion
- Characteristic length-Burgers vector
- Local stress concentrations
- Application of periodic homogenization to superposition method



Periodic Unit subject to deformation  
 $\tau_s$  [MPa]

-50      0      50

Local Stress field

Aug 08, 2013
JUACEP, Nagoya University
4




## Superposition Method

- Dislocation problem and complementary problem

$$u_i = \hat{u}_i + \hat{u}_i, \epsilon_{ij} = \hat{\epsilon}_{ij} + \hat{\epsilon}_{ij}, \sigma_{ij} = \hat{\sigma}_{ij} + \hat{\sigma}_{ij}$$

where  $u_i, \epsilon_{ij}$  and  $\sigma_{ij}$  are the microscopic displacement, strain and stress,  $(\hat{\cdot})$  and  $(\wedge)$  are dislocation and complementary fields

- Governing equations

$$\hat{\sigma}_{ij,j} = 0, \hat{\sigma}_{ij} = c_{ijkl} \hat{\epsilon}_{kl}, \hat{\epsilon}_{kl} = (\hat{u}_{k,l} + \hat{u}_{l,k})/2$$

$c_{ijkl}$ -Elastic stiffness of material

- The complementary problem is given by

$$\hat{\sigma}_{ij,i} = 0, \hat{\sigma}_{ij} = c_{ijkl} \hat{\epsilon}_{kl}, \hat{\epsilon}_{kl} = (\hat{u}_{k,l} + \hat{u}_{l,k})/2$$

[1] Van der Giessen, E., Needleman, A., 1995. Discrete dislocation plasticity: a simple planar model. Modelling and Simulation in Materials Science and Engineering 3, 689-725.

Aug 08, 2013
JUACEP, Nagoya University
5




## Macroscopic Relations

- Macroscopic stress  $\Sigma_{ij}$  is given by

$$\Sigma_{ij} = \frac{1}{V} \int \sigma_{ij} dV$$

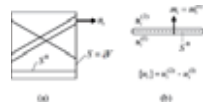
- Macroscopic strain  $E_{ij}$  is given by

$$E_{ij} = \frac{1}{2V} \int (u_i n_j + n_i u_j) dS \quad E_{ij} = \frac{1}{V} \int \epsilon_{ij} dV + \frac{1}{2V} \int_{S_D} ([u_i] m_j + m_i [u_j]) dS$$

where  $S_D$  is the set of inter surfaces on which  $u$  is discontinuous

$$u_i = E_{ij} x_j + u_i^*$$

$E_{ij} x_j$  is the macroscopic uniform component and  $u_i^*$  is the perturbed component.



Aug 08, 2013
JUACEP, Nagoya University
6

### Micro/Macro features

- The average value of stress  $\sigma_{ij}$  satisfies
 
$$\frac{1}{V} \int_V \tilde{\sigma}_{ij} dV = 0 \quad \frac{1}{V} \int_V \tilde{\epsilon}_{ij} dV = 0$$
- The macroscopic plastic strain is given by the relation
 
$$E_{ij}^p = \frac{1}{2V} \sum_{\alpha} S^{\alpha} (b_i^{(\alpha)} m_j^{(\alpha)} + m_i^{(\alpha)} b_j^{(\alpha)})$$

where  $b_i^{(\alpha)}$  is the burgers vector and  $m_i^{(\alpha)}$  is the unit normal to plane  $l^{(\alpha)}$  is the line of dislocation and  $v^{(\alpha)}$  is the velocity. Strain rate is

$$\dot{E}_{ij}^p = \frac{1}{2V} \sum_{\alpha=1}^N \left( \int_{l^{(\alpha)}} v^{(\alpha)} dl^{(\alpha)} \right) (b_i^{(\alpha)} m_j^{(\alpha)} + m_i^{(\alpha)} b_j^{(\alpha)})$$

Aug 08, 2013 JUACEP, Nagoya University 7

### Periodic BVP

- The contribution of A  $\hat{u}_i$  to macroscopic strain is
 
$$\frac{1}{V} \int_V \tilde{\epsilon}_{ij} dV = E_{ij} - E_{ij}^p \quad \hat{u}_i = (E_{ij} - E_{ij}^p) x_j$$
- The expression for  $\hat{\sigma}_{ij}$  indicates that  $\sigma_{ij}$  has the form
 
$$\sigma_{ij} = c_{ijkl} (E_{kl} - E_{kl}^p) + c_{ijkl} \tilde{\epsilon}_{kl}$$
- Substituting this in the equation for total macroscopic stress
 
$$\Sigma_{ij} = c_{ijkl} (E_{ij} - E_{ij}^p)$$

[2] Okumura, D., Ohno, N., Yamaguchi, K., 2011. Plastic size effect analysis of lamellar composites using a discrete dislocation plasticity approach, International Journal of Plasticity 27, 2040-2055

Aug 08, 2013 JUACEP, Nagoya University 8

### Flowchart

[2] Okumura, D., Ohno, N., Yamaguchi, K., 2011. Plastic size effect analysis of lamellar composites using a discrete dislocation plasticity approach, International Journal of Plasticity 27, 2040-2055

Aug 08, 2013 JUACEP, Nagoya University 9

### Hall-Petch Effect

- Grain boundary strengthening
- Pile-up activates dislocation source in another grain [7]
- Shear stress at distance ahead of boundary is
 
$$\tau_B = (\tau - \tau_0) \sqrt{\frac{d}{4\lambda}} \quad \tau_{ys} = \tau_0 + \sqrt{4\lambda} \tau_B d^{-1/2}$$
- Yielding occurs when stress concentration is large enough to activate dislocation in adjacent grain.
- $\tau_B$ ,  $\tau_0$  and  $\tau_{ys}$  are the activation, Peierls and Yield stress,  $d$  is the grain size and  $\lambda$  is the distance from grain boundary

[7] Cottrell, A.H., 1958. Theory of brittle fracture in steel and similar metals, Trans. AIME, 212

Aug 08, 2013 JUACEP, Nagoya University 10

### Checker Board Model

- All 4 edges constitute grain boundary
- Pile-up occurs along all 4 edges
- Two types of grains, Grain0 and Grain30

Schematic illustration of polycrystalline model with checker-board arrangement

Aug 08, 2013 JUACEP, Nagoya University 11

### Lamellar Model

- Only 2 edges constitute grain boundary
- Pile-up occurs along 2 edges
- Two types of grains, Grain0 and Grain30

Schematic illustration of polycrystalline model with lamellar arrangement

Aug 08, 2013 JUACEP, Nagoya University 12

### Material Parameters

Parameters	Values
$\rho_{nuc}$	$20\mu\text{m}^{-2}$
$\tau_{nuc}$ (mean)	50MPa
$\tau_{nuc}$ (sd)	5MPa
$\rho_{obs}$	$40\mu\text{m}^{-2}$
$\tau_{obs}$	150MPa
$b$	0.25nm
$E$	70GPa
$\nu$	0.33
$B$	0.1MPa ns
$\dot{\epsilon}_{12}$	$1000\text{s}^{-1}$
$\Delta t$	0.5ns

- $\rho_{nuc}$  Nucleation density
- $\tau_{nuc}$  Activation stress
- $\rho_{obs}$  Obstacle density
- $\tau_{obs}$  Obstacle strength
- $b$  Burgers vector
- $E$  Young's modulus
- $\nu$  Poisson ratio
- $B$  Drag coefficient
- $\dot{\epsilon}_{12}$  Strain rate
- $\Delta t$  Time step

Aug 08, 2013 JUACEP, Nagoya University 13

### Number of Activations

Number of activations of dislocation at distance  $\lambda$ ,  $w=1.0\mu\text{m}$ ,  $h=1.0\mu\text{m}$

Number of activations of dislocation at distance  $\lambda$ ,  $w=5.0\mu\text{m}$ ,  $h=5.0\mu\text{m}$

Number of activations of dislocation at distance  $\lambda$ ,  $w=10.0\mu\text{m}$ ,  $h=10.0\mu\text{m}$

Aug 08, 2013 JUACEP, Nagoya University 14

### Number of Activations

- Maximum dislocations from small finite distance  $\lambda$  from grain boundary
- Interaction between long range stresses and back stress
- Estimates of  $\lambda$  vary between arrangements, grain structure sensitive

S. No	Grain Size, width ( $\mu\text{m}$ )	$\lambda$ (nm) Lamellar Arrangement	$\lambda$ (nm) Checker-board arrangement
1	1	25-50	NA
2	5	50-100	200-300
3	10	100-150	300-400

Aug 08, 2013 JUACEP, Nagoya University 15

### Activation Rate

Activation rate of dislocations at distance  $\lambda$ ,  $w=1.0\mu\text{m}$ ,  $h=1.0\mu\text{m}$

Activation rate of dislocations at distance  $\lambda$ ,  $w=5.0\mu\text{m}$ ,  $h=5.0\mu\text{m}$

Activation rate of dislocations at distance  $\lambda$ ,  $w=10.0\mu\text{m}$ ,  $h=10.0\mu\text{m}$

Aug 08, 2013 JUACEP, Nagoya University 16

### Stress Field

- GB strengthening
- Softening due to low value of  $\lambda$
- Yielding occurs at about the same stress
- Shear stress along Grain30

$$\tau_{30} = (\tilde{\sigma}_{22} - \tilde{\sigma}_{11})\sin 60^\circ + \tilde{\sigma}_{12}\cos 60^\circ$$

Macro shear stress  $S_{12}$  vs macro shear strain  $E_{12}$

Aug 08, 2013 JUACEP, Nagoya University 17

### Micro shear stress field

Micro shear stress field,  $w=1.0\mu\text{m}$

Micro shear stress field,  $w=5.0\mu\text{m}$

Micro shear stress field,  $w=10.0\mu\text{m}$

Aug 08, 2013 JUACEP, Nagoya University 18

# Sriram Ganesan



## Conclusions

---

- Monte Carlo simulations for varied layer thickness
- Activation occurs at some distance from grain boundary
- Hall-Petch effect is observed
- Range of mean distance of grain activation  $\lambda$  varies from checker-board arrangement and experimental evidence for lamellar arrangement
- $\lambda$  sensitive to grain structure arrangement
- More realistic grain structure arrangement required for accurate prediction of  $\lambda$

---

Aug 08, 2013                      JUACEP, Nagoya University                      19



## References

---

- [1] Van der Giessen, E., Needleman, A., 1995. Discrete dislocation plasticity: a simple planar model. *Modelling and Simulation in Materials Science and Engineering* 3, 689-735.
- [2] Okumura, D., Ohno, N., Yamaguchi, K., 2011. Plastic size effect analysis of lamellar composites using a discrete dislocation plasticity approach. *International Journal of Plasticity* 27, 2040-2055
- [3] Lemarchand, C., Devincere, B., Kubin, L.P., 2001. Homogenization method for a discrete-continuum simulation of dislocation dynamics. *Journal of the Mechanics and Physics of Solids* 49, 1969-1982.
- [4] Belytschko, T., Grack, R., 2007. On XFEM applications to dislocations and interfaces. *International Journal of Plasticity* 23, 1721-1738.
- [5] Hirth, J.P., Lothe, J., 1982. *Theory of Dislocations*, second ed. John Wiley & Sons.
- [6] Nemat-Nasser, S., Hori, M., 1993. *Micromechanics: Overall Properties of Heterogeneous Materials*. North-Holland.
- [7] Cottrell, A.H., 1958. Theory of brittle fracture in steel and similar metals. *Trans. AIME*, 212
- [8] Shibutani, Y., Matsunaka, D., Tarumi, R., 2012. Plastic strain and temperature dependencies of Hall-Petch effect. *Journal of the society of Materials Science (in Japanese)*, Vol.61, No. 8, 724-729

---

Aug 08, 2013                      JUACEP, Nagoya University                      20

# Zhenyu Gan

**APPLICATION OF MOMENTUM-EXCHANGE-IMPACT-DAMPER ON VEHICLE COLLISION**

Speaker: Zhenyu GAN      ganzhenyu@umich.edu  
 Supervisor: Susumu HARA      haras@mech.nagoya-u.ac.jp

Mechanical Science and Engineering, Graduate School of Engineering, Nagoya University  
 Perseus-Orestes Laboratory  
 Academy for Safety Intelligence

**CONTENTS**

1. Motivation
2. The Simulation Model
3. Hardware Equipment
4. Parameter Analysis
5. Future Works

**[1] Motivation**  
 Collision Safety

Spacecraft Landing

- Large shock load
- Trip over of spacecraft

Vehicle Collision

- Large acceleration
- Energy during impact

**Traditional Structure Safety Design:**

Absorb the energy from the impact by controlled plastic deformation.

The car body are divided into three sections: the rigid non-deforming passenger compartment and the crumple zones in the front and the rear

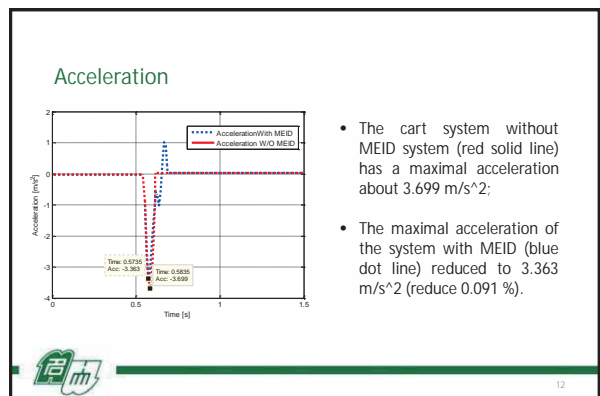
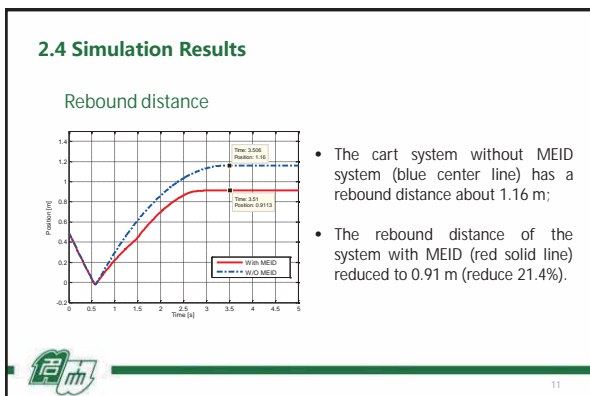
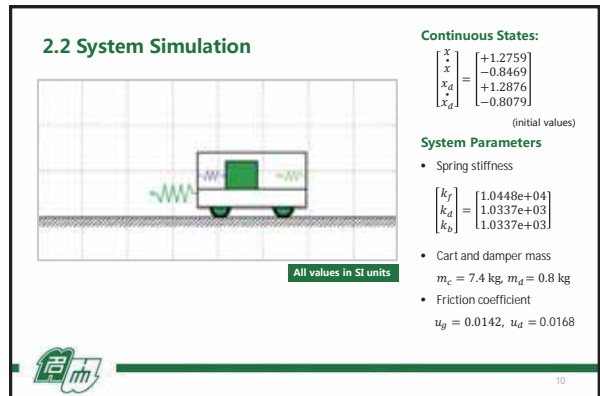
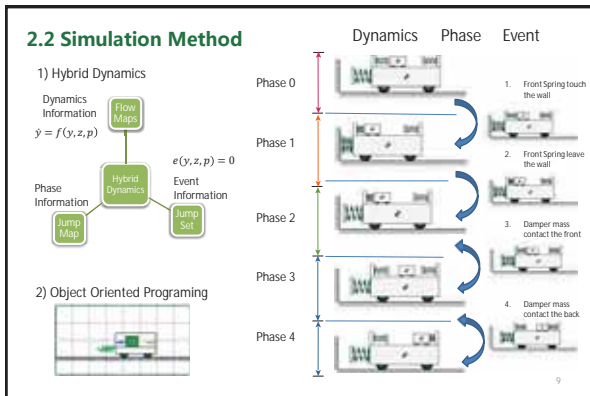
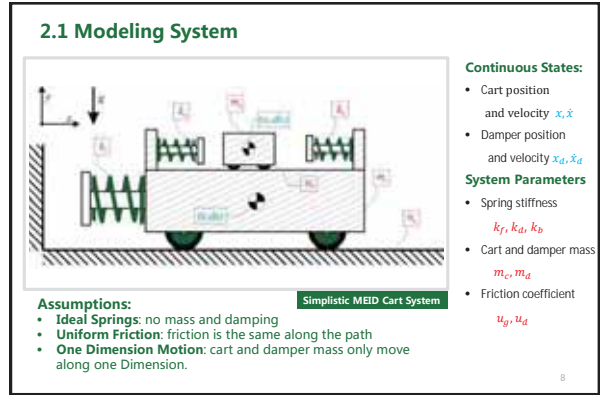
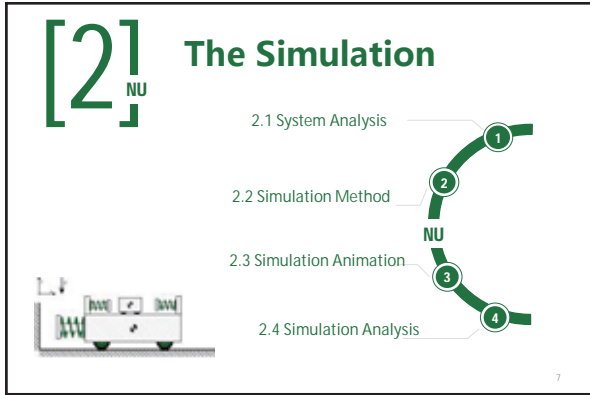
**Elastic deformation:** what if we add springs in front of the system?

Drawbacks:

- Do not dissipate energy
- Large rebound distance

**Momentum Exchange Impact Damper (MEID)**

Transferring the momentum of the system to the damper mass.



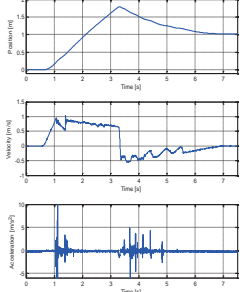
## [3] NU Hardware Equipment



- 3.1 Experimental Platform
- 3.2 Sensor Installation
- 3.3 Experiment Videos
- 3.4 Results Analysis

13

### 3.1 Experimental Platform

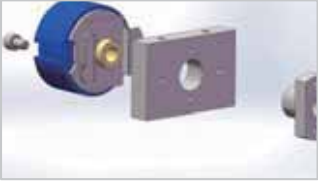



Requirement for experimental platform:

- Adjustable height for cart system to get necessary initial velocity
- Long enough to observe the system entire dynamics

14

### 3.2 Sensor Installation




Encoder Assemble Sequence  
Measure System Position, take derivative of the position to get system's velocity

Accelerometer  
Measure System acceleration.

15

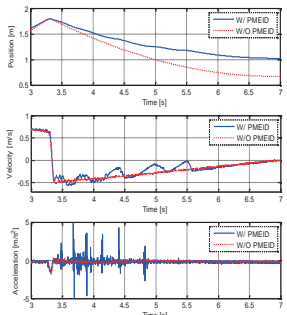
### 3.3 Experiment Videos



16

### 3.4 Results Analysis

- The rebound distance of the base mass reduces about 30% (from 1.15 m to 0.82 m);
- The first large acceleration about 17% (from 1.94 m/s<sup>2</sup> to 1.61 m/s<sup>2</sup>)

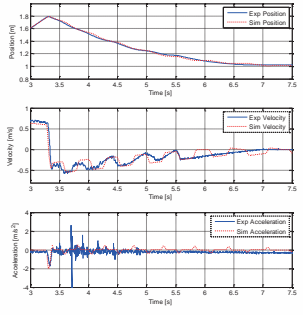


17

### 3.4 Results Analysis

First, according to the simulation results, there are at least two more oscillations after 6th second.

Second, there is a delay about 0.1s in the simulation results especially from 3.5s to 5.5s.



18

## Experimental Result Analysis

Possible Problems



Vibrate of damper mass

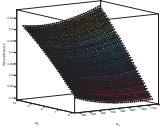


2 dimensional motion of damper mass



Oscillations of springs

## [4]<sub>NU</sub> Parameter Analysis



4.1 Mass Ratio Analysis

4.2 Damper Spring Stiffness

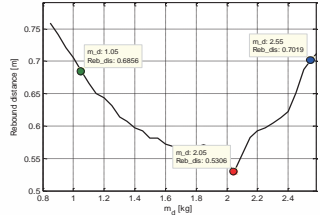
4.3 Combined Parameters Analysis



### 4.1 Mass Ratio

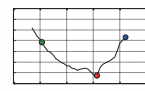
Find optimal Mass Ratio ( $\frac{m_d}{m_c+m_d}$ ) while fixed other parameters

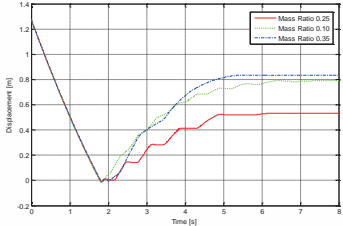




Fixed other parameters, increase mass ratio from 0.09 to 0.32 (increase  $m_d$  from 0.8 to 2.6 kg), find the minimum rebound distance at  $m_d=2.05$  kg

### Compare the three results of that major points

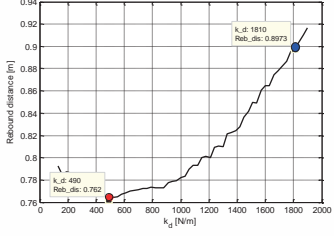




- As increasing the damper mass the frequency of the oscillation decreases.
- Trade off between friction forces and number of oscillations

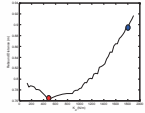
### 4.2 Damper Spring Stiffness $k_d$

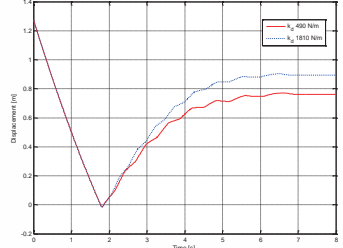




Fixed the other parameters, increase damper spring stiffness from 200 N/m to 2000 N/m, find the minimum rebound distance at  $k_d = 490$  N/m

### Compare the optimal $k_d$ with other results



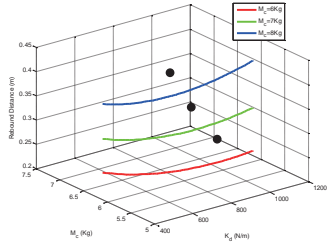


The damper spring stiffness affects the contact time of the damper and the spring thus having major influence on the number of collisions

## 4.3 Combined Parameters study

In reality the mass of the cart is not always fixed. For instance, the weight of the bus varies due to the number of people on the bus.

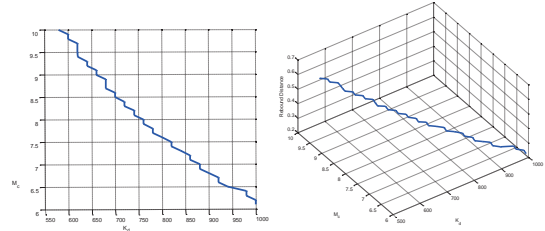
For each cart mass, we do optimal analysis to find the optimal solution of  $K_d$ .



25

## Find the optimal relationship between the two parameters

Then, we connect all the optimal solutions to find the relationship between these two parameters.



26

[5]  
NU

## Future Works

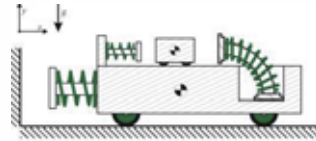
### 5.1 Passive MEID to Hybrid MEID

- Current we focus on the passive dynamics of the MEID system, after the parameters study, we want to add actuators in this system and the hybrid type momentum exchange impact damper (HMEID) could increase the robustness of the system.

27

## 5.2 Improvement of Current System

- Due to the limitations of current model, we want to improve the mechanism of current model to get better performance.
- One way may possible is that by using a bending spring to transform the horizontal momentum to vertical pressure.



28

Thanks!  
Questions?

Zhenyu Gan  
ganzhemy@umich.edu  
2013/8/8

29

## ***The 6th JUACEP Workshop***

**Date:** Thu., August 22

**Venue:** Room IB011, IB Building, Nagoya University

### **Timetable:**

13:30            Opening ~Address from Prof. Ju~  
13:40 - 16:10   Presentations by UCLA students  
                      (14 mins. presentation + 5 mins. Q&A each)  
16:10 - 16:30   Award Ceremony  
17:30 -            Farewell Banquet

~Presentation Title~

#### **1. Yaodong Wang (p.179)**

“The Effect of Adding Third Element on 4H-SiC by using Top Seeded Solution Growth”

#### **2. Owen Suyuan Liang (p.183)**

“Resistivity Measurement of CNTs Measured in a SEM”

#### **3. Justin Wang (p.186)**

“Hand Layup Fabrication with Vacuum Bagging and Compression Testing of Cross-ply Carbon Fiber Pre-Preg Tubes”

#### **4. Christopher Charles Roberts (p.188)**

“Semipolar InGaN/GaN LEDs on Patterned Silicon Substrates”

#### **5. Chung-Wen Chuang (p.194)**

“Simulation of RC Structures under Cyclic Loading using RBSM”

#### **6. Jonathan Timothy Quan (p.200)**

“Low Temperature Development of Metal Matrix Composites through Compression Torsion Process”

#### **7. Le Nguyen Khuong Ninh (p.204)**

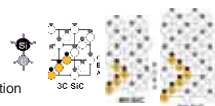
“Evaluation of Slip in Liquid Lubricant Confined in Molecularly Narrow Gap by Fiber Wobbling Method”

**The effect of adding third element on 4H-SiC by using top seeded solution growth**

Yaodong Wang

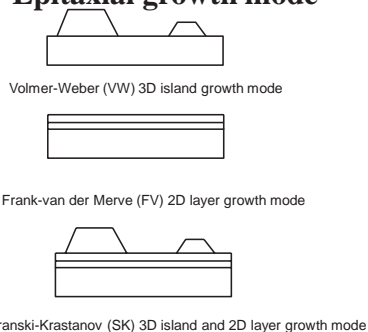
**Basics of SiC**

Wide bandgap  
High saturated velocity  
High thermal conductivity  
High operating temperature  
Harsh environment and large power application



Materials	Lattice Constant	Band gap (Eg)	Electron mobility (cm <sup>2</sup> /Vs)	Break down electric field	Saturated velocity (10 <sup>7</sup> cm/s)	Thermal conductivity (W/cmK)	Dielectric constant	Maximum operating temperature
3C-SiC	4.36	2.23	1000	4.0	2.7	3.2	9.75	1240
4H-SiC	a=3.08 c=10.08	3.2	a=720 c=650	2.0	2.0	4.5	10.0	1240
6H-SiC	a=3.08 c=15.11	3.0	a=370 c=50	2.4	2.0	4.5	9.7	1240

**Epitaxial growth mode**



**Additional growth modes**

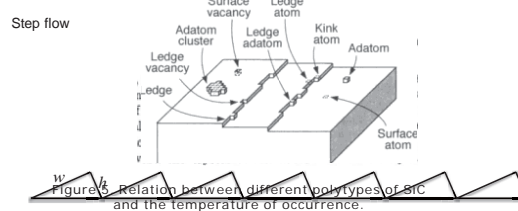


Figure 5. Relation between different polytypes of SiC and the temperature of occurrence.

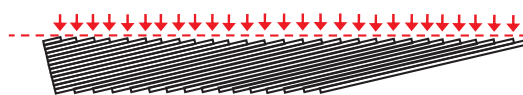
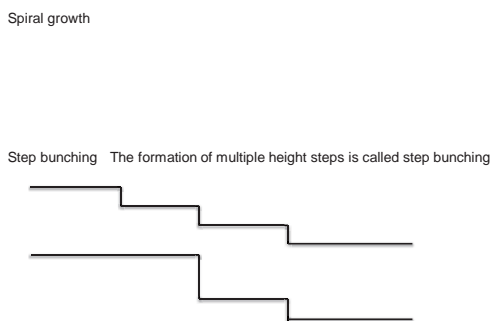
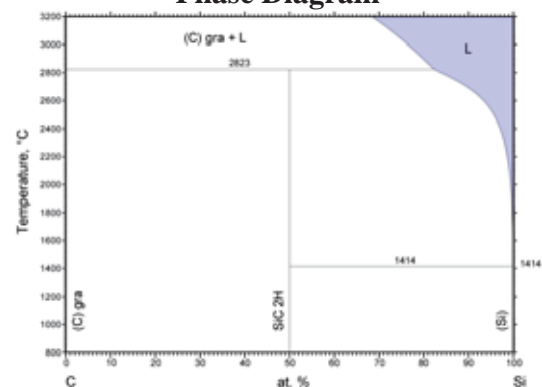


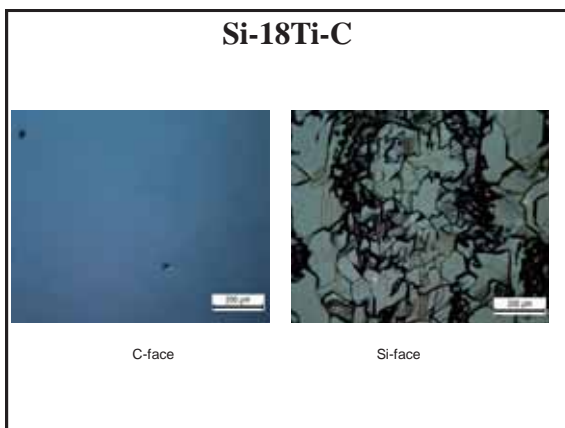
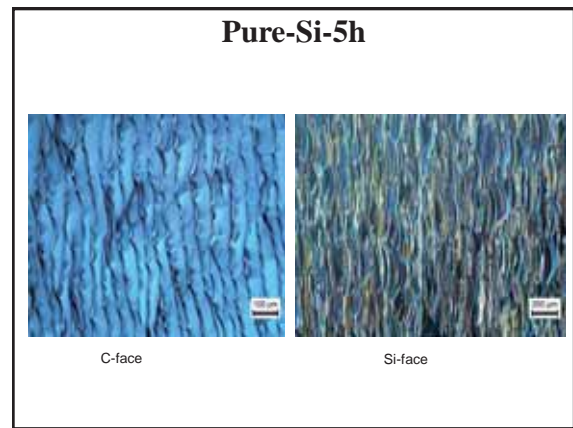
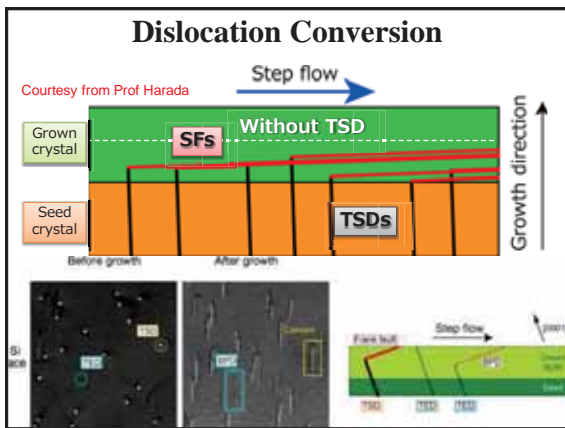
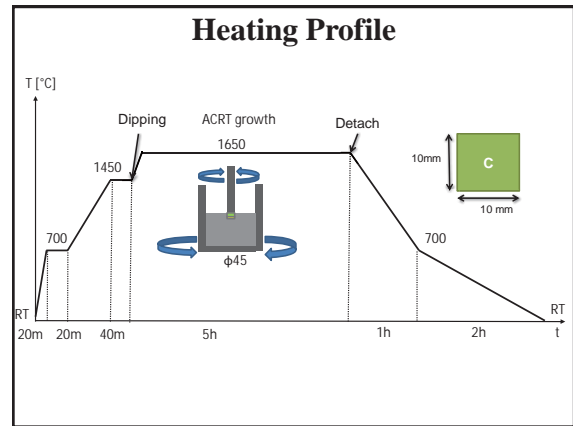
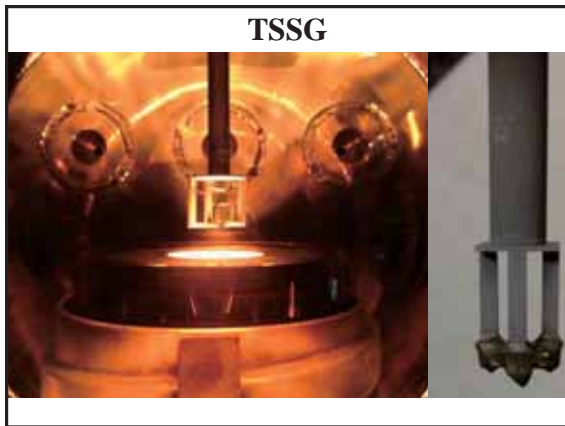
Figure 6. SiC crystal cut off-axis.

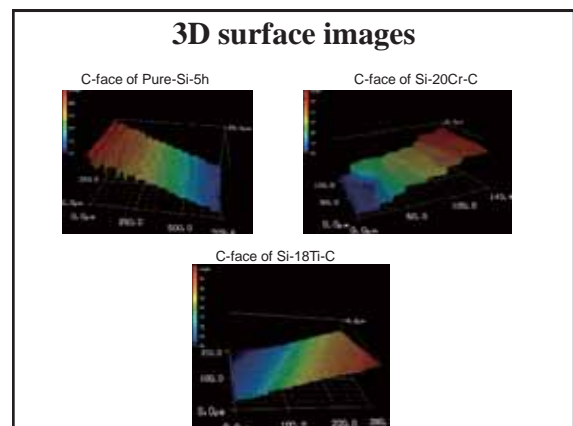
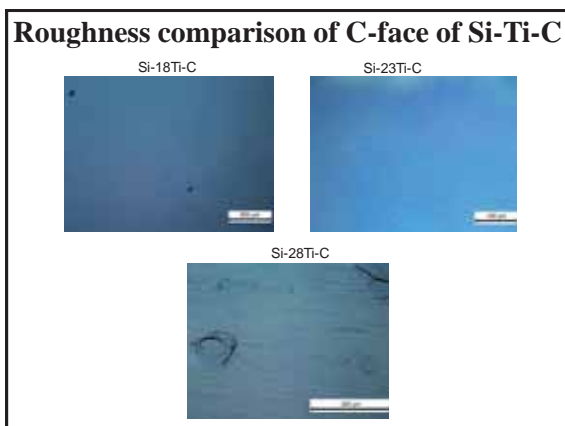
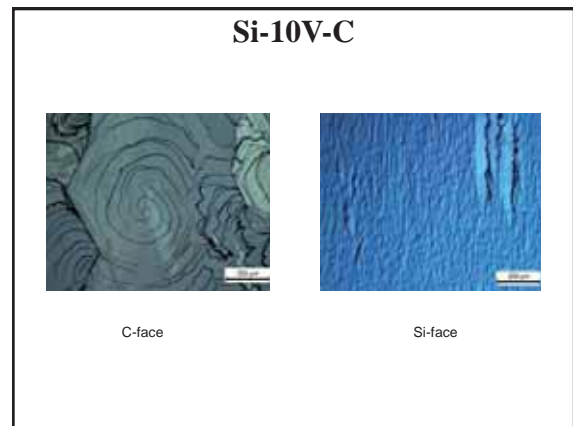
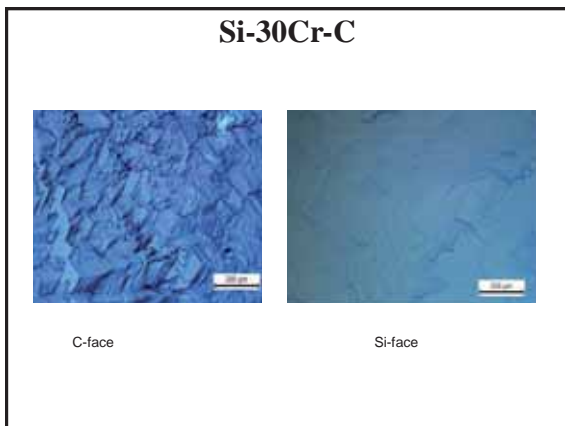
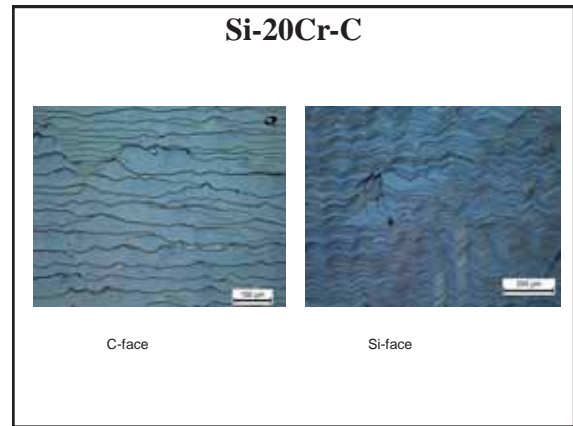
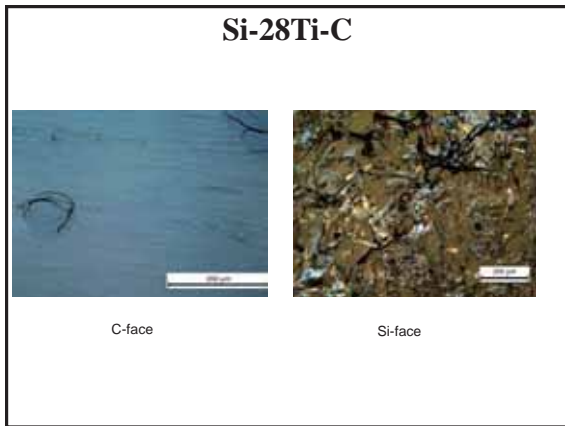
**Additional growth modes**

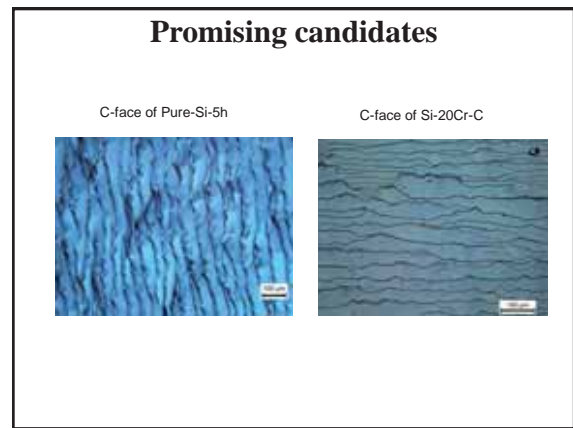
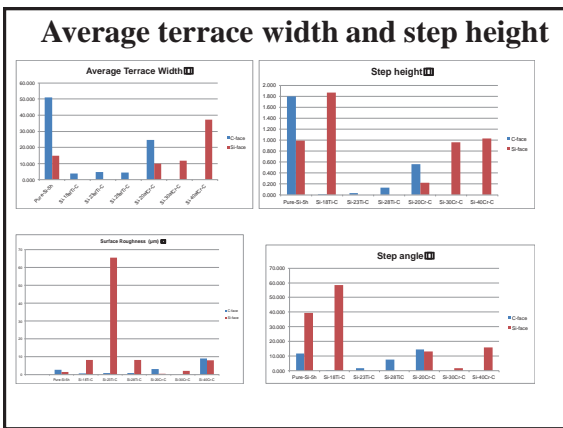
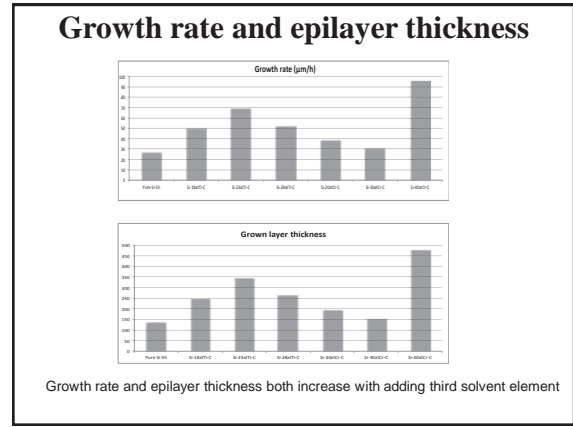
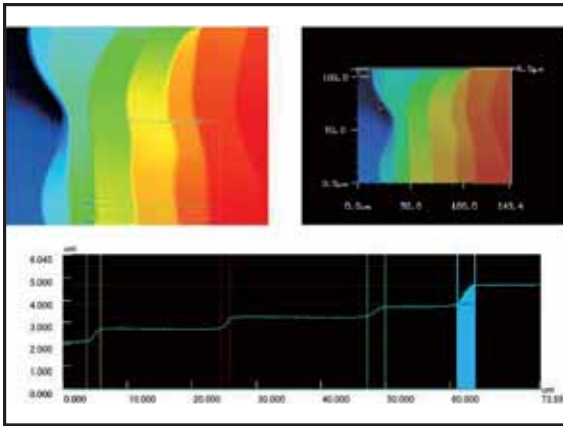


**Phase Diagram**









- ### Summary
- Large step height on C-face of Pure-Si-5h and Si-20Cr-C
  - Si-20Cr-C and Pure-Si-5h are possible candidates to observe TSD conversion on C-face
  - C-face of Si-18Ti-C are extremely smooth
  - Adding Ti and Cr can both increase epilayer thickness

# Owen Suyuan Liang

## Resistivity Measurement of CNTs Measured in a SEM

Owen Liang  
 Advisor: Professor Yahachi Saito  
 6<sup>th</sup> JUACEP Workshop  
 8-22-13



©2008 American Chemical Society, copyright and/or other rights reserved. DOI: 10.1021/bk-2008-1000

## Outline

- Introduction
- Motivation
- Theory
- Equipment Setup
- Results
- Conclusion
- Questions



## Introduction

- My Project: Two Point Probe Measurement of CNTs.
  - Apply voltage
  - Measure current
  - Measure length
  - Do calculations
  - DONE!



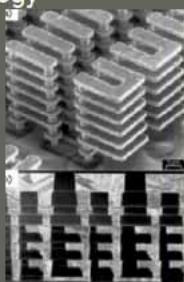
## Outline

- Introduction
- Motivation
- Theory
- Equipment Setup
- Results ~~Complaints~~
- Conclusion
- Questions



## Motivation

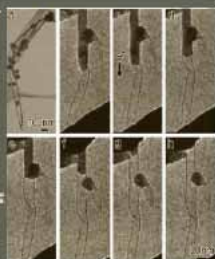
- Current transistor technology
- Interconnect technology
- Electronmigration
- Benefit of CNT
- My contribution



Researcher's contribution to the design and fabrication of interconnects. Ts, R, N, & S, 2005, Journal of Applied Physics, Vol. 98, pp. 063701.

## Motivation

- Current transistor technology
- Interconnect technology
- Electronmigration
- Benefit of CNT
- My contribution

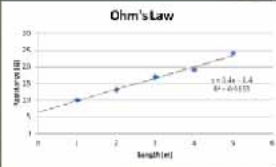


Researcher's contribution to the design and fabrication of interconnects. Ts, R, N, & S, 2005, Journal of Applied Physics, Vol. 98, pp. 063701.

# Owen Suyuan Liang

## Theory

- Ohm's Law
  - $R = (\rho/A) * L$
  - Slope =  $(\rho/A)$
  - Contact Resistance:  $R(L=0)$
- Nanomaterials:
  - Electron surface scattering



The graph shows a linear relationship between Resistance (Ω) on the y-axis (0 to 30) and Length (cm) on the x-axis (0 to 6). The data points are blue dots connected by a line. The equation of the line is  $y = 0.4x + 1.4$  and the R-squared value is  $R^2 = 0.9137$ .

## Equipment Setup



STM Tip Making Apparatus – NaOH with 0.15mm Tungsten Wire

## Equipment Setup



Kleindiek Nanomanipulators in SEM

## Equipment Setup



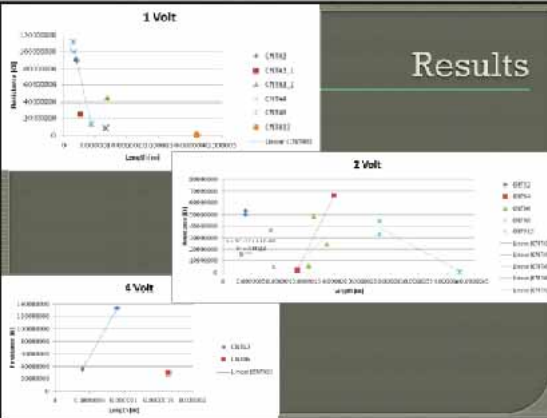

Manipulators controlled by PS2 controller

## Equipment Setup



Advantest R8340A Ultra High Resistance Meter

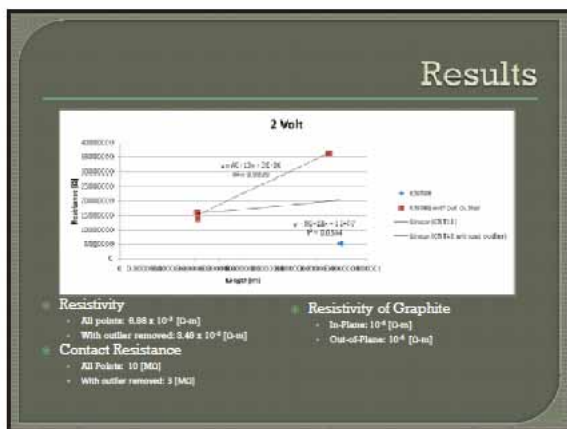
## Results



The results section contains three graphs showing Resistance (Ω) vs Length (cm) for different voltages:

- 1 Volt:** Shows a linear increase in resistance with length. The legend includes data series for CNTs 1, CNTs 2, CNTs 3, CNTs 4, and CNTs 5.
- 2 Volt:** Shows a similar linear trend. The legend includes data series for CNTs 1, CNTs 2, CNTs 3, CNTs 4, and CNTs 5.
- 4 Volt:** Shows a linear trend. The legend includes data series for CNTs 1, CNTs 2, and CNTs 3.

# Owen Suyuan Liang



## Conclusion

- Oxide removal
  - Make tips prior to measurement
  - Remove oxide by crossing tips
  - Melt W tips
- Melt CNT to tip
- Attract CNT to tip via polarization



# Justin Wang

## Hand Layup Fabrication with Vacuum Bagging and Compression Testing of Cross-ply Carbon Fiber Pre-Preg Tubes

JUSTIN WANG  
MATERIALS SCIENCE AND ENGINEERING, UCLA

ADVISOR: DR. TAKASHI ISHIKAWA  
AEROSPACE ENGINEERING, NAGOYA UNIVERSITY



JUACEP, Nagoya University 8/2013

## My Experience with Rockets



JUACEP, Nagoya University 8/2013

## The Project

- Fabricate CFRP tube
  - Cross-ply weave pre-preg
  - Vacuum bag + autoclave
  - 0/90 and ±45 orientations
- Test buckling behavior
  - Compression loading until failure
- Limited time for work
  - No metal end supports made
  - Few samples



JUACEP, Nagoya University 8/2013

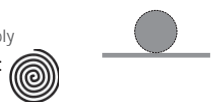
## The Tube

- Limited dimensions
  - Compression machine load limit: 200 kN
  - $F = 0.6 \frac{Eb}{r} (2\pi r h - \pi h^2)$ 
    - ×  $\sigma_{cr} = 0.6 \frac{Eh}{r} = F/A$
    - ×  $A = \pi(r+h)^2 - \pi r^2 = 2\pi r h + \pi h^2$
  - Diameter  $2r = 10$  cm → Thickness  $h < 1$  mm
    - × Each ply = 0.24 mm → 4 plies
  - Length: 15 cm (20 cm before cutting)

Mechanical properties of W3101/O112J CFRP		
$E_{1,2}$ (GPa)	G (GPa)	$\nu_{12}$
60	4.1	0.12

JUACEP, Nagoya University 8/2013

## Fabrication Considerations

- Lab optimized for vacuum bag plate fabrication
  - Need flat area for vacuum cup
  - Solution: Plate + Cylinder assembly
- Spiral lay-up method chosen:
 
- CFRP roll only in 0/90
  - Dimensions insufficient for a single 4-ply length sheet in ±45
  - Solution: Use two 2-ply sheets
- Extreme care taken with each applied film and sheet
  - Any slack will create wrinkles after cure
  - Misaligned CFRP plies will give wrong orientations

JUACEP, Nagoya University 8/2013

## Fabrication and Testing



JUACEP, Nagoya University 8/2013

## Justin Wang

### Results and Discussion

- Compression testing was not successful
  - No end supports = poor buckling results
  - Buckling on  $\pm 45$  may be due to wrinkles creating unequal strength and load distribution
- $\pm 45$  tubes had many wrinkles, 0/90 did not
  - $\pm 45$  was made second by one person
    - Additional help may improve wrapping
  - $\pm 45$  tube bagging was done poorly compared to 0/90 bagging
- Difficult to cut tubes straight
  - Aligning by eye, tube may turn as it is cut, filing required
  - Task made easier with aluminum mandrel inside at desired length

JUACEP, Nagoya University

8/2013

### Conclusions

- Fabricating a tube with vacuum bagging is possible.
- At least two people working together may improve fabrication.
- Ends supports for tube buckling tests are needed.
- More time would allow more samples, more experience, and better experimental setup.
- I want an autoclave.

JUACEP, Nagoya University

8/2013

### Acknowledgements

- Dr. Takashi Ishikawa
- Dr. Jenn-Ming Yang
- Daiki Yamagami
- JUACEP Staff

Thank you for the wonderful experience in Japan!

JUACEP, Nagoya University

8/2013

# Christopher Charles Roberts

## SEMIPOLAR INGAN/GAN LEDs ON PATTERNED SILICON SUBSTRATES

FABRICATION OF BACKSIDE CONTACTS VIA WET ETCHING

Christopher Roberts  
Amano Laboratory

### Advantages of III-N LEDs on Si

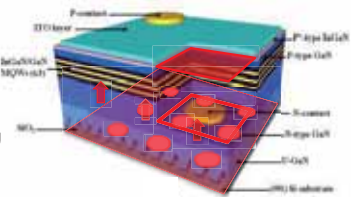
-  Silicon is a low cost substrate
-  Allows for semipolar orientations, reducing QCSE
-  Mg incorporation 10x better in (1-101) orientation
-  Thermal mismatch is avoided for die sizes below  $500 \mu\text{m}^2$

### Obstacles of III-N LEDs on Si

-  Resistive AIN buffer layer
-  Si substrate absorbs emitted light
-  Coalescing epitaxial front result in stacking faults (BSF)
-  Lower In incorporation

### Backside Contact Geometry

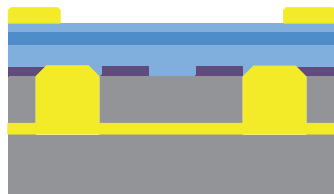
- Allows for more active surface area exposure
- Allows current to flow through AIN layer
- Better current spreading



Chiu, C. et al. Proc. SPIE 7939, Gallium Nitride Materials and Devices VI, 79391 (2011)

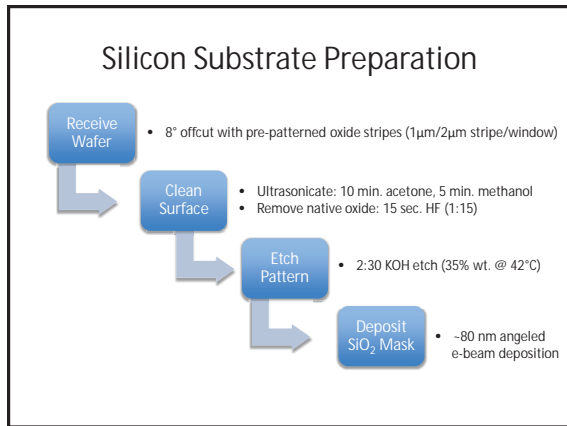
### Project Goals

- Prepare Silicon Substrate
- Grow Semipolar III-N LEDs
- Mechanical Polishing
- Etch Vias
- Deposit Contacts

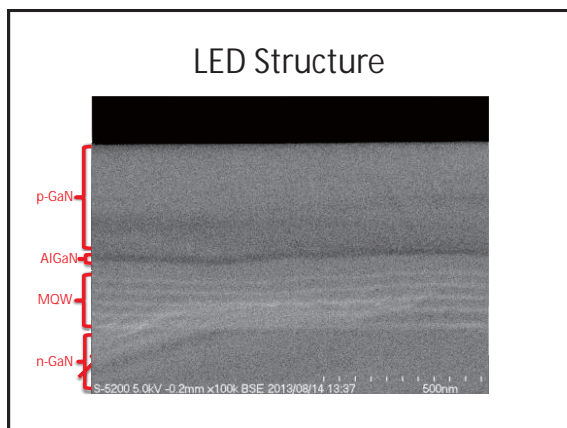
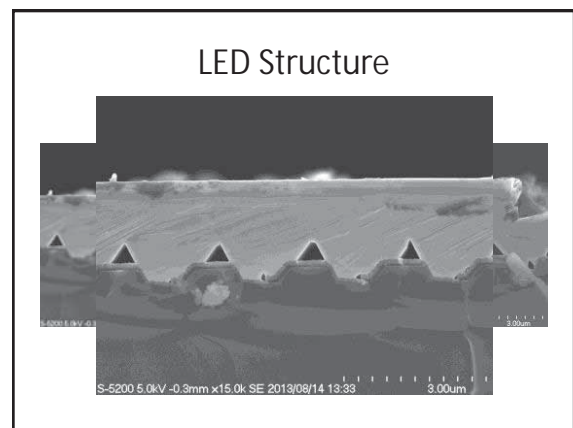
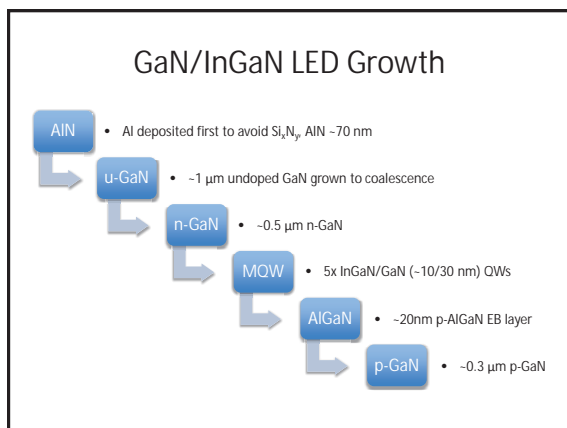


Prepare Silicon Substrate

# Christopher Charles Roberts

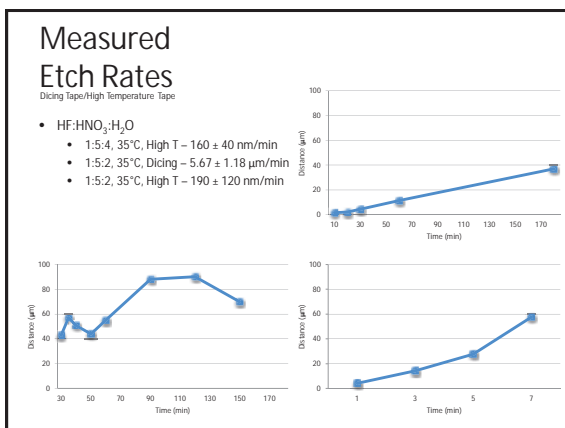
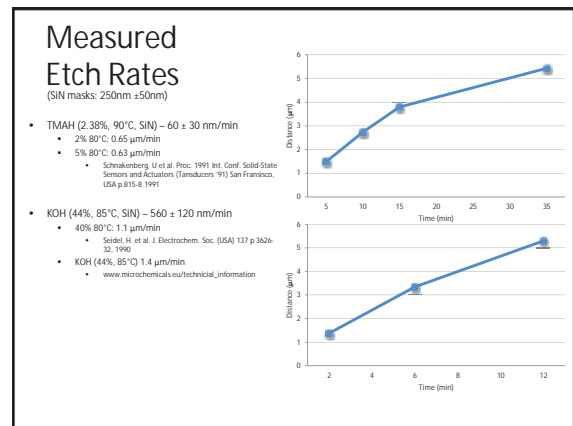
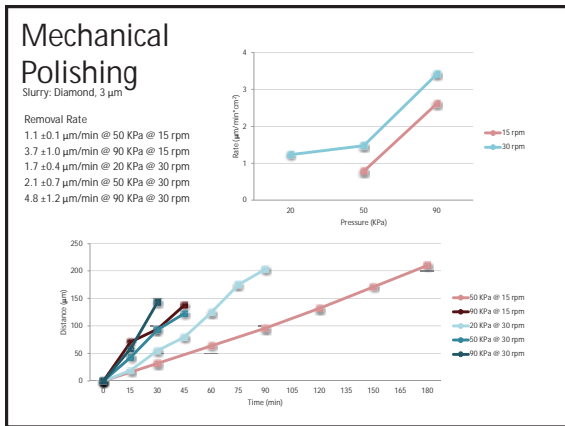


Grow Semipolar III-N LEDs



Mechanical Polishing

# Christopher Charles Roberts



## Via Etching: Mask

Mask	HF:HNO <sub>3</sub> :H <sub>2</sub> O	KOH
E-beam SiO <sub>2</sub>	Low	Moderate
Sputtered SiN <sub>x</sub>	Low	Low
Photoresist	Low	Moderate
Dicing tape	Moderate	Moderate
High T tape	High	Moderate

A microscopic image showing several circular vias etched into a substrate. A scale bar at the bottom right indicates 10  $\mu\text{m}$ .

*Christopher Charles Roberts*

HF:HNO<sub>3</sub>:H<sub>2</sub>O



KOH



HF:HNO<sub>3</sub>:H<sub>2</sub>O



HF:HNO<sub>3</sub>:H<sub>2</sub>O



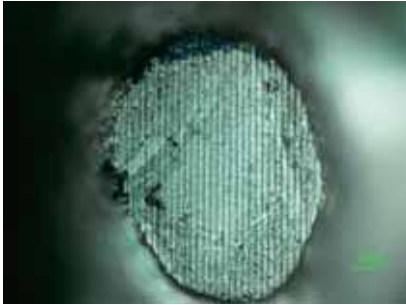
Nitride Etch-stop Layer



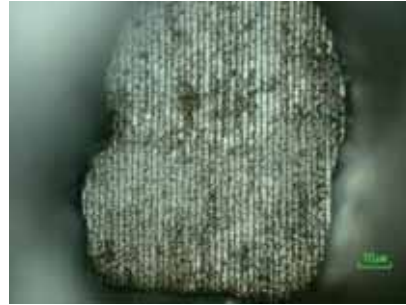
Deposit  
Contacts

*Christopher Charles Roberts*

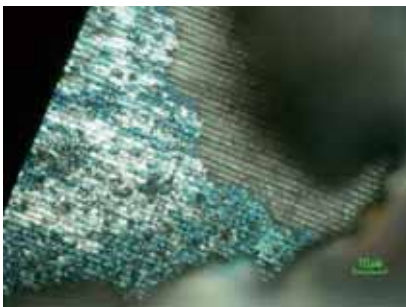
Backside Contact (Ti/Al)



Backside Contact (Ti/Al)



Shadow Effect



Fractured Nitride Layer

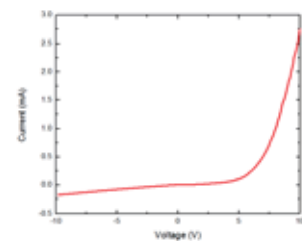


I-V  
Characteristics

I-V Characteristics

Sources of Resistance

- Unetched AlN Layer
- Non-ohmic contacts
- Poor contact between n-contact and copper board (solder paste)



*Christopher Charles Roberts*

Thank you

ありがとうございます

# Chung-Wen Chuang

August 22, 2013  
Nagoya University  
Nagoya, Japan

## Simulation of RC Structures under Cyclic Loading using RBSM

**Chung-Wen CHUANG**  
Supervisor: Professor Hikaru NAKAMURA

### CONTENTS

- Motivation of Research
- Introduction to Rigid-Body-Spring Model (RBSM)
- Examples using RBSM
  - ☐ Analytical & Experimental Results under Monotonic Loading
  - ☐ Simulation under Cyclic Loading
- Conclusions
- References

2

### CONTENTS

- **Motivation of Research**
- Introduction to Rigid-Body-Spring Model (RBSM)
- Examples using RBSM
  - ☐ Analytical & Experimental Results under Monotonic Loading
  - ☐ Simulation under Cyclic Loading
- Conclusions
- References

3

### Similar Damages due to Recent Earthquakes



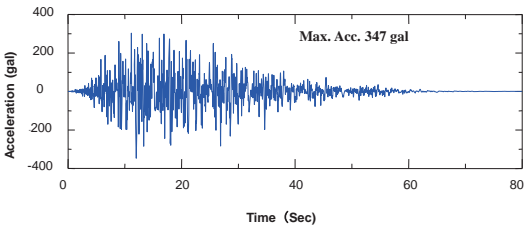
Niigata-ken Chuetsu Earthquake, 2007      Kobe Earthquake, 1995

- **Shear failure of RC columns**
- The damage due to Kobe Earthquake is severer, but they are in the same failure type.

4

### Earthquake Ground Motion

An earthquake ground motion consists of many different quantities of **cyclic loading**.



Max. Acc. 347 gal

5

### CONTENTS

- Motivation of Concrete Structures Research
- **Introduction to Rigid-Body-Spring Model (RBSM)**
- Examples using RBSM
  - ☐ Analytical & Experimental Results under Monotonic Loading
  - ☐ Simulation under Cyclic Loading
- Conclusions
- References

6

## RBSM (Rigid-Body-Spring Model)

**RBSM is an analytical model used to simulate structural behavior by springs between Rigid Bodies.**

Analytical model is divided by 3-D Voronoi particles

A number of springs are set in boundary of each surface.

This model can evaluate the effect of bending and torsional moment automatically without rotational springs.

One integral point has two kinds of springs (normal/shear)

For reduction of elements dependency

Cracks are expressed by the failure of springs and cracking behavior can be shown directly.

## Concrete Material Model

**Idea**  
no softening part is modeled in compression

a) Tensile Model of Normal Spring  
b) Compression Model of Normal Spring  
c) Shear Spring Model  
d) Mohr-Coulomb Criteria  
e) Softening Coefficient for Shear Spring

## Reinforcement Model

### modeling of reinforcement

Beam element

Zero size link element

Tensile strength  $T_{max}$

Bond-slip relationship

Stress-strain relationship

Reinforcement: beam element  
Beam nodes: attach to the concrete particles through zero-size link element  
Stress-strain relationship: bi-linear model  
Bond property: introduced into the shear spring of linked element

## CONTENTS

- Motivation of Research
- Introduction to Rigid-Body-Spring Model (RBSM)
- Examples using RBSM
  - ❑ Analytical & Experimental Results under Monotonic Loading
  - ❑ Simulation under Cyclic Loading
- Conclusions
- References

## CONTENTS

- Motivation of Research
- Introduction to Rigid-Body-Spring Model (RBSM)
- Examples using RBSM
  - ❑ Analytical & Experimental Results under Monotonic Loading
  - ❑ Simulation under Cyclic Loading
- Conclusions
- References

## Analytical Results of RBSM – Flexural Failure

Results of cantilever type of a RC beam failed in **compression flexural mode** under **monotonic loading**.

PC bar

Illustration of the cantilever type of a RC beam under monotonic loading equipped in the experiment

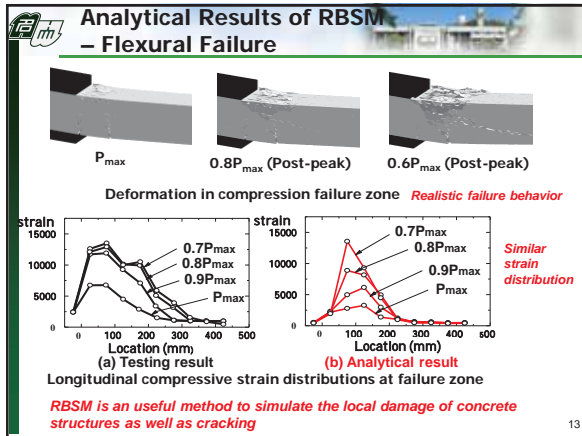
Load-displacement relationship

Analytical model with Voronoi diagram

Crack propagation behavior at peak and post-peak using RBSM

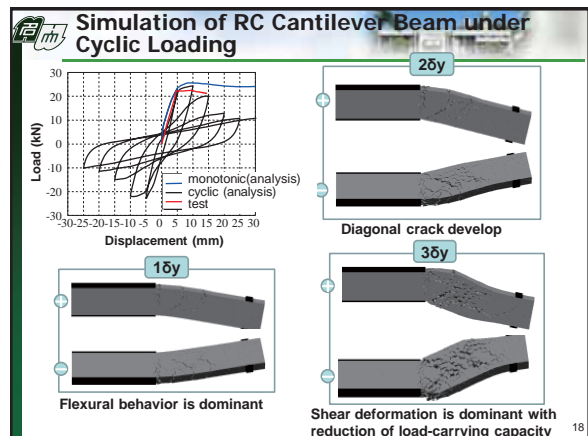
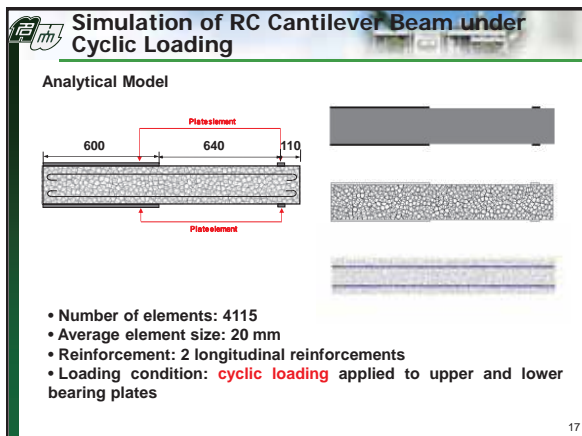
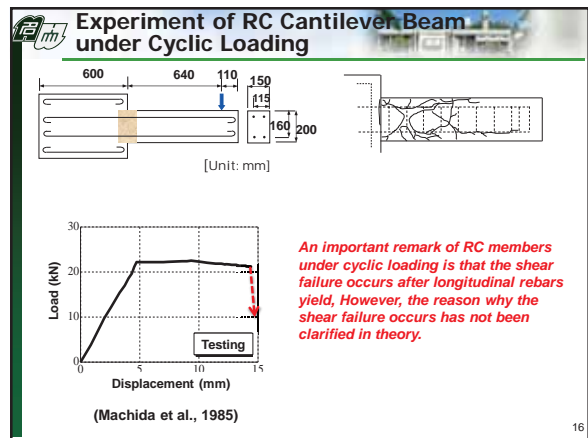
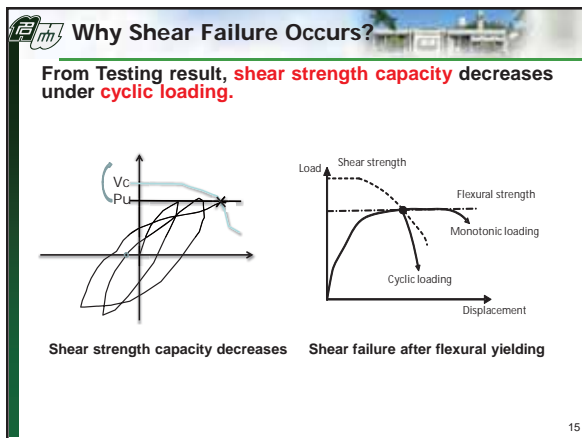
RBSM can simulate global behavior, the advantage is that it can show the realistic crack propagation behavior

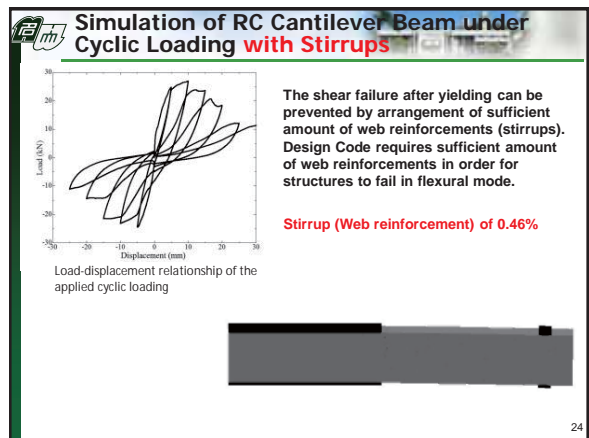
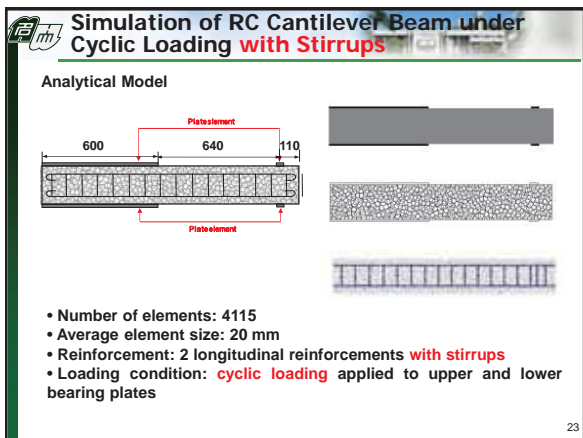
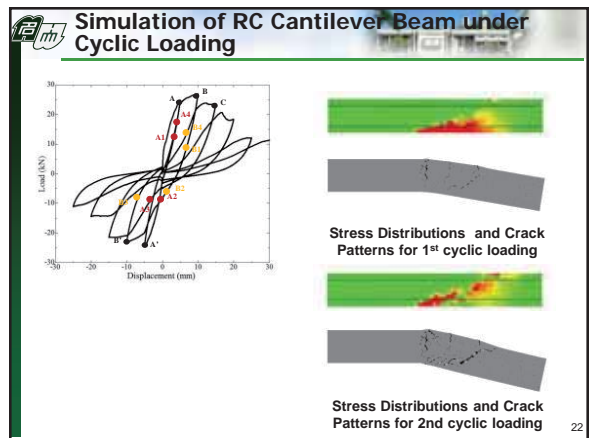
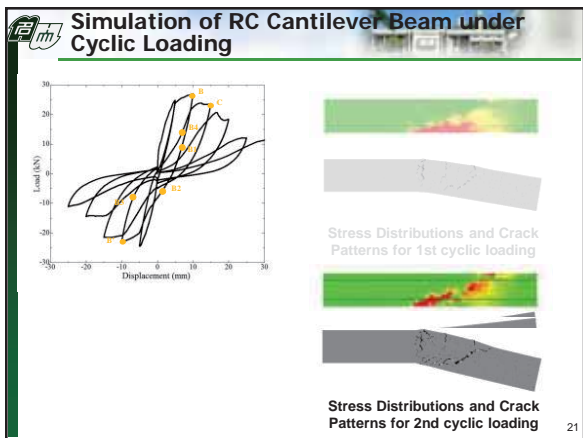
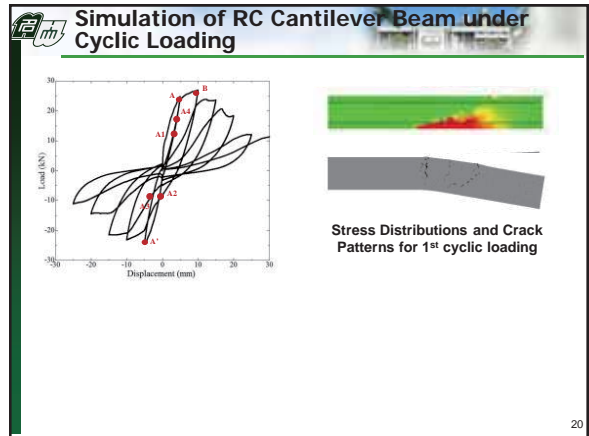
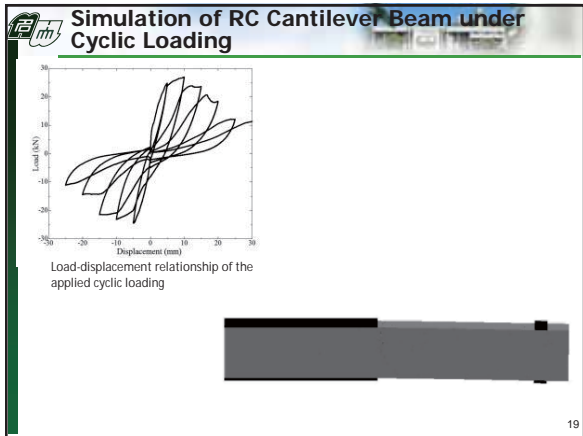
# Chung-Wen Chuang



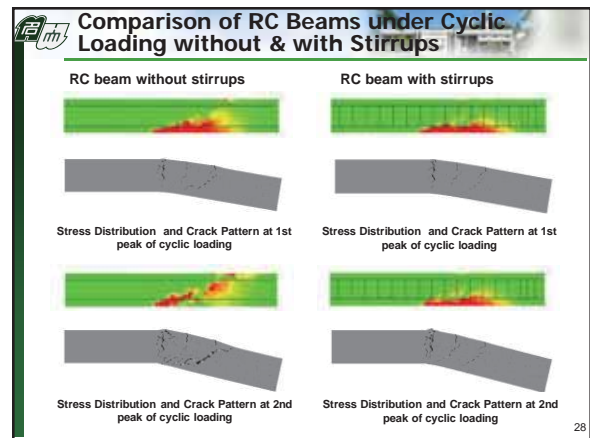
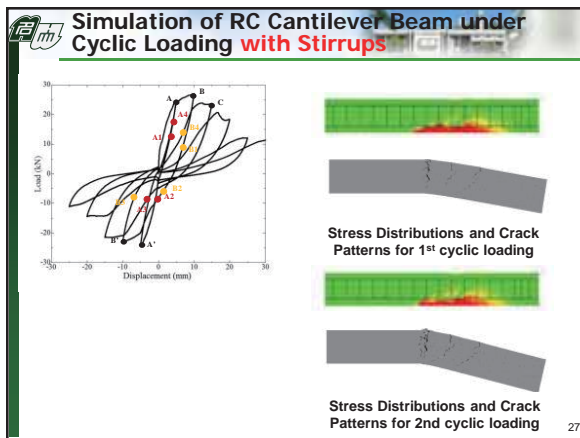
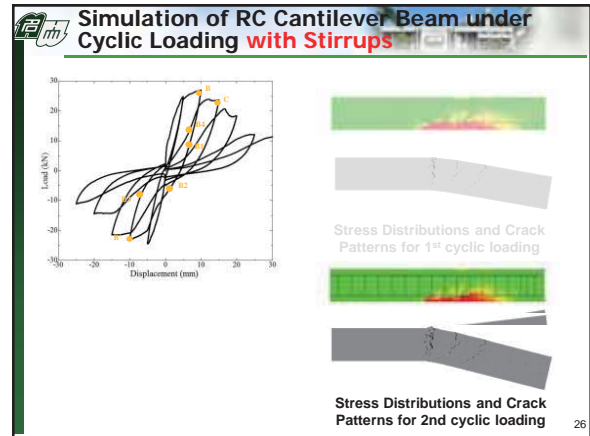
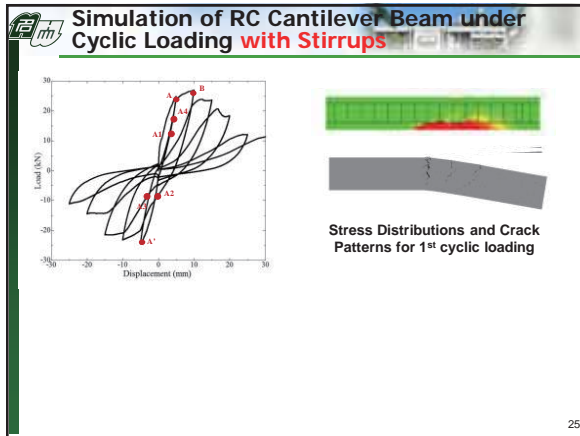
### CONTENTS

- Motivation of Research
- Introduction to Rigid-Body-Spring Model (RBSM)
- Examples using RBSM
  - ❑ Analytical & Experimental Results under Monotonic Loading
  - ❑ Simulation under Cyclic Loading
- Conclusions
- References





# Chung-Wen Chuang



**CONTENTS**

- Motivation of Research
- Introduction to Rigid-Body-Spring Model (RBSM)
- Examples using RBSM
  - Analytical & Experimental Results under Monotonic Loading
  - Simulation under Cyclic Loading
- Conclusions
- References

29

**Conclusions**

- (1) Curves simulated by 3D RBSM method show similar behavior with the testing results, so that the possibility using 3D RBSM analysis is confirmed.
- (2) 3D RBSM can simulate the shear failure under cyclic loading, realistic crack patterns and illustrative stress distributions.
- (3) Shear behavior would take over the flexural behavior gradually under cyclic loading.
- (4) Shear failure can be prevented by arrangement of sufficient web reinforcements (stirrups). Sufficient amount of web reinforcements is required in Design Code to make structures flexural failure.

NO ONE believes the results of an analysis,  
EXCEPT the person who performed it;  
EVERYONE believes the results of an experiment,  
EXCEPT the person who performed it.

30

## Chung-Wen Chuang



### References

- [1] Furuhashi, H., Nakamura, H., Yamamoto, Y., Numerical Study on Shear Strength Degradation after Flexural Yielding of RC Member Subjected to Cyclic Loading, EASEC-13 (2013).
- [2] Priestley, M. J. N., Seible, F., Carvi, G. M., Seismic Design of Retrofit of Bridges, A Wiley-Interscience Publication (1996).
- [3] Ohe, R., Yoshikawa, H., Study on shear strength degradation of single reinforced concrete columns under repeated large deformation, Doboku Gakkai Ronbunshuu E. V-56, No. 711, pp. 59-71 (2002).
- [4] Gedik, Y. H., Nakamura, H., Yamamoto, Y., Kunieda, M., Evaluation of Three-Dimensional Effects in Short Deep Beams using a Rigid-Body-Spring-Model, Cement and Concrete Composites, 33(9), pp. 978-991 (2011).
- [5] Yamamoto, Y., Nakamura, H., Kuroda, I., Furuya, N., Simulation of Crack Propagation in RC Shear Wall Using a 3D Rigid-Body-Spring Model with Random Geometry, FraMCoS-8 (2013).
- [6] Saito, S., Hikosaka, H., Numerical Analysis of Reinforced Concrete Structures Using Spring Network Model, Journal of Materials, Concrete Structures and Pavements, Vol. 44, No. 627, pp. 289-303 (1999).
- [7] Machida, A., Mutsuyoshi, H., Toyoda, K., Evaluation of the Ductility of Reinforced Concrete Members, Annual Journal of Japan Concrete Institute, Vol. 7, No. 1, pp. 629-632 (1985).

31



Thank you for your attention!



Nagoya University 名古屋大学



32

# Jonathan Timothy Quan

## Low Temperature Development of Metal Matrix Composites through Compression Torsion Process

Jonathan Quan

[Kanetake & Kobashi Lab.](#)

## Motivation and Outline

- Motivation: Develop a metal matrix composite composed of Al matrix and Fe particles using Compression Torsion Process at low temperature to avoid Al-Fe intermetallics
- Introduction
  - Metal Matrix Composites
  - Compression Torsion Process (CTP)
- CTP Experiment
  - Microscopy → Microstructure
  - Energy Dispersive Spectroscopy → element detection
  - X-ray Diffraction → intermetallic detection
  - Microhardness Testing → Mechanical improvement
- Conclusion

## Metal Matrix Composites

### Materials

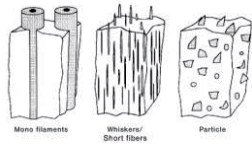
- Metals
- Ceramics
- Semiconductors
- Polymers

### Forms

- Particles (0-D)
- Fibers (1-D)
- Sheet (2-D)
- Matrix (3-D)

Iron

Aluminum



From Clyne, 1993

T. W. Clyne, P. J. Withers, *An Introduction to Metal Matrix Composites*, Cambridge University Press, Cambridge (1993).

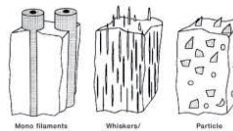
## Metal Matrix Composite Challenges

### Metal Matrix

- Light weight
- Ductility
- Easy Processing
  - Liquid
  - Liquid-Solid
  - Solid

### Reinforcement Material

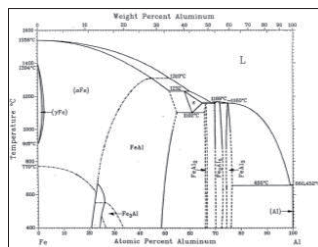
- Cost
- Mechanical Properties
  - High Modulus
  - Good strength
- Melting Temperature
- Compatibility
- Particulate/Fibrous



T. W. Clyne, P. J. Withers, *An Introduction to Metal Matrix Composites*, Cambridge University Press, Cambridge (1993).

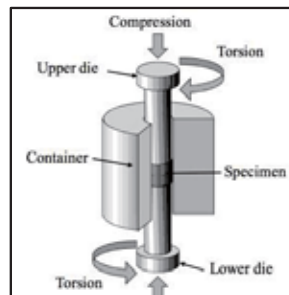
## Fe/Al joining difficulties

- Iron (steel) alloys and Aluminum alloys are dissimilar
  - Melting temperature ( $T_m$ )
  - differences
  - Thermal conductivity
- Formation of brittle Fe/Al intermetallic
  - $Fe_3Al$ ,  $FeAl$ ,  $FeAl_2$ ,  $Fe_2Al_5$ ,  $FeAl_3$
- Process Temp: Al/Fe intermetallic
  - $1273K < T_{process} < 1473K$
- Warm Working Temperature
  - $923K < T_{ww} < 1073K$
- Critical Temperature: Disorder
  - $T_{c11} = 823K$



Kobayashi, Shigeki, and Takao Yakou. "Control of intermetallic compound layers at interface between steel and aluminum by diffusion treatment." *Materials Science and Engineering: A* 338:1 (2002): 44-53.  
 Stoloff, N. S. "Iron-aluminides: present status and future prospects." *Materials Science and Engineering: A* 258:1 (1998): 1-14.  
 Campbell, Flake C., ed. *Joining: Understanding the Basics*. ASM International, 2011.  
 U.K. Kallner, T.B. Massabki, in: H. Baker (Ed.), *Binary Alloy Phase Diagrams*, ASM International, Material Park, OH, 1990, p. 147.

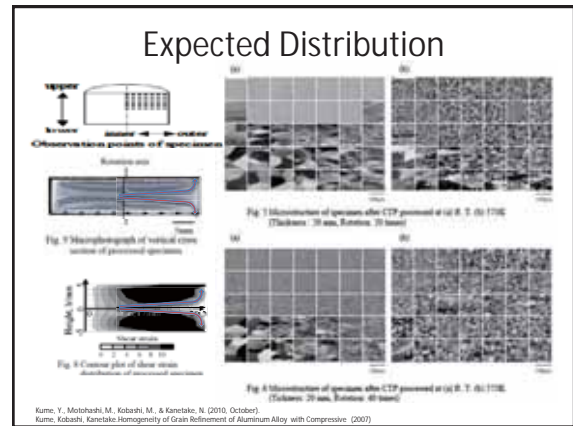
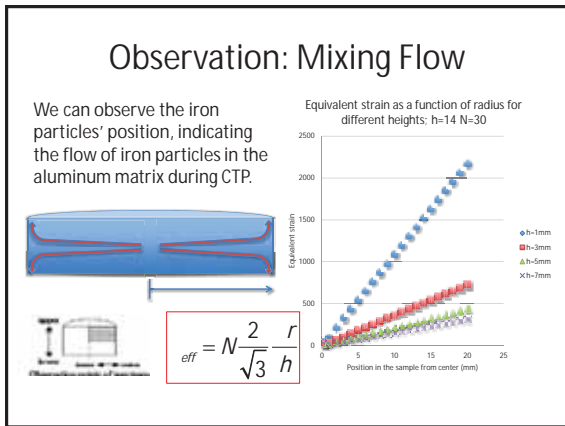
## Compression Torsion Process



1. Ultrafine grain refinement
  - Nanocrystalline material
  - Strengthening
2. Solid-State Welding
3. Consolidation of particles

Kume, Yoji, et al. "Visualization and Quantification of Severe Internal Deformation on Compressive Torsion Process." *Materials Science Forum*. Vol. 654. 2010.  
 Y. Estrin, A. Vinogradov / *Acta Materialia* 61 (2013) 792-817

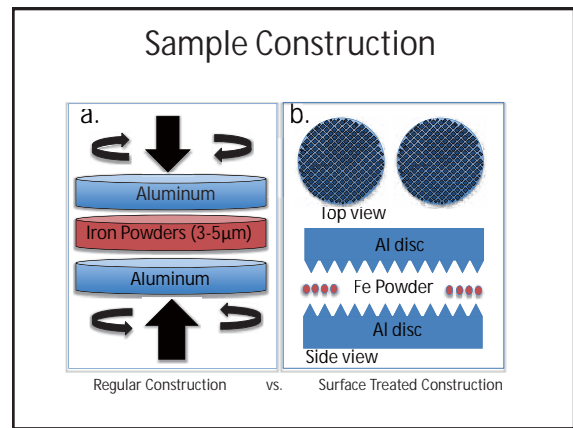
# Jonathan Timothy Quan



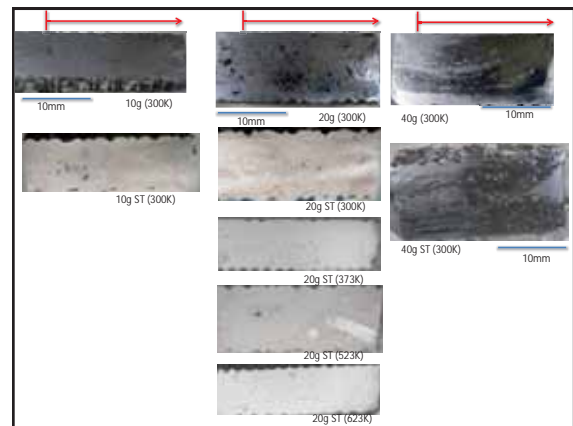
### CTP Conditions and Experimental Variables

Conditions	Value	Fe Powder (10g) → 1.0mm	Fe Powder (20g) → 2.0mm	Fe Powder (40g) → 4.0mm
Diameter (mm)	40.00			
Area (mm <sup>2</sup> )	12.66			
Force (KN)	125.60			
Pressure (MPa)	100.00			
Rotations	30			
Speed (RPM)	5			
Al disc thickness (mm)	5			
		T <sub>i</sub> =300K	T <sub>i</sub> =300K	T <sub>i</sub> =300K
		T <sub>i</sub> =300K (ST)	T <sub>i</sub> =300K (ST)	T <sub>i</sub> =300K (ST)
			T <sub>i</sub> =373K (ST)	
			T <sub>i</sub> =523K (ST)	
			T <sub>i</sub> =623K (ST)	

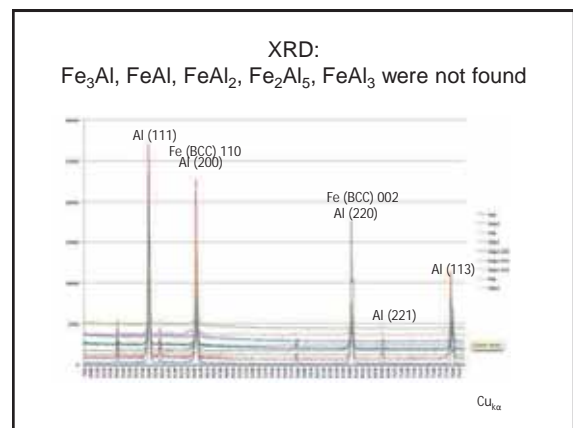
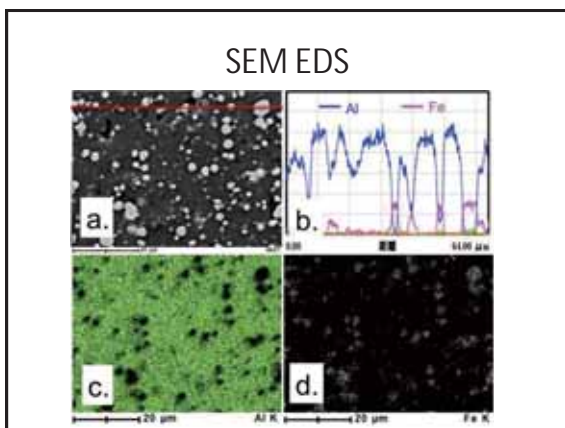
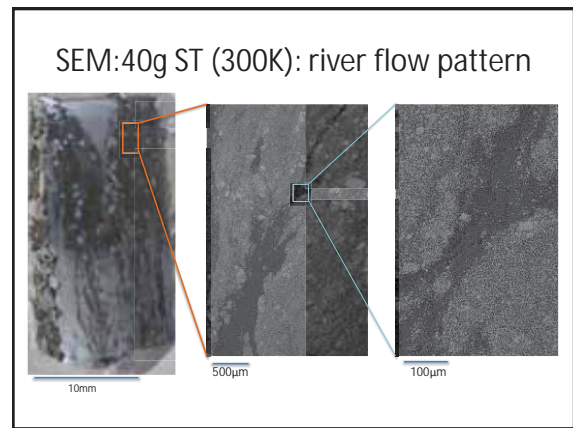
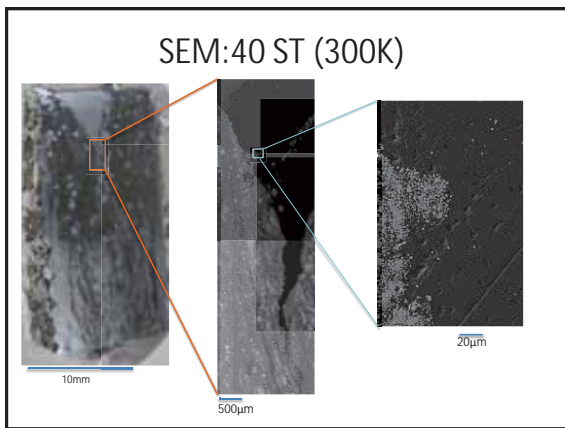
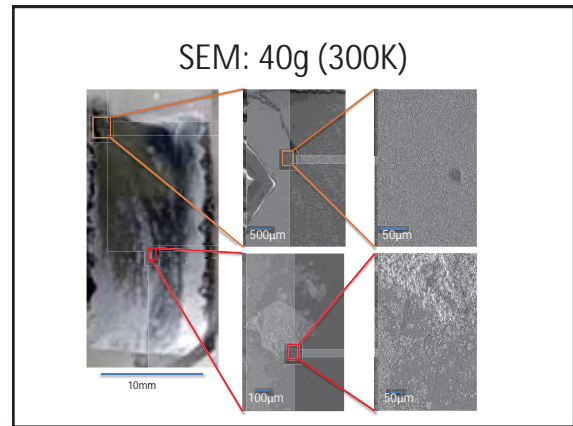
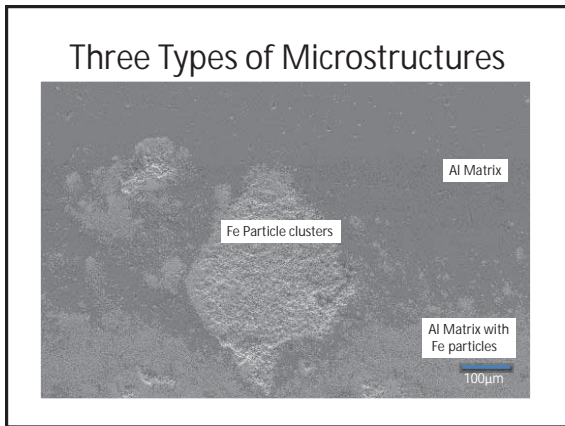
- ST: Surface treatment where the Al disc's surface was previous pressed with additional groves for better mixing under CTP
- Fe powder: 3-5µm



## Results



# Jonathan Timothy Quan

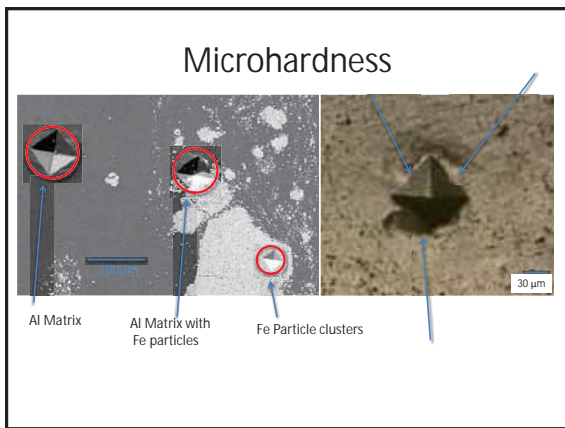
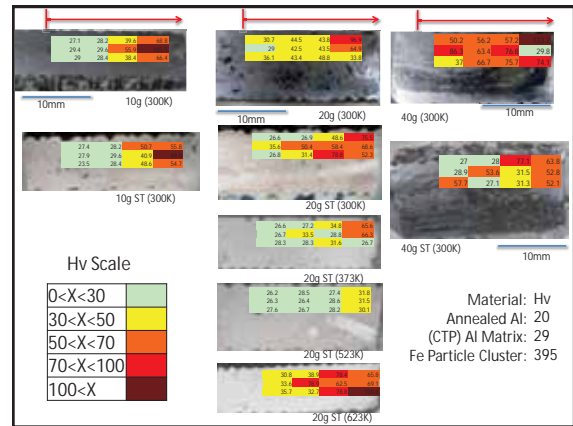


# Jonathan Timothy Quan

## Mechanical properties

Alloy	Temper	Proof Stress 0.2% (MPa)	Tensile Strength (MPa)	Shear Strength (MPa)	Elongation AS (%)	Hardness Vickers (HV)
AA1050K	H13	85	100	60	13	35
	H14	105	115	70	13	38
	H16	120	130	80	7	-
	H18	140	150	90	6	44
	O	85	90	50	43	28

Aalco, Aluminium Alloys - Aluminium 1050 Properties, Fabrication and Applications, Supplier



- ## Future work
1. XRD Mystery peaks
  2. Further mechanical tests
    - Tension
    - Compression
    - Creep
    - Fatigue
    - Fracture
  3. Modeling flow of iron particles

- ## Conclusion from Preliminary Results
- CTP is a good method for Developing Metal Matrix Composite at Low temperature using Fe powder in Al solid .
    - Observe Predictable Flow
    - Al Surface roughness conditions helps better mix the Fe powder in Al solid
    - Lack of intermetallic development
    - Iron Powder helps improve Al matrix mechanical properties

- ## Acknowledgements
- Kanetake and Kobashi Lab
    - Assistant Prof. Kume
    - Kei Uchida
    - Shohei Miyake
    - Wataru Kimura
  - JUACEP
  - Nagoya University
  - UCLA Hybrid Materials Lab

## Evaluation of Slip in Liquid Lubricant Confined in Molecularly Narrow Gap By Fiber Wobbling Method

Ninh Le

### Boundary Conditions

**Non-slip boundary condition**

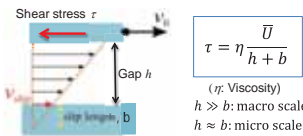
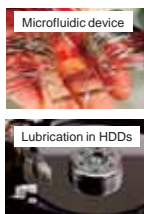
- 18<sup>th</sup> centuries: Bernoulli, Navier, Stoke
- 20<sup>th</sup> centuries: no-slip is accepted
- End of 20<sup>th</sup> centuries: revisit slip BCs

**Slip boundary condition**

Proposed by Navier and he introduced the idea of slip length  $b$

$$v_{slip} = b \frac{\partial v_0}{\partial z}$$

### Why studying slip BCs?

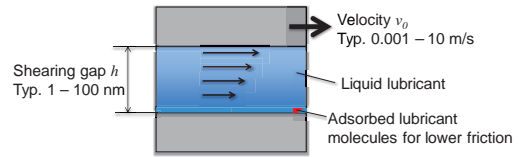


- Slip boundary condition must be considered in dealing with fluids in micro mechanical devices.
- Quantitative evaluation of slip length is essential for the estimation of shear stress.

- Factor affecting slip:
- Shear rate
  - Wettability (Adsorbed molecules)
  - Surface roughness

### Research Objective

Quantitative measurement of slip length under the conditions assumed in the lubrication systems in micro mechanical devices such as HDDs and MEMS



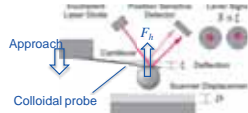
Lubrication conditions

- High shear rate:  $v_0/h = 10^4 - 10^{10} \text{ s}^{-1}$  ➔ High possibility of Slip
- Adsorbed molecules

### Previous methods to determine slip lengths

- Methods
- Atomic force microscope (AFM)
  - Surface force apparatus (SFA)

Analytical formula to calculate slip lengths  
 (Vinogradova, 1995, 169, pp. 306-312)



Measurement of drainage force  $F_h$   
 (Drainage force: Normal force required to expel the liquid out of the gap)

$$F_h = \frac{6\pi\eta r^2 v}{h} \cdot \frac{h}{3b} \left[ \left(1 + \frac{h}{6b}\right) \ln \left(1 + \frac{6b}{h}\right) - 1 \right]$$

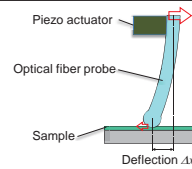
$b$ : Slip length

Disadvantage of previous measurements

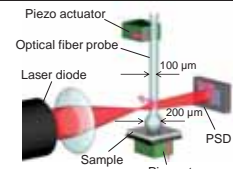
- Low shear rates  $\sim 1-10 \text{ s}^{-1}$
- Only mica substrate can be used in SFA

### Highly sensitive shear force measurement: Fiber wobbling method (FWM)

Principle of shear force detection



Deflection measurement of the probe



- Shearing gap: 1  $\mu\text{m}$  to a few nm
- Shearing velocity:  $10^6 - 10^3 \text{ m/s}$

High shear rate up to  $10^6 \text{ s}^{-1}$



## *Le Nguyen Khuong Ninh*

### Summary

- By using the FWM, I succeeded in the quantitative measurement of the slip length.
- The effect of slip became obvious at gap less than around 100 nm and caused the deviation of apparent viscosity.
- Slip length was constant at around 40 nm in the gap range of 100 nm down to 10 nm.

End

<3>

## Reports on JUACEP Program

\*The reports have been written as the JASSO (Japan Student Services Organization) scholarship report and approved to publish on here.

### **3-a. Reports on JUACEP Program**

**1: Learning outcomes**

**2: Experiences in Japan**

**3: Program contents**

**4: Influence of the career stage**

**5: Other contents**

#### ***Ambarish Krishnanand Desai***

1: Linear optimal control for stabilization of rotary single and double inverted pendulum. Hardware implementation of the closed loop feedback law for single and double rotary inverted pendulum.

Nonlinear optimal control for swing up and stabilization of rotary single inverted pendulum. Simulations in SimMechanics and Matlab.

2: Observed public life in Japan and appreciate the friendliness of people here. Visited lots of places nearby and the beautiful tourist spots. The best thing I liked here is the absence of crime. There was absolutely no fear in going to any place even without the knowledge of local language.

3: The program looks well balanced.

4: This program has given me an opportunity with actual hardware implementation of control laws. In addition it has allowed me to study and expose myself to the Nonlinear control domain, wherein I had no previous knowledge or experience. This will definitely benefit my profile whether I am going for a professional job or a PhD.

#### ***Zhenyu Gan***

1: As an exchanging student of Nagoya University, in this three months I learn a lot. In the laboratory of Prof. YAMADA I have learned the basic concepts such like PMEID, HMEID and its applications in all kinds of situations. I have designed the MEID horizontal cart model and made experiments to verify my assumptions and tried to analyse and find optimal parameters. Actually the topics here are quite similar with my research in University of Michigan. The method and framework I used previously could directly be applied to the research here. Besides the different method we used, we got similar results. So we have the opportunity to compare the pros and cons of our own ways of solution then make an improvement.

2: Not only in the laboratory of Prof. YAMADA I have learned the basic concepts such like PMEID, HMEID , but also learn the ordinary life in Japan. Every Friday afternoon in Prof. YAMADA 's Lab we have a seminar, a lot of presentations on various topics will be delivered. Each student in our laboratory shows their recent research, sometime we have a debate but I believe this kind of discussions helps us have a better understanding of our own research. Besides of the research in the Laboratory I travel around Japan to see the daily life of Japanese people and the beautiful scenery here. Even though sometimes we have a hard time to communicate with each other, I can feel their kindness and friendly.

3: There are lots of activities in this program. We have been visited the company of Toyota and the museum of JR train. We also have been to Gifu to see the cormorant fishing. Besides this kind of visiting we also involved in some real hand experiment such like the assembling internal combust engine. Also, there are all kinds of lectures we could attend. Just yesterday I attend a public lecture talked about the electrical vehicles which impressed me a lot.

4: In this period, I have to research on something I'm not familiar with at the very beginning. Everything seems quite strange to me, even simple equipment such like the encoder and accelerometer because of the language and differed software they use, which makes me very difficult for me to get used to. But a lot of my laboratory members are very friendly, they give me a lot of help and after a while I could apply my previous experience very fast. So I have more confidence in myself to a strange place. I think all these experiences could help me in the future works.

5: To be host, I really like this place, just like I told my lapidary members, if I have opportunity I will come back again with my family to travel around here and visit all my Japanese friends.

***Hao Wang***

1: I have already completed my research topic which is related to realizing self-sensing magnetic levitation using hall signal. In my research, estimated position of the levitated block is constructed by a nonlinear relationship between hall signal and current signal. By doing this, we can reduce the expense and spare more space in the physical device compared to the conventional magnetic levitation using position sensor. Furthermore, this methodology can be extended from 1DOF to

higher degree of freedom situation.

2: During this three months, I have experienced the Japanese culture from many aspects. Japanese people are friendly and nice to me. Japanese cuisine is delicious. I have learned Japanese culture and history both from my lab members and my travel to Tokyo, Kyoto, Osaka, Nara and Hiroshima.

3: Basically, I need to do the research independently which is assigned by my advisor. Every week, I have a chance to discuss my research with my advisor and get some useful idea from him. Self-motivation is very important, we need to learn by ourselves and try to collaborate with lab members by overcoming the obstacle on communication. JUACEP also provides other optional courses, lectures for enriching our lives here.

4: Since I have planned to apply for doctoral degree after I graduated from University of Michigan, this program provides me a great chance to do a project by myself. And it's also great to live in another country for 3 months. I will benefit from this experience for life long!

***Michael Bigang Ding***

1: For the JUACEP program, I stayed at Prof. Ju's lab and did research on non-contact atomic force microscopy. I learned about classical AFM and also microwave-based AFM techniques.

2: I really enjoyed my stay in Japan. Japanese culture and language is very fascinating. Also, the restaurants, tourist attractions, and shopping centers in Japan gave me a really good overall experience of life in Nagoya.

3: (1) Laboratory experience.

(2) Working with Japanese students and professors.

(3) Learning Japanese culture and language.

(4) Living independently in a foreign country.

4: In the future, I will be more willing to study and work in a foreign country. My experience in Prof. Ju's laboratory taught me many new ideas and techniques in research.

5: Overall, it was a great experience and I will recommend the JUACEP program to other graduate students in the United States.

***Nishant Mayur Narechania***

1: I worked under the guidance of Professor Kitamura in the Department of Aerospace Engineering. My research was based on numerical modeling of space physics phenomena. This is something I had never tried before though always had a strange fascination towards it. I believe I have successfully completed my research and gained valuable expertise through it. I have decided to pursue this field further and now also intend to do a PhD in it.

2: During my stay in Japan, I had the opportunity to visit many places here. I visited Tokyo, Kyoto, Hiroshima, Nara to name a few. I saw many temples and shrines which comprise the rich history of Japan. I climbed Mount Fuji which is Japan's highest mountain and also a volcano. The greatest experience for me was to live like a Buddhist monk for one day at a temple in Mount Koya. I had shojin-ryori for meals and also joined the monks in the early morning prayers. Also, the hot springs (onsen) in Gero was a first of its kind experience which I may not get anywhere else. I would also like to point out the helpfulness and courteous nature of the Japanese people which I have never seen in any other country I have visited so far.

3: The program was essentially centered on research with a faculty. It also contained add-ons like the lecture sessions. The part which I liked the most was the disassembly and reassembly of a micro-model of the internal combustion engine. Although this is not my area of research, it was a huge learning experience. I had always known the theory about I.C. engines from the courses during my Bachelors but had never encountered them hands-on. This was the first hands-on session of its kind for me which gave a thorough idea of its working. The program also arranged an industry visit to the Toyota assembly line which gave me great insight into the manufacturing of a car. The traditional cormorant-fishing was something I had no knowledge of prior to Japan.

4: Conducting research in a foreign country is always a valuable asset to the CV. It indicates experience in working in a new unfamiliar environment and adapting to the university culture of another country. This goes a long way in increasing your job

prospects and chances for further higher studies. The international experience also helped me as a great confidence-builder. Also, as a result of interacting with people from all over the world gathered here for their research/degree made me better equipped socially for interacting with the international crowd. I am pretty sure this will help me in future when working a multinational organization.

***Sriram Ganesan***

1: I was introduced to the theory of dislocations and performed Monte Carlo simulations of poly-crystal plasticity using this approach. The JUACEP program helped me augment my research at University of Michigan by exposing me to the research in this field here. The Japanese language classes helped me to get a grasp of this beautiful language. The lectures in Production Engineering and the Toyota Motor Factory trip helped us to get an insight into the advanced manufacturing practices in Japan.

2: The first thing that strikes about Japan is the politeness and humility of every person that one meets. The arrangements at International Residence at Nagoya University made us feel at home. Through this internship, I was also fortunate to visit places such as Tokyo, Kyoto, Nara and Mt. Fuji and I thoroughly enjoyed the culture and hospitality everywhere. There were many instances where people came a long way to help us out. I would definitely recommend Japan to my friends and colleagues.

3: The program contents were ideal and helped me to delve deep into research topic while at the same time helping me in appreciating the language and culture. The Toyota Motor Factory Trip along with visit to Nagara River to watch Gifu fishing, organized by the JUACEP team was one of the most enjoyable experiences. The Japanese language classes helped me to get a grasp of the language. In my opinion, a few more Japanese classes would help in conversing better.

4: I am entering the 2nd year in my PhD program and this internship gave me an important exposure to the research in my field in Japan. The lectures in Production Engineering helped me to comprehend the applications of research in industry. I hope this experience will help me to excel better in my research endeavors at the University of Michigan.

5: The entire experience in Japan was very exciting and satisfying. I would like to express my sincere gratitude to the JUACEP Program team, JASSO and my research advisors at University of Michigan and Nagoya University for providing me with this wonderful opportunity.

***Weiyu Cao***

1: My research topic during the JUACEP Program is Loop Heat Pipe (LHP). I have built a mathematical model of LHP, which could predict the characteristics of a LHP working under steady state. With the assistance of the mathematical model, I have designed and built up an experimental-use LHP. Data like the operating temperature and condenser temperature distribution were collected by thermal couple measurements. Then the mathematical model was revised according to the experimental data.

2: The experience in Japan was great. During the first month, I took several Japanese language courses, which helped me a lot during my life in Japan. During the weeks, I stayed in the Lab to do my research work. At the weekends, I went out for sightseeing. I have visited a lot of famous places in Japan, Such as Nagoya Cho, Osaka, Gifu and Hokkaido. I have also experienced all kinds of gourmet in Japan.

3: 1, Build a mathematical model for LHP

2, Parametric study by the mathematical model

3, Design and build up an experimental-use LHP

4, Test the LHP, collect data for operating characteristic and revise the model

4: The experience in JUACEP Program has given me access to the Japanese working culture, which might help me a lot if I would work in a Japanese company in the future. What's more, the research project also trained my ability to design and build up an experiment.

***Yan Zhang***

1: During the three-month research and study in Suzuki Lab of the Mechanical Department, I have been working on the application of a collision avoidance control system on a small electrical vehicle. From reading papers, I have learned the theory behind this control system. I have used the knowledge in my vehicle dynamics and control systems classes, and applied them to the real world situation. I have

developed a control program in C# to assist the steering of a small electric vehicle for obstacle avoidance. I have also built a simulation program in MATLAB. Then I have tested this program on the real vehicle and tuned parameters for more desirable results. Besides the research in the lab, I have also attended Japanese classes, from which I learned the basics of Japanese language for daily uses.

2: The experience in Japan was very unique to me. Although I was born and raised in China which is very close to Japan, the Japanese culture still attracted me deeply because of its combination of eastern and western cultures. During the stay in Japan, I was also impressed by the fact that how Japanese people conserve energy and protect the environment, comparing to USA and China, two countries which I am very familiar with. For example, in the dorm I have stayed, most of the light bulbs are LED and have automatic switch function to save energy. I have also traveled to a few places on weekends and holidays, for example Kyoto, Hokkaido, etc, where I met different people in Japan and saw both the beautiful natural scenery and traditional culture of Japan.

3: The program contains lab research work, Japanese language classes, automotive related lectures, Toyota factory field trip and train park visit. My lab research work involves building a control program for the steering assist system of an electrical vehicle. Software simulations and experiments are also involved in the program.

4: The research experience in the steering control system has made me realized the importance of control system in automobile nowadays, and given me the interests in control systems in automobiles. I have also learned about the PLC (Programmable Logic Controller) device and how to code the control program in C#, which would be very helpful for starting a career in vehicle control systems. The whole experience with Japanese automotive industries, including the lectures and plant visiting, has given me new knowledge about how car companies work and how vehicles are designed in a company.

### ***Yihao Zheng***

1: Firstly, a type of bone mimicking material was fabricated by soaking epoxy into 3D printed plaster, and its mechanical properties including friction coefficient with steel and Rockwell hardness were tested and compared with those of bovine femur specimen. The experiments results approved the similarity of friction coefficients of

created material and the bovine bone, though the hardness of the bone mimicking material turned out to be lower. Secondly, 3 types of common 3D printable polymer, ULTEM, PC, PC-ISO, were investigated with respect their friction induced wear resistant properties. Friction coefficients with steel and wear rates were compared. For individual polymer, the effect on friction coefficient of printed orientations was also studied. Additionally, via 10 Japanese courses, some basic daily used Japanese was mastered.

2: Regarding to study and research, two topics, bone simulation, and friction induced wear resistant property of 3D printed polymer were studied; 10 courses of Japanese language and a special lecture on engine assembly were attended. In daily life, I met a number of new friends including Japanese students in Nagoya University who helped me and made me reaped a lot in Japanese culture, as well as other US students in the same program. I traveled some major cities around Japan including Tokyo, Osaka, and Kyoto which helped me to gain a deeper understanding in Japanese society and culture.

3: JUACEP is a research-based educational program designed for graduate students who desire to study abroad. Scholarships are offered to both Nagoya and American university students. The program presents the perfect opportunity for students to gain engineering research experience as well as cultural experience in the USA or Japan. The program I am in is the three month JUACEP program from University of Michigan to Nagoya University. The major task for me is the research work in Umehara Lab in the Nagoya University relating to friction induced wear property of several types of material. As parts of the program, a field trip to Toyota, a special lecture on engine assembly and 10 courses of Japanese language were offered by the Nagoya University. A research report and a presentation will be given at the end of the program.

4: The program will greatly facilitate my future career. Firstly, the projects I researched were closely related to my future career path, advanced manufacturing of medical devices. Secondly, this program considerably extended my human networks. New friends in Nagoya and UCLA are great treasure for me. Thirdly, I gained a deep understanding in Japanese culture which helps me to act appropriately when I cooperate with Japanese people in the future. Last but not least, 10 courses of Japanese language enable me to make daily communication

with Japanese friends.

5: I wanted to express my heartfelt gratitude to the JUACEP program, and everyone who works for this great program, especially my advisor in Nagoya University, Prof. Umehara, and the staffs in Nagoya University JUACEP office, as well as my lab fellows who helped me a lot. I enjoyed my research and life in Japan very much and would look forward to the next chance to visit Japan.

***Yi-Kai Wang***

1: In the beginning, I chose to follow Prof. HAYAKAWA to do research about visual feedback control for table tennis robot because I would like to learn the technique of image processing. However, when I knew I have to do a lot of programming work and data analysis, I thought it was a really hard task for me. After a few discussions with professor and TA, I gradually understand the control process and principle of the whole system. Even though the program and data are complicated and all program notes and manual are in Japanese, I could follow the instruction and paper to rewrite the program finally. The most thing I learn in this lab in Nagoya University is that I could utilize my basic dynamics and signal processing knowledge on actual application, the robot manipulation. Although it's hard to reach original goal, the experiment experience is very beneficial and memorable for me.

2: The life in Japan is very different from the US. First, people are friendly at here; I nearly don't feel any racial discrimination, or maybe it's just because they are unable to distinguish me from other Japanese due to similar skin color. Although Nagoya University is in suburban area, taking subway to city center only costs me less than half hour. It's obvious that Japan is a well-ordered society. The most impressive thing is that Japan is relatively crowded compared with Western countries, but it gives me a quiet feeling. For example, I barely hear horn sound and loud gossip when I am walking on the pavement. However, this society is lacking in vitality. Just like when professors teach in the class, they only follow the power point or lecture note. The boring class makes a lot of students sleepy in the class.

3: I join the JUACEP in Nagoya University. Because the leader of this program is a professor in mechanical engineering department, there are plenty of mechanical lectures we can take. Many of them are interesting just like automobile market class told us how Toyota manages the balance between supply and demand. Actually, in Japan it's inconvenient for international students, especially for those who are not

good at Japanese. However, in our program, each student has a TA who can answer us any question about the research and daily life. For me, it's a very good opportunity to use sophisticated facility in Nagoya University. My research is to use an arm robot and two cameras to serve a ping pong.

4: I took a lot of dynamic-related classes before but I don't have any chance to use real arm robot to realize those theories. It's very possible I will enter into a robot company as a start of my career. Thus, the research provides me a very precious opportunity to know more about the robot manipulation. With the research experience in Nagoya University, it would be beneficial for my industry career.

5: I really appreciate Japan government could provide the scholarship to support us doing research at here. Even though our contribution is not important for the research development, the international interaction is good for both side students. Hope in the future, JUACEP could hold continuously that more students can have more communication.

***Yu-Shiuan Chu***

1: In the period of this three-month summer intern, I mainly did research in Prof. Kawaguchi's lab doing project of HASC (Human Activity Sensing Consortium). It's a database grabbed by mobile phone sensors on people's daily simple activities (like walk, running, going through stairs, etc.) and use Machine Learning techniques to classify those activities. The project is very useful to me through refining my knowledge of signal data processing and forcing me to use java code, which I was originally unfamiliar with. Discussing with group member is also an interesting experience. Through using Google translate or asking my teach assistant as a mediate role in discussions, I realize there are always good ways to overcome language barriers.

2: Life in Japan is fantastic, which can be observed in some small things. Since the first day I got into the campus apartment, I could've felt Japanese's opposite thinking way comparing with Americans, tiny but delicate. Room area is only half of my living room in Michigan, but contains everything inside. In addition, Public facilities in Japan are clean and function well. Bidet toilets are in widespread use in my apartment, lab building, subway station and any public restroom. Besides, Japanese people are very polite, even is the police. Once I was going home late and

was stopped by a police officer, he questioned me in a manner way that I didn't feel any uncomfortable. Through trip in Nagoya, Tokyo, Kyoto, Osaka, I can feel Japanese spirit to harmonically combine history and technology. Those small parts make Japan a lovely and charming nation.

3: The programs are helpful and inspiring. After finishing 10 basic Japanese classes, I can handle communications in daily activities like asking for route, ordering meals, etc. In the process of engine lecture, I practically disassembling/assembling/running a Diesel engine and realize that hand making is much better than brand thinking. Excursion to Toyota company plant and other scenic spots broaden my eyes to a company's seek for saving energy issue. Special lecture of "Electric Vehicle for the Future" lectured by Dr. Hiroshi Shimizu amazed me at its prospects and unlimited imagination. Each program is awesome and educative.

4: The experience of Japan summer program is definitely a great journey in my life. What signal processing skills and Java language I've learned in lab research is useful in my following studying in Michigan and the career. The culture shock in daily life and traveling in Japan broaden my eyes in the diverse globe world. It's a priceless treasure to me.

***Christopher Charles Roberts***

1: The solid-state laboratories at Nagoya University are famous for their work with III-nitride LED growth. I received training and was able to gain experience on numerous pieces of equipment that will benefit my future studies. My hosting professor allowed me to pursue a very ambitious research project, and with the help of his students I am now familiar with many of the processes necessary to fabricate high quality III-N LEDs.

2: I was able to explore much of Nagoya, Kyoto, and Osaka. Japan's specialty foods and drinks are delicious. The history and beauty of Japan is astounding. I especially appreciate the incorporation of nature into everyday life. The people of Japan are very respectful of each other and the environment. I greatly enjoyed my experiences while studying in Japan.

3: I highly enjoyed the events related to Japanese culture. The lectures and engineering programs gave me valuable insight into fields of engineering I was not

familiar with. The guest speakers offered valuable insight into the future of many important fields, such as the manufacturing of the electric vehicle. Touring the Toyota manufacturing plant increased my appreciation to the fine detail and great efficiency that can be achieved through proper consideration. The Japanese language course was sufficient to allow for full study of the language in a short amount of time. Overall, the program content was highly enjoyable.

4: The research I was able to perform has given me the invaluable, hands-on experience that will greatly benefit my future work. Having experienced another culture for a sufficient period of time has also improved my appreciation for subtle cultural differences, which I hope will benefit my career with regards to future international interactions.

#### ***Chung-Wen Chuang***

1: My learning experience mainly includes two parts while studying in Nagoya University, and they are research- and Japanese-learning parts. For the research-learning part, under the instruction of the professor, the teaching assistant and lab mates, I performed mechanical and physical behavior of reinforced concrete (RC) structures, such as visual crack propagation, loading-displacement relation, prediction of the shear failure and/or flexural failure, etc., using a discrete-type numerical analysis modeling, namely Riding-Body-Spring Model (RBSM). For the Japanese-learning part, through several Japanese language classes associated with some field trips, e.g., Toyota Motor Factory visit and Ukai watching trip in Nagara River, I learned much knowledge about the Japanese language, culture and features, etc.

2: Through the instruction of the research theory, the introduction of the Japanese culture, and the share of the life experience from faculty, lab mates and friends, I gained invaluable professional knowledge, interacting skills and cultural experience at Nagoya University and in Japan. On the other hand, I also shared ideas and thoughts of my study and life in the US with them by means of several presentations and meetings at Nagoya University. In addition, I am very impressed by the Japanese working culture and spirit. They enjoy what they do and devoted their respectable energy and power to the work, even unstoppable during weekends.

3: The JUACEP summer program in 2013 primarily includes the following contents:

1) Research at individual laboratory; 2) Field trips and factory visits; 3) Additional lectures, e.g., lectures by the NUSIP program and Introduction to Production Engineering; 4) Handicraft exercise; 5) Japanese language classes; 6) Special events, such as the orientation for UCLA students, auditing the presentations by University of Michigan students, etc.

4: Not only intercommunicating diverse thoughts and backgrounds with faculty and peers but also experiencing Japanese cultural features and appearances is an exciting aspect of this JUACEP program provided to me. I am sure the JUACEP program offered by Nagoya University will allow me to thrive and further fulfill my life. To be specific, what I have learned from this program, even throughout the Japan, is to accept innovative and creative ideas and thoughts from distinct fields, to appreciate superior technologies in life, to respect experience and wisdom from elders, and to learn energetic and enthusiastic attitude in working. With all the experiences I have gained in Japan, I am more confident to face any uncertainty in the future.

5: Fortunately, during my stay at the Nagoya University, I have experienced some rare occasions happened in the Nagoya University and/or my laboratory, e.g., the annual convention by Japan Concrete Institute (JCI) and the job workshop by Civil Engineering and Architecture Department of Aichi-ken government. It is my honor to meet and intercommunicate with those people of great ability and profession.

***Jonathan Timothy Quan***

1: This was a great program for a number of learning experiences. First, I got to learn about the Japanese Culture: Lifestyle, habits, norms, food, language, everyday conversation, and cultural values. Second, I really enjoyed learning Japanese. Having a 5 week class was a lot of fun and very beneficial. Third, I really enjoyed my research and the opportunity to interact with my Japanese colleagues. It's good to know that there are others who understand the same field as me.

2: Three experiences stand out to me. First, I really enjoyed how professional everyone was, especially the JUACEP program. Second, I really enjoyed the opportunity to work in a Japanese lab. Third, the public transportation in Nagoya and the rest of Japan is very fun and convenient.

3: I really enjoyed all of the opportunities that the Juacep program provided. I really enjoyed the field trip out to the Toyota plant. It was very inspirational for my work here in Nagoya. The engine building opportunity was also very fun and reward. Finally, I am still very amazed by the wonderful staff Juacep has employed. They are all very professional and nice.

4: I really enjoy the research I am doing and it was very fun working in a Japanese lab this summer. I believe it has opened my eyes and I am now very open in doing collaborations with Japan, especially Nagoya University, in the future. I also believe that the work here in Japan has also strengthened my skills as a materials scientist.

5: I really like our dormitory. It is close and convenient. The only complaint I have is that the gender rule from allowing visitors. However, I do understand that there is potential legal issue so it is something out of the Juacep control. Maybe it is also a cultural difference that I am not aware of.

***Justin Wang***

1: I've learned how to make carbon fiber plates using the VARTM method from my TA. The equipment in Nagoya University is newer and more numerous than what we have available at UCLA.

2: Exploring Japan was fun. I've been for Kyoto, Osaka, and Tokyo in addition to around Nagoya. While only a few days were spent outside of Nagoya, my friends and I saw a few festivals and many famous locations. We ate good food as well.

3: The engine assembly workshop was a great experience and I learned a lot. The Japanese language course was too short and unfortunately I couldn't learn as much as I wanted. It's better if students study Japanese before coming to Japan.

4: I am still set on obtaining work in the aerospace field after graduate school, as opposed to continuing study and research to obtain a PhD.

***Le Nguyen Khoung Ninh***

1: I have obtained consistent results with the previous study. I am analysing the data of the new study and will bring out the conclusion before the end of the study.

2: I really enjoy staying in Japan. Aside from studying, I have learned a lot about Japanese culture and visited some places here. I wish I can come back to Japan and stay for a longer time.

3: I have learned about the experimental methods in investigating the near-field liquid flow. I have used one of the methods developed by Prof. Kenji Fukuzawa's group to study the viscoelastic properties of liquid lubricant confined in nanoscale gaps.

4: Learning a new experimental technique and the background study of the research has broadened my knowledge and my skills in conducting researches. Everything I have learned during this program will certainly be helpful in obtaining a job in the near future.

***Owen Suyuan Liang***

1: During my research in Japan, I gained more SEM experience. One big benefit of Japanese universities is the amount of high quality equipment, such as SEM, and I took advantage of that. I also made STM tips to measure the resistivity of CNTs. While this will not affect my current research in the States, I believe knowledge of such a process may lead me to get trained to use a STM. Throughout my daily life in Japan, I got to improve my Japanese. I took Japanese classes before and to actually use it in a real-life setting was very rewarding.

2: Before coming to Japan, I was fascinated by the food and thus I geared my trips to taste the various local cuisines. The first few weekends, my group stayed in Nagoya and had local specialties such as hitsumabushi, misokatsu, tenmatsu, etc. Soon after, we went to Kyoto and Osaka to experience the shinkansen. Luckily, we went at the time of the Gion Festival in Kyoto and got to experience the multiple food stalls. We were amazed at the amount of people and the fact that a whole street had to be closed down for such an event. We saw historic sites such as Kyomizudera, Ryoanji, and Kinkakuji. Later on, we even went to the Nagoya Sumo Tournament, Osaka aquarium, various castles in Nagoya, Ueno-Iga, and Oogaki, etc. We also saw many firework shows that dwarf the American equivalent.

3: The main part of JUACEP was the research, but it also included some other events. The big event held by the JUACEP office was a tour to the Toyota factory, the JR Train

Museum, and in the evening, Ukai Fishing. I was amazed at the accuracy of the various welding robotic arms at the Toyota factory that actually spot welded various different models of Toyota. The JR Train Museum was uniquely interesting for me because I got to test out the shinkansen simulator which allowed me to test drive the newest model of the shinkansen (N700). The Ukai Fishing was interesting to see as I never had seen fishing quite like it. Ukai fishing is a method of using cormorant birds to swallow fish and regurgitate them out. The next event held by the program was disassembling and re-assembling a small gasoline-powered engine. This engine had one horsepower and originally was made to power a propeller for a RC plane. It was an interesting experience for me because I never took apart an engine before.

4: The SEM experience I gained will help in my future career and my current research back in the States. By future career, I can image many companies that value microscopy experience. For my research, as mentioned earlier, my Professor was thinking about training someone in my group for STM and perhaps this experience will allow me to get trained on such a machine. In addition, research topic on carbon nanotubes is closely related to my current research topic on graphene in the US. The reason I choose Saito Lab group in Nagoya University was for that purpose. I wanted to expand my knowledge base to beyond just graphene and in general, novel carbon materials.

5: I found this program very useful. A couple of things that could be improved upon: I really enjoyed the program events and wished there were more. I also found the payment date very inconvenient for my group. We leave the 23rd of August but will get paid on the 19th so money was tight up that point.

***Yaodong Wang***

1: Solution growth of single crystal 4H-SiC. Using Top Seeded Solution Growth method, nearly thermal equilibrium, to grow 4H-type silicon carbide, which is a promising wide bandgap semiconductor for future power devices. It is known that SiC is suffered with myriad of dislocations, which degrades the device performance significantly. By using solution growth methods, dislocations on the surface of SiC can be significantly reduced. Specifically, I study by adding third element into the solvent expecting to observe dislocation conversion on the surface.

2: First and foremost, the JUACEP program provides the excellent opportunity for

UCLA students to conduct research at Nagoya with sufficient funding to cover their living expenses. Also, during the stay at Nagoya, there are a series of organized field trip to Toyota etc. In addition, labmates from each individual lab are always very helpful and friendly to our summer research students. Their considerable help reduces our language barrier significantly. From my personal perspectives, I have learned and had experiences of a variety of experimental instruments and techniques including Nomarski Microscope, Confocal Laser Microscope, EBSD, X-ray rocking curve measurement and TEM. In all, this program has achieved my great personal satisfaction.

3: By adding the third element into the Si-C-X solution, it is expected to observe dislocation conversion on the carbon face. Samples have been prepared by using Top Seeded Solution Growth method (TSSG) and epilayer was grown on the 4H-type SiC seed crystal substrate. The epilayer thickness was measured and growth rate was calculated. Cross-sectional TEM samples were prepared by Ion Milling method to observe dislocation conversion. And surface etching was conducted to observe dislocation density.

4: The experience at Nagoya University shall help my job exploration in Japanese companies in U.S. I have intention to pursue a high-tech related job. And Japan has a variety of high-tech companies across the world. I hope that the summer internship I have at Nagoya will have positive effect on my job research of Japanese companies.

5: People at Nagoya University are always helpful and friendly to me. I have received considerable help from university wide to research lab. I have sincere appreciation that Nagoya University funds my tuition and living expenses for my stay in Japan. Along the way, I received considerable help from my lab mates. Without their help I could not able to conduct my own experiments. In all, I am truly grateful for this summer internship program.

<4>

## Appendix

## 4-a. Pictures

-Orientation-



-Welcome Luncheon -



-Japanese Language Class-





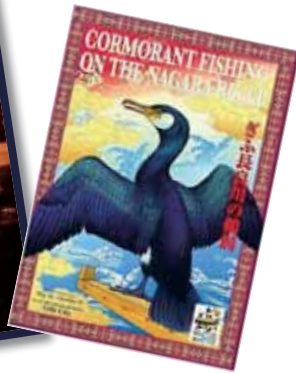
Toyota Plant Tour



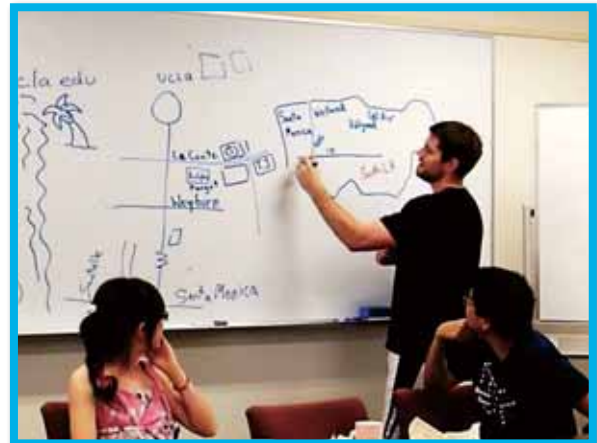
JR SCMaglev & Railway Park



*Gifu Castle & Nagara River*



-Round-table Discussion with Prof. Yang (UCLA)-

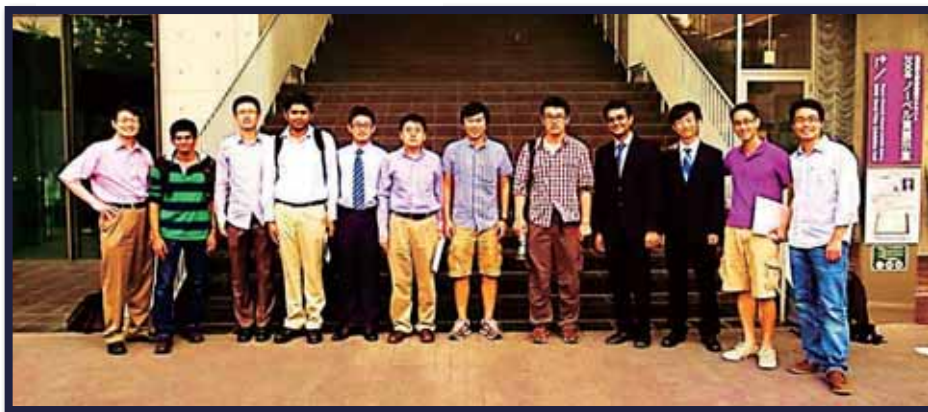


-Handcraft Exercise-

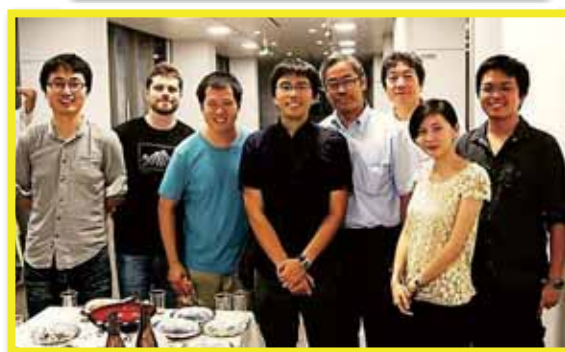




-Award Ceremony-



-Farewell-



## 4-b. Handout Materials

### JUACEP Summer Program 2013 Orientation

For University of Michigan students: Tuesday, May 14 2013

10:00 [ES Hall]

Welcome address

Prof. Yang Ju, JUACEP Leader

Introduction of faculty, staff and participating students

*Academic Information*

- A) Schedule
- B) Handcraft Exercise
- C) Japanese Language Class –text book
- D) NUSIP Lectures
- E) Introduction to Production Engineering
- F) Field Trip – Toyota, SCMAGLEV & Railway Park
- G) JASSO Scholarship Report
- H) Evaluation

*Life Information*

- A) Promise –sign and submit the paper
- B) Housing –room list
- C) Use of PCs on Campus –set up with each TA
- D) Student ID Card
- E) Medical and Health Care
  - Medical Services
  - Health Precautions
- F) Student Life
  - Refuse Disposal at Nagoya University
  - Public Transportation in Nagoya City
  - If involved in a Traffic Accident
  - Compliance with Japanese Law
  - Safety Guide
  - Culture Shock
  - Differences in Academic Culture
  - Cope with Stress
  - Harassment

11:30 Introduction of lab teachers

12:00 Welcome lunch @ Chez Jiroud

~Welcome from the dean of Graduate School of Engineering ~

13:30 [ES031]

Stipend, tuition fee, admission fee, health insurance fee and Japanese text book fee  
Introduction to lab TAs

## JUACEP Summer Program 2013 Orientation

For UCLA students: Tuesday, June 18 2013

10:30 [ES Hall]

Welcome address from JUACEP Faculty

Introduction of faculty, staff and participating students

*Academic Information*

A) Schedule

B) Handcraft Exercise

C) Japanese Language Class –text book

D) NUSIP Lectures

E) Introduction to Production Engineering

F) Field Trip – Toyota, SCMAGLEV & Railway Park

G) JASSO Scholarship Report

H) Evaluation

*Life Information*

A) Promise –sign and submit the paper

B) Housing –room list

C) Use of PCs on Campus –set up with each TA

D) Student ID Card

E) Medical and Health Care

- Medical Services

- Health Precautions

F) Student Life

- Refuse Disposal at Nagoya University

- Public Transportation in Nagoya City

- If involved in a Traffic Accident

- Compliance with Japanese Law

- Safety Guide

- Culture Shock

- Differences in Academic Culture

- Cope with Stress

- Harassment

11:30 Introduction of lab teachers and TAs

12:00 Welcome lunch @ Chez Jiroud

~ Welcome from the leader of JUACEP ~

-----  
13:30 June 19 for UCLA students [ES031]

-Stipend, tuition fee, admission fee, health insurance fee and Japanese textbook fee

## Housing

### ***International Residence Yamate***

(10 minutes' walk from Higashiyama Campus)

Address: 165 Takamine-cho, Showa-ku, Nagoya 466-0811, Japan

Phone: 052-835-5575 (office)

Facilities: This is a three-story building with 106 single rooms (approximately 15m<sup>2</sup>).

It houses a lounge, a recyclable trash area, two laundry rooms, mail boxes, and an administrative office.

Each room is furnished with a bed with bedding(\*), desk, chair, desk lamp, open closet, storage shelf, air conditioner, Internet connection, TV connection, wastepaper bin, sink, induction heating (IH) cooker (1), microwave oven, refrigerator-freezer, ventilation fan, unit bathroom/ toilet and curtains (2 sets), etc.

(\*)Bedding: Set for each room comprises quilt (1), blanket (1), bedpad (1), pillow (1), quilt cover (2), bedsheet (2), pillow slip (2).

Three Japanese graduate students live on each floor in International Residence Yamate as tutors.

## PC & ID

### **Use of PCs on Campus**

Wireless internet connection is available on campus including the Satellite PC Lab in the main library, and other areas on campus. If you want to connect our lap top PC to Nagoya University Wireless Network (NUWNET), please go to 'ECIS computer web page' (<http://eee.ecis.nagoya-u.ac.jp/computer/instr.html>) After receiving your ID and password, you must take the online Information Security Training and pass the test within a week. To pass the test, you must score at least 80% and retake the test until your score 80% or above.

### **Student ID Card**

A student ID card has many functions. It will let you into the university libraries, and with the card you may borrow books from the library. The card lets you get student discounts at museums, theatres and so on.

## Medical and Health Care

### **1. Medical Services**

If you suffer from continuous headaches, a loss of appetite, or you cannot sleep well, etc., you should seek the advice of a doctor before the condition gets worse. These symptoms may be a sign of fatigue or exhaustion. They may also be psychological or psychosomatic symptoms, which are treatable by specialist doctors. In addition to taking care of your own health, please pay attention to your friends' health and encourage them to see a doctor, if they are feeling unwell.

**(1) The Health Administration Office** Students can undergo physical examinations, receive health advice, first-aid and arrange psychiatric counseling at this facility. There is no charge for using any of these services.

Tel: 052-789-3970

[Office Hours for Health Services]

Treatment	Time	Mon	Tue	Wed	Thu	Fri
Physical Examinations & First-Aid	10:00 – 11:30	○	○	○	○	○
	13:30 – 16:30	○	○	○	○	○
Psychiatric Counseling	10:00 – 12:00	○	○	○	○	○
	13:30 – 16:30	○	○	-	○	○

\*Note: Appointments are necessary for psychiatric counseling services. Please call the office 052-788-6276 for appointments.

The Health Administrative Office is open between 9:00 - 12:00, 13:00 - 17:00 for first aid.

## **(2) Calling an Ambulance**

Telephone 119 or press the RED button on a public phone for connection, free of charge. Although it is possible to speak English, it would probably be helpful for you to say the following: **Kyukyusha** (ambulance) **o onegai shimasu. Basho wa** (your location) **desu.** (I am calling for an ambulance. I am at...location.) This number is also used for requesting fire engines (**shobosha**). In Japan, ambulances are available 24 hours a day, free of charge.

## **2. Health Precautions**

### **(1) Food Poisoning**

Great care should be taken with regard to eating habits during the extreme summer weather in Japan. To avoid food spoilage, check the expiration date before buying food, apply heat to raw foods and be careful not to keep food in the refrigerator for an excessive amount of time. To guard against food poisoning, always wash culinary items with hot water. In the past, there was a frightening outbreak of O-157, a bacterial food poisoning disease. There was also an incident where students enrolled at Nagoya University were poisoned by eating wild mushrooms.

### **(2) Necessary measures to prevent the spread of infectious diseases**

If you are traveling from Japan to another country, please seek travel advice regularly until the time of departure. Please follow the basic rules of hygiene to avoid being infected.

The Ministry of Foreign Affairs of Japan: <http://www.anzen.mofa.go.jp/>

World Health organization: <http://www.who.int/en/>

## Student Life

### **1. Refuse Disposal at Nagoya University**

A sorting system for refuse disposal is used at Nagoya University. There are trash cans for “combustible refuse”, “incombustible refuse”, and recycle bins for “empty bottles”, “empty cans”, and “PET bottles” all over campus. In addition, there are boxes and a reverse vending machine near the Co-op. The sorted refuse will be recycled. Newspapers or magazines are collected by recycle companies. Used paper products such as used copy paper are collected and recycled. Students are kindly requested to be mindful when they throw away their rubbish and to use the correct bins to help waste reduction and the reuse of recyclable materials.

### **2. Public Transportation**

#### 1. Subway and City Bus Tickets:

- ① Manaca: Manaca is a pre-paid pass that can be used for both subway trains and buses operated by Nagoya City. Various types of Manaca can be purchased. It can be used for Meitetsu buses and trains, Aonami lines, Yutorito lines and Toyohashi railroad. It is a rechargeable card.
- ② One-day ticket: One-day tickets allow for unlimited rides for one day. One-day tickets for all bus, subway, and bus & subway routes are available. Ticket, Donichi-Eco-Kippu, that can be used on Saturdays, Sundays, holidays and the 8th of every month can be also purchased.

These tickets include a discounted admission fee for some tourist facilities in Nagoya city such as Nagoya Castle or the Tokugawa Museum.

They can be purchased at any subway station. For further information, refer to the following website:

<http://www.kotsu.city.nagoya.jp/> (Japanese)

#### 2. Useful Links:

The following websites provide information on available transport services, time-tables, etc..

HYPERDIA: <http://www.hyperdia.com/en/>

### **3. If involved in a traffic accident.**

If you are involved in a traffic accident, remain calm and do the following:

1. If anyone is injured, dial 119 for an ambulance.
2. Move any dangerous including vehicles, off the road to prevent other accidents.
3. Report the accident immediately, even if it is small, to a nearby police station and obtain a report of the accident.

4. Write down the license plate number of the car concerned as well as the name, address and age of the driver, after requesting to see his/her driver's license.
5. If there are witnesses, write down their names, addresses and telephone numbers.
6. Make detailed notes of the accident and take photographs, if possible.
7. See a doctor, even if you think that you are all right, because sometimes symptoms can take time to occur.
8. Consult your insurance company as soon as possible.

#### **4. Compliance with Japanese Law**

During their stay in Japan, any student who commits a crime, misdemeanor or any other illegal act, will be subject to legal procedures according to Japanese Law. Nagoya University also takes strict disciplinary measures against students who commit crimes or misdemeanors, and may expel them from university.

##### (1) Prohibition of Narcotics

In Japan, the possession and sale, for personal use or otherwise, of all narcotics and any illegal substances are strictly prohibited. If offered, refuse them. If leaving Japan temporarily, never agree to look after a stranger's luggage at the airport.

##### (2) Drinking and Smoking Restrictions

In Japan, people aged under 20 are not allowed to drink or smoke. Smoking is not allowed in many places, including stations, public facilities and within the campus. Nagoya city has special zones where smoking on the street is banned. If found smoking there, you will be fined.

Driving a car, riding a motorcycle or bicycle after drinking any amount of alcohol is a serious offence in Japan, and can also cause accidents. Never drive after drinking. Those who accept a ride in a car that is driven by a drunk driver or those who offer alcohol to a driver are all subject to punishment under Japanese law.

##### (3) Others

Whilst inside a shop, removing product wrappers, price tags or putting products into pockets or bags before actually paying for them may be treated as an attempt to shoplift in Japan. Talking loudly on your mobile phone or chatting with friends in public places, such as on a train, can cause disturbance in Japan.

#### **5. Safety Guide**

Japan is not as safe as most people think. There is the risk of crime anywhere in the world, including Japan. This is what you can do avoid problems.

- ◆ Avoid going out alone at night and keep away from deserted places.
- ◆ Many bag-snatchings occur in Nagoya. Keep your handbag close when walking on the street.
- ◆ Do not answer phone calls from unknown numbers. Do not open the door to strangers, even if they claim that they are representing certain companies. Lock and chain the door of your apartment when you are at home.
- ◆ There are deserted or dark places on campus which you should avoid. There is the risk of theft inside

and outside of buildings. Please always protect your property.

## **6. Culture shock**

Although “culture shock” is generally understood as a temporary shock felt when confronted by different cultural customs, ways of thinking and behavior patterns, it actually refers to a psychological state of depression caused by a succession of failure experiences in unfamiliar social situations. Culture shock is temporary and everybody goes through it to some extent in the process of cultural adaptation. General symptoms of culture shock include negative feelings such as: losing self confidence, feeling depressed, attributing all failure to yourself, feeling that nobody understands you, feeling inadequate, etc. Accordingly, you may lose all motivation to talk with Japanese people or to attend classes. Most of these psychological reactions are, again, very natural in the process of cultural adaptation. Please take time to cope with each single event in your life, and you will be able to overcome these emotions sooner or later.

## **7. Differences in “academic culture”**

It is widely accepted that different values, behavioral and communication patterns exist from culture to culture. However, we often fail to realize that there are also differences in “academic culture”, such as expected roles of academic advisers and students, classroom communication, evaluation criteria, etc. Such differences can also be a major cause of your stress. For example, the relationship between academic adviser and advisee is considered particularly important at the graduate level education in Japan. Some knowledge of the Japanese academic culture will help you achieve your goal more smoothly.

## **8. Cope with Stress**

If you feel pressured by stress or lose confidence in your ability to study, you should think about releasing yourself from these negative emotions. Achieving good results in your studies may take a certain amount of time, and ought to be viewed as an accumulative process. Sometimes, you will need to take a break. If you feel tired, do not push yourself too hard and try to enjoy some of your favorite foods, recreation, and physical exercise. It is also recommended that you talk with your friends, academic adviser, or international students advisors/counselors. Moreover, please do not consider the process of cultural adaptation solely as a cause of stress; you can learn tremendously about various cultures, including your own, from this process.

< Visit the office of ECIS Advising & Counseling Services >

If you feel that you cannot deal with stress or feel a sense of isolation or frustration, do not hesitate to ask for help from international counselors at the ECIS Advising & Counseling Services. There is an international student counselor who will support your personal and psychological concerns. A discussion with an international student counselor can help achieve a useful perspective on culture shock and insights into Japanese culture.

ECIS Advising & Counseling Services (7th floor, West Wing of IB Bldg.)

<http://www.isa.provost.nagoya-u.ac.jp/en/>

## **9. Harassment**

Nagoya University has set up a Harassment Consultation Center to prevent and eliminate the occurrence of any kinds of harassment, such as sexual harassment and academic harassment. Professional counselors deal with inquiries with utmost respect for their clients' feelings and wishes. Where the necessity arises, claims will be referred to the Committee for the Prevention of Harassment for investigation and arbitration. The Harassment Consultation Center works on issues of any degree of gravity. If you observe someone suffering from any kind of harassment, you may also come and report the case. In addition to the Harassment Consultation Center, each School at Nagoya University has appointed a faculty member as contact person (cf. see below). For English language consultation, you may visit the representative at the Education Center for International Students (ECIS). All consultation will be kept strictly confidential.

Nagoya University Harassment Consultation Center (Appointments by fax or E-mail)

Tel: 052-789-5806 (9:30-16:00)

Fax: 052-789-5968

E-mail: [sh-help@post.jimu.nagoya-u.ac.jp](mailto:sh-help@post.jimu.nagoya-u.ac.jp)

URL: <http://www.sh-help.provost.nagoya-u.ac.jp/>Contact persons at each School (including ECIS)

URL: <http://www.sh-help.provost.nagoya-u.ac.jp/pdf/madoguchi.pdf>>

# Campus Map

## Higashiyama Campus



### Main Buildings

- 1** Administration Bureau Buildings
- 2** Toyoda Auditorium / Symposion
- 3** Nagoya University Museum
- 4** University Library (Central Library)
- 5** Noyori Conference Hall
- 6** Noyori Materials Science Laboratory
- 7** Akasaki Institute

### Graduate School / School Buildings

- 8** Graduate School / School of Engineering Buildings
- 9** Engineering and Science Building (Central Building of Graduate School of Engineering / Particle and Astrophysical Science Building)
- 10** Graduate School / School of Science Buildings
- 11** Graduate School of Mathematics Building
- 12** Science and Agricultural Building
- 13** Graduate School of Bioagricultural Sciences / School of Agricultural Sciences Building
- 14** Environmental Studies Hall  
-Graduate School of Environmental Studies
- 15** Graduate School / School of Economics Building
- 16** Graduate School / School of Law Building
- 17** Graduate School of International Development Building
- 18** Graduate School of Education and Human Development / School of Education Building
- 19** Integrated Research Building (Arts and Social Sciences)
- 20** Graduate School / School of Letters Building
- 21** Central Building for Liberal Arts and Sciences  
-School of Informatics and Sciences Building  
-Institute of Liberal Arts & Sciences
- 22** Building A for Liberal Arts and Sciences
- 23** Graduate School of Languages and Cultures Building
- 24** Graduate School of information Science Building

### Centers / Institute Buildings

- 25** Center for Developmental Clinical Psychology and Psychiatry
- 26** Center for the Studies of Higher Education
- 27** Education Center for International Students
- 27a** Advising & Counseling Services, ECIS
- 28** Center for Asian Legal Exchange
- 29** Information Technology Center
- 30** Kobayashi-Maskawa Institute for the Origin of Particles and the Universe (KMI)
- 31** Research Center for Materials Science
- 32** Bioscience and Biotechnology Center
- 33** Radioisotope Research Center
- 34** Research Institute of Environmental Medicine
- 35** Hydrospheric Atmospheric Research Center
- 36** Institute for Advanced Research Hall
- 37** Solar-Terrestrial Environment Laboratory
- 38** Eco Topia Science Institute
- 39** International Cooperation Center for Agricultural Education
- 40** Research Laboratory Building
- 41** Research Center of Health, Physical Fitness and Sports

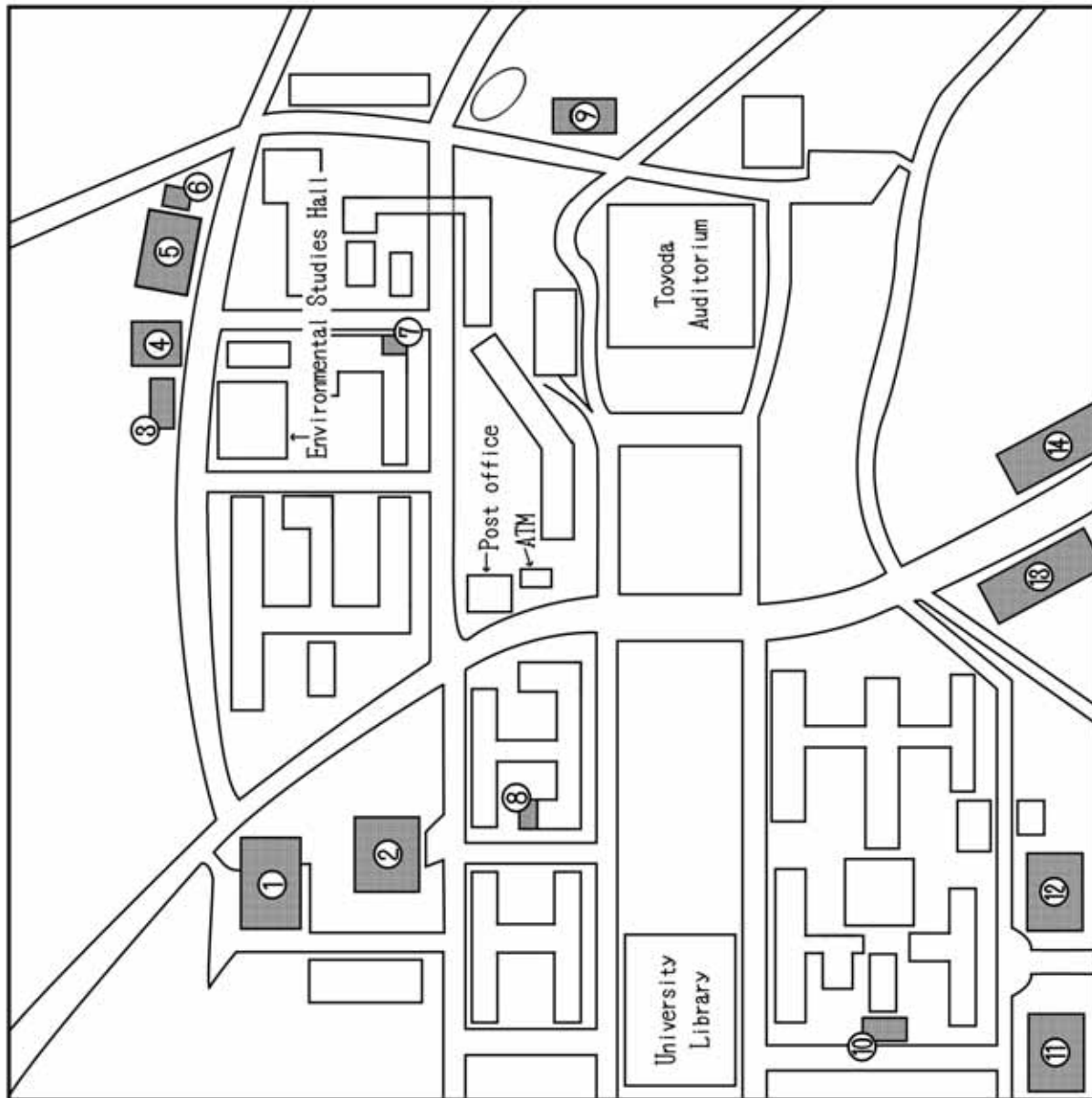
### Conference Halls & Galleries

- 42** Noyori Conference Hall
- 43** Noyori Materials Science Laboratory, Lecture Hall
- 44** Engineering and Science Building, ES Auditorium
- 45** Science South Building, Sakata & Hirata Hall
- 46** Environmental Studies Hall, Lecture Hall
- 47** Integrated Building (IB), Lecture Room
- 48** Graduate School / School of Economics, Conference Hall
- 49** Graduate School of International Development, Auditorium
- 50** Integrated Research Building (Arts and Social Sciences), Conference Room

\*International Planning Division. (2012). *Nagoya University Handbook For Foreign Researchers*. Nagoya, Japan: Nagoya University.

# DINING MAP

- ①Hokubu Shokudo / Cafeteria
- ②Shichimittei / Cafeteria
- ③Cafe Fronte / Coffee Shop
- ④Dining Forest / Cafeteria
- ⑤Restaurant Haranoki
- ⑥Rikei Shop / Convenience Store
- ⑦Craig's Cafe / Coffee Shop
- ⑧IB Cafe / Coffee Shop
- ⑨Shokuin Shokudo / Cafeteria
- ⑩Family Mart / Convenience Store
- ⑪Friendly Nanbu / Cafeteria
- ⑫Nanbu Shokudo / Cafeteria
- ⑬Hello Kid / Hamburger Steak Restaurant
- LAWSON / Convenience Store
- Bento Man / Lunchbox Shop
- Botantei / Chinese Restaurant
- ⑭Cafe Terrace Cremes / Coffee Shop
- Tsubokitei / Grilledmeat (yakimiku) Restaurant
- Kourantei
- GRAN PIATTO / Italian Restaurant



## Hospitals around Nagoya University (※English OK)

### *Nagoya Daini Red Cross Hospital*

Address: 2-9 Myoken-cho, Showa-ku, Nagoya

Tel: (052) 832-1121

Mon-Fri: 8:00-11:00

Closed on Sat, Sun, holidays

### *Watanabe Clinic*

Address: 1F Nikkou Yamate-dori Building, 3 -9-1 Yamate-dori, Showa-ku, Nagoya

Tel: (052)861-3450

Mon-Sat: 9:00-11:30

Mon, Wed-Fri: 16:00-17:30

Closed on Sun, holidays

### *Kai Clinic*

Address: 32-2 Myoken-cho, Showa-ku, Nagoya

Tel: (052)836-9136

Mon-Sat: 9:00-12:00

Mon-Wed, Fri: 18:00-20:30

Closed on Sun, holidays

### *Yamate Dermatologist*

Address: 2-9-1 Yamate-dori, Showa-ku, Nagoya

Tel: (052)836-4115

Mon, Tue, Thu-Sat: 9:30-12:30

Mon, Tue, Thu, Fri: 16:30-19:30

Sat: 14:30-17:30

Closed on Wed, Sun, holidays

### *Fujimi Dentist*

Address: 139 Yagotohujimi, Showa-ku, Nagoya

Tel: (052)835-3200

Mon-Wed, Fri, Sat: 9:30-12:30

Mon-Wed, Fri, Sat: 14:00-19:00

Closed on Thu, Sun, holidays



